


รายงานวิจัยฉบับสมบูรณ์

โครงการ ระเบียบวิธีเชิงตัวเลขที่ถูกต้องและมีประสิทธิภาพสำหรับคำนวณข้อมูลด้านการแตกร้าวสำหรับรอยแตกร้าวใด ๆ ในตัวกลางยืดหยุ่นเชิงเส้นสามมิติ

โดย รศ.ดร. จรูญ รุ่งอมรรัตน์ และคณะ

ธันวาคม 2556

สัญญาเลขที่ MRG5380159

รายงานวิจัยฉบับสมบูรณ์

โครงการ ระเบียบวิธีเชิงตัวเลขที่ถูกต้องและมีประสิทธิภาพสำหรับคำนวณข้อมูลด้านการแตกร้าวสำหรับรอยแตกร้าวใด ๆ ในตัวกลางยืดหยุ่นเชิงเส้นสามมิติ

โดย รศ.ดร. จรูญ รุ่งอมรรัตน์ และ ศ.ดร.ธีรพงศ์ เสนจันทร์ฒิไชย
ภาควิชาวิศวกรรมโยธา
คณะวิศวกรรมศาสตร์
จุฬาลงกรณ์มหาวิทยาลัย

สนับสนุนโดยสำนักงานคณะกรรมการการอุดมศึกษา และสำนักงานกองทุนสนับสนุนการวิจัย และจุฬาลงกรณ์มหาวิทยาลัย
(ความเห็นในรายงานนี้เป็นของผู้วิจัย สกอ. และ สกว. ไม่จำเป็นต้องเห็นด้วยเสมอไป)

ACKNOWLEDGEMENTS

The principal investigator gratefully acknowledges support provided by the Thailand Research Fund, Commission on Higher Education, and Chulalongkorn University (Grant No. MRG 5380159), and would also like to thank Professor Teerapong Senjuntichai for his useful guidance during the course of this investigation.

The investigator also would like to thank Professor Mark E. Mear from the Department of Aerospace Engineering and Engineering Mechanics, University of Texas at Austin, USA for his helpful suggestions and comments.

JAROON RUNGAMORNRAT

Department of Civil Engineering
Faculty of Engineering
Chulalongkorn University
August 2009

ABSTRACT

Project Code: MRG5380159

Project Title: Accurate and efficient numerical techniques for computing fracture data for arbitrary cracks in 3D linear elastic media

Investigators: Jaroon Rungamornrat and Teerapong Senjuntichai, Department of Civil Engineering, Faculty of Engineering, Chulalongkorn University

Email Address: Jaroon.r@chula.ac.th and Teerapong.S@chula.ac.th

Project Period: 2 years

Abstract: This investigation proposed an accurate and efficient numerical technique for stress analysis of un-cracked body and cracks in three-dimensional elastic media. The technique is established in a general context allowing the treatment of arbitrary-shaped cracks in both infinite and finite bodies, three-dimensional media made of generally anisotropic elastic materials, infinite bodies containing localized complex zones, and fractures with nano-scale influences. A pair of weakly singular, weak-form boundary integral equations for the displacement and traction is developed and successfully implemented in terms of the weakly singular, symmetric Galerkin boundary element method SGBEM and SGBEM-FEM coupling to determine the unknown crack-face and related boundary data. The crucial features of the proposed numerical technique are associated with the reduction of one spatial dimension of the key governing equation and all kernels contained in the involved boundary integral equations are only weakly singular allowing standard continuous interpolation functions to be used in the numerical approximation. Once the jump and sum crack-face displacement data is determined, it forms a sufficient set of information essential for independently extracting the mixed-mode stress intensity factors and the T-stresses. The accuracy of this data in the vicinity of the crack front is enhanced by using special crack-tip elements that contain proper shape functions and extra degrees of freedom along the crack front. With incorporation of these special elements, a pair of explicit and concise expressions for the stress intensity factors and for the T-stresses can be derived. To investigate the accuracy and efficiency of the proposed numerical technique, extensive numerical experiments are performed on various boundary value problems involving un-cracked bodies and cracks in both infinite and finite media. From the numerical study, the proposed technique is found promising and computationally robust for three-dimensional fracture analysis.

Keywords: cracks, integral equations, SGBEM, nano-scale influence, stress intensity factors, T-stresses

บทคัดย่อ

รหัสโครงการ: MRG5380159

ชื่อโครงการ: ระเบียบวิธีเชิงตัวเลขที่ถูกต้องและมีประสิทธิภาพสำหรับคำนวณข้อมูลด้านการแตกร้าวสำหรับรอยแตกร้าวใดๆ ในตัวกลางยืดหยุ่นเชิงเส้นสามมิติ

ชื่อนักวิจัย: รศ.ดร.จรูญ รุ่งอมรรัตน์ และ ศ.ดร. ธีรพงศ์ เสนจันทร์ฒิไชย ภาควิชาวิศวกรรมโยธา คณะวิศวกรรมศาสตร์ จุฬาลงกรณ์มหาวิทยาลัย

อีเมล์: Jaroon.r@chula.ac.th and Teerapong.S@chula.ac.th

ระยะเวลาโครงการ: 2 ปี

บทคัดย่อ: งานวิจัยนี้นำเสนอระเบียบวิธีเชิงตัวเลขที่ถูกต้องและมีประสิทธิภาพในการวิเคราะห์หน่วยแรงของวัตถุยืดหยุ่นสามมิติทั้งที่มีและไม่มีรอยแตกร้าว ระเบียบวิธีดังกล่าวพัฒนาขึ้นในกรอบทั่วไปที่สามารถจำลองรอยแตกร้าวรูปร่างใดๆในวัตถุไร้ขอบเขตและมีขอบเขตจำกัด วัตถุสามมิติที่ทำมาจากวัสดุยืดหยุ่นที่มีคุณสมบัติขึ้นกับทิศทาง วัตถุไร้ขอบเขตที่มีส่วนย่อยซับซ้อน และปัญหารอยแตกร้าวที่พิจารณาอิทธิพลในระดับนาโน สมการเชิงปริพันธ์พื้นผิวเอกฐานต่ำสำหรับการขจัดและแรงที่ผิวที่พัฒนาขึ้น ถูกนำมาใช้สำหรับพัฒนาระเบียบวิธีกาเลอร์คินบาวดารีเอลิเมนต์แบบเอกฐานต่ำ และระเบียบวิธีร่วมกับวิธีไฟไนต์เอลิเมนต์เพื่อหาตัวไม่ทราบค่าที่ผิวรอยแตกร้าวและขอบเขตของโดเมน จุดเด่นของระเบียบวิธีที่นำเสนอคือสมการกำกับหลักมีมิติที่ลดลงหนึ่งมิติ และเคอร์เนลทุกตัวที่เกี่ยวข้องกับสมการปริพันธ์มีความเป็นเอกฐานต่ำ ทำให้สามารถใช้ฟังก์ชันพื้นฐานแบบต่อเนื่องในการประมาณคำตอบได้ ปริมาณที่เกี่ยวข้องกับการกระโดดและการรวมของการขจัดบนผิวรอยแตกร้าวที่คำนวณได้สามารถใช้ในการหาค่าตัวประกอบความเข้มของความเค้นและหน่วยแรงทีได้ ความถูกต้องของข้อมูลดังกล่าวที่บริเวณขอบรอยแตกร้าวสามารถปรับปรุงได้โดยใช้ชิ้นส่วนย่อยพิเศษที่มีฟังก์ชันรูปร่างแบบพิเศษ และระดับขั้นความอิสระเพิ่มเติมที่ขอบรอยแตกร้าว นอกจากนี้การใช้ชิ้นส่วนพิเศษนี้ทำให้สามารถพัฒนาสูตรในการคำนวณตัวประกอบความเข้มของความเค้นและหน่วยแรงทีได้โดยตรง การตรวจสอบความถูกต้องและประสิทธิภาพของระเบียบวิธีเชิงตัวเลขที่นำเสนอ อาศัยการทดลองเชิงตัวเลขสำหรับปัญหาค่าขอบเขตที่มีความหลากหลายทั้งที่

เกี่ยวข้องกับวัตถุไร้ขอบเขตและที่มีขอบเขตจำกัดทั้งที่มีและไม่มีรอยแตกร้าว และจากการศึกษาดังกล่าวพบว่าระเบียบวิธีที่นำเสนอมีความ สามารถเชิงคำนวณที่เหมาะกับการวิเคราะห์ปัญหารอยแตกร้าวในวัตถุสามมิติ

คำสำคัญ: รอยแตกร้าว, สมการปริพันธ์, SGBEM, อิทธิพลในระดับนาโน, ตัวประกอบความเข้มของความเค้น, หน่วยแรงที

TABLE OF CONTENTS

Acknowledgements ii

Abstract (English) iii

Abstract (Thai) iv

Table of contents vi

List of figures viii

List of Tables xiv

Chapter I INTRODUCTION 1

1.1 Motivation and research significance 1

1.2 Background and review 2

1.3 Objectives 5

1.4 Scope of work 5

1.5 Methodology 6

1.6 Contribution 6

Chapter II FORMULATION 8

2.1 Problem description 8

2.2 Basic field equations 9

2.3 Standard integral relations 9

2.4 Decomposition of kernels 11

2.5 Completely regularized boundary integral relation for displacement 12

2.6 Completely regularized boundary integral relation for traction 14

2.7 Symmetric formulation for SGBEM 15

2.8 Formulation for SGBEM-FEM coupling 16

2.9 Formulation for cracks in infinite medium with nano-scale influence 21

Chapter III NUMERICAL IMPLEMENTATION 26

3.1 Discretization 26

3.2 Numerical integration 28

3.3 Evaluation of kernels 29
3.4 Determination of stress intensity factors and T-stresses 29
3.5 Coupling of SGBEM and commercial FE package 32
Chapter IV NUMERICAL RESULTS 34
4.1 Results from SGBEM 34
4.2 Results from SGBEM-FEM coupling 49
4.3 Influence of nano-scale influence 61
Chapter V CONCLUSION 70
References 72
Appendix A Publications 76
Appendix B Reprints 77

LIST OF FIGURES

2.1	Schematic of a three-dimensional body containing cracks	8
2.2	(a) Schematic of three-dimensional infinite medium containing crack and Localized complex zone and (b) schematic of BEM-region Ω^B and FEM-region Ω^F	18
2.3	(a) Schematic of three-dimensional infinite elastic medium containing an isolated crack and (b) prescribed traction on crack surfaces	21
2.4	Schematics of (a) the bulk material, (b) the zero-thickness layer S_c^+ and (c) the zero-thickness layer S_c^-	22
3.1	Schematic of crack-tip element and local coordinate system for calculation of stress intensity factors and T-stresses	30
4.1.1	Schematic of penny-shaped crack in infinite medium under (a) remote uniaxial tension and (b) remote pure bending	34
4.1.2	Three meshes adopted in the analysis of penny-shaped crack under uniformly distributed pressure	35
4.1.3	Normalized mode-I stress intensity factor versus angular coordinate for penny-shaped crack in isotropic infinite medium under remote pure bending	36
4.1.4	Normalized normal T-stress versus angular coordinate for penny-shaped crack in isotropic infinite medium under remote pure bending	36
4.1.5	Configuration of compact tension (CT) specimen recommended by ASTM E399-90 (1997)	38
4.1.6	Configuration of compact tension (CT) specimen used in the analysis	38
4.1.7	Coarse mesh or Mesh-1 for CT specimen thickness $t/a=1$	39
4.1.8	Medium mesh or Mesh-2 for CT specimen thickness $t/a=1$	40
4.1.9	Fine mesh or Mesh-3 for CT specimen thickness $t/a=1$	40

4.1.10 Normalized mode-I stress intensity factor along the crack front for CT specimen thickness $t/a = 1$. Results are reported for three meshes and three materials and *s* denotes the distance measured from the center of the crack front 41
4.1.11 Normalized mode-I stress intensity factor along the crack front for CT specimen thickness $t/a = 4$. Results are reported for three meshes and three materials and *s* denotes the distance measured from the center of the crack front 42
4.1.12 Normalized mode-I stress intensity factor along the crack front for CT specimen for sufficiently large thicknesses along with the plane strain solution from ASTM E399-90 (1997). Results are reported for isotropic material with $\nu = 0.1$ and *s* denotes the distance measured from the center of the crack front 43
4.1.13 Normalized mode-I stress intensity factor along the crack front for CT specimen for sufficiently large thicknesses along with the plane strain solution from ASTM E399-90 (1997). Results are reported for isotropic material with $\nu = 0.3$ and *s* denotes the distance measured from the center of the crack front 43
4.1.14 Normalized mode-I stress intensity factor versus the normalized distance along the crack front for various thicknesses and $\nu = 0$ 44
4.1.15 Normalized mode-I stress intensity factor versus the normalized distance along the crack front for various thicknesses and $\nu = 0.1$ 45
4.1.16 Normalized mode-I stress intensity factor versus the normalized distance along the crack front for various thicknesses and $\nu = 0.3$ 45
4.1.17 Normalized mode-I stress intensity factor versus the normalized distance along the crack front for various thicknesses and $\nu = 0.5$ 46
4.1.18 Normalized mode-I stress intensity factor versus the normalized distance along the crack front for various Poisson's ratios and $t/a = 1$ 47
4.1.19 Normalized mode-I stress intensity factor versus the normalized distance along the crack front for various Poisson's ratios and $t/a = 5$ 47

4.1.20 Normalized mode-I stress intensity factor versus the normalized distance along the crack front for various Poisson's ratios and $t/a = 10$ 48
4.1.21 Normalized mode-I stress intensity factor versus the normalized distance along the crack front for various Poisson's ratios and $t/a = 40$ 48
4.2.1 (a) Schematic of three-dimensional infinite medium containing spherical void and (b) schematic of BEM-region and FEM-region 49
4.2.2 Three meshes adopted in the analysis for FEM-region; meshes for BEM-region are identical to the interface mesh of FEM-region 50
4.2.3 Normalized radial displacement versus normalized radial coordinate for isotropic, linearly elastic material with $\nu = 0.3$ 51
4.2.4 Normalized radial stress versus normalized radial coordinate for isotropic, linearly elastic material with $\nu = 0.3$ 51
4.2.5 Normalized radial displacement versus normalized radial coordinate for isotropic, linearly elastic material with $\nu = 0.3$. Results are obtained from mesh-3 for both the coupling technique and the FEM with domain truncation 52
4.2.6 Normalized radial stress versus normalized radial coordinate for isotropic, linearly elastic material with $\nu = 0.3$. Results are obtained from mesh-3 for both the coupling technique and the FEM with domain truncation 53
4.2.7 Normalized radial displacement versus normalized radial coordinate for isotropic hardening material with $E_2 = 0$ 54
4.2.8 Normalized radial stress versus normalized radial coordinate for isotropic hardening material with $E_2 = 0$ 54
4.2.9 (a) Schematic of infinite medium containing penny-shaped crack, (b) crack under uniform normal traction σ_0, and (c) crack under uniform shear traction τ_0 55
4.2.10 (a) Schematic of selected FEM-region and the remaining BEM-region and (b) three meshes adopted in the analysis 55

4.2.11 Normalized mode-II and mode-III stress intensity factors for isolated penny-shaped crack subjected to shear traction. Results are reported for isotropic material with $\nu = 0.3$, zinc and graphite reinforced composite 57

4.2.12 Schematic of infinite medium containing spherical void of radius a and penny-shaped crack of radius a and subjected to uniform pressure at surface of void 58

4.2.13 (a) Decomposition of domain into BEM-region and FEM-region by a fictitious spherical surface of radius $4a$ and (b) three meshes adopted in analysis 58

4.2.14 Normalized mode-I stress intensity factors of penny-shaped crack embedded within infinite medium containing spherical void under uniform pressure 59

4.2.15 Normalized mode-I stress intensity factor of penny-shaped crack embedded within infinite medium containing spherical void under uniform pressure. Results are reported for isotropic hardening material with $E_1 = E$ and $E_2 = E/3$ 60

4.2.16 Maximum normalized mode-I stress intensity factor versus applied pressure at surface of void. Results are reported for isotropic linearly elastic material with $\nu = 0.3$ and two isotropic hardening materials 60

4.3.1 (a) Schematic of a penny-shaped crack of radius *a* embedded in an isotropic, linear elastic infinite medium subjected to uniformly distributed normal traction $t_3^+ = -t_3^- = t^0$; (b) Meshes adopted in the analysis. Mesh-1: 8 elements and 29 nodes. Mesh-2: 32 elements and 105 nodes. Mesh-3: 128 elements and 401 nodes 62

4.3.2 Penny-shaped crack under uniformly distributed normal traction, for $E = 107\ GPa$, $\nu = 0.33$ and residual surface tension $\tau^s = 0.6056\ N/m$: (a) Normalized crack opening displacement, (b) Normalized stress σ_{11}/t^0 in the vicinity of crack-front, (c) Normalized stress σ_{22}/t^0 in the vicinity of crack-front, and (d) Normalized stress σ_{33}/t^0 in the vicinity of crack-front 63

4.3.3 Penny-shaped crack under uniformly distributed normal traction, for $E = 107\ GPa,\ \nu = 0.33$ for different residual surface tension τ^s: (a) Normalized crack opening displacement and (b) Normalized stress σ_{33}/t^0 in the vicinity of crack-front 64

4.3.4 Penny-shaped crack under uniformly distributed normal traction, for different crack radii $a_0 = a/\Lambda = 0.5, 1.0, 5.0$ for $E = 107\ GPa,\ \nu = 0.33$, $\tau^s = 0.6056\ N/m$: (a) Normalized crack opening displacement and (b) Normalized stress σ_{33}/t^0 in the vicinity of crack-front 64

4.3.5 (a) Schematics of an elliptical crack embedded in an isotropic, linear elastic infinite medium subjected to uniformly distributed normal traction $t_3^+ = -t_3^- = t^0$ and (b) Meshes adopted in the analysis 65

4.3.6 Elliptical crack under uniformly distributed normal traction, for different aspect ratios $a/b = 1, 2, 3$ for $E = 107\ GPa,\ \nu = 0.33,\ \tau^s = 0.6056\ N/m$: (a) Normalized crack opening displacement along minor axis and (b) Normalized stress σ_{33}/t^0 in the vicinity of crack-front along minor axis 65

4.3.7 Elliptical crack under uniformly distributed normal traction for different residual surface tension τ^s, for $E = 107\ GPa,\ \nu = 0.33$, for different aspect ratios $a/b = 2, 3$: (a) Normalized crack opening displacement along minor axis and (b) Normalized stress σ_{33}/t^0 in the vicinity of crack-front along minor axis 66

4.3.8 Elliptical crack under uniformly distributed normal traction for different crack radii $a_0 = a/\Lambda = 0.5, 1.0, 5.0$ for $E = 107\ GPa,\ \nu = 0.33,\ \tau^s = 0.6056\ N/m$, for different aspect ratios $a/b = 2, 3$: (a) Normalized crack opening displacement along minor axis and (b) Normalized stress σ_{33}/t^0 in the vicinity of crack-front along minor axis 67

4.3.9 (a) Schematic of a pair of penny-shaped cracks of radius *a* embedded in an isotropic, linear elastic infinite medium subjected to uniformly

distributed normal traction $t_3^+ = -t_3^- = t^0$ and (b) Meshes adopted for each crack. Mesh-1: 8 elements and 29 nodes. Mesh-2: 32 elements and 105 nodes. Mesh-3: 128 elements and 401 nodes 67

4.3.10 Normalized crack opening displacement for a pair of penny-shaped cracks with radius $a_0 = 10$ and $h/a = 2.4$ under uniformly distributed normal traction, for $E = 107\,GPa$, $\nu = 0.33$ and $\tau^s = 0.6056\,N/m$ 68

4.3.11 Normalized maximum crack opening displacement for a pair of identical penny-shaped cracks under uniform normal traction, for E = 107 *GPa*, ν = 0.33: (a)-(c) $a_0 = 1$ and (d)-(f) $a_0 = 10$. 69

LIST OF TABLES

4.1.1 Normalized mode-I stress intensity factors and normal T-stress T_{11} for isolated penny-shaped crack subjected to remote uniaxial tension. Results are reported for $\nu = 0.3$ 35

4.1.2 Normalized mode-I stress intensity factors and normal T-stress T_{11} for isolated penny-shaped crack embedded in transversely isotropic medium and subjected to uniform pressure 37

4.1.3 Elastic constants (GPa) for zinc and cadmium. The axis of material symmetry is taken to direct along the x_3-coordinate direction 39

4.2.1 Non-zero elastic constants for zinc and graphite-reinforced composite (where axis of material symmetry is taken to direct along the x_3-coordinate direction) 56

4.2.2 Normalized mode-I stress intensity factor for isolated penny-shaped crack subjected to uniform normal traction 56

CHAPTER I

INTRODUCTION

1.1 Motivation and Research Significance

Flaws and cracks are induced naturally within materials constituting both engineering and non-engineering components either during manufacturing processes or during their service life applications. Presence of such defects in the components generally produces stress concentration and reduction of the global strength, results in fatigue growth and damage accumulations, and finally can lead to ultimate failure and loss of functions of such components. Therefore, fracture analysis and design becomes an essential and necessary ingredient in the damage/fatigue evaluation and assessment process in order to ensure safety and integrity of the designed components. For various classes of materials (e.g. glass, composites, concrete, rock, cast iron, etc.), the fracture-induced failure mechanism assumes in a brittle fashion and any inelastic deformation is merely contained within a small region in the vicinity of the crack front (viz. small scale yielding pertains). As a result, a mathematical model based upon linear elasticity is well-suited and sufficient for performing a stress analysis of such cracked bodies. It is known that a crack induced within a body acts as a local stress riser and, upon the linear elasticity theory, a local stress field is essentially singular along the crack front. The dominant behavior of such local singular stress field is commonly and completely characterized by a singular term resulting from a careful study of asymptotic fields in the neighborhood of the crack front. Such dominant term is known as the K-field and involves generally three parameters termed mode-I, mode-II and mode-III stress intensity factors. These fracture data (i.e. stress intensity factors) are vital and play an important role in linear elastic fracture analysis. In particular, knowledge of the stress intensity factors not only provides a measure of the dominant stress field around the crack front but also forms a basis in the investigation of crack growth and fatigue analysis. Besides the K-field, the second term in the asymptotic expansion (known as the T-stress) has recently gained significant attention from various investigators. This term is nonsingular but generates a constant stress field in the region ahead of the crack front. The T-stress has been found significantly useful in several circumstances such as prediction of the size and shape of a crack-tip plastic zone, investigation of the level of crack-tip stress tri-axiality and crack-tip constraint, investigation of stability behavior of crack growth, etc. The stress intensity factors along with the T-stress forms a two-parameter fracture model widely used in the recent failure/damage evaluation and assessment.

While asymptotic stress analysis in the local region near the crack front provides essential information about characteristics of some of leading terms in the expansion and their dependence on crack configuration, geometry of the body, loading conditions and material properties, it yields no information on the values of the stress intensity factors and the T-stress along the crack front and this still requires solving the boundary value problem associated with the entire cracked body. Note also that complexity posed by the presence of the stress singularity in the local region near the crack front and the need to formulate the problem within the three-dimensional context render such full boundary value problem theoretically and computationally challenging. Another nontrivial task is associated with the

post-process, once the problem is globally resolved, in order to accurately extract those essential fracture data (i.e. the stress intensity factors and the T-stress). On the basis of a careful literature search, works related to this specific area (see more details in the following section of background and review) are still relatively limited and this motivates the current investigation. In this study, we propose an efficient and accurate means to extract both the stress intensity factors and the T-stress for cracks in three-dimensional elastic bodies. The technique is to be established in a general context allowing the treatment of cracks in both infinite media and finite bodies, arbitrary crack configurations including planar and non-planar cracks, generally anisotropic elastic materials, and consideration of nano-scale influence and soft elastic solids. Results from the proposed investigation are anticipated not only to provide an alternative, more accurate and more efficient approach to existing techniques but also to ideally close the still existing gap of knowledge.

1.2 Background and Review

It is well known that both the stress intensity factors and the T-stress are essential fracture data that plays a significant role in linear elastic fracture mechanics (LEFM); in particular, they completely characterize the first two leading terms in the asymptotic expansion of the local stress field in the neighborhood of the crack front (e.g. Williams, 1957; Cotterell and Rice, 1980; Ting, 1985; Leblond, 1989; Leblond and Torlai, 1992). The stress intensity factors provide a measure of the dominant behavior of the local stress field while the latter represents the constant terms in that asymptotic expansion. From an extensive study on the asymptotic behavior of fields near the crack front along with a careful dimensional analysis, both the stress intensity factors and the T-stress has been found strongly dependent on the crack configuration and overall geometry of the cracked body, properties of constituting materials, and loading conditions (e.g. Broek, 1982; Sanford, 2003; Anderson, 2005). Nevertheless, values of the stress intensity factors and the T-stress cannot be obtained directly from the asymptotic analysis but it still requires solving the boundary value problem associated with the entire cracked body.

As a result of complexity posed by the presence of stress singularity along the crack front, analytical solutions for corresponding boundary value problems (or more precisely the solutions for the stress intensity factors and the T-stress) are limited to simple crack configurations (e.g. straight cracks in 2D problems and penny-shaped and elliptical cracks in 3D problems), simple loading conditions (e.g. pure mode-I loading and pure shear traction), simple domains (e.g. infinite 2D and 3D bodies), and simple linear elastic materials (e.g. isotropic solids). Some of those relevant investigations include the work of Westergaard (1939), Kassir and Sih (1975), Fabrikant (1989), Chen (2000), Wang (2004), Kirilyuk and Levchuk (2007). In three-dimensional applications, fractures problems are often mixed-mode and geometries of the body and cracks can possibly be very sophisticated and this, therefore, requires robust computational techniques to accurately obtain such fracture data.

Boundary integral equation methods (BIEMs) has been found efficient and attractive for linear elasticity and linear fracture analysis since the spatial dimension of the key governing equation is less than that of the domain by one (e.g. Brebbia and Dominguez, 1983; Cruse, 1988). This crucial feature renders this group of methods gaining significant benefit in terms of computational efficiency and effort required for mesh generation; in particular, only the boundary of the domain and the crack surface require discretization. Such advantage becomes more apparent when three-dimensional problems and bodies containing

multiple or non-planar cracks are involved. Various investigators have successfully implemented the BIEMs to model cracks in both linear elastic infinite domain (e.g. Weaver, 1977; Gu and Yew, 1988; Xu and Ortiz, 1993; Xu, 2000) and finite domain (e.g. Martha *et al*., 1992; Pan and Yuan, 2000; Li *et al*., 1998; Frangi *et al*., 2002; Ariza *et al*., 2004; Rungamornrat and Mear, 2008b; Rungamornrat and Mear, 2011). Besides that the boundary value problem associated with the entire cracked body must be solved accurately and efficiently, an algorithm to extract the stress intensity factors and the T-stressed at any point along the crack front from the solved crack-face data must receive special attention since it significantly influences the accuracy of numerical solutions.

For stress intensity factor calculation, quarter-point elements have commonly been employed in various investigations to capture the square root singularity of the local stress field near the crack front (e.g. Xu and Ortiz, 1993; Xu, 2000; Ariza *et al*., 2004). Although such elements provide proper shape functions that can represent the singular term in the local stress expansion, the order of approximation is still relatively low and, therefore, sufficiently small quarter-point elements must be used along the crack front in order to obtain reasonably accurate results. In addition, a nontrivial extrapolation technique must be adopted to post-process crack-face data on the quarter-point element to obtain the stress intensity factors. Li *et al*. (1998) implemented a weakly singular, symmetric Galerkin boundary element method (SGBEM) with use of special crack-tip elements along the crack front to perform stress analysis of isotropic, linearly elastic cracked bodies. This special crack-tip element possesses two superior features than those of the quarter-point element in that its shape functions can represent local stress field near the crack front to sufficiently high order and it contains extra degrees of freedom along the crack front that correspond directly to the gradient of the relative crack-face displacement. The former feature allows the use of a relatively large size of crack-tip elements while the latter feature provides a means to extract the stress intensity factors in a straightforward fashion. Frangi *et al*. (2002) offered an identical weakly singular SGBEM to that by Li *et al*. (1998) but, instead of using special crack-tip elements, they simply utilized standard elements along the crack front along with a special (unidentified) extrapolation technique to compute the stress intensity factors for cracks in isotropic elastic media. While their presented numerical results exhibit good accuracy, use of standard basis functions to accurately capture the singular field near the crack front and the extrapolation technique employed are still questionable. Later, Rungamornrat and Mear (2008b) generalized the crack-tip elements developed by Li *et al* (1998) and then utilized them in the implementation of the weakly singular SGBEM for modeling cracks in three-dimensional anisotropic media. While their boundary integral equations were derived within the context of general anisotropy and the numerical scheme to extract the stress intensity factors has proven promising, numerical results were reported only for cracks in isotropic and transversely isotropic solids. On the basis of a careful literature search, no other recent advance in boundary integral equation methods for calculation of the stress intensity factors for cracks in elastic media has been found. In this investigation, we propose an accurate and more efficient numerical scheme for computing the mixed-mode stress intensity factors for cracks of arbitrary shape contained in three-dimensional isotropic and generally anisotropic media. The weakly singular SGBEM, developed in a broad context by Rungamornrat and Senjuntichai (2009) and Rungamornrat (2009), is to be employed as a supporting computational tool for solving the boundary value problem associated with the entire cracked body.

A vast number of researches towards the development of both analytical and numerical techniques for determining the T-stress of cracks in linearly elastic media has also been well recognized and gained significant attention from various investigators in the past three decades. Some of those relevant works are briefly summarized below not only to demonstrate the history and current advances in this specific area but also to identify the gap of knowledge to be emphasized in the present investigation. Within the context of two-dimensional boundary value problems, Rice (1974) originally studied the influence of the T-stress on the estimation of the plastic zone size and shape using Barrenblatt-Dugdale yielding model. Du and Hancock (1991) investigated the influence of the T-stress on the plastic zone size and shape for a plane strain crack using Von-Mises yield criterion and they concluded that the plastic zone is enlarged and rotated forward for the negative T-stress and is reduced and rotated backward for the positive T-stress. Fett (1997) determined the T-stress in an edge cracked rectangular finite plate by first using a boundary collocation technique to construct Green's functions for a pair of normal point forces and then applied them to obtain a solution for the prescribed arbitrary normal traction. Later, Fett (1998) employed the same technique to calculate the T-stress in rectangular plates and circular disks with edged crack and center crack subjected to both tensile and bending loads. Wang (2001) used weight-function technique and finite element method to determine the T-stress for various test specimens including a single edge cracked plate (SECP), a double edge cracked plate (DECP) and a center cracked plate (CCP) under uniform, linear, parabolic and cubic normal traction acting to the crack surfaces. Fett and Rizzi (2006) applied the weight-function technique and finite element method to compute T-stress of a compact tension crack (CT), a double cantilever crack (DCC) and an edge cracked bar (ECB) loaded by near-tip normal traction. Fett et al. (2006) studied the T-stress for kinked and forked cracks in two-dimensional isotropic plate subjected to traction on the crack surface by using a technique of Green's function. Zhou et al. (2013) employed a symplectric expansion method to determine the T-stress for an edged crack in an isotropic, linearly elastic plate bonded by two different materials. This symplectic expansion method was found to be capable of treating either mixed or complex boundary conditions.

For three-dimensional fracture analysis and modeling, Wang (2002) determined the T-stress for a semi-elliptical, surface-breaking crack in an isotropic, linear elastic finite thick plate subjected to tensile and bending loads at both ends. In his work, the finite element method was utilized to determine field quantities and the interaction integral formula was adopted to extract the T-stress along the crack front. In 2003, Wang and Bell extended the work of Wang (2003) to be capable of modeling more general end loading conditions such as uniform, linear, parabolic, and cubic loads. Later, Wang (2004) presented an analytical solution for the T-stress of a penny-shaped crack embedded in an isotropic linear elastic infinite body under the action of remote tension and bending by using the potential-theory-based method and Hankel's transformation. Qu and Wang (2006) modeled a corner quarter-elliptical crack in a thick plate under the tensile and bending loads at both ends by using the finite element method along with the interaction integral formula to obtain the T-stress. Kirilyuk and Levchuk (2007) generalized the work of Wang (2004) to solve for the elastic T-stress of a flat-elliptical crack in an isotropic, linearly elastic, infinite body under remote tension and bending by using the method of potential theory and a special collection of harmonic functions. Schutte and Molla-Abbasi (2007) and Molla-Abbasi and Schutte (2008) applied the potential-theory-based method, technique of Green's function, Hankel's

transformation and a finite element method to calculate the T-stress of both penny-shaped and flat-elliptical cracks embedded in a three-dimensional isotropic infinite domain under remote mixed-mode tractions. The influence of the T-stress on estimation of the plastic zone size using the Von-Mises yielding criterion was also investigated. Lewis and Wang (2008) employed the finite element technique to compute the elastic T-stress for a circumferential crack in an isotropic finite cylinder subjected to either tensile and bending loads at its ends or uniform, linear, parabolic and cubic normal tractions on the crack surface. Recently, Meshii et al. (2010) used the finite element method to determine the elastic T-stress of a semi-elliptical crack embedded in a three-dimensional isotropic finite cylinder under uniform, linear, parabolic and cubic normal tractions on the crack surface.

While various investigations have been devoted to the development of techniques to determine of the T-stress, most of existing works were restricted only to either cracks in two-dimensional, isotropic bodies (e.g., Shah *et al*., 2006; Yu *et al*., 2006; Ananthasayanam *et al*., 2007; Profant *et al*., 2008; Chen *et al*. 2008; Chen *et al*., 2009) or three-dimensional problems with specific crack and domain configurations (e.g. Lewis and Wang, 2008; Molla-Abbasi and Schutte, 2008). The principal investigator is unaware of any advance of techniques that are capable of comprehensively solving the elastic T-stress for cracks of arbitrary geometry embedded in a general, three-dimensional media made of generally anisotropic materials (e.g., transversely isotropic and orthotropic solids), and this serves as the key motivation of the proposed investigation aiming to fill such gap of knowledge.

1.3 Objectives

The key objectives of the current investigation are

(1) to develop a proper mathematical model, in terms of weakly singular boundary integral equations and other appropriate forms, that governs the data essential and sufficient for computing the fracture information along the crack front including the crack opening displacement, mixed-mode stress intensity factors and the elastic T-stress for cracks in three-dimensional, linearly elastic media with and without consideration of nano-scale influence, and

(2) to develop efficient and accurate numerical techniques such as the SGEBM and SGBEM-FEM coupling to extract fracture information along the crack front (e.g., crack opening displacement, stress intensity factors, and the T-stress) for isolated cracks in both isotropic and generally anisotropic linearly elastic infinite and finite media

1.4 Scope of Work

Scope of the present study and assumptions relevant to the development are summarized as follows:

(1) the boundary value problem considered in this investigation is *linear* and governed by the theory of local linear elasticity;

(2) a body associated with the boundary value problem is three-dimensional and can be either infinite (associated with a whole space) or finite;

(3) a body is assumed to be free of a body force;

(4) a constituting material is assumed to be linearly elastic and spatially independent (or homogeneous) but there is no restriction of its properties on the directional

dependence. The latter allows the treatment of both isotropic and generally anisotropic materials; and

(5) the crack configuration or geometry can be represented by a piecewise smooth surface otherwise it is arbitrary. Planar and non-planar cracks, embedded and surface breaking cracks, single and multiple cracks can be treated.

1.5 Methodology

The present study consists of several main tasks with methodology, procedures, and involved fundamental theories for each task being briefly summarized as follows:

(1) basic field equations governing the body containing cracks (i.e., equilibrium equations, strain-displacement relation, and constitutive law) are derived from the classical theory of linear elasticity where the constituting material is assumed to be fully anisotropic;

(2) the nano-scale influence is modeled by Gurtin-Murdoch surface elasticity model;

(3) key governing equations are formulated in terms of weakly-singular, weak-form boundary integral equations for the displacement and traction where the special decompositions of strongly singular and hyper-singular kernels are utilized along with the integration by parts via Strokes' theorem;

(4) the key governing equation to describe the nano-scale influence follows the standard technique of weight residual;

(5) symmetric formulations for various types of boundary value problems are established by properly employing both the displacement and traction boundary integral equations and the final form involves unknown displacement and traction on the ordinary boundary and the unknown jump and sum of the displacement across the crack surface;

(6) selected numerical techniques based on the weakly-singular, symmetric Galerkin boundary element method (SGBEM) and the coupling with standard finite element method (FEM) are implemented to construct the approximate solution of all primary unknowns (i.e., displacement and traction on the ordinary boundary and jump and sum of the displacement across the crack surface);

(7) special local interpolation functions (enriched by square-root functions along with the introduction of extra degrees of freedom along the crack front) are employed to accurately model the jump and sum of the displacement across the crack surface in the vicinity of the crack front;

(8) extrapolation-free formula for determining both the stress intensity factors and elastic T-stresses are established in terms of the solved jump and sum of the displacement local to the crack front; and

(9) formulation, numerical procedure, and implementation of an in-house computer code are extensively verified with reliable benchmark solutions

1.6 Contribution

The significant contribution gained from the present study is an accurate and efficient numerical technique for computing the essential fracture data such as relative crack-face displacement, the mixed-mode stress intensity factors, and the T-stress for cracks in three-dimensional elastic media with and without the consideration of nano-scale influence. The

attractive features of the proposed technique are that it allows the treatment of cracks in both infinite and finite media, is applicable to cracks of arbitrary configuration (including both planar and non-planar cracks and embedded and surface breaking cracks), and applies to both isotropic and generally anisotropic materials. The numerical technique will be implemented in terms of a computer code that is user friendly and constitutes a well-suited tool for stress analysis of elastic bodies containing cracks. This robust computational tool could potentially be beneficial in the investigation of various aspects of fracture phenomena, e.g. crack growth simulation and fatigue/damage evaluation and assessment. In addition, the developed numerical procedure can readily be coupled with a standard finite element method to solve a larger class of boundary value problems (e.g., problems involving cracks and localized nonlinear zones and treatment of nano-scale influence to simulate the behavior and responses of nano-cracks).

CHAPTER II

FORMULATION

This chapter summarizes the problem description, basic field equations, the conventional boundary integral relations for the displacement and stress, the decomposition of strongly singular and hyper-singular kernels, the development of completely regularized boundary integral equations, and the formulation of the governing equations for the boundary value problem of a medium containing cracks.

2.1 Problem Description

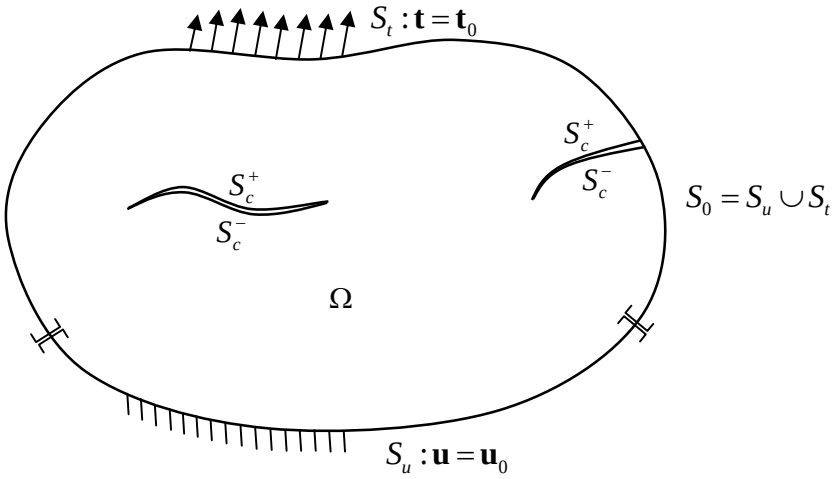

Figure 2.1: Schematic of a three-dimensional body containing cracks

Let us consider a three-dimensional body Ω which is made of a homogeneous, generally anisotropic, linearly elastic material with prescribed elastic constants E_{ijkl} and contains an embedded crack and a surface breaking crack as shown schematically in Figure 2.1. The body is assumed to be nice in the sense that any differential and integral operations involved in the development presented further below are valid when they are performed on this body. The total boundary of the body consists of the ordinary boundary, denoted by S_0, and the surface of the cracks, represented by two geometrically identical surfaces S_c^+ and S_c^-. The ordinary boundary S_0 can be decomposed into a surface S_u on which the displacement is prescribed (i.e., $\mathbf{u} = \mathbf{u}_0 \ \forall \mathbf{x} \in S_u$) and a surface S_t on which the traction is prescribed (i.e., $\mathbf{t} = \mathbf{t}_0 \ \forall \mathbf{x} \in S_t$) whereas, on the crack surface, the traction is fully prescribed (i.e., $\mathbf{t} = \mathbf{t}_{c0} \ \forall \mathbf{x} \in S_c^+ \cup S_c^-$). In the present study, all the surfaces S_0, S_c^+ and S_c^- are assumed to be sufficiently smooth (i.e., the unit normal vector is well defined) and the body is free of the body force. For convenience in further development, a reference Cartesian coordinate system $\{\mathbf{0}; x_1, x_2, x_3\}$ with the origin $\mathbf{0}$ is introduced.

2.2 Basic Field Equations

Behavior of the body Ω is governed by a classical theory of linear elasticity as briefly indicated below. In the absence of the body force, the stress field $\boldsymbol{\sigma} = \boldsymbol{\sigma}(\mathbf{x})$ (with its components in the reference coordinate system $\{\mathbf{0}; x_1, x_2, x_3\}$ denoted by σ_{ij}) must be divergence free everywhere, i.e.,

$$\sigma_{ij,j} = 0 \tag{2.1}$$

where $()_{,j} = \partial() / \partial x_j$. From here to what follows, all indices range from 1 to 3 and repeated indices imply the summation over their range. The stress field $\boldsymbol{\sigma} = \boldsymbol{\sigma}(\mathbf{x})$ is related linearly to the strain field $\boldsymbol{\varepsilon} = \boldsymbol{\varepsilon}(\mathbf{x})$ via the generalized Hooke's law, i.e.,

$$\sigma_{ij} = E_{ijkl}\varepsilon_{kl} \tag{2.2}$$

where E_{ijkl} are prescribed elastic constants which are spatially independent and satisfy following symmetries: $E_{ijkl} = E_{ijlk} = E_{jikl} = E_{klij}$. For the special case of isotropy, the elastic constants involve only two independent material parameters and take a simple form:

$$E_{ijkl} = \mu(\delta_{ik}\delta_{jl} + \delta_{il}\delta_{jk}) + \lambda\delta_{ij}\delta_{kl} \tag{2.3}$$

where μ and λ are Lame's constants and δ_{ij} is Kronecker-delta symbol. The relationship between the strain field $\boldsymbol{\varepsilon} = \boldsymbol{\varepsilon}(\mathbf{x})$ and the displacement field $\mathbf{u} = \mathbf{u}(\mathbf{x})$ are governed by linearized kinematics or infinitesimal deformation theory, i.e.,

$$\varepsilon_{ij} = \frac{1}{2}\left(u_{i,j} + u_{j,i}\right) \tag{2.4}$$

In addition, the traction $\mathbf{t}$ at any point on a sufficiently smooth surface can be related to the stress at the same point as

$$t_i = \sigma_{ij} n_j \tag{2.5}$$

where $\mathbf{n}$ is a unit normal to the surface. The relations (2.1), (2.2) and (2.4) are basic field equations governing all unknown field quantities $\mathbf{u} = \mathbf{u}(\mathbf{x})$, $\boldsymbol{\varepsilon} = \boldsymbol{\varepsilon}(\mathbf{x})$ and $\boldsymbol{\sigma} = \boldsymbol{\sigma}(\mathbf{x})$.

2.3 Standard Integral Relations

By applying Somigliana's identity to a body Ω, it leads to a boundary integral relation for the displacement at any interior point $\mathbf{x} \in \Omega$ (see Rungamornrat and Mear, 2008a):

$$\begin{aligned} u_p(\mathbf{x}) = & \int_{S_c^+} U_j^p(\boldsymbol{\xi} - \mathbf{x}) \Sigma t_j(\boldsymbol{\xi}) dA(\boldsymbol{\xi}) - \int_{S_c^+} S_{ij}^p(\boldsymbol{\xi} - \mathbf{x}) n_i(\boldsymbol{\xi}) \Delta u_j(\boldsymbol{\xi}) dA(\boldsymbol{\xi}) \\ & + \int_{S_0} U_j^p(\boldsymbol{\xi} - \mathbf{x}) t_j(\boldsymbol{\xi}) dA(\boldsymbol{\xi}) - \int_{S_0} S_{ij}^p(\boldsymbol{\xi} - \mathbf{x}) n_i(\boldsymbol{\xi}) u_j(\boldsymbol{\xi}) dA(\boldsymbol{\xi}) \end{aligned} \tag{2.6}$$

where $\Sigma t_j(\xi) = t_j(\xi^+) + t_j(\xi^-)$ denotes the sum of tractions on both crack surfaces; $\Delta u_j(\xi) = u_j(\xi^+) - u_j(\xi^-)$ denotes the jump of the displacement across the crack surface; $U_j^p(\xi - \mathbf{x})$ is the displacement fundamental solution; and $S_{ij}^p(\xi - \mathbf{x})$ is the generalized stress fundamental solution. The explicit form for $U_j^p(\xi - \mathbf{x})$ and $S_{ij}^p(\xi - \mathbf{x})$ for general anisotropy is given by

$$U_j^p(\xi - \mathbf{x}) = \frac{1}{8\pi^2 r} \oint_{\mathbf{z}\cdot\mathbf{r}=0} (\mathbf{z},\mathbf{z})_{kl}^{-1} z_i z_j ds(\mathbf{z}) \tag{2.7}$$

$$S_{ij}^p(\xi - \mathbf{x}) = E_{ijkl} \frac{\partial U_k^p(\xi - \mathbf{x})}{\partial \xi_l} \tag{2.8}$$

where $\mathbf{r} = \xi - \mathbf{x}$, $r = \|\mathbf{r}\|$, $(\mathbf{z},\mathbf{z})_{kl} = z_i E_{iklj} z_j$ and the closed contour integral is to be evaluated over a unit circle $\|\mathbf{z}\|$ = 1 on a plane defined by $\mathbf{z}\cdot\mathbf{r} = 0$. It is important to remark that the fundamental solutions $U_j^p(\xi - \mathbf{x})$ and $S_{ij}^p(\xi - \mathbf{x})$ are singular at $\xi = \mathbf{x}$ of $\mathcal{O}(1/r)$ and $\mathcal{O}(1/r^2)$, respectively. For the special case of isotropy, $U_j^p(\xi - \mathbf{x})$ and $S_{ij}^p(\xi - \mathbf{x})$ take a simple form:

$$U_j^p(\zeta) = \frac{1}{16\pi(1-\nu)\mu r}\left\{(3-4\nu)\delta_{pj} + \frac{\zeta_p \zeta_j}{r^2}\right\} \tag{2.9}$$

$$S_{ij}^p(\zeta) = \frac{1}{8\pi(1-\nu)r^2}\left\{\frac{1-2\nu}{r}(\zeta_p \delta_{ij} - \zeta_i \delta_{pj} - \zeta_j \delta_{pi}) - \frac{3\zeta_p \zeta_i \zeta_j}{r^3}\right\} \tag{2.10}$$

where $\zeta = \xi - \mathbf{x}$, ν is Poisson ratio, and μ is elastic shear modulus. It is worth noting that in the integral relation (2.6), the integrals over the entire crack surfaces $S_c^+ \cup S_c^-$ reduces to the integrals over a single surface S_c^+ due to the fact that S_c^+ and S_c^- are geometrically identical with opposite unit normal vectors and the functions $U_j^p(\xi - \mathbf{x})$ and $S_{ij}^p(\xi - \mathbf{x})$ are continuous on the crack surfaces.

By taking derivative of the integral relation (2.6) to obtain the displacement gradient and then applying the relations (2.2) and (2.4), it leads to a boundary integral relation for the stress at any interior point $\mathbf{x}$:

$$\begin{aligned}\sigma_{lk}(\mathbf{x}) = &-\int_{S_c^+} S_{lj}^k(\xi - \mathbf{x}) \Sigma t_j(\xi) dA(\xi) + \int_{S_c^+} \Sigma_{ij}^{lk}(\xi - \mathbf{x}) n_i(\xi) \Delta u_j(\xi) dA(\xi) \\ &- \int_{S_0} S_{lj}^k(\xi - \mathbf{x}) t_j(\xi) dA(\xi) + \int_{S_0} \Sigma_{ij}^{lk}(\xi - \mathbf{x}) n_i(\xi) u_j(\xi) dA(\xi)\end{aligned} \tag{2.11}$$

where $\Sigma_{iJ}^{lK}(\xi - \mathbf{x})$ is a function defined in terms of the elastic constants E_{ijkl} by

$$\Sigma_{ij}^{lk}(\boldsymbol{\xi}-\mathbf{x}) = E_{lkpq}\frac{\partial S_{ij}^{p}(\boldsymbol{\xi}-\mathbf{x})}{\partial \xi_q} \tag{2.12}$$

It is remarked that the function $\Sigma_{iJ}^{lK}(\boldsymbol{\xi}-\mathbf{x})$ is singular at a point $\boldsymbol{\xi}=\mathbf{x}$ of $\mathcal{O}(1/r^2)$.

It is worth noting that the boundary integral relations (2.6) and (2.11) can be used to determine the displacement and stress at any interior point **x** provided that all unknown data of the displacement and traction on the boundary and the crack surface is completely known. By taking an appropriate limit process of the boundary integral relation (2.6) to a point on the total boundary of the body, it yields the displacement boundary integral equation. For a body containing no crack, such integral equation is sufficient for determining all unknown data on the boundary. However, for a body containing cracks, such equation is mathematically degenerate since it contains incomplete information of the traction on the crack surface (i.e., it contains only the sum of the traction). To overcome this mathematical difficulty, techniques based on the domain decomposition to partition a body along the crack surfaces were proposed (e.g., Blandford *et al*, 1981; Saez *et al*, 1997). However, such strategy possesses several major drawbacks; for instance, the large number of additional unknowns that are introduced along the cut, the difficulty of the decomposition for a body containing non-planar or multiple cracks, and the treatment of singularity of the traction along the cut ahead of the crack front. An attractive alternative is to employ the traction boundary integral equation for the crack surface. Such equation can readily be obtained from the boundary integral relation for the stress (2.11) via taking appropriate limit process to a point on the crack surface S_c^+. While the conventional traction boundary integral equation is sufficient for analysis of crack problems, it contains both strongly singular and hyper-singular kernels that render the involved integrals difficult to be treated theoretically and numerically. To alleviate the strong mathematical requirement posed by the conventional traction boundary integral equation, various regularization procedures have been introduced to obtain singularity-reduced integral equations (e.g., Weaver, 1977; Bui, 1977, Gu and Yew, 1988; Xu and Ortiz, 1993; Bonnet, 1995; Xu, 2000; Li and Mear, 1998; Li et al., 1998; Rungamornrat, 2008a,b).

2.4 Decompositions of kernels

To aid the regularization procedure described further below, the strongly singular kernel $S_{ij}^{p}(\boldsymbol{\xi}-\mathbf{x})$ and the hyper singular kernel $\Sigma_{iJ}^{lK}(\boldsymbol{\xi}-\mathbf{x})$ are, first, decomposed into two parts as follows (see details of development in the work of Rungamornrat and Mear (2008a) and Rungamornrat and Senjuntichai (2009)):

$$S_{ij}^{p}(\boldsymbol{\xi}-\mathbf{x}) = H_{ij}^{p}(\boldsymbol{\xi}-\mathbf{x}) + \varepsilon_{ism}\frac{\partial}{\partial \xi_s}G_{mj}^{p}(\boldsymbol{\xi}-\mathbf{x}) \tag{2.13}$$

$$\Sigma_{ij}^{lk}(\boldsymbol{\xi}-\mathbf{x}) = -E_{ijkl}\delta(\boldsymbol{\xi}-\mathbf{x}) + \varepsilon_{lsm}\frac{\partial}{\partial \xi_s}\varepsilon_{irt}\frac{\partial}{\partial \xi_r}C_{mj}^{tk}(\boldsymbol{\xi}-\mathbf{x}) \tag{2.14}$$

where ε_{ism} denotes the alternating symbol; $\delta(\boldsymbol{\xi}-\mathbf{x})$ denotes the Dirac-delta distribution centered at **x**; and $H_{ij}^{p}(\boldsymbol{\xi}-\mathbf{x})$, $G_{mj}^{p}(\boldsymbol{\xi}-\mathbf{x})$ and $C_{mj}^{tk}(\boldsymbol{\xi}-\mathbf{x})$ are functions defined by

$$H_{ij}^{p}(\boldsymbol{\xi}-\mathbf{x}) = -\delta_{jp}\frac{\xi_i - x_i}{4\pi r^3} \tag{2.15}$$

$$G_{mj}^{p}(\boldsymbol{\xi}-\mathbf{x}) = \frac{\varepsilon_{mqa}E_{qjkl}}{8\pi^2 r}\oint_{\mathbf{z}\cdot\mathbf{r}=0}(\mathbf{z},\mathbf{z})_{kp}^{-1}z_a z_l ds(\mathbf{z}) \tag{2.16a}$$

$$C_{mj}^{tk}(\boldsymbol{\xi}-\mathbf{x}) = \frac{A_{mtsl}^{kjap}}{8\pi^2 r}\oint_{\mathbf{z}\cdot\mathbf{r}=0}(\mathbf{z},\mathbf{z})_{ap}^{-1}z_s z_l ds(\mathbf{z}) \tag{2.16b}$$

with the constants A_{mtsl}^{kjap} defined by

$$A_{mtsl}^{kjap} = \varepsilon_{ptd}\varepsilon_{pmq}\left\{E_{djpl}E_{qkms} - \frac{1}{3}E_{lmps}E_{djkq}\right\} \tag{2.17}$$

It is evident that the function $H_{ij}^{p}(\boldsymbol{\xi}-\mathbf{x})$ is independent of material constants and singular at a point $\boldsymbol{\xi}=\mathbf{x}$ of $\mathcal{O}(1/r^2)$ whereas $G_{mj}^{p}(\boldsymbol{\xi}-\mathbf{x})$ and $C_{mj}^{tk}(\boldsymbol{\xi}-\mathbf{x})$ depends primarily on material properties and singular at a point $\boldsymbol{\xi}=\mathbf{x}$ of $\mathcal{O}(1/r)$. For the special case of isotropy, the kernels $G_{mj}^{p}(\boldsymbol{\xi}-\mathbf{x})$ and $C_{mj}^{tk}(\boldsymbol{\xi}-\mathbf{x})$ admit following closed form in terms of elementary functions

$$G_{mj}^{p}(\boldsymbol{\xi}-\mathbf{x}) = \frac{1}{8\pi(1-\nu)r}\left[(1-2\nu)\varepsilon_{mpj} + \frac{(\xi_p - x_p)(\xi_a - x_a)}{r^2}\varepsilon_{ajm}\right] \tag{2.18}$$

$$C_{mj}^{tk}(\boldsymbol{\xi}-\mathbf{x}) = \frac{\mu}{4\pi(1-\nu)r}\left[(1-\nu)\delta_{tk}\delta_{mj} + 2\nu\delta_{km}\delta_{tj} - \delta_{kj}\delta_{tm} - \frac{(\xi_k - x_k)(\xi_j - x_j)}{r^2}\delta_{tm}\right] \tag{2.19}$$

2.5 Completely regularized boundary integral relation for displacement

To establish the singularity reduced integral relation for the displacement at any interior point **x**, the special decomposition (2.13) is first substituted into the integral relation (2.6) and then performing the integration by parts of terms associated with the function $G_{mj}^{p}(\boldsymbol{\xi}-\mathbf{x})$. The final result is given by

$$\begin{aligned} u_p(\mathbf{x}) = &\int_{S_c^+} U_j^p(\boldsymbol{\xi}-\mathbf{x})\Sigma t_j(\boldsymbol{\xi})dA(\boldsymbol{\xi}) - \int_{S_c^+} H_{ij}^p(\boldsymbol{\xi}-\mathbf{x})n_i(\boldsymbol{\xi})\Delta u_j(\boldsymbol{\xi})dA(\boldsymbol{\xi}) + \int_{S_c^+} G_{mj}^p(\boldsymbol{\xi}-\mathbf{x})D_m\Delta u_j(\boldsymbol{\xi})dA(\boldsymbol{\xi}) \\ &+ \int_{S_0} U_j^p(\boldsymbol{\xi}-\mathbf{x})t_j(\boldsymbol{\xi})dA(\boldsymbol{\xi}) - \int_{S_0} H_{ij}^p(\boldsymbol{\xi}-\mathbf{x})n_i(\boldsymbol{\xi})u_j(\boldsymbol{\xi})dA(\boldsymbol{\xi}) + \int_{S_0} G_{mj}^p(\boldsymbol{\xi}-\mathbf{x})D_m u_j(\boldsymbol{\xi})dA(\boldsymbol{\xi}) \end{aligned} \tag{2.20}$$

where D_m is a surface differential operator defined by

$$D_m = n_i\varepsilon_{ism}\frac{\partial}{\partial\xi_s} \tag{2.21}$$

Note that the condition Δu_j vanishes along the crack front have been utilized. By taking limit $\mathbf{x} \to \mathbf{y} \in S \equiv S_0 \cup S_c^+$ of (2.20), we obtain a boundary integral equation for the displacement as

$$c(\mathbf{y})u_p^*(\mathbf{y}) = \int_{S_c^+} U_j^p(\xi-\mathbf{y})\Sigma t_j(\xi)dA(\xi) - \int_{S_c^+} H_{ij}^p(\xi-\mathbf{y})n_i(\xi)\Delta u_j(\xi)dA(\xi) + \int_{S_c^+} G_{mj}^p(\xi-\mathbf{y})D_m\Delta u_j(\xi)dA(\xi)$$
$$+\int_{S_0} U_j^p(\xi-\mathbf{y})t_j(\xi)dA(\xi) - \int_{S_0} H_{ij}^p(\xi-\mathbf{y})n_i(\xi)u_j(\xi)dA(\xi) + \int_{S_0} G_{mj}^p(\xi-\mathbf{y})D_m u_j(\xi)dA(\xi) \tag{2.22}$$

where $c(\mathbf{y})$ = 1/2 if the surface is sufficiently smooth at a point $\mathbf{y}$ (i.e., the unit normal $\mathbf{n}$ is well-defined at a point $\mathbf{y}$), otherwise $c(\mathbf{y}) \in (0, 1)$ and $u_p^*(\mathbf{y})$ is defined by

$$u_p^*(\mathbf{y}) = \begin{cases} u_p(\mathbf{y}); & \mathbf{y} \in S_o \\ u_p^+(\mathbf{y}) + u_p^-(\mathbf{y}); & \mathbf{y} \in S_c^+ \end{cases} \tag{2.23}$$

By multiplying (2.22) by a sufficiently smooth test function $\tilde{t}_p(\mathbf{y})$ and then integrating the result over the total boundary $S \equiv S_0 \cup S_c^+$, we obtain a weakly-singular, weak-form boundary integral equation for the displacement as

$$\frac{1}{2}\int_S \tilde{t}_p(\mathbf{y})u_p^*(\mathbf{y})dS(\mathbf{y}) = \int_S \tilde{t}_p(\mathbf{y})\int_S U_j^p(\xi-\mathbf{y})\pi_j(\xi)dS(\xi)dS(\mathbf{y})$$
$$+\int_S \tilde{t}_p(\mathbf{y})\int_S G_{mj}^p(\xi-\mathbf{y})D_m\upsilon_j(\xi)dS(\xi)dS(\mathbf{y}) \tag{2.24}$$
$$-\int_S \tilde{t}_p(\mathbf{y})\int_S H_{ij}^p(\xi-\mathbf{y})n_i(\xi)\upsilon_j(\xi)dS(\xi)dS(\mathbf{y})$$

where

$$\pi_j(\xi) = \begin{cases} t_j(\xi); & \xi \in S_o \\ \Sigma t_j = t_j^+(\xi) + t_j^-(\xi); & \xi \in S_c^+ \end{cases}, \tag{2.25}$$

$$\upsilon_j(\xi) = \begin{cases} u_j(\xi); & \xi \in S_o \\ \Delta u_j = u_j^+(\xi) - u_j^-(\xi); & \xi \in S_c^+ \end{cases}. \tag{2.26}$$

and the function $c(\mathbf{y})$ simply reduces to 1/2 due to the assumption that the total boundary of the body is piecewise smooth (i.e., a set of points $\mathbf{y}$ where the unit normal $\mathbf{n}$ is not well-defined is of measure zero). It should be remarked that the boundary integral equation (2.24) contains only weakly singular kernels $\{U_j^p(\xi-\mathbf{x}),\ G_{mj}^p(\xi-\mathbf{x}),\ H_{ij}^p(\xi-\mathbf{y})n_i(\xi)\}$ of $\mathcal{O}(1/r)$ (also see details in the work of Xiao (1998)).

2.6 Completely regularized boundary integral relation for traction

To obtain a weakly singular, weak-form boundary integral equation for the traction, a similar procedure as described above is employed. First, the special decompositions (2.13) and (2.14) are substituted into the boundary integral relation for the stress (2.11) and then the integration by parts via Stokes' theorem is performed. The singularity-reduced boundary integral relation for the stress is given by

$$\sigma_{ik}(\mathrm{x}) = \varepsilon_{irt}\frac{\partial}{\partial x_r}\left[\int_S C_{mj}^{tk}(\xi-\mathbf{x})D_m \upsilon_j(\xi)dS(\xi) + \int_S G_{tk}^{j}(\xi-\mathbf{x})\pi_j(\xi)dS(\xi)\right] - \int_S H_{ik}^{j}(\xi-\mathbf{x})\pi_j(\xi)dS(\xi) \tag{2.27}$$

where the translational property of both kernels G_{mJ}^{P} and C_{mJ}^{tK} has been used. It should be remarked that the boundary integral relation for the stress (2.27) still contains strongly singular kernels of $\mathcal{O}(1/r^2)$. By further forming the product $n_l(\mathbf{y})\sigma_{lk}(\mathbf{x})$ where $\mathbf{y}\in S$ and then taking appropriate limit $\mathbf{x}\to\mathbf{y}$, it leads to a boundary integral equation for the traction as

$$\rho(\mathbf{y})t_k^*(\mathbf{y}) = D_t\int_S C_{mj}^{tk}(\xi-\mathbf{y})D_m\upsilon_j(\xi)dS(\xi) + D_t\int_S G_{tk}^{j}(\xi-\mathbf{y})\pi_j(\xi)dS(\xi) - \int_S n_l(\mathbf{y})H_{lk}^{j}(\xi-\mathbf{y})\pi_j(\xi)dS(\xi) \tag{2.28}$$

where $\rho(\mathbf{y})$ = 1/2 if the surface is sufficiently smooth at $\mathbf{y}$ otherwise $\rho(\mathbf{y}) \in (0, 1)$ and $t_k^*(\mathbf{y})$ is defined by

$$t_k^*(\mathbf{y}) = \begin{cases} t_k(\mathbf{y}); & \mathbf{y}\in S_o \\ t_k^+(\mathbf{y}) - t_k^-(\mathbf{y}); & \mathbf{y}\in S_c^+ \end{cases}. \tag{2.29}$$

Upon multiplying the boundary integral equation (2.28) by the following sufficiently smooth test function

$$\tilde{\upsilon}_k(\mathbf{y}) = \begin{cases} \tilde{u}_k(\mathbf{y}), & \mathbf{y}\in S_o \\ \Delta\tilde{u}_k(\mathbf{y}), & \mathbf{y}\in S_c^+ \end{cases}, \tag{2.30}$$

forming the integration of the result over the total boundary S, performing an integration by parts via Stoke's theorem and using the fact that the test function $\Delta\tilde{u}_k(\mathbf{y})$ satisfies the homogeneous condition along the crack front, it finally yields a weakly singular, weak-form integral equation for the traction:

$$-\frac{1}{2}\int_S \tilde{\upsilon}_k(\mathbf{y})t_k^*(\mathbf{y})dS(\mathbf{y}) = \int_S D_t\tilde{\upsilon}_k(\mathbf{y})\int_S C_{mj}^{tk}(\boldsymbol{\xi}-\mathbf{y})D_m\upsilon_j(\boldsymbol{\xi})dS(\boldsymbol{\xi})dS(\mathbf{y})$$
$$+\int_S D_t\tilde{\upsilon}_k(\mathbf{y})\int_S G_{tk}^{j}(\boldsymbol{\xi}-\mathbf{y})\pi_j(\boldsymbol{\xi})dS(\boldsymbol{\xi})dS(\mathbf{y}) \qquad (2.31)$$
$$+\int_S \tilde{\upsilon}_k(\mathbf{y})\int_S H_{ik}^{j}(\boldsymbol{\xi}-\mathbf{y})n_i(\mathbf{y})\pi_j(\boldsymbol{\xi})dS(\boldsymbol{\xi})dS(\mathbf{y})$$

Again, from the assumption that the total boundary of the domain is piecewise smooth, the function $\rho(\mathbf{y})$ simply reduces to 1/2. It should be remarked that the boundary integral equation (2.31) contains only weakly singular kernels $\{C_{mj}^{tk}(\boldsymbol{\xi}-\mathbf{y}), G_{mj}^{p}(\boldsymbol{\xi}-\mathbf{x}), H_{ij}^{p}(\boldsymbol{\xi}-\mathbf{y})n_i(\mathbf{y})\}$ of $\mathcal{O}(1/r)$ (also see details in the work of Xiao (1998)).

2.7 Symmetric formulation for SGBEM

Now, a symmetric formulation of the boundary value problem in terms of weakly singular, weak form boundary integral equations developed in sections 2.5 and 2.6 is established as a basis for the development of the well known numerical technique called the symmetric Galerkin boundary element method (SGBEM). More specifically, a system of governing integral equations can be obtained as follows: (i) the weakly singular, weak-form integral equation for the displacement (2.24) is applied to the surface S_u with $\tilde{t}_p = 0$ on the surface $S_T \equiv S_t \cup S_c^+$, (ii) the weakly singular, weak-form integral equation for the traction (2.31) is applied to the surface S_t with $\tilde{\upsilon}_P = 0$ on $S_u \cup S_c^+$, and the weakly singular, weak-form integral equation for the traction (2.31) is applied to the surface S_c^+ with $\tilde{\upsilon}_P = 0$ on $S_u \cup S_t$. The final set of governing integral equations is given explicitly by

$$\mathcal{A}_{uu}(\tilde{\mathbf{t}},\mathbf{t}) + \mathcal{B}_{ut}(\tilde{\mathbf{t}},\mathbf{u}) + \mathcal{B}_{uc}(\tilde{\mathbf{t}},\Delta\mathbf{u}) = \mathcal{R}_1(\tilde{\mathbf{t}}) \qquad (2.32)$$

$$\mathcal{B}_{ut}(\mathbf{t},\tilde{\mathbf{u}}) + \mathcal{C}_{tt}(\tilde{\mathbf{u}},\mathbf{u}) + \mathcal{C}_{tc}(\tilde{\mathbf{u}},\Delta\mathbf{u}) = \mathcal{R}_2(\tilde{\mathbf{u}}) \qquad (2.33)$$

$$\mathcal{B}_{uc}(\mathbf{t},\Delta\tilde{\mathbf{u}}) + \mathcal{C}_{ct}(\Delta\tilde{\mathbf{u}},\mathbf{u}) + \mathcal{C}_{cc}(\Delta\tilde{\mathbf{u}},\Delta\mathbf{u}) = \mathcal{R}_3(\Delta\tilde{\mathbf{u}}) \qquad (2.34)$$

where the bi-linear integral operators $\mathcal{A}_{PQ}$, $\mathcal{B}_{PQ}$ and $\mathcal{C}_{PQ}$ (with $P, Q \in \{u, t, c\}$) are defined by

$$\mathcal{A}_{PQ}(\mathbf{X},\mathbf{Y}) = \int_{S_P} \tilde{X}_k(\mathbf{y})\int_{S_Q} U_j^k(\boldsymbol{\xi}-\mathbf{y})Y_j(\boldsymbol{\xi})dS(\boldsymbol{\xi})dS(\mathbf{y}) \qquad (2.35)$$

$$\mathcal{B}_{PQ}(\mathbf{X},\mathbf{Y}) = \int_{S_P} \tilde{X}_k(\mathbf{y})\int_{S_Q} G_{mj}^{k}(\boldsymbol{\xi}-\mathbf{y})D_mY_j(\boldsymbol{\xi})dS(\boldsymbol{\xi})dS(\mathbf{y})$$
$$-\int_{S_P} \tilde{X}_p(\mathbf{y})\int_{S_Q} H_{ij}^{p}(\boldsymbol{\xi}-\mathbf{y})n_i(\boldsymbol{\xi})Y_j(\boldsymbol{\xi})dS(\boldsymbol{\xi})dS(\mathbf{y}) \qquad (2.36)$$

$$\mathscr{C}_{PQ}\left(\mathbf{X},\mathbf{Y}\right)=\int_{S_P} D_t\tilde{X}_k(\mathbf{y})\int_{S_Q} C_{mj}^{tk}(\xi-\mathbf{y})D_m Y_j(\xi)dS(\xi)dS(\mathbf{y}) \tag{2.37}$$

and the linear integral operators $\mathscr{R}_1$ and $\mathscr{R}_2$ are defined, in terms of the prescribed data on the boundary, by

$$\mathscr{R}_1\left(\tilde{\mathbf{t}}\right)=\frac{1}{2}\int_{S_u}\tilde{t}_p(\mathbf{y})u_p(\mathbf{y})dS(\mathbf{y})-\mathscr{A}_{ut}\left(\tilde{\mathbf{t}},\mathbf{t}\right)-\mathscr{A}_{uc}\left(\tilde{\mathbf{t}},\Sigma\mathbf{t}\right)-\mathscr{B}_{uu}\left(\tilde{\mathbf{t}},\mathbf{u}\right) \tag{2.38}$$

$$\mathscr{R}_2\left(\tilde{\mathbf{u}}\right)=-\frac{1}{2}\int_{S_t}\tilde{u}_k(\mathbf{y})t_k(\mathbf{y})dS(\mathbf{y})-\mathscr{B}_{tt}\left(\mathbf{t},\tilde{\mathbf{u}}\right)-\mathscr{B}_{ct}\left(\Sigma\mathbf{t},\tilde{\mathbf{u}}\right)-\mathscr{C}_{tu}\left(\tilde{\mathbf{u}},\mathbf{u}\right) \tag{2.39}$$

$$\mathscr{R}_3\left(\Delta\tilde{\mathbf{u}}\right)=-\frac{1}{2}\int_{S_c^+}\Delta\tilde{u}_k(\mathbf{y})\Delta t_k(\mathbf{y})dS(\mathbf{y})-\mathscr{B}_{tc}\left(\mathbf{t},\Delta\tilde{\mathbf{u}}\right)-\mathscr{B}_{cc}\left(\Sigma\mathbf{t},\Delta\tilde{\mathbf{u}}\right)-\mathscr{C}_{cu}\left(\Delta\tilde{\mathbf{u}},\mathbf{u}\right) \tag{2.40}$$

It is evident that the governing integral equations (2.32)-(2.34) are in a symmetric form, i.e. $\mathscr{A}_{uu}\left(\tilde{\mathbf{t}},\mathbf{t}\right)=\mathscr{A}_{uu}\left(\mathbf{t},\tilde{\mathbf{t}}\right)$, $\mathscr{C}_{tt}\left(\tilde{\mathbf{u}},\mathbf{u}\right)=\mathscr{C}_{tt}\left(\mathbf{u},\tilde{\mathbf{u}}\right)$, $\mathscr{C}_{cc}\left(\Delta\tilde{\mathbf{u}},\Delta\mathbf{u}\right)=\mathscr{C}_{cc}\left(\Delta\mathbf{u},\Delta\tilde{\mathbf{u}}\right)$, and $\mathscr{C}_{ct}\left(\Delta\tilde{\mathbf{u}},\mathbf{u}\right)=\mathscr{C}_{tc}\left(\mathbf{u},\Delta\tilde{\mathbf{u}}\right)$. (2.32)-(2.34) form a complete set of governing integral equations sufficient for solving the unknown displacement $\mathbf{u}$ on the surface S_t, the unknown traction $\mathbf{t}$ on the surface S_u and the unknown jump of the displacement $\Delta\mathbf{u}$ on the crack surface S_c^+. For the special case of cracks in an infinite medium, a system of integral equations (2.32)-(2.34) simply reduces to a single integral equation

$$\mathscr{C}_{cc}\left(\Delta\tilde{\mathbf{u}},\Delta\mathbf{u}\right)=-\frac{1}{2}\int_{S_c^+}\Delta\tilde{u}_k(\mathbf{y})\Delta t_k(\mathbf{y})dS(\mathbf{y})-\mathscr{B}_{cc}\left(\Sigma\mathbf{t},\Delta\tilde{\mathbf{u}}\right) \tag{2.41}$$

Once all these primary unknowns are determined, other quantities of interest can readily be obtained. For instance, the sum of the displacement across the crack surface, denoted by $\Sigma\mathbf{u}$, can be computed from the weak-form equation (2.24) by taking $\tilde{t}_p=0$ on the surface S_0, i.e., it can be obtained from

$$\frac{1}{2}\int_{S_c^+}\tilde{t}_p(\mathbf{y})\Sigma u_p(\mathbf{y})dS(\mathbf{y})=\mathscr{A}_{cu}\left(\tilde{\mathbf{t}},\mathbf{t}\right)+\mathscr{A}_{ct}\left(\tilde{\mathbf{t}},\mathbf{t}\right)+\mathscr{A}_{cc}\left(\tilde{\mathbf{t}},\Sigma\mathbf{t}\right)+\mathscr{B}_{cu}\left(\tilde{\mathbf{t}},\mathbf{u}\right)+\mathscr{B}_{ct}\left(\tilde{\mathbf{t}},\mathbf{u}\right)+\mathscr{B}_{cc}\left(\tilde{\mathbf{t}},\Delta\mathbf{u}\right) \tag{2.42}$$

The displacement and stress at any interior point **x** can also be computed from the singularity-reduced integral relations (2.20) and (2.27), respectively.

2.8 Formulation for SGBEM-FEM coupling

While the SGBEM (based on the boundary integral equations) has gained significant success in the analysis of linear elasticity and fracture problems, the method still contains certain

unfavorable features leading to its limited capability to solve various important classes of boundary value problems. For instance, the method either becomes computationally inefficient or experiences mathematical difficulty when applied to solve problems involving nonlinearity and non-homogeneous media. As the geometry of the domain becomes increasingly complex and its size and surface to volume ratio are relatively large (requiring a large number of elements to reasonably represent the entire boundary of the domain), the method tends to consume considerable computational resources in comparison with the standard finite element method (FEM). Although the SGBEM yields a symmetric system of linear equations, the coefficient matrix is fully dense and each of its entries must be computed by means of a double surface integration. To further enhance the modeling capability of the SGBEM for analysis of elasticity and fracture problems, a coupling method based on the SGBEM and FEM has become an attractive alternative. The fundamental idea is to decompose the entire domain into two regions and then apply the SGBEM to model a local region with small surface-to-volume ratio and possibly containing the displacement discontinuities (e.g. cracks and dislocations) and the FEM to model the remaining majority of the domain possibly exhibiting complex behavior (e.g. material nonlinearity and non-homogeneous data). The primary objective is to compromise between the requirement of computational resources and accuracy of predicted results.

A pair of weakly singular, weak-form boundary integral equations established in the previous sections is in a form well-suited for establishing the formulation of the SGBEM-FEM coupling. The development of SGBEM-FEM coupling equations for cracks in a finite body can be found in the work of Rungamornrat and Mear (2011). In this section, the coupling formulation capable of modeling an infinite medium containing cracks and localized complex zones is presented.

Consider a three-dimensional infinite medium Ω which contains an isolated crack and a localized complex zone as shown schematically in Figure 2.2(a). The crack is represented by two geometrical coincident surfaces S_c^+ and S_c^- with their unit outward normal being denoted by $\mathbf{n}^+$ and $\mathbf{n}^-$, respectively, and the localized complex zone is denoted by Ω^L. In the present study, the medium is assumed to be free of a body force and loading on its remote boundary, and both surfaces of the crack are subjected to prescribed self-equilibrated traction defined by $\mathbf{t}_c = \mathbf{t}_c^+ = -\mathbf{t}_c^-$. Now, let us introduce an imaginary surface S_I to decompose the body Ω into two sub-domains, an unbounded 'BEM-region' denoted by Ω^B and a finite 'FEM-region' denoted by Ω^F, as indicated in Figure 2.2(b). The surface S_I is selected such that the localized complex zone and the crack are embedded entirely in the FEM-region and in the BEM-region, respectively (i.e. $S_c^+ \cup S_c^- \subset \Omega^B$ and $\Omega^L \subset \Omega^F$) and, in addition, the BEM-region must be linearly elastic. To clearly demonstrate the role of the interface between the two sub-regions in the formulation presented below, we define $\{S_{BI}, \mathbf{t}_{BI}, \mathbf{u}_{BI}\}$ and $\{S_{FI}, \mathbf{t}_{FI}, \mathbf{u}_{FI}\}$ as the interface, the unknown traction and the unknown displacement on the interface of the BEM-region Ω^B and the FEM-region Ω^F, respectively. It is important to emphasize that the interfaces S_{BI} and S_{FI} are in fact identical to the imaginary surface S_I. While the formulation is presented, for brevity, only for a domain containing a single crack and a single localized complex zone, it can readily be extended to treat multiple cracks and multiple complex zones; in such particular case, several FEM-regions are admissible.

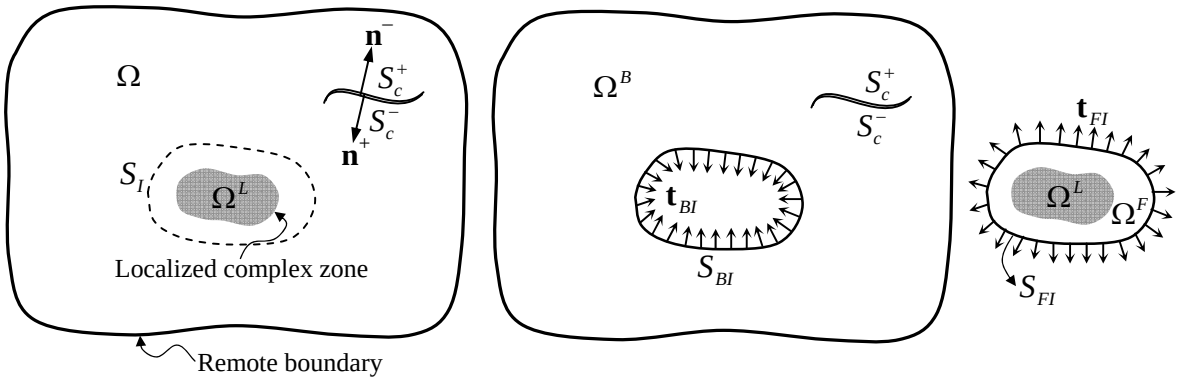

(a) (b)

Figure 2.2 (a) Schematic of three-dimensional infinite medium containing crack and localized complex zone and (b) schematic of BEM-region Ω^B and FEM-region Ω^F

2.8.1 Governing equations for Ω^B

The total boundary of the BEM-region Ω^B, denoted by S_B, consists of the crack surface $S_{Bc} \equiv S_c$ on which the traction is fully prescribed and the interface S_{BI} where neither the traction nor the displacement is known a priori. Note again that the subscript '*B*' is added only to emphasize that those surfaces are associated with the BEM-region. To form a set of governing integral equations for this region, a pair of weakly singular, weak-form displacement and traction boundary integral equations developed in sections 2.5 and 2.6 is employed.

Towards obtaining a system of governing integral equations for the BEM-region Ω^B, the weakly singular, weak-form boundary integral equation for the traction (2.31) is applied directly to the crack surface S_{Bc} (with the test function being chosen such that $\tilde{\mathbf{v}} = 0$ on S_{BI}) and to the interface S_{BI} (with the test function being chosen such that $\tilde{\mathbf{v}} = 0$ on S_{Bc}), and the weakly singular, weak-form boundary integral equation for the displacement (2.24) is applied only to the interface S_{BI} (with the test function being chosen such that $\tilde{\mathbf{t}} = 0$ on S_{Bc}). A final set of three integral equations is given concisely by

$$\begin{aligned}
&\mathscr{C}_{cc}(\tilde{\mathbf{v}}, \Delta\mathbf{u}) \quad + \mathscr{B}_{Ic}(\mathbf{t}_{BI}, \tilde{\mathbf{v}}) \quad + \mathscr{C}_{cI}(\tilde{\mathbf{v}}, \mathbf{u}_{BI}) \qquad = -2\mathscr{F}_{Bc}(\tilde{\mathbf{v}}, \mathbf{t}_c) \\
&\mathscr{B}_{Ic}(\tilde{\mathbf{t}}_{BI}, \Delta\mathbf{u}) \quad + \mathscr{A}_{II}(\tilde{\mathbf{t}}_{BI}, \mathbf{t}_{BI}) \quad + \mathscr{D}_{II}(\tilde{\mathbf{t}}_{BI}, \mathbf{u}_{BI}) \qquad = 0 \\
&\mathscr{C}_{Ic}(\tilde{\mathbf{u}}_{BI}, \Delta\mathbf{u}) \quad + \mathscr{D}_{II}(\mathbf{t}_{BI}, \tilde{\mathbf{u}}_{BI}) \quad + \mathscr{C}_{II}(\tilde{\mathbf{u}}_{BI}, \mathbf{u}_{BI}) \qquad = -2\mathscr{F}_{BI}(\tilde{\mathbf{u}}_{BI}, \mathbf{t}_{BI})
\end{aligned} \tag{2.43}$$

where $\{\tilde{\mathbf{u}}_{BI}, \tilde{\mathbf{t}}_{BI}\}$ are sufficiently smooth test functions defined on the interface S_{BI} and all additional integral operators are defined, with subscripts $P, Q \in \{I, c\}$ being introduced to clearly indicate the surface of integration, by

$$\mathcal{F}_{BP}(\mathbf{X},\mathbf{Y}) = \frac{1}{2}\int_{S_{BP}} X_i(\mathbf{y})Y_i(\mathbf{y})dS(\mathbf{y}) \tag{2.44}$$

$$\mathcal{D}_{II}(\mathbf{X},\mathbf{Y}) = \mathcal{B}_{II}(\mathbf{X},\mathbf{Y}) - \mathcal{F}_{BI}(\mathbf{X},\mathbf{Y}) \tag{2.45}$$

It should be noted that the symmetry of the integral operator $\mathcal{C}_{PQ}(\mathbf{X},\mathbf{Y})$ renders the left hand side of the system (2.43) being in a symmetric form. Although such symmetric formulation can readily be obtained, the right hand side of (2.43) still contains the unknown traction on the interface $\mathbf{t}_{BI}$. The treatment of a term $\mathcal{F}_{BI}(\tilde{\mathbf{u}}_{BI},\mathbf{t}_{BI})$ will be addressed once the formulation for the FEM-region Ω^F is established.

2.8.2 Governing equations for Ω^F

Let us consider, next, the FEM-region Ω^F. For generality, the entire boundary of this particular region can be decomposed into two surfaces: the interface S_{FI} on which both the traction $\mathbf{t}_{FI}$ and the displacement $\mathbf{u}_{FI}$ are unknown a priori and the surface S_{FT} on which the traction $\mathbf{t}_{FT}$ is fully prescribed. The existence of the surface S_{FT} is apparent for the case that the FEM-region contains embedded holes or voids. It is also important to emphasize that in the development of a key governing equation for Ω^F, the traction $\mathbf{t}_{FI}$ is treated, in a fashion different from that for the BEM-region, as unknown data instead of the primary unknown variable. In addition, to be capable of modeling a complex localized zone embedded within the FEM-region, a constitutive model governing the material behavior utilized in the present study is assumed to be sufficiently general allowing the treatment of material nonlinearity, anisotropy and inhomogeneity. The treatment of such complex material models has been extensively investigated and well-established within the context of nonlinear finite element methods (e.g., Oden and Carey, 1984; Bathe, 1990; Belytschko et al., 2000) and those standard procedures also apply to the current implementation and will not be presented for brevity. Here, we only outline the key governing equation for the FEM-region and certain unknowns and data necessary connected to those for the BEM-region.

Following standard formulation of the finite element technique, the weak-form equation governing the FEM-region can readily be obtained via the weight residual technique or the principle of virtual work, and the final weak-form equation can be expressed in a concise form by

$$\mathcal{K}_{FF}(\tilde{\mathbf{u}},\boldsymbol{\sigma}) = 2\mathcal{F}_{FI}(\tilde{\mathbf{u}}_{FI},\mathbf{t}_{FI}) + 2\mathcal{F}_{FT}(\tilde{\mathbf{u}}_{FT},\mathbf{t}_{FT}) \tag{2.46}$$

where $\boldsymbol{\sigma}$ denotes a stress tensor; $\tilde{\mathbf{u}}$ is a suitably well-behaved test function defined over the domain Ω^F; $\tilde{\mathbf{u}}_{FI}$ and $\tilde{\mathbf{u}}_{FT}$ are the restriction of the test function $\tilde{\mathbf{u}}$ on the interfaces S_{FI} and S_{FT}, respectively; and all involved integral operators are defined, with subscripts $P \in \{I,T\}$, by

$$\mathcal{K}_{FF}(\tilde{\mathbf{u}},\boldsymbol{\sigma}) = \int_{\Omega^F} \tilde{\varepsilon}_{ij}(\mathbf{y})\sigma_{ij}(\mathbf{y})dV(\mathbf{y}) \tag{2.47}$$

$$\mathcal{F}_{FP}(\mathbf{X},\mathbf{Y}) = \frac{1}{2}\int_{S_{FP}} X_i(\mathbf{y})Y_i(\mathbf{y})dS(\mathbf{y}) \tag{2.48}$$

in which $\tilde{\varepsilon}_{ij}(\mathbf{y})$ denotes the virtual strain tensor defined by $\tilde{\varepsilon}_{ij}(\mathbf{y}) = \left(\partial\tilde{u}_i/\partial y_j + \partial\tilde{u}_j/\partial y_i\right)/2$. Note again that a function form of the stress tensor in terms of the primary unknown depends primarily on a constitutive model employed. For a special case of the FEM-region being made of a homogeneous, linearly elastic material, the stress tensor can be expressed directly and explicitly in terms of elastic constants E_{ijkl} and the strain tensor $\boldsymbol{\varepsilon}$ (i.e., $\sigma_{ij} = E_{ijkl}\varepsilon_{kl}$), and within the context of an infinitesimal deformation theory (i.e., $\varepsilon_{ij}(\mathbf{y}) = \left(\partial u_i/\partial y_j + \partial u_j/\partial y_i\right)/2$), the integral operator $\mathcal{K}_{FF}$ can be expressed directly in terms of the displacement $\mathbf{u}$ as

$$\mathcal{K}_{FF}(\tilde{\mathbf{u}},\mathbf{u}) = \int_{\Omega^F} \tilde{u}_{i,j}(\mathbf{y})E_{ijkl}u_{k,l}(\mathbf{y})dV(\mathbf{y}) \tag{2.49}$$

It should be remarked that the factor of one-half in the definition (2.48) has been introduced for convenience to cast this term in a form analogous to that for $\mathcal{F}_{BP}$ given by (2.44), and this, as a result, leads to the factor of two appearing on the right hand side of (2.46). It is also worth noting that the first term on the right hand side of (2.46) still contains the unknown traction on the interface $\mathbf{t}_{FI}$.

2.8.3 Governing equations for Ω

A set of governing equations of the entire domain Ω can directly be obtained by combining a set of weakly singular, weak-form boundary integral equations (2.43) and the virtual work equation (2.46). In particular, the last equation of (2.43) and the equation (2.46) are properly combined and this finally leads to

$$\begin{aligned}
&\mathcal{C}_{CC}(\tilde{\mathbf{v}},\Delta\mathbf{u}) + \mathcal{B}_{IC}(\mathbf{t}_{BI},\tilde{\mathbf{v}}) + \mathcal{C}_{CI}(\tilde{\mathbf{v}},\mathbf{u}_{BI}) &&= -2\mathcal{F}_{BC}(\tilde{\mathbf{v}},\mathbf{t}_C)\\
&\mathcal{B}_{IC}(\tilde{\mathbf{t}}_{BI},\Delta\mathbf{u}) + \mathcal{A}_{II}(\tilde{\mathbf{t}}_{BI},\mathbf{t}_{BI}) + \mathcal{D}_{II}(\tilde{\mathbf{t}}_{BI},\mathbf{u}_{BI}) &&= 0\\
&\mathcal{C}_{IC}(\tilde{\mathbf{u}}_{BI},\Delta\mathbf{u}) + \mathcal{D}_{II}(\mathbf{t}_{BI},\tilde{\mathbf{u}}_{BI}) + \mathcal{C}_{II}(\tilde{\mathbf{u}}_{BI},\mathbf{u}_{BI}) - \mathcal{K}_{FF}(\tilde{\mathbf{u}},\boldsymbol{\sigma}) &&= \mathcal{E} + 2\mathcal{F}_{FT}(\tilde{\mathbf{u}}_{FT},\mathbf{t}_{FT})
\end{aligned} \tag{2.50}$$

where $\mathcal{E}$ is given by

$$\mathcal{E} = -2\left[\mathcal{F}_{BI}(\tilde{\mathbf{u}}_{BI},\mathbf{t}_{BI}) + \mathcal{F}_{FI}(\tilde{\mathbf{u}}_{FI},\mathbf{t}_{FI})\right] \tag{2.51}$$

From the continuity of the traction and displacement across the interface of the BEM-region and FEM-region (i.e. $\mathbf{t}_{BI}(\mathbf{y}) + \mathbf{t}_{FI}(\mathbf{y}) = \mathbf{0}$ and $\mathbf{u}_{BI}(\mathbf{y}) = \mathbf{u}_{FI}(\mathbf{y})$ for all $\mathbf{y} \in S_I = S_{BI} = S_{FI}$), the test functions $\tilde{\mathbf{u}}_{BI}$ and $\tilde{\mathbf{u}}$ are chosen such that $\tilde{\mathbf{u}}_{BI}(\mathbf{y}) = \tilde{\mathbf{u}}_{FI}(\mathbf{y})$ for all $\mathbf{y} \in S_I = S_{BI} = S_{FI}$ and, as a direct consequence, $\mathcal{E}$ identically vanishes. It is therefore evident that the left hand side of (2.50) involves only prescribed boundary data and, in addition, if the integral operator $\mathcal{K}_{FF}$ possesses a symmetric form, (2.50) constitutes a symmetric formulation for the boundary value problem currently treated.

2.9 Formulation for cracks in infinite medium with nano-scale influence

In this section, a pair of weakly singular, weak-form integral equations (2.24) and (2.31) is employed along with the finite element equation to formulate a set of governing equations for cracks in an infinite medium with consideration of the nano-scale influence. The primary objective is to investigate the elastic field and related fracture information for cracks of nano-size in which the surface free energy and the size-dependency of responses are significant.

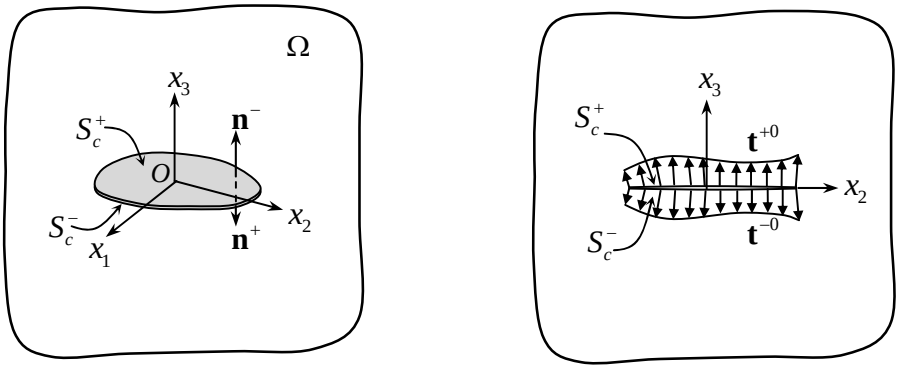

(a) (b)

Figure 2.3 (a) Schematic of three-dimensional infinite elastic medium containing an isolated crack and (b) prescribed traction on crack surfaces

Consider a three-dimensional, infinite, elastic medium Ω containing an isolated, planar crack as shown schematically in Figure 2.3(a). The reference Cartesian coordinate system $\{O; x_1, x_2, x_3\}$ is also shown. The bulk material is made of a homogeneous, isotropic, linearly elastic material with shear modulus μ and Poisson's ratio ν. The crack surfaces which are geometrically identical are represented by S_c^+ and S_c^- and with corresponding outward unit normal $\mathbf{n}^+$ and $\mathbf{n}^-$, respectively. The medium is assumed to be free of body forces and remote loading but subjected to prescribed tractions $\mathbf{t}^{+0}$ and $\mathbf{t}^{-0}$ on S_c^+ and S_c^-, respectively (Figure 2.3(b)). In addition, infinitesimally thin layers on the crack surfaces (mathematically modeled by zero thickness layers perfectly bonded to the crack surfaces) possess constant residual surface tension under unstrained conditions which is denoted by τ^s.

In the formulation of the boundary value problem, the medium is decomposed into three parts: the bulk material, the zero-thickness layer S_c^+ and the zero-thickness layer S_c^- as shown in Figure 2.4. The bulk material is simply the whole medium without the two infinitesimally thin layers on the crack surfaces. Since both layers have zero thickness, the geometry of the bulk material is therefore identical to that of the whole medium (i.e., it can also be completely described by the region Ω and the two crack surfaces S_c^+ and S_c^-).

The key difference between the bulk material and the original medium is that the bulk material is homogeneous and the crack surfaces S_c^+ and S_c^- in the bulk material part are subjected to unknown tractions (exerted directly by the two layers) $\mathbf{t}^{+b}$ and $\mathbf{t}^{-b}$, respectively.

The layer S_c^+ is treated as a two-sided surface with one side subjected to the prescribed traction $\mathbf{t}^{+0}$ and the other side subjected to the traction $\mathbf{t}^{+s}$ exerted by the bulk material (Figure 2.4(b)). Similarly, the layer S_c^- is treated as a two-sided surface with one side subjected to the prescribed traction $\mathbf{t}^{-0}$ and the other side subjected to the traction $\mathbf{t}^{-s}$ exerted by the bulk material (Figure 2.4(c)). In what follows, Greek subscripts denote field quantities associated with the surface and take the values 1, 2 while the Latin subscripts take the values 1, 2, 3. We remark that, in the development to follow, it will suffice to make reference to the single crack surface $S_c \equiv S_c^+$.

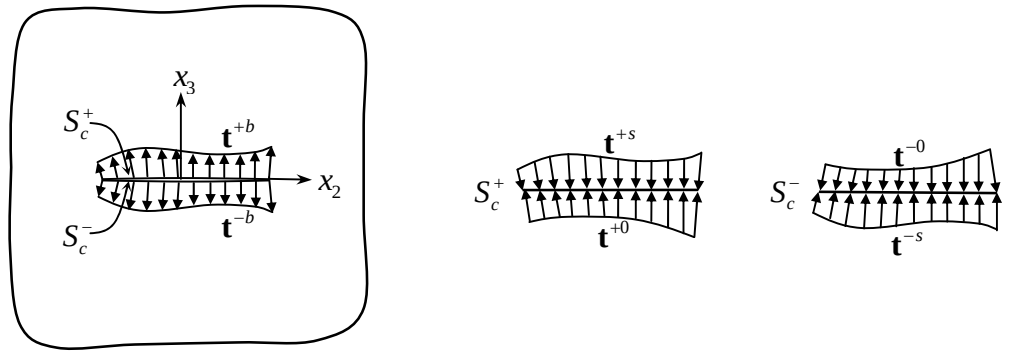

(a) (b) (c)

Figure 2.4 Schematics of (a) the bulk material, (b) the zero-thickness layer S_c^+ and (c) the zero-thickness layer S_c^-

2.9.1 Governing equations for bulk material

Since the bulk material is made of homogeneous, isotropic, linear elastic material, its behavior is governed by the classical theory of linear elasticity. By specializing results developed in sections 2.5 and 2.6 to isolated cracks in infinite media, the weakly singular, weak-form displacement and traction boundary integral equations in terms of the traction data $\mathbf{t}^{+b}$ and $\mathbf{t}^{-b}$ and the displacement data $\mathbf{u}^{+b}$ and $\mathbf{u}^{-b}$ on the crack surfaces S_c^+ and S_c^- become

$$\begin{aligned}\frac{1}{2}\int_{S_c^+}\tilde{t}_p^{\Sigma}(\mathbf{y})u_p^{b\Sigma}(\mathbf{y})dS(\mathbf{y}) &= \int_{S_c^+}\tilde{t}_p^{\Sigma}(\mathbf{y})\int_{S_c^+}U_j^p(\boldsymbol{\xi}-\mathbf{y})t_j^{b\Sigma}(\boldsymbol{\xi})dS(\boldsymbol{\xi})dS(\mathbf{y}) \\ &+\int_{S_c^+}\tilde{t}_p^{\Sigma}(\mathbf{y})\int_{S_c^+}G_{mj}^p(\boldsymbol{\xi}-\mathbf{y})D_m u_j^{b\Delta}(\boldsymbol{\xi})dS(\boldsymbol{\xi})dS(\mathbf{y}) \\ &-\int_{S_c^+}\tilde{t}_p^{\Sigma}(\mathbf{y})\int_{S_c^+}H_{ij}^p(\boldsymbol{\xi}-\mathbf{y})n_i(\boldsymbol{\xi})u_j^{b\Delta}(\boldsymbol{\xi})dS(\boldsymbol{\xi})dS(\mathbf{y})\end{aligned} \tag{2.52}$$

$$\begin{aligned}-\frac{1}{2}\int_{S_c}\tilde{u}_k^{\Delta}(\mathbf{y})t_k^{b\Delta}(\mathbf{y})dS(\mathbf{y}) &= \int_{S_c}D_t\tilde{u}_k^{\Delta}(\mathbf{y})\int_{S_c}C_{mj}^{tk}(\boldsymbol{\xi}-\mathbf{y})D_m u_j^{b\Delta}(\boldsymbol{\xi})dS(\boldsymbol{\xi})dS(\mathbf{y}) \\ &+\int_{S_c}D_t\tilde{u}_k^{\Delta}(\mathbf{y})\int_{S_c}G_{tk}^j(\boldsymbol{\xi}-\mathbf{y})t_j^{b\Sigma}(\boldsymbol{\xi})dS(\boldsymbol{\xi})dS(\mathbf{y}) \\ &+\int_{S_c}\tilde{u}_k^{\Delta}(\mathbf{y})\int_{S_c}H_{lk}^j(\boldsymbol{\xi}-\mathbf{y})n_l(\mathbf{y})t_j^{b\Sigma}(\boldsymbol{\xi})dS(\boldsymbol{\xi})dS(\mathbf{y})\end{aligned} \tag{2.53}$$

where $t_j^{b\Sigma} = t_j^{+b} + t_j^{-b}$, $u_j^{b\Delta} = u_j^{+b} - u_j^{-b}$, $\{\tilde{t}_p^{\Sigma}, \tilde{u}_k^{\Delta}\}$ are sufficiently smooth test functions, and the kernels $\{U_j^p, G_{mj}^p, C_{mj}^{tk}\}$ for isotropic elastic materials are given explicitly by (2.9), (2.18), and (2.19), respectively.

2.9.2 Governing equations for two layers

The two layers S_c^+ and S_c^- shown in Figure 2.4(b) and 2.4(c) are considered as infinitesimally thin membranes adhered perfectly to the bulk material. The behavior of these two layers is modeled by Gurtin-Murdoch surface elasticity theory by ignoring terms associated with the surface elastic constants. It has been pointed out by various investigations that the influence of the surface Lamé constants on the out-of-plane responses in the region very near the surface is negligibly weak (e.g., Intarit, 2012; Intarit, 2013; Nan and Wang, 2012; Pinyochotiwong et al., 2013). The simplified version of the Gurtin-Murdoch model is therefore considered suitable for modeling planar crack problems when mode-I behavior is of primary interest.

The equilibrium equations, the surface constitutive relations and the strain-displacement relationship of the layers S_c^+ and S_c^- are therefore given by (Gurtin and Murdoch, 1975; Gurtin and Murdoch, 1978)

$$\sigma_{i\beta,\beta}^s + t_i^s + t_i^o = 0 \tag{2.54}$$

$$\sigma_{\alpha\beta}^s = \tau^s \delta_{\alpha\beta} + \tau^s \varepsilon_{\gamma\gamma}^s \delta_{\alpha\beta} - 2\tau^s \varepsilon_{\alpha\beta}^s + \tau^s u_{\alpha,\beta}^s \quad , \quad \sigma_{3\beta}^s = \tau^s u_{3,\beta}^s \tag{2.55}$$

$$\varepsilon_{\alpha\beta}^s = \tfrac{1}{2}\left(u_{\alpha,\beta}^s + u_{\beta,\alpha}^s\right) \tag{2.56}$$

where $\sigma_{i\beta}^s, \varepsilon_{\alpha\beta}^s, u_i^s$ represent stress, strain and displacement components within the layer. To construct the weak-form equation, we multiply the equilibrium equation (2.54) with a sufficiently smooth test function $\tilde{u}_i^s$ and then integrate the result over the entire crack surface to obtain

$$\int_{S_c^+} \tilde{u}_i^s \sigma_{i\beta,\beta}^s dS + \int_{S_c^+} \tilde{u}_i^s t_i^s dS + \int_{S_c^+} \tilde{u}_i^s t_i^0 dS = 0 \tag{2.57}$$

By using the fact that τ^s is spatially independent, it can be readily verified that $\sigma_{\alpha\beta,\beta}^s = 0$. With such condition along with carrying out the integration by parts of the first term using the Gauss-divergence theorem, it leads to

$$\int_{S_c^+} \tilde{u}_{3,\beta}^s \sigma_{3\beta}^s dS - \int_{S_c^+} \tilde{u}_i^s t_i^s dS = \int_{\partial S_c^+} \tilde{u}_3^s \sigma_{3\beta}^s n_\beta dS + \int_{S_c^+} \tilde{u}_i^s t_i^0 dS \tag{2.58}$$

Substituting (2.55) into (2.56) finally yields

$$\tau^s \int_{S_c^+} \tilde{u}_{3,\beta}^s u_{3,\beta}^s dS - \int_{S_c^+} \tilde{u}_i^s t_i^s dS = \int_{\partial S_c^+} \tilde{u}_3^s \sigma_{3\beta}^s n_\beta dS + \int_{S_c^+} \tilde{u}_i^s t_i^0 dS \tag{2.59}$$

Note that the weak-form equation (2.59) applies to both crack surfaces. For instance, the weak-form equations for the surface S_c^+ and surface S_c^- can be obtained explicitly by

$$\tau^s \int_{S_c^+} \tilde{u}_{3,\beta}^{+s} u_{3,\beta}^{+s} dS - \int_{S_c^+} \tilde{u}_i^{+s} t_i^{+s} dS = \int_{\partial S_c^+} \tilde{u}_3^{+s} \sigma_{3\beta}^{+s} n_\beta dS + \int_{S_c^+} \tilde{u}_i^{+s} t_i^{+0} dS \tag{2.60}$$

$$\tau^s \int_{S_c^+} \tilde{u}_{3,\beta}^{-s} u_{3,\beta}^{-s} dS - \int_{S_c^+} \tilde{u}_i^{-s} t_i^{-s} dS = \int_{\partial S_c^+} \tilde{u}_3^{-s} \sigma_{3\beta}^{-s} n_\beta dS + \int_{S_c^+} \tilde{u}_i^{-s} t_i^{-0} dS \tag{2.61}$$

where superscripts "+" and "–" are added to differentiate quantities defined on each crack surface. Since the integral equations governing the bulk are derived in terms of the unknown sum and jump of quantities across the crack surface, it is natural to establish the weak-form equations governing the surface in terms of the same type of unknowns. This can be readily accomplished by forming two linear combinations of (2.60) and (2.61) as follows: (i) choosing $\tilde{u}_i^{+s} = \tilde{u}_i^{-s} = \tilde{u}_i^{s\Sigma}$ and then adding (2.60) to (2.61) and (ii) choosing $\tilde{u}_i^{+s} = \tilde{u}_i^{-s} = \tilde{u}_i^{s\Delta}$ and then subtracting (2.60) from (2.61). Such pair of equivalent weak-form equations is given by

$$\tau^s \int_{S_c^+} \tilde{u}_{3,\beta}^{s\Sigma} u_{3,\beta}^{s\Sigma} dS - \int_{S_c^+} \tilde{u}_i^{s\Sigma} t_i^{s\Sigma} dS = \int_{\partial S_c^+} \tilde{u}_3^{s\Sigma} \sigma_{3\beta}^{s\Sigma} n_\beta dS + \int_{S_c^+} \tilde{u}_i^{s\Sigma} t_i^{0\Sigma} dS \tag{2.62}$$

$$\tau^s \int_{S_c^+} \tilde{u}_{3,\beta}^{s\Delta} u_{3,\beta}^{s\Delta} dS - \int_{S_c^+} \tilde{u}_i^{s\Delta} t_i^{s\Delta} dS = \int_{\partial S_c^+} \tilde{u}_3^{s\Delta} \sigma_{3\beta}^{s\Delta} n_\beta dS + \int_{S_c^+} \tilde{u}_i^{s\Delta} t_i^{0\Delta} dS \tag{2.63}$$

where superscripts "Σ" and "Δ" indicate the sum and jump of quantities across the crack surface. It should be remarked further that since the jump of the displacement along the crack-front vanishes identically, the test function $\tilde{u}_i^{s\Delta}$ is chosen to satisfy the homogeneous condition $\tilde{u}_i^{s\Delta} = 0$ on ∂S_c^+. The weak-form equations (2.62) and (2.63) now take the form

$$\tau^s \int_{S_c^+} \tilde{u}_{3,\beta}^{s\Sigma} u_{3,\beta}^{s\Sigma} dS - \int_{S_c^+} \tilde{u}_i^{s\Sigma} t_i^{s\Sigma} dS = \int_{S_c^+} \tilde{u}_i^{s\Sigma} t_i^{0\Sigma} dS \tag{2.64}$$

$$\tau^s \int_{S_c^+} \tilde{u}_{3,\beta}^{s\Delta} u_{3,\beta}^{s\Delta} dS - \int_{S_c^+} \tilde{u}_i^{s\Delta} t_i^{s\Delta} dS = \int_{S_c^+} \tilde{u}_i^{s\Delta} t_i^{0\Delta} dS \tag{2.65}$$

Equations (2.64) and (2.65) constitute a set of weak-form equations governing the unknown quantities $\{u_i^{s\Delta}, t_i^{s\Delta}, u_i^{s\Sigma}, t_i^{s\Sigma}\}$. It is worth noting that the formulation presented above is not restricted only to applied normal traction to the crack surface, although the mathematical model of the surface is suitable for pure mode-I loading. Due to the vanishing $\sigma_{\alpha\beta,\beta}^s$, the

equilibrium equation (2.54) indicates that the applied shear traction is transmitted directly to the crack surface of the bulk material.

2.9.3. Governing equations for whole medium

Since the two layers S_c^+ and S_c^- are adhered perfectly to the bulk material, the displacements and tractions along the interface of the two layers and the bulk material must be continuous. This yields the following continuity conditions:

$$u_i^{s\Delta} = u_i^{b\Delta} \equiv u_i^{\Delta} \tag{2.66}$$

$$u_i^{s\Sigma} = u_i^{b\Sigma} \equiv u_i^{\Sigma} \tag{2.67}$$

$$t_i^{s\Delta} = -t_i^{b\Delta} \equiv -t_i^{\Delta} \tag{2.68}$$

$$t_i^{s\Sigma} = -t_i^{b\Sigma} \equiv -t_i^{\Sigma} \tag{2.69}$$

Substituting (2.66)-(2.69) into (2.52), (2.53), (2.64) and (2.65) leads to a system of four equations involving four unknown functions $\{u_i^{\Delta}, t_i^{\Delta}, u_i^{\Sigma}, t_i^{\Sigma}\}$. By choosing appropriate test functions, (2.53) and (2.65) can be combined and the unknown t_i^{Δ} can be eliminated. The final system of three equations involving three unknown functions $\{u_i^{\Delta}, u_i^{\Sigma}, t_i^{\Sigma}\}$ is given by

$$\begin{aligned}
&\mathscr{A}(\tilde{\mathbf{u}}^{s\Sigma}, \mathbf{u}^{\Sigma}) + \mathscr{B}(\tilde{\mathbf{u}}^{s\Sigma}, \mathbf{t}^{\Sigma}) &&= \bar{\mathscr{R}}_1(\tilde{\mathbf{u}}^{s\Sigma}) \\
&\mathscr{B}(\tilde{\mathbf{t}}^{\Sigma}, \mathbf{u}^{\Sigma}) - \mathscr{A}_{cc}(\tilde{\mathbf{t}}^{\Sigma}, \mathbf{t}^{\Sigma}) - \mathscr{B}_{cc}(\tilde{\mathbf{t}}^{\Sigma}, \mathbf{u}^{\Delta}) &&= 0 \\
&\quad - \mathscr{B}_{cc}(\mathbf{t}^{\Sigma}, \tilde{\mathbf{u}}^{\Delta}) + \mathscr{E}(\tilde{\mathbf{u}}^{\Delta}, \mathbf{u}^{\Delta}) &&= \bar{\mathscr{R}}_2(\tilde{\mathbf{u}}^{\Delta})
\end{aligned} \tag{2.70}$$

where the additional bilinear integral operators $\mathscr{A}, \mathscr{B}, \mathscr{E}$ are defined by

$$\mathscr{A}(\mathbf{X}, \mathbf{Y}) = \frac{\tau^s}{2} \int_{S_c^+} X_{3,\alpha}(\mathbf{y}) Y_{3,\alpha}(\mathbf{y}) dS(\mathbf{y}) \tag{2.71}$$

$$\mathscr{B}(\mathbf{X}, \mathbf{Y}) = \frac{1}{2} \int_{S_c^+} X_p(\mathbf{y}) Y_p(\mathbf{y}) dS(\mathbf{y}) \tag{2.72}$$

$$\mathscr{E}(\mathbf{X}, \mathbf{Y}) = -\mathscr{C}_{cc}(\mathbf{X}, \mathbf{Y}) + \mathscr{A}(\mathbf{X}, \mathbf{Y}) \tag{2.73}$$

where the linear integral operators $\{\bar{\mathscr{R}}_1, \bar{\mathscr{R}}_2\}$ are defined, in terms of prescribed data $\mathbf{t}^{0\Sigma}$ and $\mathbf{t}^{0\Delta}$, by

$$\bar{\mathscr{R}}_1(\mathbf{X}) = \frac{1}{2} \int_{S_c^+} X_l(\mathbf{y}) t_l^{0\Sigma}(\mathbf{y}) dS(\mathbf{y}) \tag{2.74}$$

$$\bar{\mathscr{R}}_2(\mathbf{X}) = \frac{1}{2} \int_{S_c^+} X_l(\mathbf{y}) t_l^{0\Delta}(\mathbf{y}) dS(\mathbf{y}) \tag{2.75}$$

CHAPTER III

NUMERICAL IMPLEMENTATION

This section briefly summarizes numerical procedures adopted to construct numerical solutions of a set of governing equations (2.32)-(2.34), (2.50), and (2.70), and to post-process certain quantities of interest such as stress intensity factors, T-stresses, and stress at interior points. The discretization of all governing equations by standard Galerkin strategy is discussed first. Then, components essential for numerical evaluation of weakly singular and nearly singular double surface integrals, evaluations of kernels for general anisotropic materials, and determination of general mixed-mode stress intensity factors and T-stress are addressed. Finally, the key strategy for establishing the coupling between the in-house weakly singular SGBEM code and the reliable commercial finite element package is discussed.

3.1 Discretization

A standard Galerkin strategy is adopted to construct an approximate version of a system of governing equations (2.32)-(2.34) for SGBEM, (2.50) for SGBEM-FEM coupling, and (2.70) for consideration of nano-scale influence.

For the case of SGBEM, only the boundary of the domain and/or the crack surface need to be discretized. In such discretization, interpolation functions constructed locally based on standard two-dimensional isoparametric C^0 elements (e.g, 8-node quadrilateral and 6-node triangular elements) are employed throughout to approximate all primary unknowns except for the jump of the displacement across the crack surface where special 9-node crack-tip elements are employed to accurately capture its asymptotic behavior near the singularity zone. Shape functions of these special elements are properly enriched by square-root functions (resulting from asymptotic expansion of fields in the vicinity of the crack front) and, in addition, extra degrees of freedom are introduced along the edge of elements adjacent to the crack front to directly represent the gradient of the relative crack-face displacement (see details development in the work of Li et al. (1998) and Rungamornrat and Mear (2008b)). These positive features also enable the calculation of the mixed-mode stress intensity factors (i.e., mode-I, mode-II and mode-III stress intensity factors) in an accurate and efficient manner with use of reasonably coarse meshes. Unlike the jump of the displacement, the sum of the displacement across the crack face is approximated by standard C^0 interpolation functions everywhere.

For SGBEM-FEM coupling, the discretization of the governing equations of the BEM-region is achieved in the same fashion as described above whereas, for the finite element equations, all primary unknowns are approximated by standard three-dimensional, isoparametric C^0 elements (e.g., ten-node tetrahedral elements, fifteen-node prism elements and twenty-node brick elements). Details of discretization procedure and element-wise interpolation functions can be found in various literatures (e.g., Oden and Carey, 1984; Bathe, 1990; Belytschko et al., 2000). It is important to note that meshes on the interfaces of the two regions conform (i.e., the two discretized interfaces are geometrically identical). A simple means to generate those conforming interfaces is to mesh the FEM-region first and then use its surface mesh as the interface mesh of the BEM-region. With this strategy, all nodal points

on both discretized interfaces are essentially coincident. The key advantage of using conforming meshes is that the strong continuity of the displacement, the traction, and the test functions across the interface can be enforced exactly and, as a result, the condition $\mathcal{E} = 0$ is also satisfied in the discretization level. It should be emphasized also that nodes on the interface of the BEM-region contains six degrees of freedom (i.e., three displacement degrees of freedom and three traction degrees of freedom) while nodes on the FEM-region contains only three displacement degrees of freedom.

For the SGBEM-FEM coupling with consideration of surface stress effects, standard C^0 interpolation functions are utilized in the approximation of both trial and test functions. In particular, the following approximation for the test functions and the trial functions is introduced:

$$\tilde{u}_i^{s\Sigma} = \sum_{p=1}^{N} \tilde{U}_{3(p-1)+i}^{s\Sigma} \Phi_p \; ; \quad u_i^{\Sigma} = \sum_{q=1}^{N} U_{3(q-1)+i}^{\Sigma} \Phi_q \tag{3.1}$$

$$\tilde{u}_i^{\Delta} = \sum_{p=1}^{N} \tilde{U}_{3(p-1)+i} \Phi_p \; ; \quad u_i^{\Delta} = \sum_{q=1}^{N} U_{3(q-1)+i}^{\Delta} \Phi_q \tag{3.2}$$

$$\tilde{t}_i^{\Sigma} = \sum_{p=1}^{N} \tilde{T}_{3(p-1)+i} \Phi_p \; ; \quad t_i^{\Sigma} = \sum_{q=1}^{N} T_{3(q-1)+i}^{\Sigma} \Phi_q \tag{3.3}$$

where N is the number of nodal points; Φ_q is nodal basis functions at node q; $U_{3(q-1)+i}^{\Sigma}$, $U_{3(q-1)+i}^{\Delta}$, and $T_{3(q-1)+i}^{\Sigma}$ are nodal degrees of freedom associated with the sum of the displacement, the jump of the displacement and the sum of the traction across the crack surfaces, respectively; and $\tilde{U}_{3(p-1)+i}^{s\Sigma}$, $\tilde{U}_{3(p-1)+i}$, and $\tilde{T}_{3(p-1)+i}$ are arbitrary nodal quantities. Substituting (3.1)-(3.3) into (2.70) along with using the arbitrariness of $\tilde{U}_{3(p-1)+i}^{s\Sigma}$, $\tilde{U}_{3(p-1)+i}$, and $\tilde{T}_{3(p-1)+i}$, leads to a system of linear algebraic equations

$$\begin{bmatrix} \mathbf{A} & \mathbf{B} & \mathbf{0} \\ \mathbf{B}^T & \mathbf{C} & \mathbf{D} \\ \mathbf{0} & \mathbf{D}^T & \mathbf{E} \end{bmatrix} \begin{Bmatrix} \mathbf{U}^{\Sigma} \\ \mathbf{T}^{\Sigma} \\ \mathbf{U}^{\Delta} \end{Bmatrix} = \begin{Bmatrix} \mathbf{R}_1 \\ \mathbf{0} \\ \mathbf{R}_2 \end{Bmatrix} \tag{3.4}$$

where the sub-matrices $\mathbf{A}, \mathbf{B}, \mathbf{C}, \mathbf{D}, \mathbf{E}$ are associated with the bilinear operators $\mathcal{A}, \mathcal{B}, \mathcal{A}, \mathcal{B}, \mathcal{E}$; sub-vector $\mathbf{R}_1, \mathbf{R}_2$ correspond to the linear operators $\bar{\mathcal{R}}_1, \bar{\mathcal{R}}_2$; $\mathbf{U}^{\Sigma}$ is vector of nodal quantities of the sum of the displacement; $\mathbf{U}^{\Delta}$ is vector of nodal quantities of the jump of the displacement and $\mathbf{T}^{\Sigma}$ is vector of nodal quantities of the sum of the traction. The sub-matrices **A**, **B**, **C**, **D**, **E** and sub-vectors $\mathbf{R}_1, \mathbf{R}_2$ are given explicitly by

$$[\mathbf{A}]_{3(p-1)+3,3(q-1)+3} = \frac{\tau^s}{2} \int_{S_c^+} \Phi_{p,\gamma}(\boldsymbol{y}) \Phi_{q,\gamma}(\boldsymbol{y}) dS(\boldsymbol{y}) \tag{3.5}$$

$$[\mathbf{B}]_{3(p-1)+i,3(q-1)+j} = \frac{1}{2} \int_{S_c^+} \delta_{ij} \Phi_p(\boldsymbol{y}) \Phi_q(\boldsymbol{y}) dS(\boldsymbol{y}) \tag{3.6}$$

$$[\mathbf{C}]_{3(p-1)+i,3(q-1)+j} = -\int_{S_c^+} \Phi_p(\boldsymbol{y}) \int_{S_c^+} U_j^i(\xi - \boldsymbol{y}) \Phi_q(\xi) dS(\xi) dS(\boldsymbol{y}) \tag{3.7}$$

$$\begin{aligned}[\mathbf{D}]_{3(p-1)+i,3(q-1)+j} = &-\int_{S_c^+} \Phi_p(\boldsymbol{y}) \int_{S_c^+} G_{mj}^i(\boldsymbol{\xi} - \boldsymbol{y}) D_m \Phi_q(\boldsymbol{\xi}) dS(\boldsymbol{\xi}) dS(\boldsymbol{y}) \\ &+ \int_{S_c^+} \Phi_p(\boldsymbol{y}) \int_{S_c^+} H_{mj}^i(\boldsymbol{\xi} - \boldsymbol{y}) n_m(\boldsymbol{\xi}) \Phi_q(\boldsymbol{\xi}) dS(\boldsymbol{\xi}) dS(\boldsymbol{y})\end{aligned} \tag{3.8}$$

$$[\mathbf{E}]_{3(p-1)+i,3(q-1)+j} = -\int_{S_c^+} D_t \Phi_p(\boldsymbol{y}) \int_{S_c^+} C_{mj}^{ti}(\boldsymbol{\xi} - \boldsymbol{y}) D_m \Phi_q(\boldsymbol{\xi}) dS(\boldsymbol{\xi}) dS(\boldsymbol{y}) + [\mathbf{A}]_{3(p-1)+i,3(q-1)+j} \tag{3.9}$$

$$[\mathbf{R}_1]_{3(p-1)+i} = \frac{1}{2} \int_{S_c^+} \Phi_p(\mathbf{y}) t_i^{0\Sigma}(\mathbf{y}) dS(\mathbf{y}) \tag{3.10}$$

$$[\mathbf{R}_2]_{3(p-1)+i} = \frac{1}{2} \int_{S_c^+} \Phi_p(\mathbf{y}) t_i^{0\Delta}(\mathbf{y}) dS(\mathbf{y}) \tag{3.11}$$

$$[\mathbf{U}^{\Sigma}]_{3(q-1)+i} = U_{3(q-1)+i}^{\Sigma}; \quad [\mathbf{U}^{\Delta}]_{3(q-1)+i} = U_{3(q-1)+i}^{\Delta}; \quad [\mathbf{T}^{\Sigma}]_{3(q-1)+i} = T_{3(q-1)+i}^{\Sigma} \tag{3.12}$$

3.2 Numerical integration

For the finite element equations, all integrals arising from the discretization of the weak-form equation contain only regular integrands without the kernel and, as a result, they can be efficiently and accurately integrated by standard Gaussian quadrature. In the contrary, numerical evaluation of integrals arising from the discretization of the boundary integral equations is nontrivial since it involves the treatment of three types of double surface integrals (i.e., regular double surface integrals, weakly singular double surface integrals and nearly singular double surface integrals). The regular double surface integral arises when it involves a pair of remote outer and inner elements (i.e., the distance between any source and field points is relatively large when compared to the size of the two elements). This renders its integrand nonsingular and well-behaved and, as a result, allows the integral to be accurately and efficiently integrated by standard Gaussian quadrature.

The weakly singular double surface integral arises when the outer surface of integration is the same as the inner surface. For this particular case, the source and field points can be identical and this renders the integrand singular of order $1/r$. While the integral of this type exists in an ordinary sense, it was pointed out by Xiao (1998) that the numerical integration by Gaussian quadrature becomes computationally inefficient and such inaccurate evaluation can significantly pollute the quality of approximate solutions. To circumvent this situation, a series of transformations such as a well-known triangular polar transformation and a logarithmic transformation is applied first both to remove the singularity and to regularize the rapid variation of the integrand. The final integral contains a nonsingular integrand well-suited to be integrated by Gaussian quadrature. Details of this numerical quadrature can be found in the work of Li and Han (1985), Hayami and Brebbia (1988) and Xiao (1998).

The most challenging task is to compute nearly singular integrals involving relatively close or adjacent inner and outer elements. Although the integrand is not singular, it exhibits rapid variation in the zone where both source and field points are nearly identical. Such complex behavior of the integrand was found very difficult and inefficient to be treated by standard Gaussian quadrature Xiao (1998). To improve the accuracy of such quadrature, the triangular polar transformation is applied first and then a series of logarithmic transformations

is adopted for both radial and angular directions to further regularize the rapid-variation integrand. The resulting integral was found well-suited for being integrated by standard Gaussian quadrature (e.g., Hayami, 1992; Hayami and Matsumoto, 1994; Xiao, 1998).

3.3 Evaluation of kernels

To further reduce the computational cost required to form the coefficient matrix contributed from the BEM-region, all involved kernels $n_i(\boldsymbol{\xi})H_{ij}^{p}(\boldsymbol{\xi}-\mathbf{y})$, $n_i(\mathbf{y})H_{ij}^{p}(\boldsymbol{\xi}-\mathbf{y})$, $U_i^{p}(\boldsymbol{\xi}-\mathbf{y})$, $G_{mj}^{p}(\boldsymbol{\xi}-\mathbf{y})$, $C_{mj}^{tk}(\boldsymbol{\xi}-\mathbf{y})$ must be evaluated in an efficient manner for any pair of source and field points $\{\boldsymbol{\xi},\mathbf{y}\}$. For the first two kernels $n_i(\boldsymbol{\xi})H_{ij}^{p}(\boldsymbol{\xi}-\mathbf{y})$ and $n_i(\mathbf{y})H_{ij}^{p}(\boldsymbol{\xi}-\mathbf{y})$, they only involve the calculation of a unit normal vector $\mathbf{n}$ and the elementary function H_{ij}^{p}. This can readily be achieved via a standard procedure. For the last three kernels, the computational cost is significantly different for isotropic and anisotropic materials. For isotropic materials, such kernels only involve elementary functions and can therefore be evaluated in a straightforward fashion. On the contrary, the kernels $U_i^{p}(\boldsymbol{\xi}-\mathbf{y})$, $G_{mj}^{p}(\boldsymbol{\xi}-\mathbf{y})$ and $C_{mj}^{tk}(\boldsymbol{\xi}-\mathbf{y})$ for general anisotropy are expressed in terms of a line integral over a unit circle (see equations (2.7), (2.16a) and (2.16b)). Direct evaluation of such line integral for every pair of points $(\boldsymbol{\xi},\ \mathbf{y})$ arising from the numerical integration is obviously computationally expensive. To avoid this massive computation, a well-known interpolation technique (e.g., Rungamornrat and Mear, 2008b; Rungamornrat and Mear, 2011) is employed to approximate values of those kernels. Specifically, the interpolant of each kernel is formed based on a two-dimensional grid using standard quadratic shape functions. Values of kernels at all grid points are obtained by performing direct numerical integration of the line integral via Gaussian quadrature and then using the relations (2.7), (2.16a) and (2.16b). The accuracy of such approximation can readily be controlled by the refinement of the interpolation grid.

3.4 Determination of stress intensity factors and T-stresses

Stress intensity factors and T-stresses are quantities that play an important role in linear elastic fracture mechanics in the prediction of crack growth initiation and propagation direction and also in the fatigue-life assessment. This fracture data provides a complete measure of the dominant behavior of the stress field in a local region surrounding the crack front. To obtain highly accurate stress intensity factors and T-stresses, we supply the proposed numerical technique with two crucial components, one associated with the use of special crack-tip elements to accurately capture the near-tip field and the other corresponding to the use of an explicit formula to extract such fracture data. The latter feature is a direct consequence of the extra degrees of freedom being introduced along the crack front to represent the gradient of relative crack-face displacement and the finite in-plane strain components local to the crack front. Once a discretized system of algebraic equations is solved, nodal quantities along the crack front and nodal sum of the displacement on the crack-tip elements are extracted and then post-processed to obtain the stress intensity factors and T-stresses, respectively.

An explicit expression for the mixed-mode stress intensity factors in terms of nodal data along the crack front, local geometry of the crack front, and material properties is shown

briefly below (details of the development can be found in the work of Li *et al*. (1998) for cracks in isotropic media and Rungamornrat and Mear (2008b) for cracks in general anisotropic media).

Consider a crack-tip element located along the crack front where $\mathbf{x}_c$ denotes the coordinate of a node located on the crack front, $\{\mathbf{x}_c; x_1, x_2, x_3\}$ is a local Cartesian coordinate system with origin at $\mathbf{x}_c$ and $\{\mathbf{e}_1, \mathbf{e}_2, \mathbf{e}_3\}$ be a set of orthonormal base vectors as shown schematically in Figure 3.1.

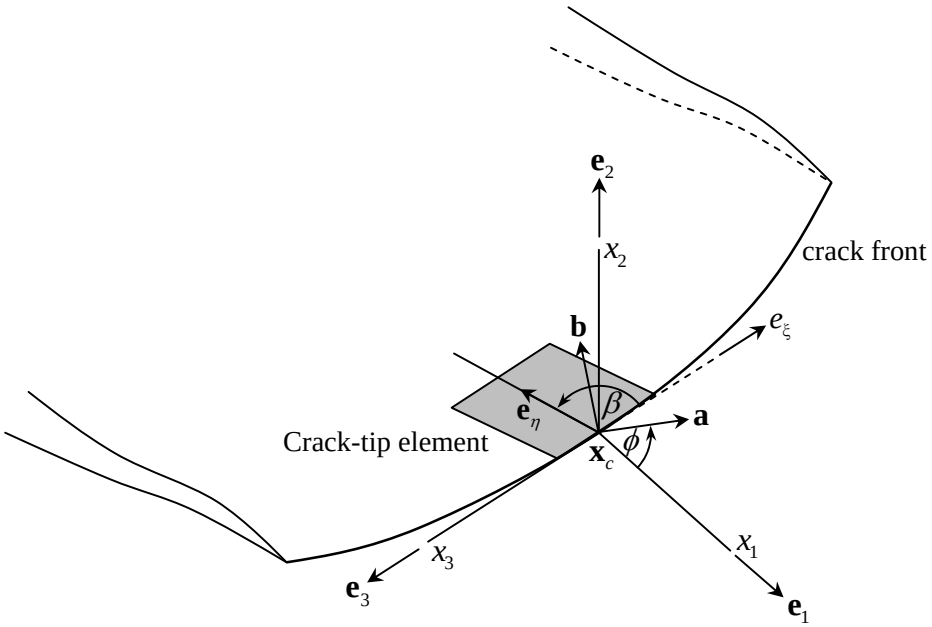

Figure 3.1 Schematic of crack-tip element and local coordinate system for calculation of stress intensity factors and T-stresses

The mode-I, mode-II, and mode-III stress intensity factors, denoted by $\{K_I, K_{II}, K_{III}\}$, are defined by

$$\begin{Bmatrix} K_I \\ K_{II} \\ K_{III} \end{Bmatrix} = \lim_{x_1 \to 0^+} \sqrt{2\pi x_1} \begin{Bmatrix} \sigma_{22} \\ \sigma_{12} \\ \sigma_{23} \end{Bmatrix} \tag{3.13}$$

where the quantities $\{\sigma_{22}, \sigma_{12}, \sigma_{23}\}$ are components of the stress tensor with respected to the local Cartesian coordinate system. While the definition (3.13) is fundamental, it is not well-suited within the context of a weakly singular SGBEM. This is due to that certain components of the generalized stress ahead of the crack front must be post-processed and that the limit must properly be carried out.

An alternative expression of the stress intensity factors equivalent to the definition (3.13), in terms of the relative crack-face displacement data in the neighborhood of the crack front, was proposed by Xu (2000) for general anisotropic materials. Such expression is given explicitly by

$$k_j(\mathbf{x}_c) = \frac{\sqrt{2\pi}}{4} B_{jp}(\mathbf{x}_c) \lim_{x_1 \to 0^-} \left(\frac{\Delta u_p(\mathbf{x})}{\sqrt{-x_1}} \right) \tag{3.14}$$

where $k_1 = K_{II}$, $k_2 = K_I$, $k_3 = K_{III}$ and

$$B_{jp}(\mathbf{x}_c) = \frac{1}{2\pi} \int_0^{2\pi} \left[(\mathbf{a},\mathbf{a})_{jp} - (\mathbf{a},\mathbf{b})_{jm} (\mathbf{b},\mathbf{b})^{-1}_{mn} (\mathbf{b},\mathbf{a})_{np} \right] d\phi \tag{3.15}$$

in which $\mathbf{a}$ and $\mathbf{b}$ are orthonormal vectors contained in the $x_1 - x_2$ plane, $(\mathbf{a},\mathbf{b})_{jm} = a_n E_{njml} b_l$, ϕ is an angle between the vectors $\mathbf{a}$ and $\mathbf{e}_1$ as indicated in Figure 3.1, and Δu_p denote the relative crack-face displacement. It is worth noting that components of all quantities appearing in (3.14) and (3.15) are taken with respect to the local coordinate system defined at point $\mathbf{x}_c$. By exploiting Taylor series expansion along with the crucial feature of the crack-tip element, the expression (3.14) can further be simplified to

$$k_J(\mathbf{x}_c) = \sqrt{\frac{\pi}{2J \sin\beta}} B_{JP}(\mathbf{x}_c) u^*_P(\mathbf{x}_c) \tag{3.16}$$

where β is angle satisfying $\sin\beta = -\mathbf{e}_n . \mathbf{e}_1$,

$$u^*_P(\mathbf{x}_c) = \sum_{i=1}^{9} u^e_{P(i)} \psi_i(\xi_c, -1) \ , \tag{3.17}$$

$$J = \left\| \frac{\partial \mathbf{r}_c}{\partial \eta}(\xi_c, -1) \right\| \ , \tag{3.18}$$

$$\mathbf{e}_n = \frac{1}{J} \frac{\partial \mathbf{r}_c}{\partial \eta}(\xi_c, -1) \ , \tag{3.19}$$

$$\mathbf{r}_c(\xi, n) = \mathbf{x}(\xi, n) - \mathbf{x}_c \ , \tag{3.20}$$

with $(\xi_c, -1)$ denoting the natural coordinates of $\mathbf{x}_c$ and $u^e_{p(i)}$ representing the components of nodal data at the ith node, $\mathbf{u}^e_{(i)}$, with respect to the local coordinate system. It is important to point out that the formula (3.16) allows the stress intensity factors to be computed only in terms of the data at nodes located on the crack front. This is due to the fact that $\psi_i(\xi_c, -1)$ vanishes for nodes not on the crack front.

The T-stresses along the crack front, referring to the local coordinate system shown in Figure 3.1, contains three independent components denoted by T_{11}, T_{33} and T_{13} where the first two components are termed the normal T-stresses and the last one is a shear T-stress. Values of the T-stresses T_{11}, T_{33} and T_{13} at the point $\mathbf{x}_c$ can be related to the finite part of the strain tensor at the limiting point of the point $\mathbf{x}_c$ on the crack surface, denoted by ε_{kl}, via the stress-strain relation:

$$T_{ij} = E_{ijkl}\varepsilon_{kl} \tag{3.21}$$

where $T_{ij} = T_{ji}$, $\varepsilon_{ij} = \varepsilon_{ji}$, the components T_{22}, T_{12} and T_{23} are known and equal to the prescribed traction at a limiting point of the point $\mathbf{x}_c$ on the crack surface. The components ε_{11}, ε_{33} and ε_{13} can be computed from the information of the sum of the displacement across the crack surface in the neighborhood of the point $\mathbf{x}_c$ via the following relations

$$\varepsilon_{11} = \frac{1}{2}\lim_{\mathbf{x}\to\mathbf{x}_c}\frac{\partial\Sigma u_1}{\partial x_1} = \frac{1}{2}\frac{\partial\Sigma u_1}{\partial x_1}(\mathbf{x}_c) \tag{3.22}$$

$$\varepsilon_{33} = \frac{1}{2}\lim_{\mathbf{x}\to\mathbf{x}_c}\frac{\partial\Sigma u_3}{\partial x_3} = \frac{1}{2}\frac{\partial\Sigma u_3}{\partial x_3}(\mathbf{x}_c) \tag{3.23}$$

$$\varepsilon_{13} = \frac{1}{4}\lim_{\mathbf{x}\to\mathbf{x}_c}\left\{\frac{\partial\Sigma u_1}{\partial x_3} + \frac{\partial\Sigma u_3}{\partial x_1}\right\} = \frac{1}{4}\left\{\frac{\partial\Sigma u_1}{\partial x_3} + \frac{\partial\Sigma u_3}{\partial x_1}\right\}(\mathbf{x}_c) \tag{3.24}$$

The derivatives involved in the expressions (3.22)-(3.24) can readily be computed within the crack-tip elements. By using the prescribed information of T_{22}, T_{12} and T_{23} and the computed strain components ε_{11}, ε_{33} and ε_{13}, the unknown strain components ε_{22}, ε_{12} and ε_{23} and the T-stresses T_{11}, T_{33} and T_{13} at the point $\mathbf{x}_c$ can be determined by solving a system of six linear algebraic equations (3.21).

3.5 Coupling of SGBEM and commercial FE package

To further enhance the modeling capability of the SGBEM-FEM coupling, the weakly singular SGBEM can be coupled with a reliable commercial finite element package that supports user-defined subroutines. The key objective is to exploit available vast features of such FE package (e.g., mesh generation, user-defined elements, powerful linear and nonlinear solvers, and various material models, etc.) to treat a complex, localized FEM-region and utilize the SGBEM in-house code to supply information associated with the majority of the domain that is unbounded and possibly contains isolated discontinuities.

In the coupling procedure, the governing equation for the BEM-region is first discretized into a system of linear algebraic equations. The corresponding coefficient matrix and the vector involving the prescribed data are constructed using the in-house code and they can be viewed as a stiffness matrix and a load vector of a ‘super element’ containing all degrees of freedom of the BEM-region. This piece of information is then imported into the commercial FE package via a user-defined-subroutine channel and then assembled with element stiffness matrices contributed from the discretized FEM-region. Since meshes of both interfaces (one associated with the BEM-region and the other corresponding to the FEM-region) are conforming, the assembly procedure can readily be achieved by using a proper numbering strategy. Specifically, nodes on the interface of the BEM-region are named identical to nodes on the interface of the FEM-region (associated with the same displacement degrees of freedom). It is important to emphasize that all interface nodes of the BEM-region possess six degrees of freedom (i.e. three displacement degrees of freedom and three traction

degrees of freedom) but there are only three (displacement) degrees of freedom per interface node of the FEM-region. To overcome such situation, each interface node of the BEM-region is fictitiously treated as double nodes where the first node is chosen to represent the displacement degrees of freedom and is numbered in the same way as its coincident interface node of the FEM-region whereas the second node is chosen with different name to represent the traction degrees of freedom. With this particular scheme, the assembling procedure follows naturally that for a standard finite element technique.

Once the coupling analysis is complete, nodal quantities associated with the BEM-region are extracted from the output file generated by the FE package and then post-processed for quantities of interest. For instance, the displacement and stress within the BEM-region can readily be computed from the standard displacement and stress boundary integral relations presented in sections 2.5 and 2.6, and the stress intensity factors and T-stresses can be calculated using an explicit expression proposed in section 3.4.

CHAPTER IV

NUMERICAL RESULTS

To demonstrate the accuracy and capabilities of the SGBEM and SGBEM-FEM coupling with and without consideration of nano-scale influence, extensive numerical experiments on various boundary value problems involving finite and infinite bodies.

4.1 Results from SGBEM

Problems with existing analytical solutions are considered first. These problems serve not only to verify the formulation of governing equations and its numerical implementation but also as a means to investigate the dependence of the numerical solutions on mesh refinement. The method is then applied to solve more complex boundary value problems. Analytical solutions to these problems are not available, and they may be of little direct technological relevance. They are chosen for analysis here simply because the additional complexity introduced by the crack configurations and geometry of the body allows us to further explore the effectiveness of the proposed technique for solving complex problems.

4.1.1 Penny-shaped crack in isotropic elastic medium under remote loading

Consider an isolated penny-shaped crack of radius a embedded in an infinite medium as shown in Figure 4.1.1. The medium is subjected to either remote uniaxial tension or remote pure bending (see Figure 4.1.1). In the analysis, the material is chosen to be isotropic, linearly elastic with Young's modulus E and Poisson ratio $\nu = 0.3$ in order to allow the comparison with the analytical solutions proposed by Wang (2004). To demonstrate the convergent behavior of numerical results for both stress intensity factors and T-stresses, three meshes shown in Figure 4.1.2 are adopted in the numerical study.

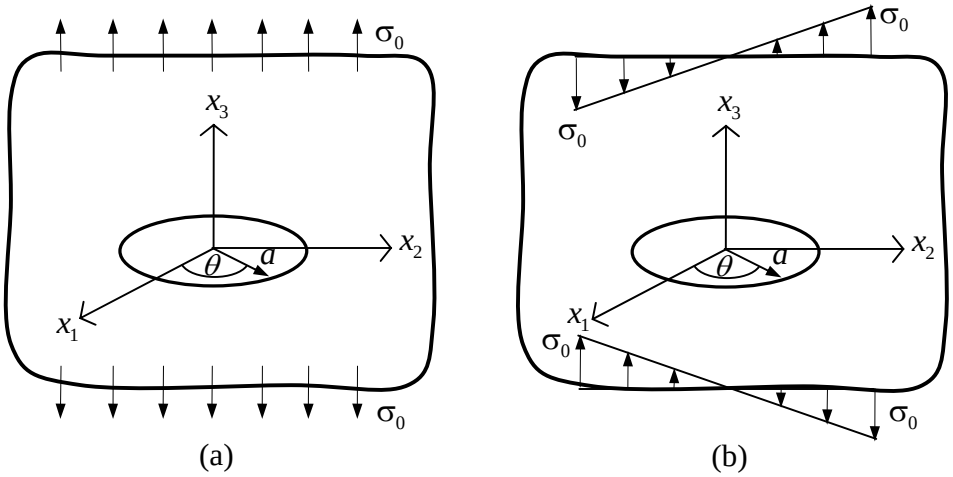

Figure 4.1.1 Schematic of penny-shaped crack in infinite medium under (a) remote uniaxial tension and (b) remote pure bending

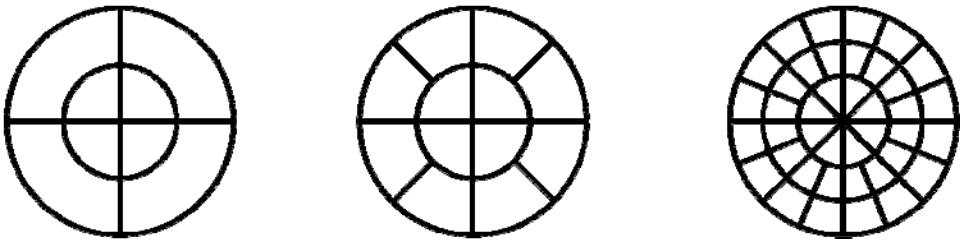

Mesh-1 Mesh-2 Mesh-3

Figure 4.1.2 Three meshes adopted in the analysis of penny-shaped crack under uniformly distributed pressure

The mode-I stress intensity factor K_I and the normal T-stress T_{11} obtained from the three meshes for the remote uniaxial tension loading condition are reported in Table 4.1.1. The computed results are normalized by the following exact solution obtained from the work of Wang (2004): $K_{I,exact} = 2\sigma_0\sqrt{a/\pi}$ and $T_{11,exact} = -(1+2\nu)\sigma_0/2$. It is evident from this set of results that numerical solutions for both the stress intensity factors and the T-stresses show excellent agreement with the benchmark solution. In particular, the coarsest mesh with only 8 elements yield the results with error less than 1%. The highly accurate feature results directly from the use of special crack-tip elements along the crack tip to accurately capture the jump of the displacement across the crack surface in the vicinity of the crack boundary. For the medium subjected to remote pure bending, both the mode-I stress intensity factor and the normal T-stress varies as a function of position along the crack front. The normalized mode-I stress intensity factors obtained from the three meshes are reported in Figure 4.1.3 whereas the normalized normal T-stress are shown in Figure 4.1.4 along with the following solution provided by Wang (2004): $K_{I,exact} = 4\sigma_o\sqrt{a/\pi}\cos\theta/3$ and $T_{11,exact} = -(3/4+\nu/2)\sigma_o\cos\theta$.

Table 4.1.1 Normalized mode-I stress intensity factors and normal T-stress T_{11} for isolated penny-shaped crack subjected to remote uniaxial tension. Results are reported for $\nu = 0.3$.

Mesh	$K_I / K_{I,exact}$	$T_{11} / T_{11,exact}$
1	0.9949	0.9917
2	1.0003	0.9984
3	1.0006	0.9978

4.1.2 Penny-shaped crack in transversely isotropic medium under uniform pressure

To demonstrate the capability of the technique to treat material anisotropy, let us consider a similar problem of penny-shaped crack of radius a embedded in a transversely isotropic, infinite medium as shown schematically in Figure 4.1.1. Non-zero material constants are chosen to be E_{1111} = 16.09x10^6 psi, E_{1122} = 3.35x10^6 psi, E_{1133} = 5.01x10^6 psi, E_{3333} = 6.10x10^6 psi, and E_{1313} = 3.83x10^6 psi. In the analysis, the same three meshes illustrated in Figure 4.1.2 are employed to investigate the convergence of numerical solutions.

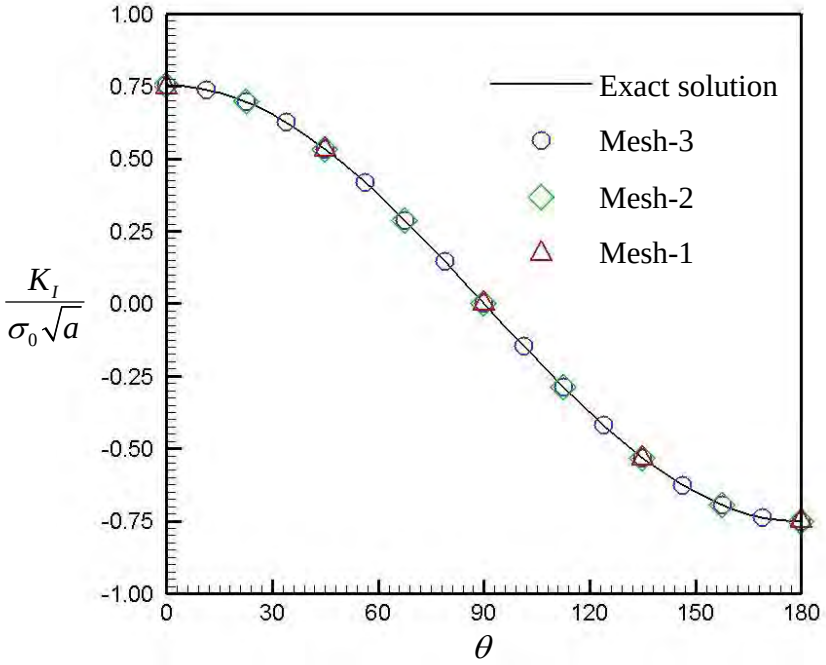

Figure 4.1.3 Normalized mode-I stress intensity factor versus angular coordinate for penny-shaped crack in isotropic infinite medium under remote pure bending

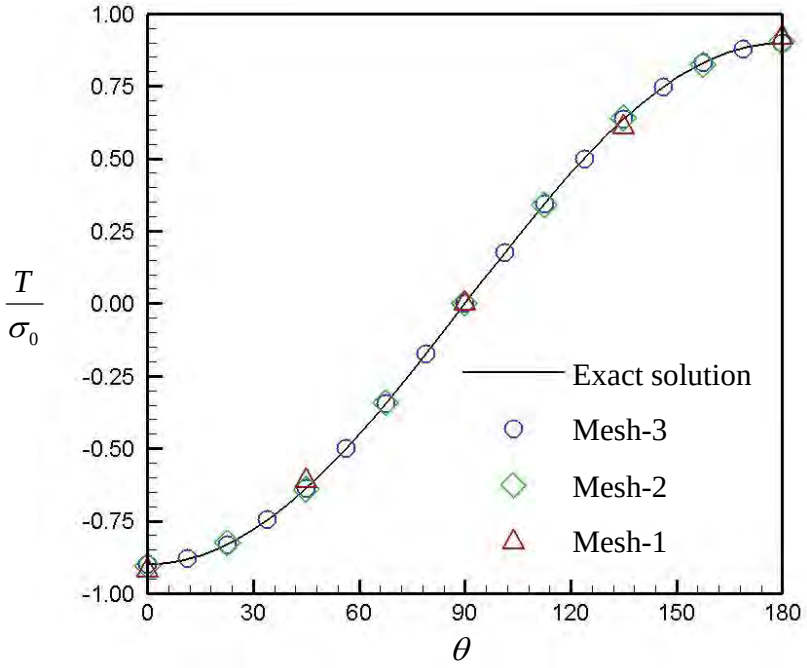

Figure 4.1.4 Normalized normal T-stress versus angular coordinate for penny-shaped crack in isotropic infinite medium under remote pure bending

The mode-I stress intensity factor K_I and the normal T-stress T_{11} obtained from the three meshes are reported in Table 4.1.2. The computed results for mode-I stress intensity factors are normalized by the closed form solution presented by Fabrikant (1989): $K_{I,exact} = 2\sigma_0\sqrt{a/\pi}$. For the case of normal T-stress, the computed solutions are normalized by that obtained from the finest mesh (i.e., Mesh-3) since the analytical solution for such quantity cannot be found in the literature. It is evident that the proposed technique yields highly accurate stress intensity factor although the coarse mesh with only few degrees of freedom has been employed. Similarly, results for the normal T-stress shows the good convergence with only weak dependence on the level of mesh refinement.

Table 4.1.2 Normalized mode-I stress intensity factors and normal T-stress T_{11} for isolated penny-shaped crack embedded in transversely isotropic medium and subjected to uniform pressure

Mesh	$K_I / K_{I,exact}$	$T_{11} / T_{11,Mesh-3}$
1	0.9913	0.9897
2	0.9984	0.9948
3	0.9997	1.0000

4.1.3 Influence of thickness on stress intensity factors

Once accuracy and convergence of the implemented SGBEM has been fully tested, it is applied to solve various complex fracture problems. Here, the technique is utilized to investigate the influence of the thickness of a body on the value and distribution of the stress intensity factor along the crack front.

Consider a particular cracked body with its configuration similar to a compact tension (CT) testing specimen. ASTM E399-90 (1997) has recommended the geometries of the CT specimen in the experiment for the plane strain fracture toughness K_{IC} as shown in Figure 4.1.5. The ratio between the crack length a (measured from the center of each hole to the crack front) and the specimen width W (measured from the center of each hole to the back face of the specimen) must be chosen in the range of 0.45 to 0.55 and the thickness is recommended to be $0.5W$. The entire width (measured from the back face to the front face) is equal to $1.25W$. A pair of equal and opposite loads is to be applied at the holes of radius $0.25W$ to open the crack. The distance between the center of each hole and the crack plane is equal to $0.275W$ and the distance from the crack plane to the top and bottom surface of the specimen is equal to $0.6W$. Details of a small starter notch in front of the crack plane can be found in ASTM E399-90 (1997). In the modeling, we choose a configuration as shown in Figure 4.1.6 to represent the CT specimen shown in Figure 4.1.5. The difference between this model and the actual CT specimen is due to the removal of the notch and then replacing it by a through-the-thickness crack. It is worth noting that this simplification should not significantly alter the behavior of the problem but substantially reduces the meshing effort. In the analysis, we choose $a/W = 0.5$ and the thickness of the specimen is varied in order to investigate its influence on the distribution of the stress intensity factor. The applied loads at

both holes are assumed to be uniformly distributed over the upper part of the upper hole and the lower part of the hole.

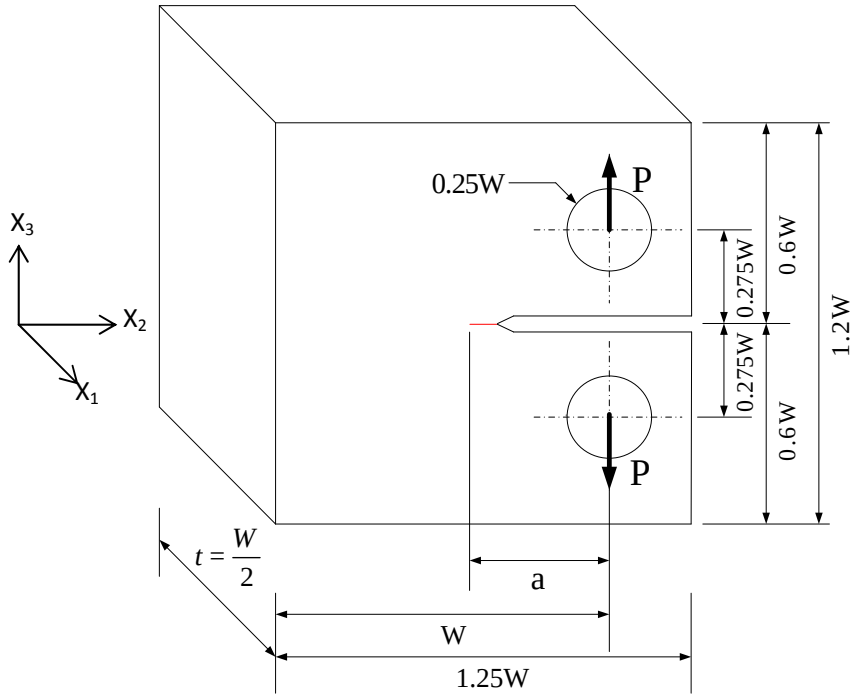

Figure 4.1.5 Configuration of compact tension (CT) specimen recommended by ASTM E399-90 (1997)

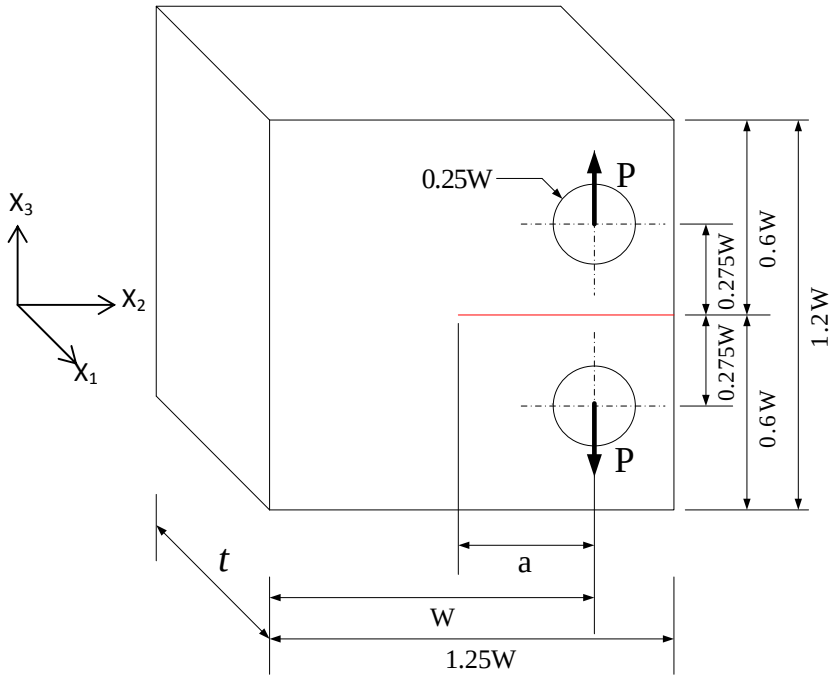

Figure 4.1.6 Configuration of compact tension (CT) specimen used in the analysis

In the construction of a finite element mesh on the boundary of the CT specimen and the crack surface, the number of distorted elements and elements with a large aspect ratio is minimized, a finer mess is utilized in regions where fields are anticipated to be complex such as regions near the crack front and vertices, and a mesh with smooth transition is employed to connect the fine mesh region and the coarse mesh region. Three types of elements are utilized in the discretization of the CT specimen: (i) standard 6-node triangular elements and standard 8-node quadrilateral elements, (ii) 9-node quadrilateral crack-tip elements, and (iii) special 9-node quadrilateral elements. More specifically, elements in the second category are utilized only along the entire crack front whereas on the front and back faces of the specimen, two elements of the last type must be used to connect the crack-tip element and the standard elements. The remaining boundary and crack surface are discretized by elements in the first category.

In the present study, three meshes, a coarse mesh denoted by Mesh-1, a medium mesh denoted by Mesh-2 and a fine mesh denoted by Mesh-3, are constructed as shown in Figures 4.1.7-4.1.9 for a specimen of thickness $t/a = 1$. In the analysis, we consider three different materials, one associated with an isotropic material with Poisson's ratio $\nu = 0.30$ and the other two corresponding to the transversely isotropic material with elastic constants chosen to be those for zinc and cadmium as given in Table 4.1.3. It should be noted that for the last two materials, the axis of material symmetry is chosen to direct perpendicular to the crack surface.

Table 4.1.3 Elastic constants (GPa) for zinc and cadmium. The axis of material symmetry is taken to direct along the x_3-coordinate direction.

Materials	E_{1111}	E_{1122}	E_{1133}	E_{3333}	E_{1313}
Zinc	161	34.2	50.1	61	38.3
Cadmium	115.8	39.8	40.6	51.4	20.4

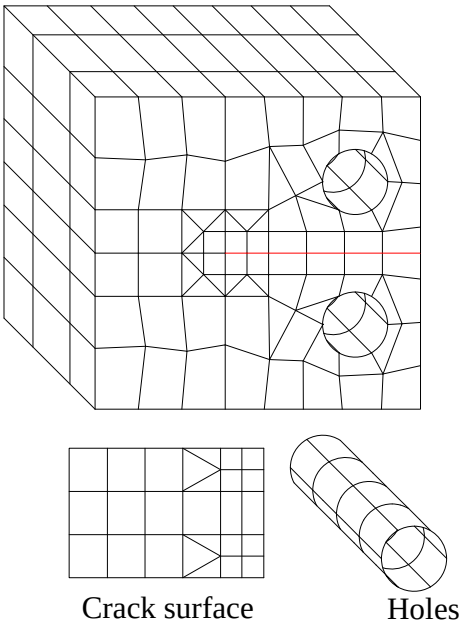

Figure 4.1.7 Coarse mesh or Mesh-1 for CT specimen thickness $t/a = 1$

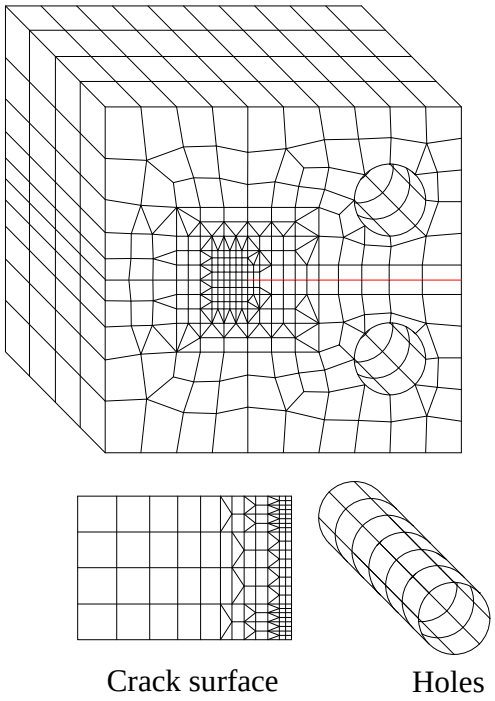

Figure 4.1.8 Medium mesh or Mesh-2 for CT specimen thickness $t / a = 1$

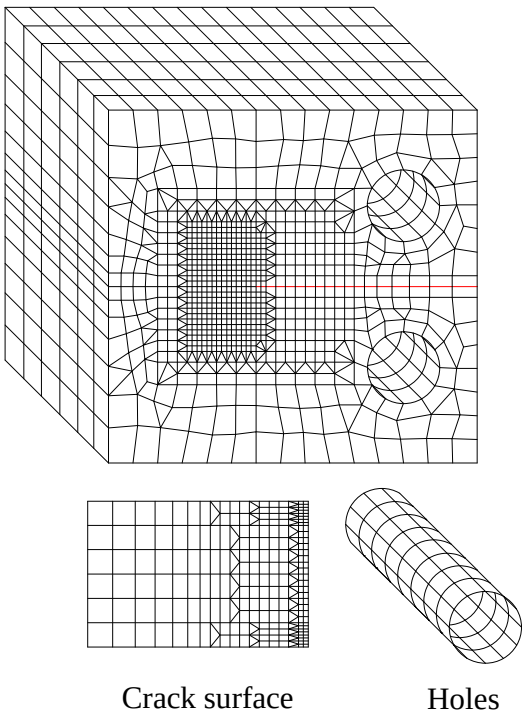

Figure 4.1.9 Fine mesh or Mesh-3 for CT specimen thickness $t / a = 1$

Numerical results for the mode-I stress intensity factor along the crack front are reported for three materials and three meshes in Figure 4.1.10. It is evident that results obtained from the Mesh-2 and Mesh-3 are almost identical while those from the Mesh-1 exhibit slight difference especially very near the vertices where the stress intensity factor drops very rapidly. This should imply the rapid convergence and the weak dependency on the level of mesh refinement for both isotropic and anisotropic cases. Next, we investigate the convergence behavior of numerical results for the same specimen but with the thickness $t/a = 4$. Meshes used in the analysis for this particular case are obtained by simply scaling coordinates in the direction along the thickness of the three meshes shown in Figures 4.1.7-4.1.9. Again, results of the mode-I stress intensity factor (see Figure 4.1.11) lead to the same conclusion as the previous case and, in particular, stretching meshes in the thickness direction by four times still does not alter the convergence characteristic of the numerical solutions. It is worth noting that approximate solutions of this high quality can be achieved via the use of relatively coarse meshes due mainly to the application of special crack-tip elements along the crack front. Since the medium mesh and the fine mesh yields results of comparable accuracy while the latter consumes substantially more computational time, a level of refinement similar to that for the former mesh will be used in the construction of meshes for a CT specimen of other thicknesses in the parametric study to explore the behavior of the stress intensity factor.

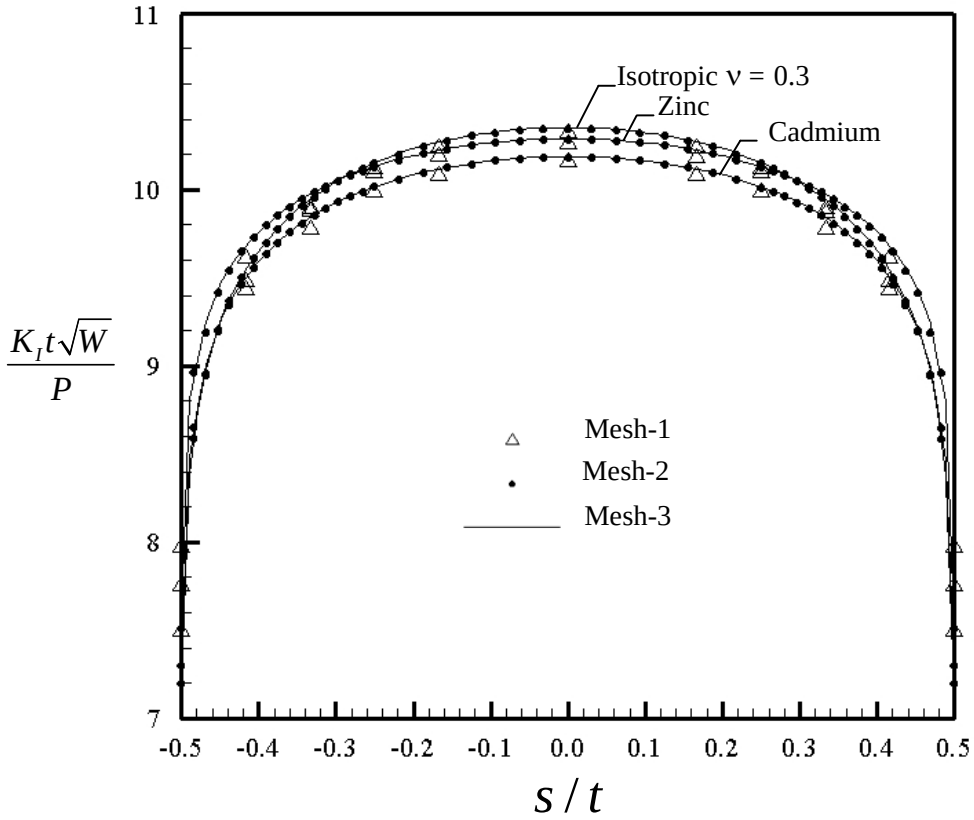

Figure 4.1.10 Normalized mode-I stress intensity factor along the crack front for CT specimen thickness $t/a = 1$. Results are reported for three meshes and three materials and s denotes the distance measured from the center of the crack front.

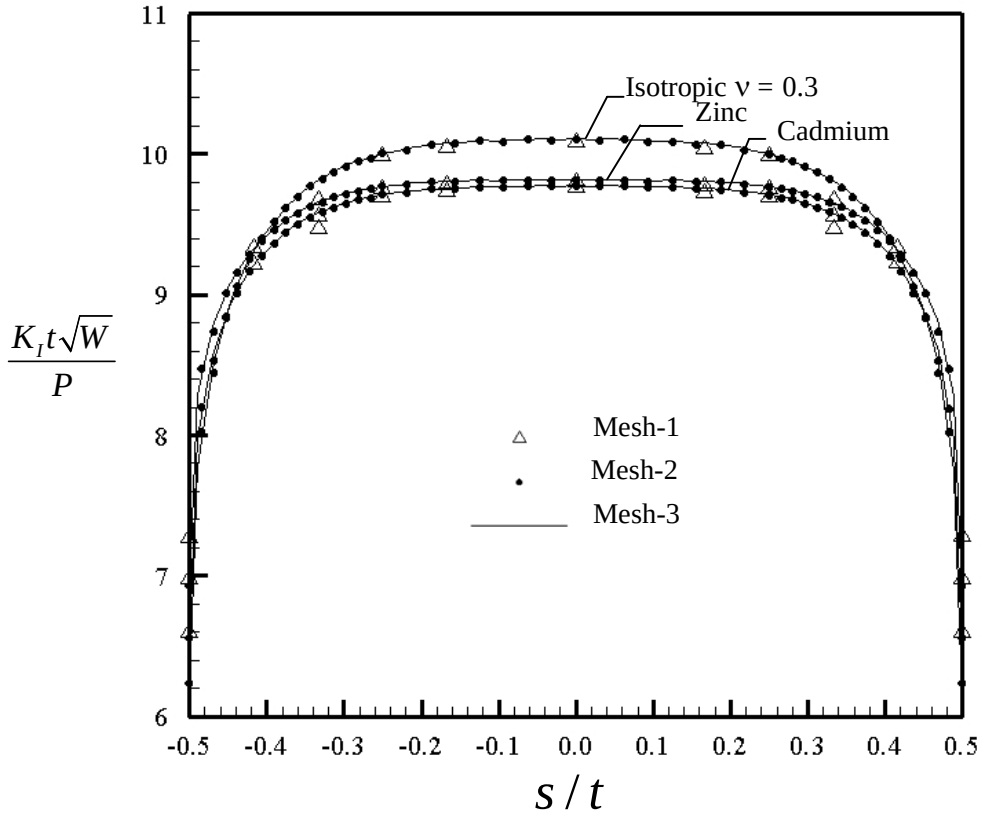

Figure 4.1.11 Normalized mode-I stress intensity factor along the crack front for CT specimen thickness $t/a = 4$. Results are reported for three meshes and three materials and s denotes the distance measured from the center of the crack front.

To verify the numerical results obtained from the weakly singular SGBEM, comparisons with existing benchmark solutions for a two-dimensional plane strain case and for isotropic materials are performed. Consider a CT specimen of sufficiently large thickness to ensure the existence of a plane strain condition in the central region of the crack front. Numerical results obtained from a mesh with the same level of refinement as the medium mesh shown in Figure 4.1.8 are reported along with the plane strain solution proposed by ASTM E399-90 (1997) in Figure 4.1.12 for Poisson ratio $\nu = 0.1$ and in Figure 4.1.13 for Poisson ratio $\nu = 0.3$. It is evident that the SGBEM solutions (in the region exhibiting the plane strain condition) show very good agreement with the benchmark solution. Besides this verification, it should be noted that extensive verification of the weakly singular SGBEM and its formulation used in the present study was already performed by Li *et al*. (1998) and Rungamornrat and Mear (2008b) for various crack problems associated with both isotropic and transversely isotropic media.

To construct meshes for the CT specimen of various thicknesses, the medium mesh for $t/a = 1$ shown in Figure 4.1.8 is used as a prototype. Two following simple strategies, (i) mesh stretching along the crack front direction and (ii) adding an inner layer, are employed.

The mesh stretching is applied first to obtain a series of meshes for several thicknesses without adding nodes and elements but simply scaling the coordinate along the crack front.

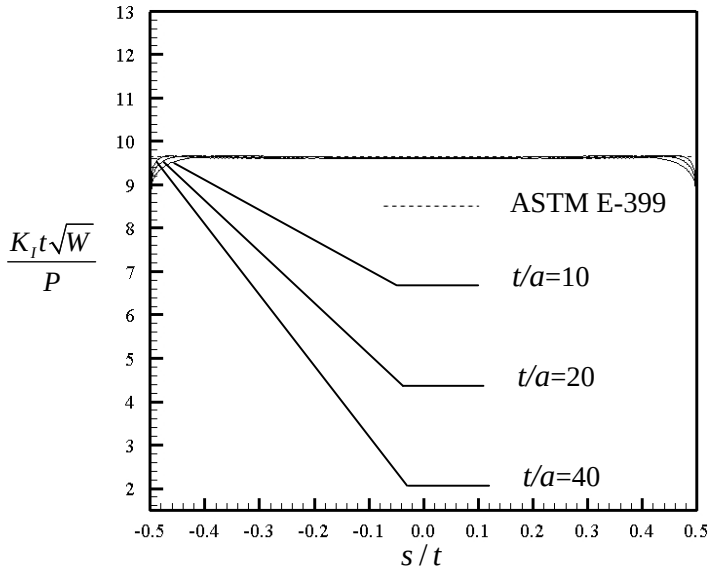

Figure 4.1.12 Normalized mode-I stress intensity factor along the crack front for CT specimen for sufficiently large thicknesses along with the plane strain solution from ASTM E399-90 (1997). Results are reported for isotropic material with $\nu = 0.1$ and s denotes the distance measured from the center of the crack front.

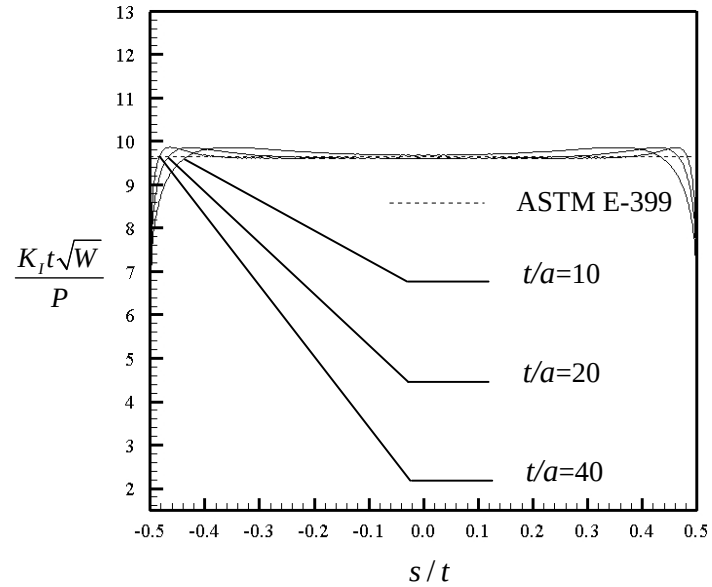

Figure 4.1.13 Normalized mode-I stress intensity factor along the crack front for CT specimen for sufficiently large thicknesses along with the plane strain solution from ASTM E399-90 (1997). Results are reported for isotropic material with $\nu = 0.3$ and s denotes the distance measured from the center of the crack front.

To explore the influence of the specimen thickness and material constants on the behavior of the stress intensity along the crack front for the isotropic case, we perform the analysis for various thicknesses $t/a \in \{1, 2, 3, 4, 5, 10, 20, 40\}$ and several values of Poisson's ratio $\nu \in \{0, 0.05, 0.10, 0.15, 0.20, 0.25, 0.30, 0.35, 0.40, 0.45, 0.50\}$ for each thickness. It should be noted that the stress intensity factor exhibits material dependence only on the Poisson's ratio ν not the Young's modulus E. The normalized mode-I stress intensity factors, denoted by $K_I t\sqrt{W}/P$, is reported as a function of the normalized distance along the crack front, denoted by s/t, in Figure 4.1.14 for $\nu = 0$, Figure 4.1.15 for $\nu = 0.10$, Figure 4.1.16 for $\nu = 0.30$, and Figure 4.1.17 for $\nu = 0.50$. For each plot, the plane strain stress intensity factor proposed by ASTM E-399 is also reported to allow the comparison and discussion. From this set of results, following findings are summarized.

For Poisson's ratio $\nu = 0$, the plane strain condition dominates the entire crack front with no regard of the specimen thickness and, in addition, the computed results exhibit excellent agreement with the benchmark solution except in the region close to the surface breaking points. The slightly oscillated behavior of numerical solutions observed in that region is due to the fact that the (reduced-order) special crack-tip element and the adjacent modified boundary element containing the vertices cannot accurately capture the asymptotic field. Note in addition that the stress field at the vertex, for this particular case, is singular of the same order as that for the interior point of the crack front. For small Poisson's ratio (i.e. $\nu \le 0.1$), the stress intensity factor varies along the crack front but such variation is still insignificant for all thicknesses considered. The rapid decrease of the stress intensity factor is observed in the neighborhood of the surface breaking point. This implies that the singularity of the stress field at the vertex is of order less than $1/\sqrt{r}$.

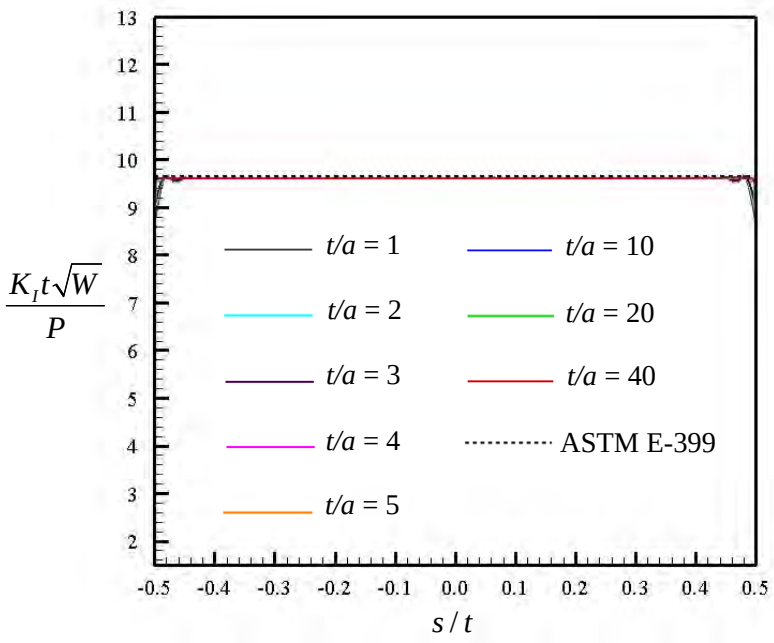

Figure 4.1.14 Normalized mode-I stress intensity factor versus the normalized distance along the crack front for various thicknesses and $\nu = 0$

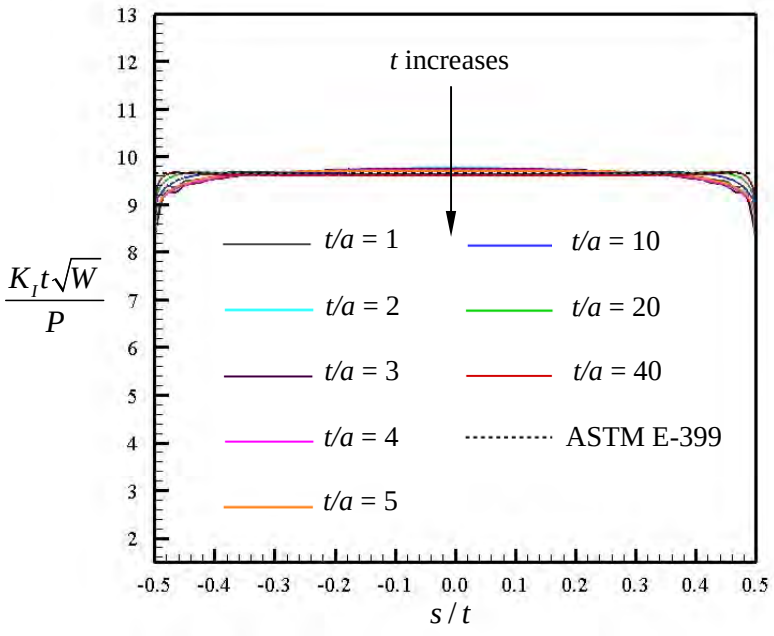

Figure 4.1.15 Normalized mode-I stress intensity factor versus the normalized distance along the crack front for various thicknesses and ν = 0.1

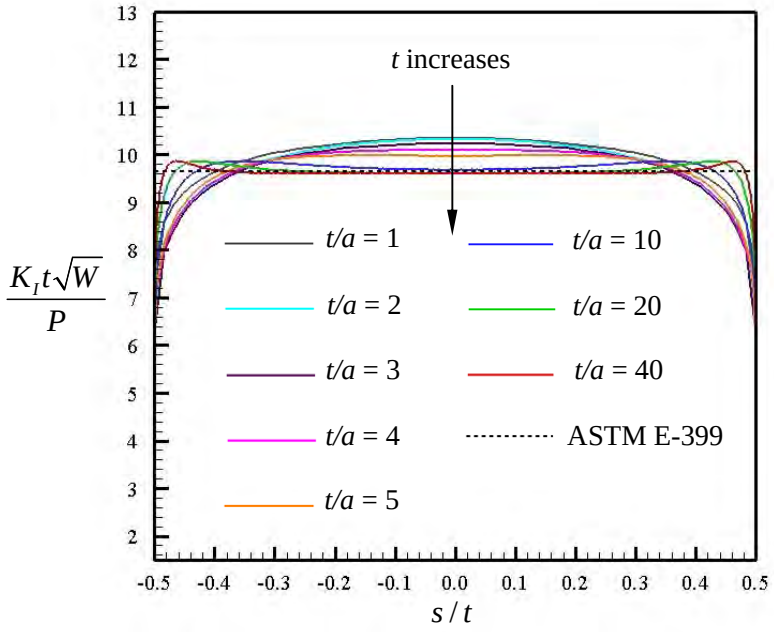

Figure 4.1.16 Normalized mode-I stress intensity factor versus the normalized distance along the crack front for various thicknesses and ν = 0.3

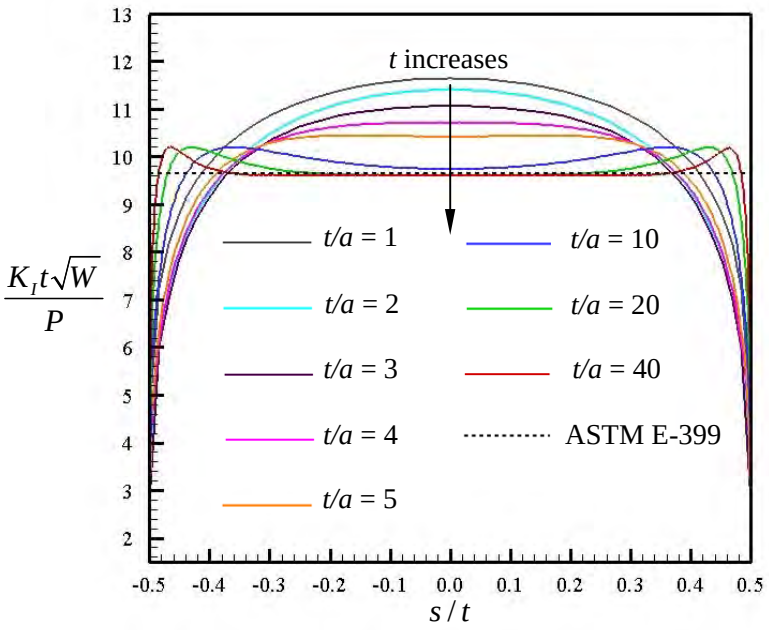

Figure 4.1.17 Normalized mode-I stress intensity factor versus the normalized distance along the crack front for various thicknesses and $\nu = 0.5$

For moderate and large Poisson's ratio (i.e. $\nu \geq 0.2$), the variation of the stress intensity factor across the thick becomes more significant and depends primarily on the specimen thickness. For a specimen with small thickness (i.e. $t/a \leq 5$), the stress intensity factor attains its maximum value at the center of the crack front and monotonically decreases to zero at the two vertices. The slight rate of decrease is observed for the majority of the crack front except in a layer near the outer boundary where the rapid drop occurs. In addition, the three-dimensional analysis yields the stress intensity factor higher than the plane strain value for a large portion of the crack front. For a specimen with sufficiently large thickness (i.e. $t/a \geq 10$), the stress intensity factor starts to converge to the plane strain value in the central region of the crack front and the converged zone spreads towards the vertices as the thickness increases. For a specimen with the maximum thickness $t/a = 40$, the plane strain dominated zone covers more than 70% of the crack front for all values of Poisson's ratio treated.

To additionally demonstrate the influence of the Poisson's ratio on both the distribution and magnitude of the stress intensity factor across the thickness, we create different plots between $K_I t\sqrt{W}/P$ and s/t by fixing the specimen thickness but varying the Poisson's ratio. Results are reported in Figure 4.1.18 for a thinnest specimen ($t/a = 1$), in Figure 4.1.19 for $t/a = 5$, in Figure 4.1.20 for $t/a = 10$, and in Figure 4.1.21 for $t/a = 40$. It can be concluded from these plots that the thickness of a specimen significantly affects the characteristic of the distribution (i.e. shape) of the stress intensity factor along the crack front while the Poisson's ratio only influence its magnitude. More specifically, the larger the Poisson's ratio, the higher the stress intensity factor is observed.

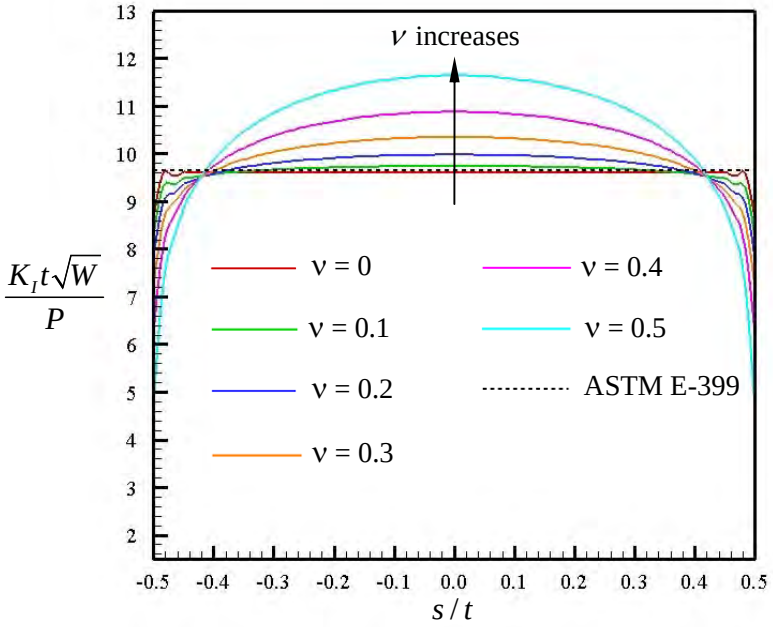

Figure 4.1.18 Normalized mode-I stress intensity factor versus the normalized distance along the crack front for various Poisson's ratios and $t/a = 1$

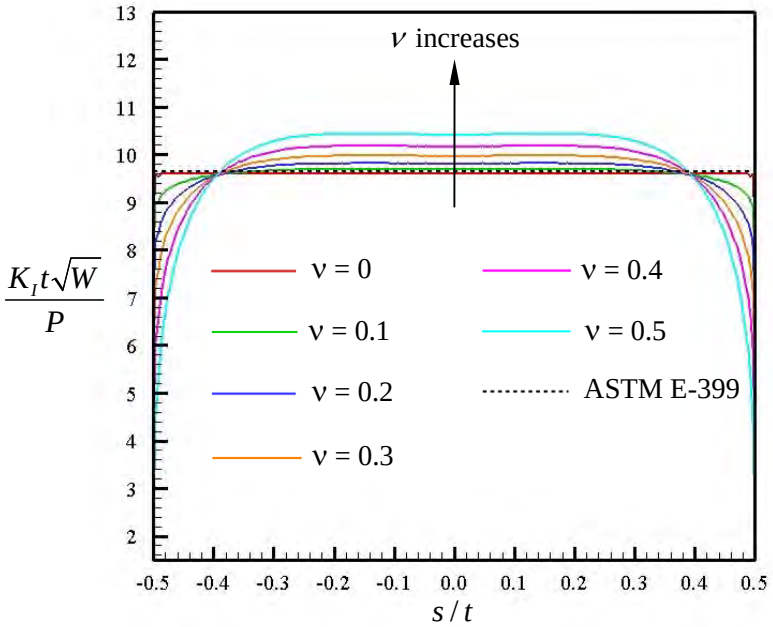

Figure 4.1.19 Normalized mode-I stress intensity factor versus the normalized distance along the crack front for various Poisson's ratios and $t/a = 5$

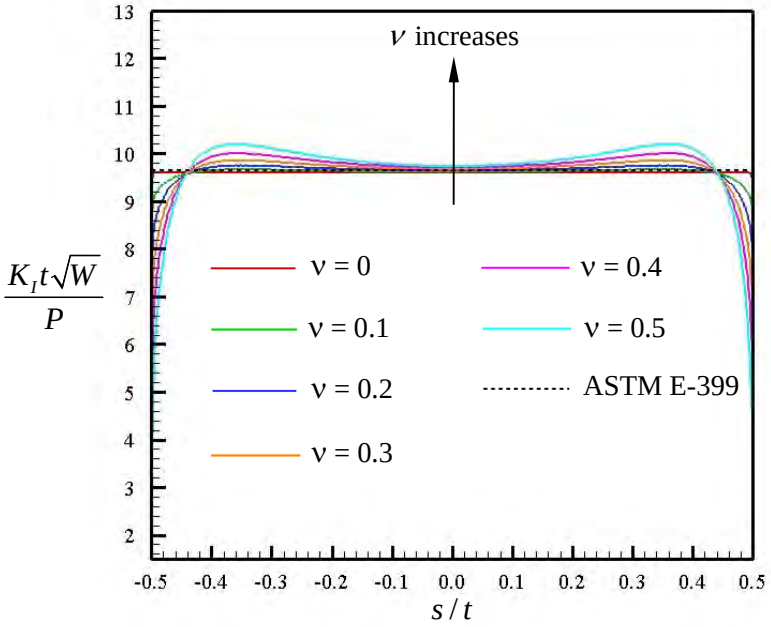

Figure 4.1.20 Normalized mode-I stress intensity factor versus the normalized distance along the crack front for various Poisson's ratios and $t/a = 10$

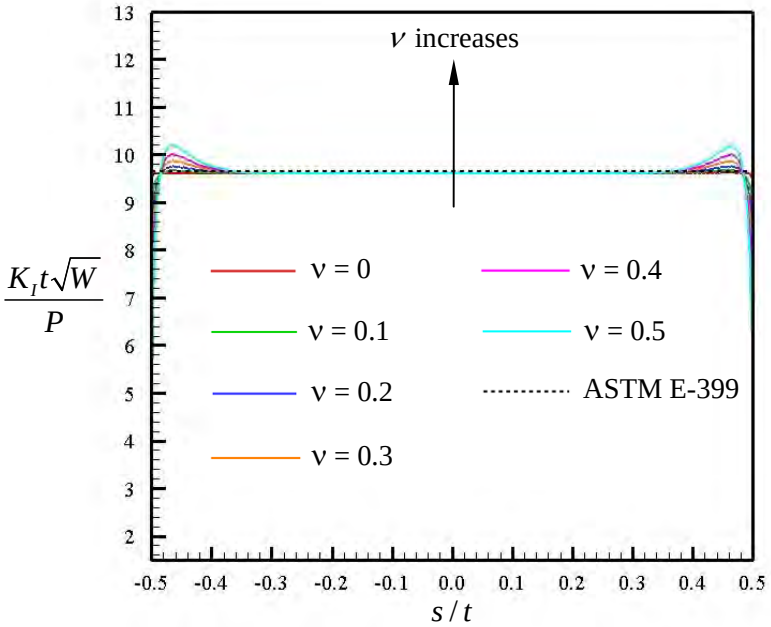

Figure 4.1.21 Normalized mode-I stress intensity factor versus the normalized distance along the crack front for various Poisson's ratios and $t/a = 40$

4.2 Results from SGBEM-FEM coupling

As a means to verify both the formulation and the numerical implementations of the SGBEM-FEM coupling, numerical experiments are first carried out for boundary value problems in which the analytical solution exists. In the analysis, a series of meshes is adopted in order to investigate both the convergence and accuracy of the numerical solutions. Once the method is tested, it is then applied to solve more complex boundary value problems in order to demonstrate its capability and robustness. For brevity of the presentation, a selected set of results are reported and discussed as follows.

4.2.1 Isolated spherical void under uniform pressure

Consider an isolated spherical void of radius a embedded in a three-dimensional infinite medium as shown schematically in Figure 4.2.1(a). The void is subjected to uniform pressure σ_0. In the analysis, two constitutive models are investigated: one associated with an isotropic, linearly elastic material with Young's modulus E and Poisson ratio $\nu = 0.3$ and the other chosen to represent an isotropic hardening material obeying J_2-flow theory of plasticity (e.g., Lubiliner, 1990). For the latter material, the uniaxial stress-strain relation is assumed in a bilinear form with E_1 and E_2 denoting the modulus in the elastic regime and the modulus of the hardening zone, respectively, and σ_y and ε_y denoting the initial yielding stress and its corresponding strain, respectively.

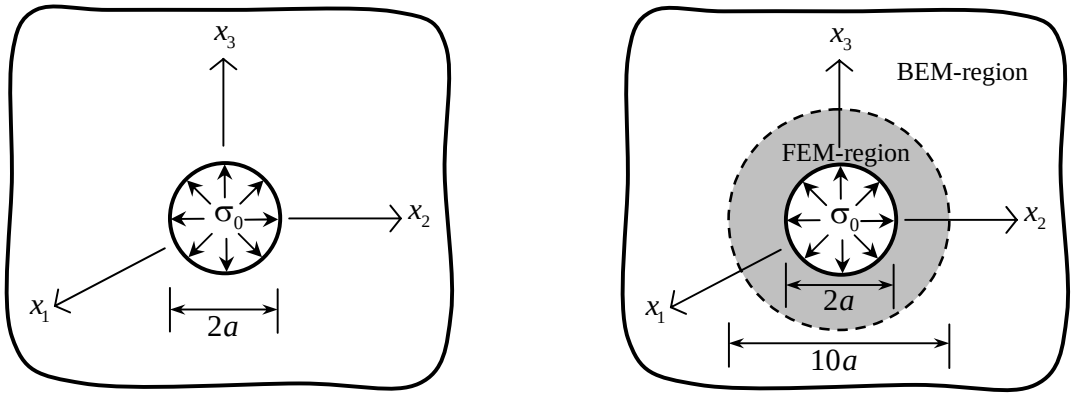

Figure 4.2.1 (a) Schematic of three-dimensional infinite medium containing spherical void and (b) schematic of BEM-region and FEM-region

To test the coupling technique, we first decompose the body into two regions by a fictitious spherical surface of radius $5a$ and centered at the origin as shown by a dashed line in Figure 4.2.1. It is important to remark that such a surface must be chosen relatively large compared to the void to ensure that the inelastic zone that may exist (for the second constitutive model) is fully contained in the FEM-region. In the experiments, three different meshes are adopted as shown in Figure 4.2.2. Although meshes for the BEM-region are not shown, they can simply obtain from the interface meshes of the FEM-region. As clearly

illustrated in the figure, mesh-1, mesh-2 and mesh-3 consist of 12, 32, 144 boundary elements and 24, 128, 1152 finite elements, respectively.

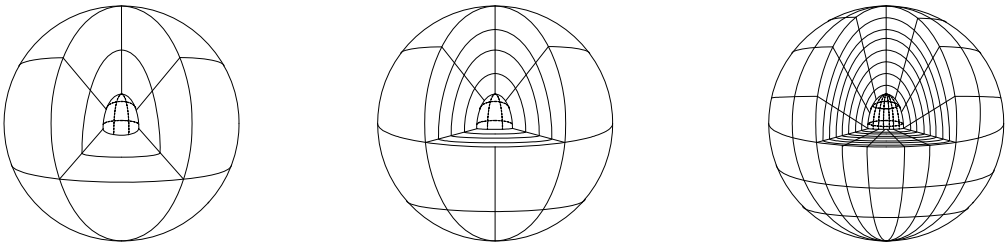

mesh-1 mesh-2 mesh-3

Figure 4.2.2 Three meshes adopted in the analysis for FEM-region; meshes for BEM-region are identical to the interface mesh of FEM-region

4.2.1.1 Results for isotropic linearly elastic material

For linear elasticity, this particular boundary value problem admits the closed form solution (e.g., Sokolnikoff, 1956). Since the problem is spherically symmetric, only the radial displacement u_r and the normal stress components $\{\sigma_{rr}, \sigma_{\theta\theta}, \sigma_{\phi\phi}\}$ are non-zero and they are given explicitly by (note that these quantities are referred to a standard spherical coordinate system $\{r, \theta, \phi\}$ with its origin located at the center of the void)

$$u_r(r) = \frac{1+\nu}{2E}\sigma_0 \frac{a^3}{r^2} \tag{4.2.1}$$

$$\sigma_{rr}(r) = -2\sigma_{\theta\theta}(r) = -2\sigma_{\phi\phi}(r) = -\sigma_0\left(\frac{a}{r}\right)^3 \tag{4.2.2}$$

This analytical solution is employed as a means to validate the proposed formulation and the numerical implementation. Numerical solutions for the radial displacement obtained from the three meshes are reported and compared with the exact solution in Figure 4.2.3. As evident from this set of results, the radial displacement obtained from the mesh-2 and the mesh-3 is highly accurate with only slight difference from the exact solution while that obtained from the mesh-1 is reasonably accurate except in the region very near the surface of the void. The discrepancy of solutions observed in the mesh-1 is due to that the level of refinement is too coarse to accurately capture the geometry and responses in the local region near the surface of the void.

We further investigate the quality of numerical solutions for stresses. Since all non-zero stress components are related by equation (4.2.2), only results for the radial stress component are reported. Figure 5 shows the normalized radial stress obtained from the three meshes and the exact solution versus the normalized radial coordinate. It is observed that the mesh-3 yields results that are almost indistinguishable from the exact solution, whereas the mesh-1 and mesh-2 give accurate results for relatively large r and the level of accuracy decreases as the distance r approaches a. It is noted by passing that the degeneracy of the

accuracy in computing stress is common in a standard, displacement-based, finite element technique.

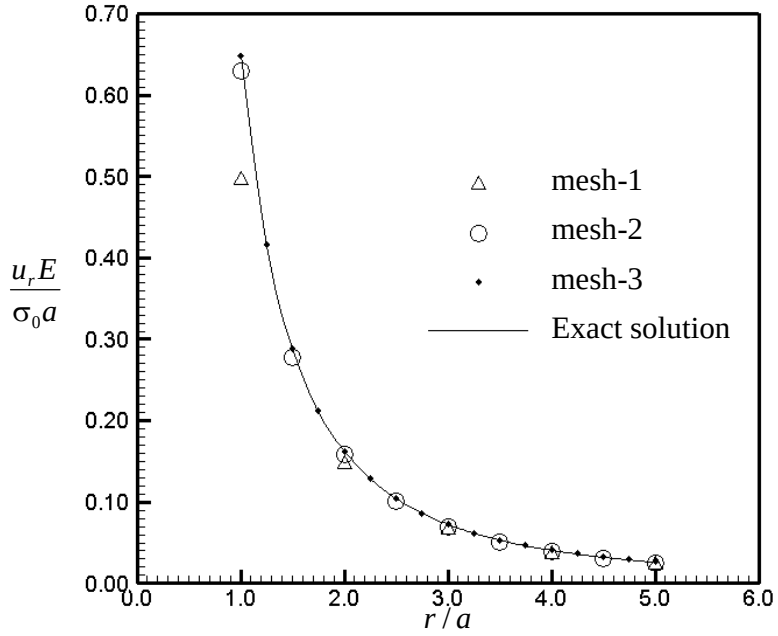

Figure 4.2.3 Normalized radial displacement versus normalized radial coordinate for isotropic, linearly elastic material with $\nu = 0.3$

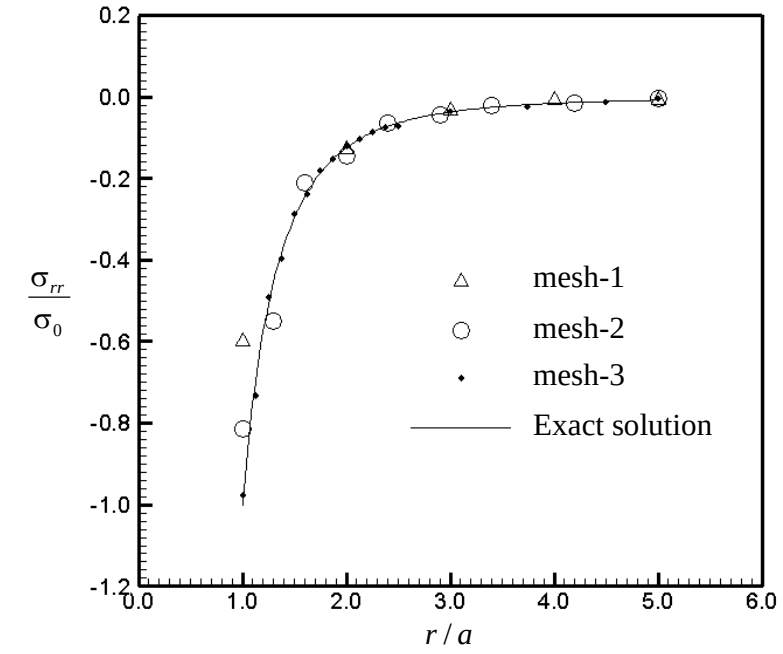

Figure 4.2.4 Normalized radial stress versus normalized radial coordinate for isotropic, linearly elastic material with $\nu = 0.3$

To demonstrate the important role of the SGBEM in the treatment of an unbounded part of the domain instead of truncating the body as practically employed in the finite element modeling, we perform another FE analysis of the FEM-region alone without coupling with the BEM-region but imposing zero displacement condition at its interface. The radial displacement and the radial stress obtained for this particular case using the mesh-3 are reported along with the exact solution and those obtained from the coupling technique in Figures 4.2.5 and 4.2.6, respectively. As evident from these results, numerical solutions obtained from the FEM with a domain truncation strategy deviate from the exact solution when it moves close to the truncation surface while the proposed technique yields almost identical results to the exact solution. The concept of domain truncation to obtain a finite body is simple but it still remains to choose a proper truncation surface and boundary conditions to be imposed on that surface to mimic the original boundary value problem. This coupling technique provides an alternative to treat the whole domain without any truncation and difficulty to treat the remote boundary.

4.2.1.2 Isotropic hardening material

For this particular case, we focus attention to the material with no hardening modulus (i.e., $E_2 = 0$) since the corresponding boundary value problem admits the closed form solution. For a sufficiently high applied pressure σ_0, a layer close to the boundary of the void become inelastic and the size of such inelastic zone (measured by the radius r_0) becomes larger as σ_0 increases. By incorporating J_2-flow theory of plasticity and spherical symmetry, the radial displacement and the radial stress can be obtained exactly as given below.

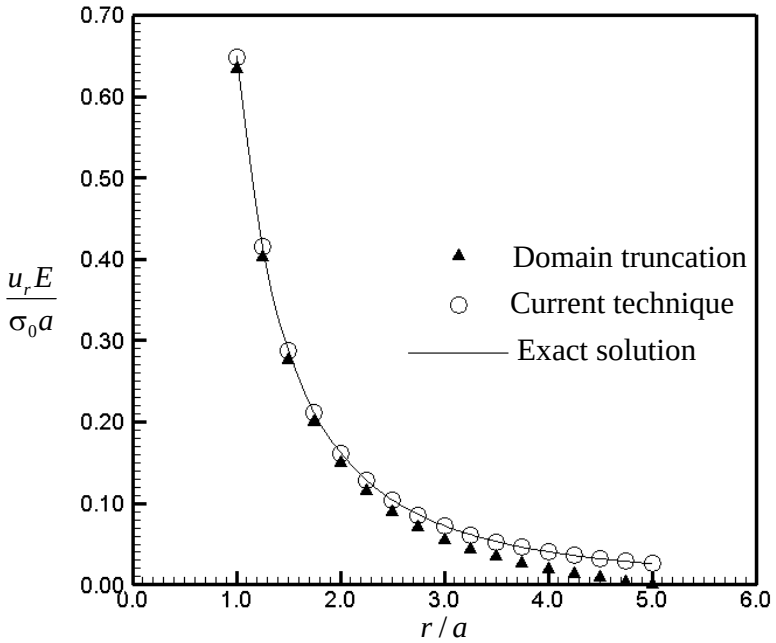

Figure 4.2.5 Normalized radial displacement versus normalized radial coordinate for isotropic, linearly elastic material with $\nu = 0.3$. Results are obtained from mesh-3 for both the coupling technique and the FEM with domain truncation.

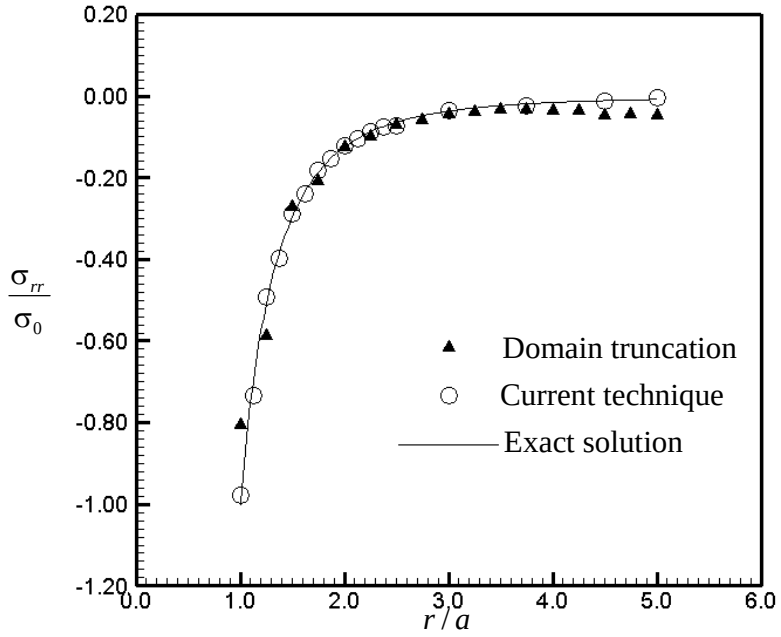

Figure 4.2.6 Normalized radial stress versus normalized radial coordinate for isotropic, linearly elastic material with $\nu = 0.3$. Results are obtained from mesh-3 for both the coupling technique and the FEM with domain truncation.

$$u_r(r) = \begin{cases} \dfrac{1-2\nu}{E}\left\{2\sigma_y \ln(r/a) - \sigma_0\right\} r + \dfrac{1-\nu}{E}\sigma_y \left(\dfrac{r_0^3}{r^2}\right) & ; \quad r < r_0 \\ \dfrac{\sigma_y (1+\nu)}{3E}\left(\dfrac{r_0^3}{r^2}\right) & ; \quad r \geq r_0 \end{cases} \tag{4.2.3}$$

$$\sigma_{rr}(r) = \begin{cases} 2\sigma_y \ln(r/a) - \sigma_0 & ; \quad r < r_0 \\ -\dfrac{2\sigma_y}{3}\left(\dfrac{r_0}{r}\right)^3 & ; \quad r \geq r_0 \end{cases} \tag{4.2.4}$$

where the Poisson ratio ν is taken to be 0.3 and $r_0 = ae^{\left(\frac{\sigma_0}{2\sigma_y} - \frac{1}{3}\right)}$ is the radius of an inelastic zone. In the analysis, the pressure $\sigma_0 = 1.625\sigma_y$ is chosen to ensure that the medium contains an inelastic zone; in fact, this selected applied pressure corresponds to $r_0 = 1.615a$. Numerical results obtained from the current technique are reported along with the exact solution in Figure 4.2.7 for the normalized radial displacement and in Figure 4.2.8 for the normalized radial stress. It can be concluded from computed solutions that they finally converge to the exact solution as the mesh is refined. In particular, results obtained from the mesh-3 are nearly indistinguishable from the benchmark solution. It should be pointed out that results obtained from the same level of mesh refinement for this particular case are less accurate than those obtained for the linear elasticity case. This is due to complexity posed by the presence

of an inelastic zone near the surface of the void and, in order to capture this behavior accurately, it requires sufficiently fine meshes.

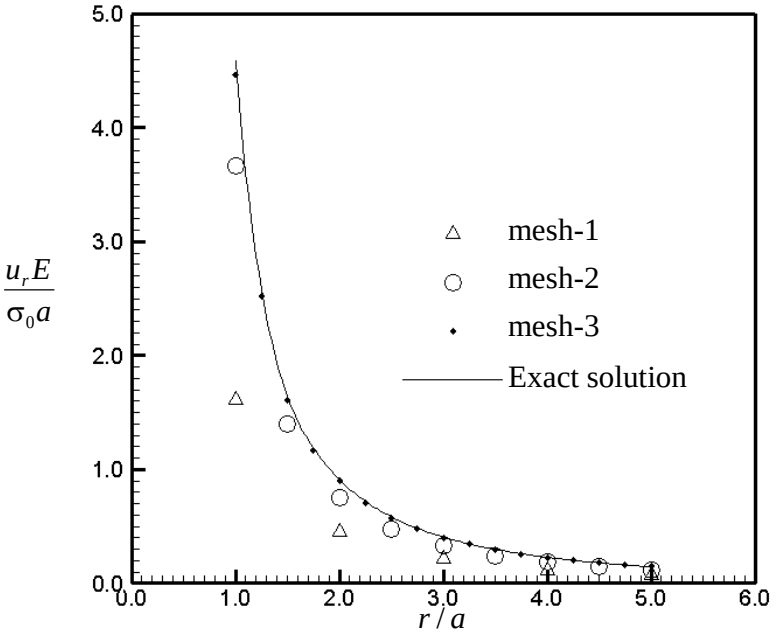

Figure 4.2.7 Normalized radial displacement versus normalized radial coordinate for isotropic hardening material with $E_2 = 0$

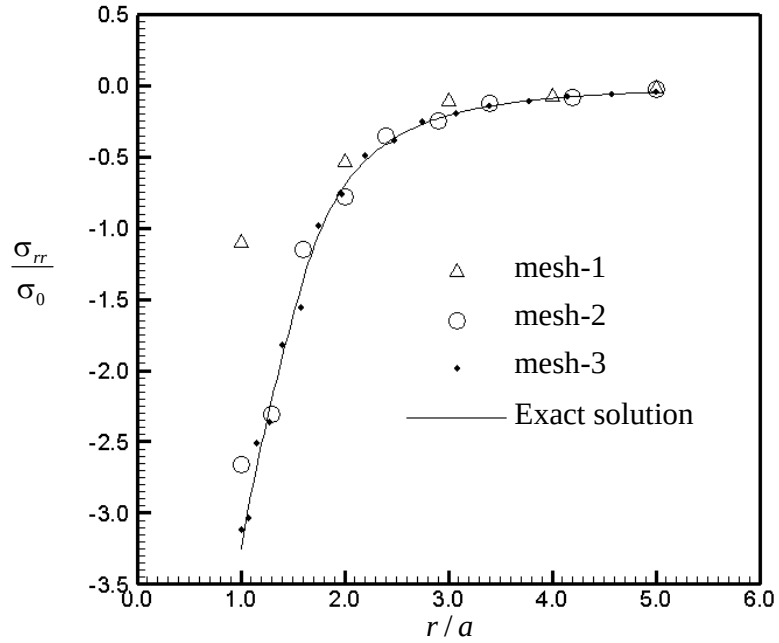

Figure 4.2.8 Normalized radial stress versus normalized radial coordinate for isotropic hardening material with $E_2 = 0$

4.2.2 Isolated penny-shaped crack in infinite medium

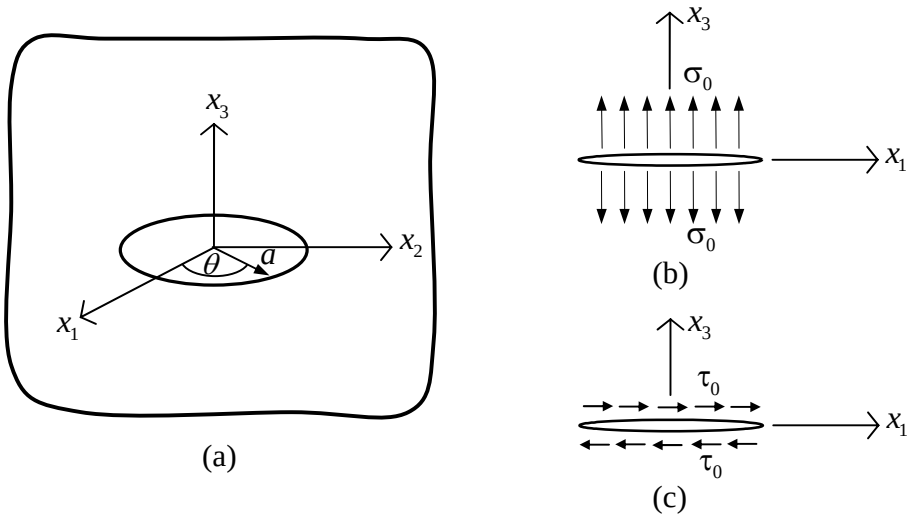

Figure 4.2.9 (a) Schematic of infinite medium containing penny-shaped crack, (b) crack under uniform normal traction σ_0, and (c) crack under uniform shear traction τ_0

Consider, next, a penny-shaped crack of radius a which is embedded in a linearly elastic, infinite medium as shown schematically in Figure 4.2.9(a). The body is made of either an isotropic material with Poisson's ratio $\nu = 0.3$ or zinc and graphite-reinforced composite. The last two materials are transversely isotropic with the axis of material symmetry directing along the x_3-axis and their elastic constants are given in Table 4.2.1. The crack is subjected to two types of traction boundary conditions: the uniform normal traction σ_0 (i.e. $t_1 = t_2 = 0$, $t_3 = \sigma_0$) as shown in Figure 4.2.9(b) and the uniform shear traction τ_0 along the x_1-axis (i.e. $t_1 = \tau_0$, $t_2 = t_3 = 0$) as shown in Figure 4.2.9(c).

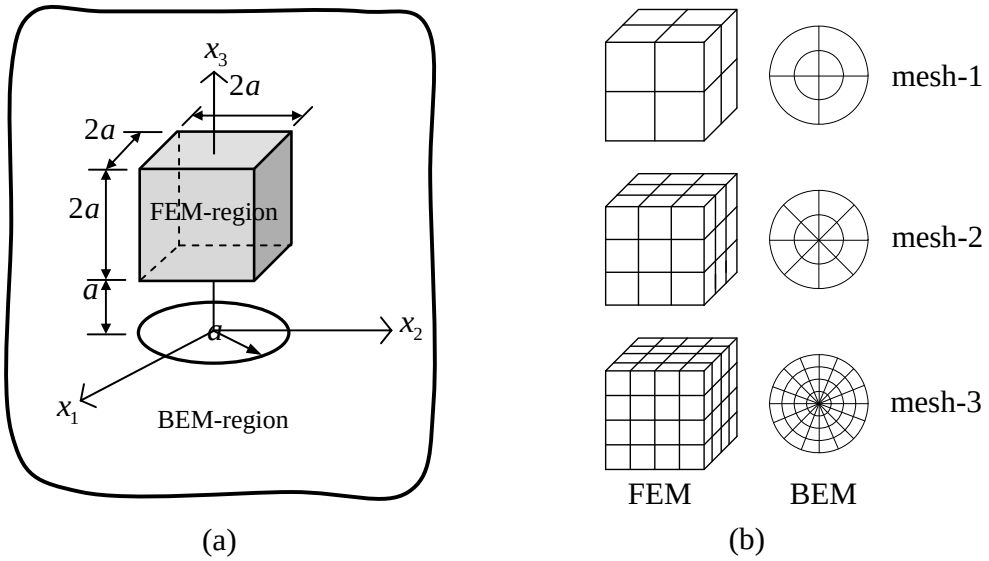

Figure 4.2.9 (a) Schematic of selected FEM-region and the remaining BEM-region and (b) three meshes adopted in the analysis

Table 4.2.1 Non-zero elastic constants for zinc and graphite-reinforced composite (where axis of material symmetry is taken to direct along the x_3-coordinate direction)

Non-zero elastic constants	$(\times 10^6)$ psi	
	Zinc	Graphite-reinforced composite
E_{1111}	16.09	14.683
E_{1122}	3.35	6.986
E_{1133}	5.01	5.689
E_{3333}	6.10	144.762
E_{1313}	3.83	4.050

The first loading condition gives rise to a pure opening-mode problem with the mode-I stress intensity factor along the crack front being constant and independent of material properties while the second loading condition yields non-zero mode-II and mode-III stress intensity factors that vary along the crack front. The analytical solutions for both cases can be found in the work of Fabrikant (1989). As a means to verify the coupling formulation and implementation, we choose the FEM-region to be a cube of dimensions 2*a*x2*a*x2*a* centered at (0, 0, 2*a*) as illustrated in Figure 4.2.10(a). In the analysis, we generate three meshes for both the crack surface and the FEM-region as shown in Figure 4.2.10(b).

For the first loading condition, numerical solutions for the mode-I stress intensity factor normalized by the exact solution are reported in Table 4.2.2 for all three materials. Clearly from these results, the current technique yields highly accurate stress intensity factors with error less than 1.5%, 0.6% and 0.1% for mesh-1, mesh-2 and mesh-3, respectively. The weak dependence of numerical solutions on the level of mesh refinement is due mainly to the use of special crack-tip elements to model the near-tip field and directly capture the gradient of relative crack-face displacement along the crack front. Relatively coarse mesh can therefore be employed in the analysis to obtain sufficiently accurate stress intensity factors.

Table 4.2.2 Normalized mode-I stress intensity factor for isolated penny-shaped crack subjected to uniform normal traction

Mesh	Isotropic material, $K_1 / K_{1,exact}$		Transversely isotropic material, $K_1 / K_{1,exact}$			
			Zinc		Graphite-reinforced composite	
	$\theta^\circ = 0$	$\theta^\circ = 90$	$\theta^\circ = 0$	$\theta^\circ = 90$	$\theta^\circ = 0$	$\theta^\circ = 90$
1	0.9919	0.9920	0.9890	0.9890	0.9841	0.9841
2	1.0008	1.0008	1.0001	1.0001	1.0053	1.0053
3	1.0002	1.0002	1.0004	1.0004	1.0006	1.0001

For the second loading condition, the normalized mode-II and mode-III stress intensity factors (K_2 and K_3) are shown in Figure 4.2.11 for isotropic material, zinc and graphite-reinforced composite. Based on this set of results, it can be concluded again that numerical solutions obtained from the three meshes are in excellent agreement with the exact solution; in particular, a coarse mesh also yields results of high accuracy. It should also be remarked that for this particular loading condition, the material anisotropy play a significant role on values of the mixed-mode stress intensity factors.

4.2.3 Infinite medium containing both penny-shaped crack and spherical void

As a final example, we choose to test the proposed technique by solving a more complex boundary value problem in order to demonstrate its capability. Let us consider an infinite medium containing a spherical void of radius a and a penny-shaped crack of the same radius as shown schematically in Figure 4.2.12. The medium is subjected to uniform pressure σ_0 on the surface of the void whereas the entire surface of the crack is traction free. In the analysis, two constitutive models are investigated: one associated with an isotropic, linearly elastic material with Young's modulus E and Poisson ratio $\nu = 0.3$ and the other corresponding to an isotropic hardening material with the bilinear uniaxial stress-strain relation similar to that previously employed. The primary quantity to be sought is the mode-I stress intensity factor along the crack front induced by the application of the pressure to the void. In addition, influence of an inelastic zone induced in the high load intensity region on such fracture data is also of interest.

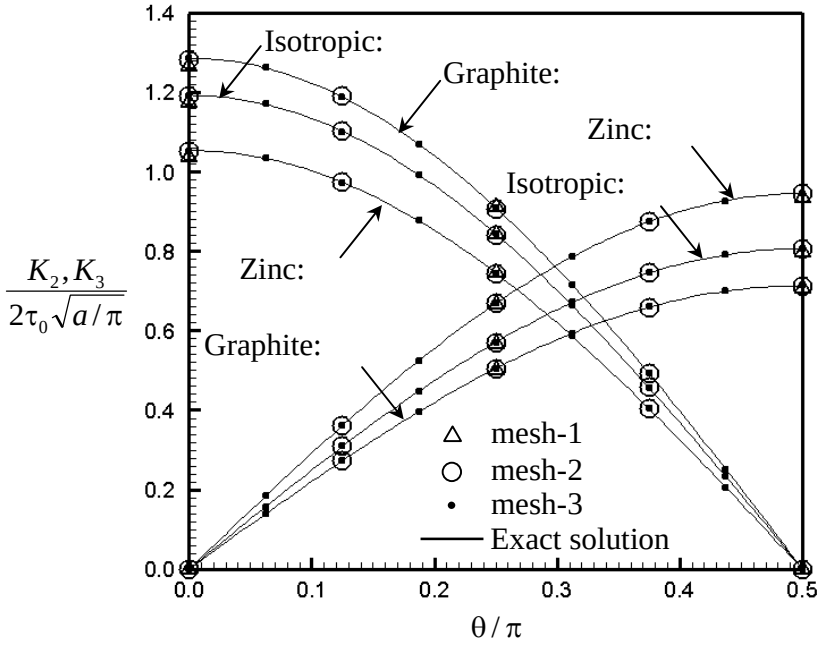

Figure 4.2.11 Normalized mode-II and mode-III stress intensity factors for isolated penny-shaped crack subjected to shear traction. Results are reported for isotropic material with ν = 0.3, zinc and graphite reinforced composite.

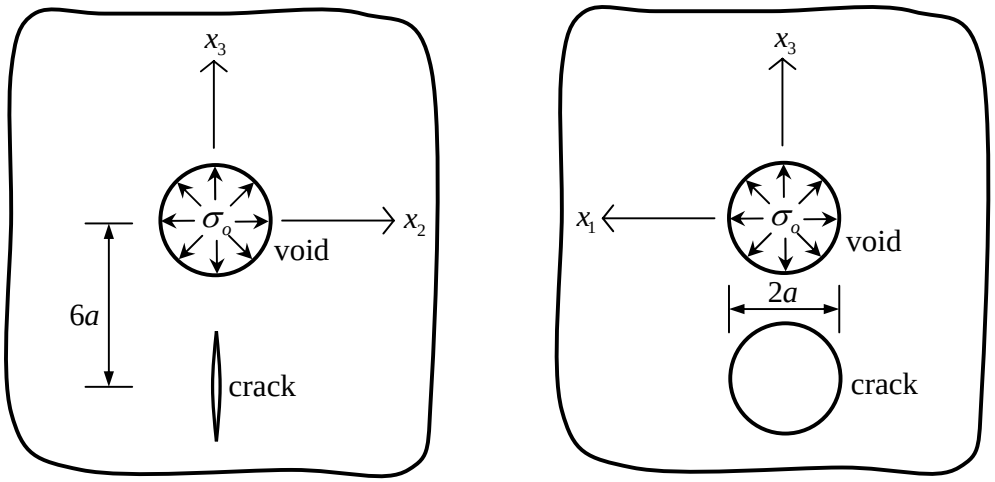

Figure 4.2.12 Schematic of infinite medium containing spherical void of radius a and penny-shaped crack of radius a and subjected to uniform pressure at surface of void

In the modeling, we first decompose the medium into the FEM-region and the BEM-region using a fictitious spherical surface of radius $4a$ centered at the same location as the void as shown in Figure 4.2.13(a). Three meshes are adopted in numerical experiments as shown in Figure 14(b). In particular, the FEM-region, the interface and the crack surface consists of {24, 12, 8}, {128, 32, 16}, and {1024, 128, 64} elements for mesh-1, mesh-2 and mesh-3, respectively. It should be noted also that the mesh-1 is obviously very coarse; in particular, only eight elements are utilized to discretize the entire crack surface and only four relatively large crack-tip elements are used along the crack front.

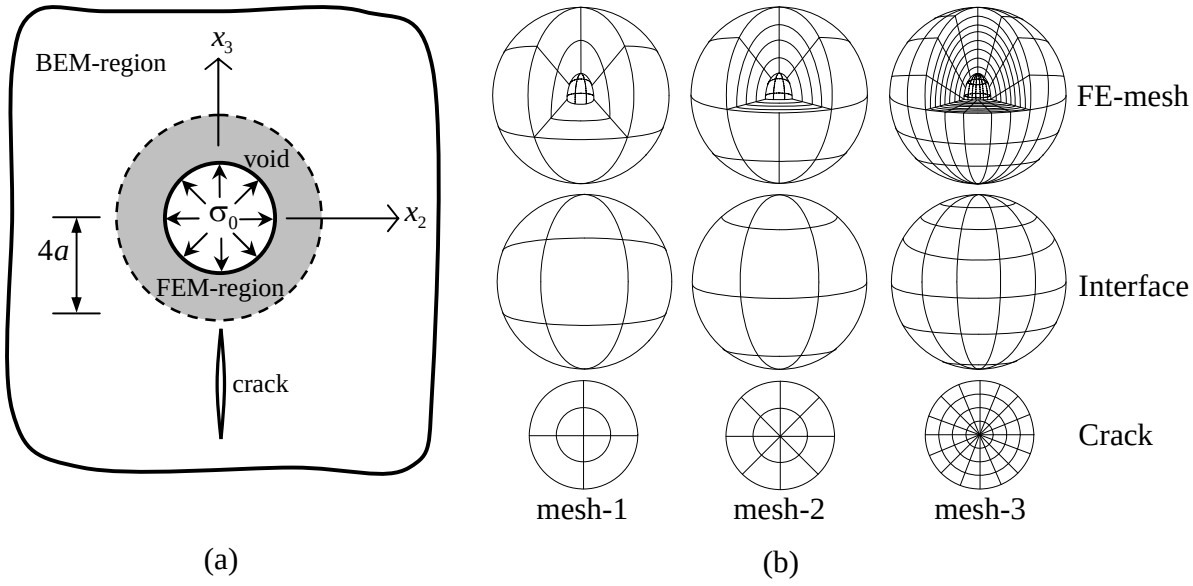

Figure 4.2.13 (a) Decomposition of domain into BEM-region and FEM-region by a fictitious spherical surface of radius $4a$ and (b) three meshes adopted in analysis

First, the analysis is carried out for the elastic material with Poisson ratio $\nu = 0.3$ and the computed mode-I stress intensity factors are normalized and then reported as a function of angular position along the crack front for all three meshes in Figure 4.2.14. This set of results implies that the obtained numerical solutions exhibit good convergence; in particular, results obtained from the mesh-2 and mesh-3 are of comparable quality while results obtained from the mesh-1 still deviate from the converged solution. As confirmed by this convergence study, only the mesh-3 is used to generate other sets of useful results.

Next, we consider a medium made of an isotropic hardening material. In the analysis, we choose the modulus $E_1 = E$ and Poisson ratio $\nu = 0.3$ for the linear regime and choose either $E_2 = E/3$ or $E_2 = 0$ for the hardening regime. With this set of material parameters, the behavior in the linear regime (for a small level of applied pressure) is identical to that obtained in the previous case. To investigate the influence of the inelastic zone induced near the surface of the void on the stress intensity factor along the crack front, we carry out various experiments by varying the applied pressure σ_0. The distribution of the stress intensity factor along the crack front is reported in Figure 4.2.15 for a hardening material with $E_1 = E$ and $E_2 = E/3$ under five levels of the applied pressure $\sigma_0 \in \{0.25\sigma_y, 1.00\sigma_y, 1.25\sigma_y, 1.50\sigma_y, 1.75\sigma_y\}$. The body is entirely elastic at $\sigma_0 = 0.25\sigma_y$, slightly passes the initial yielding at $\sigma_0 = 1.00\sigma_y$, and possesses a larger inelastic zone as the pressure increases further.

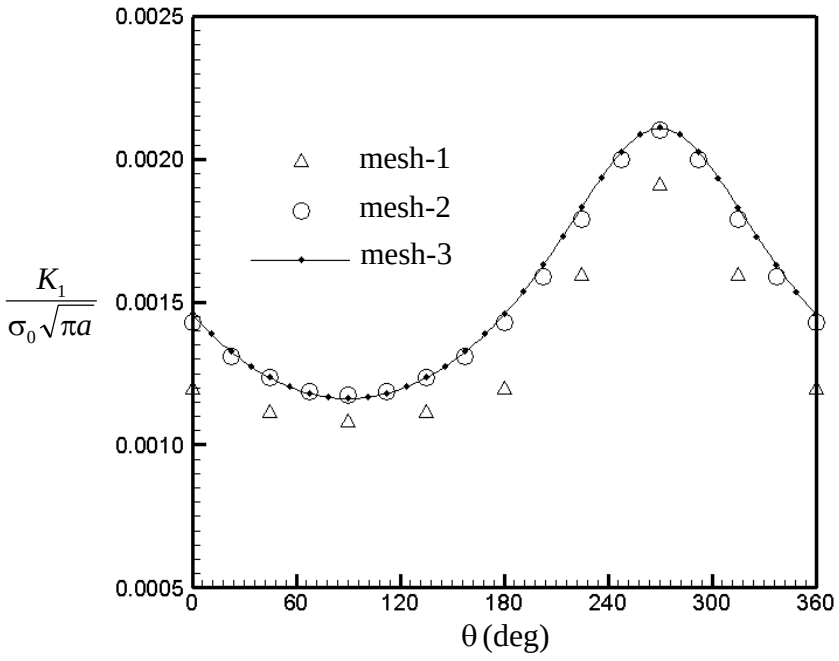

Figure 4.2.14 Normalized mode-I stress intensity factors of penny-shaped crack embedded within infinite medium containing spherical void under uniform pressure

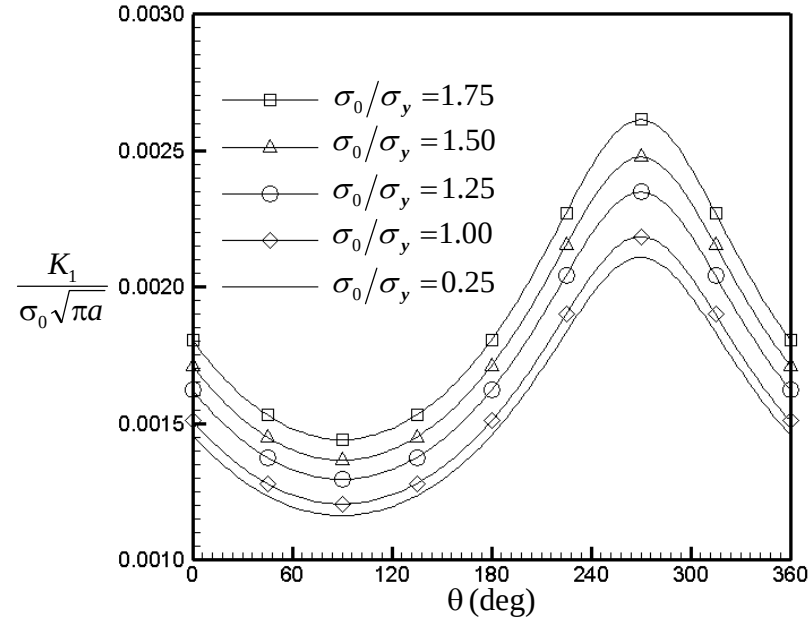

Figure 4.2.15 Normalized mode-I stress intensity factor of penny-shaped crack embedded within infinite medium containing spherical void under uniform pressure. Results are reported for isotropic hardening material with $E_1 = E$ and $E_2 = E/3$.

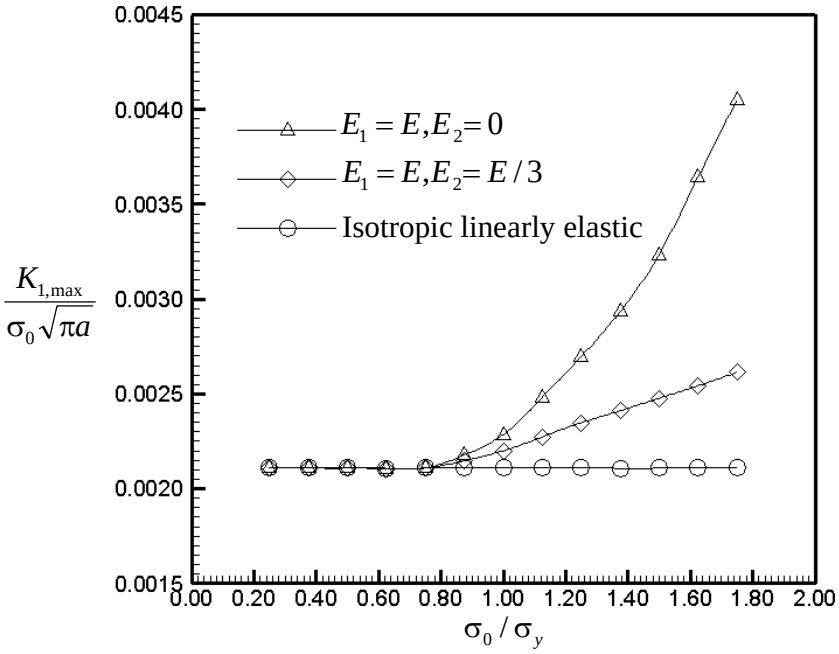

Figure 4.2.16 Maximum normalized mode-I stress intensity factor versus applied pressure at surface of void. Results are reported for isotropic linearly elastic material with $\nu = 0.3$ and two isotropic hardening materials.

It is obvious from Figure 4.2.15 that the presence of an elastic zone significantly alters the normalized values of the stress intensity factor from the linear elastic solution and such discrepancy becomes more apparent as the level of applied pressure increases. The localized inelastic zone acts as a stress riser; i.e. it produces the stress field of higher intensity around the crack and this therefore yields the higher normalized stress intensity factor when compared with the linear elastic case. Figure 4.2.16 shows an additional plot between the maximum normalized stress intensity factors versus the normalized applied pressure for both an isotropic linearly elastic material and two isotropic hardening materials (associated with $E_2 = 0$ and $E_2 = E/3$). Results for both materials are identical for a low level of the applied pressure (since the entire body is still elastic) and, for a higher level of the applied pressure, the maximum stress intensity factor for the case of the hardening material is significant larger than that for the linear elastic material. In addition, such discrepancy tends to increase as the hardening modulus decreases.

4.3 Influence of nano-scale influnece

First, to verify the formulation and numerical implementation, the penny-shaped crack in an unbounded domain is considered, to compare results with existing benchmark solutions. Next the elliptical crack and two interacting penny-shaped cracks in an unbounded domain are considered. In the analysis, three meshes with different levels of refinement are utilized to investigate the convergence of solutions. Nine-node isoparametric elements are used to discretize the entire crack-front while the other parts of the crack surfaces are discretized by eight-node and six-node isoparametric elements. The material Si [100] is used for all of numerical examples, where properties of the bulk material and residual surface tension $E = 107\,GPa$, $\nu = 0.33$ and $\tau^s = 0.6056\,N/m$ are obtained from Miller and Shenoy (2000). For convenience in the handling of numerical analysis, presentation of results and demonstration of the influence of residual surface tension, all involved quantities are normalized in a proper fashion. For instance, the unknown sum of the traction is normalized by the shear modulus μ (i.e., $t_0^{\Sigma} = t^{\Sigma}/\mu$); the unknown sum and jump of the crack-face displacement are normalized by a special length scale $\Lambda = \tau^s/\mu = 0.01506\,nm$ (i.e., $u_0^{\Delta} = u^{\Delta}/\Lambda$ and $u_0^{\Sigma} = u^{\Sigma}/\Lambda$); all characteristic lengths representing the geometry of the crack such as the crack radius *a*, semi-major axis *a* and semi-minor axis *b* are normalized by the length scale Λ (e.g., $a_0 = a/\Lambda$ and $b_0 = b/\Lambda$); and the prescribed traction on the crack surface is normalized by the shear modulus μ (i.e., $t_{i0} = t_i^0/\mu$) .

4.3.1 Penny-shaped crack in infinite domain

As a means for verifying the current technique, the problem of a penny-shaped crack of radius *a* embedded in an isotropic, linear elastic infinite medium is considered (Figure 4.3.1(a)). The crack is subjected to self-equilibrated, uniformly distributed normal traction $t_3^+ = -t_3^- = t^0$. This problem has been previously solved by Intarit et al. (2012) and Intarit (2013) using Hankel integral transforms with a solution technique for dual integral equations and will be the benchmark solution to validate the proposed FEM-SGBEM technique. The three meshes of the crack surface are shown in Figure 4.3.1(b).

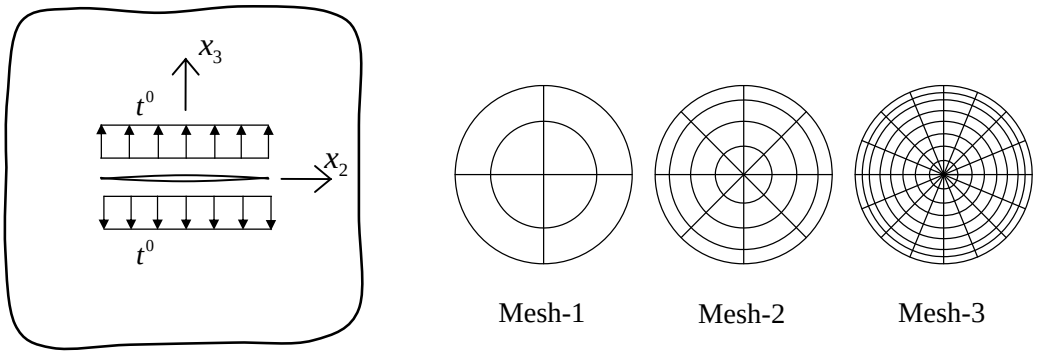

(a) (b)

Figure 4.3.1 (a) Schematic of a penny-shaped crack of radius *a* embedded in an isotropic, linear elastic infinite medium subjected to uniformly distributed normal traction $t_3^+ = -t_3^- = t^0$; (b) Meshes adopted in the analysis. Mesh-1: 8 elements and 29 nodes. Mesh-2: 32 elements and 105 nodes. Mesh-3: 128 elements and 401 nodes.

The normalized crack opening displacement and normalized stresses in the vicinity of crack-front, when the influence of the residual surface tension is taken into account, are shown in Figure 4.3.2. Results are compared with those obtained by an analytical technique proposed by Intarit et al. (2012) and Intarit (2013). It is seen that the current technique yields solutions that agree very well with the benchmark solutions for both crack opening displacement and stresses σ_{11}, σ_{22}, σ_{33} in the vicinity of crack-front. To further examine the influence of residual surface tension, the normalized crack opening displacement and the normalized vertical stress σ_{33} in the vicinity of crack-front with different values of residual surface tension τ^s ranging from 0 to 1.0 *N/m* are shown in Figure 4.3.3. It can be concluded that the residual surface tension exhibits significant influence on the crack opening displacement and the vertical stress. In particular, as τ^s becomes larger, the deviation of results from the classical case (i.e., without residual surface tension) significantly increases and, clearly, it makes the elastic medium much stiffer.

To demonstrate the size-dependent behavior of results due to the presence of residual surface tension, the crack opening displacement and the vertical stress in the vicinity of the crack-front are shown in Figure 4.3.4 for both the classical case and the present study. It is evident that, by including the residual surface tension effects in the mathematical model, the solutions exhibit size-dependent behavior. In particular, the normalized crack opening displacement and vertical stress in the vicinity of crack-front depend significantly on the crack size and this is in contrast with the classical case where the normalized crack opening displacement and normalized vertical stress are independent of crack radius.

4.3.2 Elliptical crack in infinite domain

To demonstrate the capability of the proposed technique for treating mode-I cracks of arbitrary shape, an elliptical crack embedded in an isotropic, linear elastic infinite domain is considered (see Figure 4.3.5(a)). The crack-front is parameterized in terms the parameter t by

$$x_1 = a\cos t, \quad x_2 = b\sin t, \quad x_3 = 0; \quad t \in [0, 2\pi] \tag{4.3.1}$$

where a and b are the major and minor semi-axes of the crack, respectively. The crack is subjected to a self-equilibrated, uniformly distributed normal traction $t_3^+ = -t_3^- = t^0$. Numerical results are presented for the aspect ratio $a/b = 1, 2, 3$ with the three meshes shown in Figure 4.3.5(b) used to model the elliptic crack.

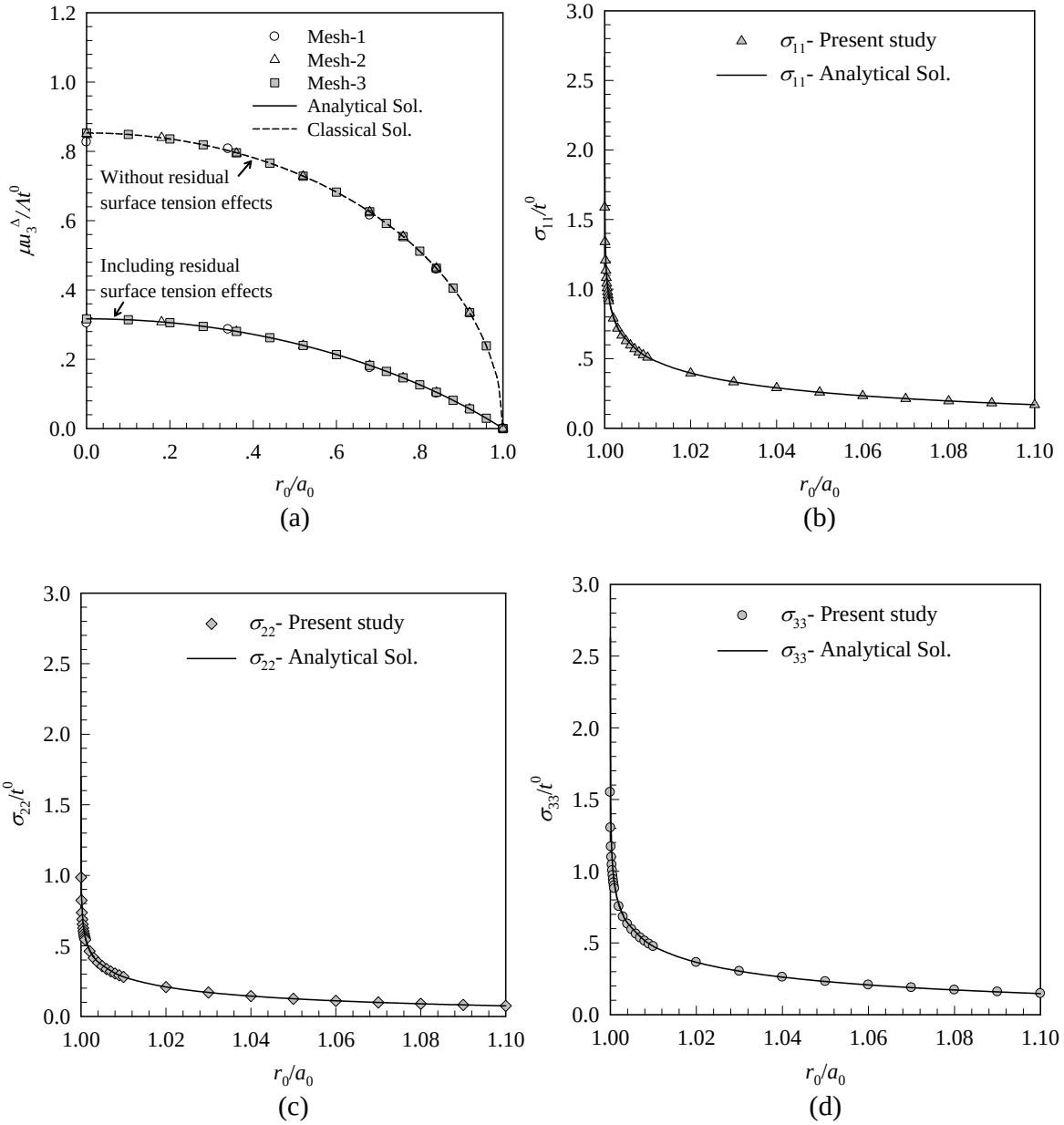

Figure 4.3.2 Penny-shaped crack under uniformly distributed normal traction, for $E = 107\ GPa$, $\nu = 0.33$ and residual surface tension $\tau^s = 0.6056\ N/m$: (a) Normalized crack opening displacement, (b) Normalized stress σ_{11}/t^0 in the vicinity of crack-front, (c) Normalized stress σ_{22}/t^0 in the vicinity of crack-front, and (d) Normalized stress σ_{33}/t^0 in the vicinity of crack-front.

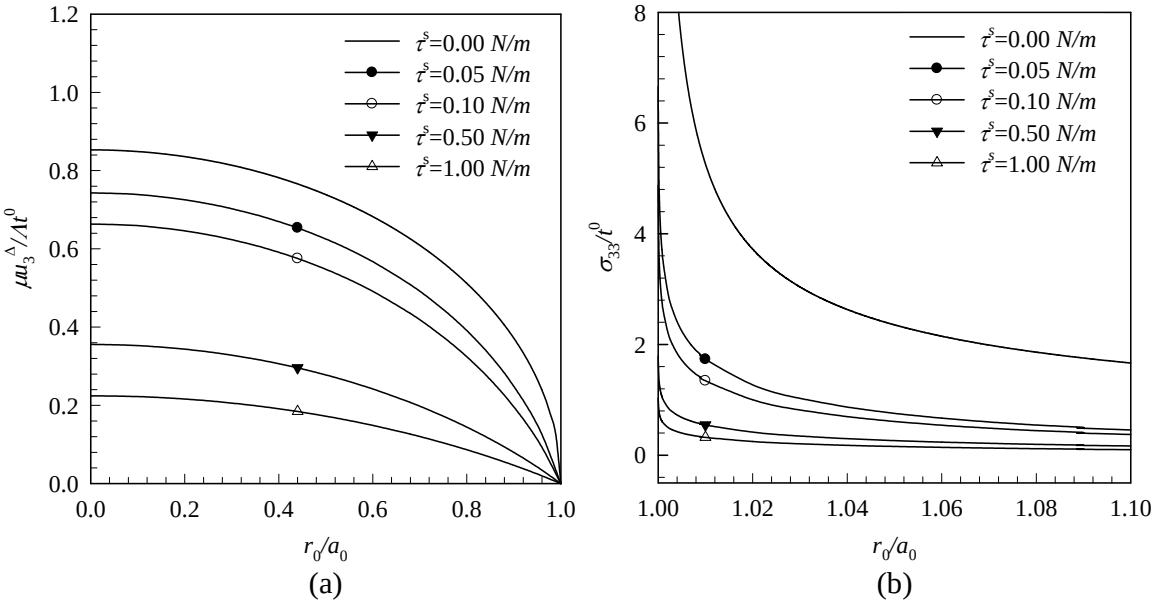

Figure 4.3.3 Penny-shaped crack under uniformly distributed normal traction, for $E = 107\ GPa,\ \nu = 0.33$ for different residual surface tension τ^s: (a) Normalized crack opening displacement and (b) Normalized stress σ_{33}/t^0 in the vicinity of crack-front.

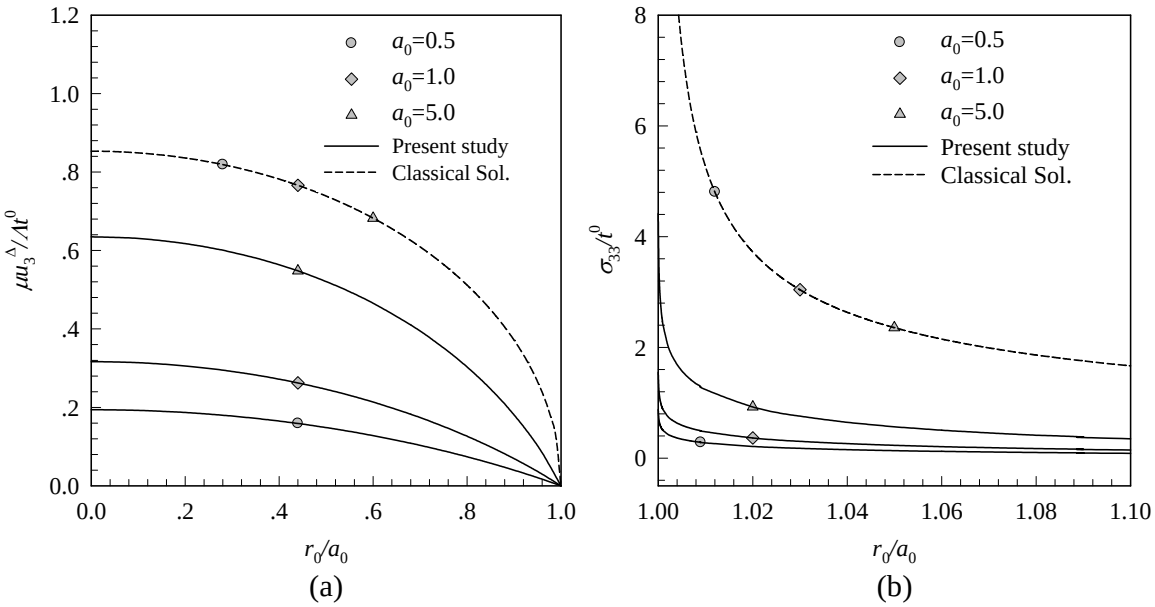

Figure 4.3.4 Penny-shaped crack under uniformly distributed normal traction, for different crack radii $a_0 = a/\Lambda = 0.5, 1.0, 5.0$ for $E = 107\ GPa,\ \nu = 0.33,\ \tau^s = 0.6056\ N/m$: (a) Normalized crack opening displacement and (b) Normalized stress σ_{33}/t^0 in the vicinity of crack-front.

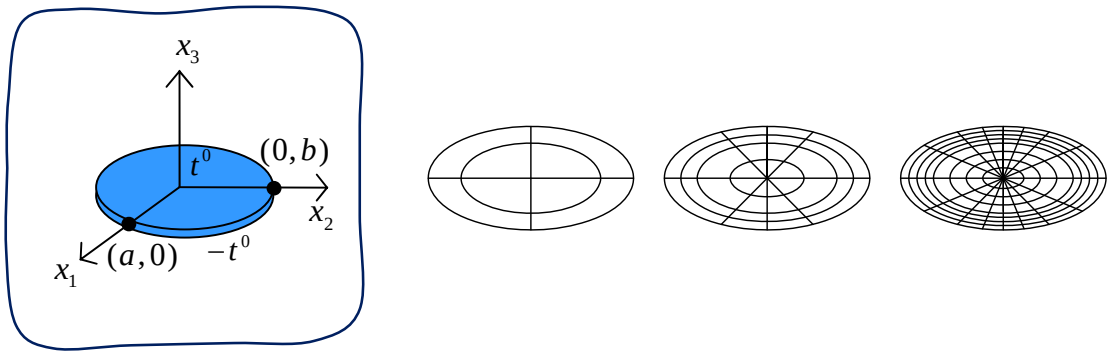

(a) (b)

Figure 4.3.5 (a) Schematics of an elliptical crack embedded in an isotropic, linear elastic infinite medium subjected to uniformly distributed normal traction $t_3^+ = -t_3^- = t^0$ and (b) Meshes adopted in the analysis

The normalized crack opening displacement and the normalized stress σ_{33}/t^0 along the minor axis, when the influence of the residual surface tension is included, are presented in Figure 4.3.6 for aspect ratio $a/b = 1,2,3$. Clearly, converged results of crack opening displacement are obtained with Mesh-2 and Mesh-3 for all three aspect ratios (see Figure 4.3.6(a)). As be seen in Figure 4.3.6, when the aspect ratio a/b increases, the influence of residual surface tension on the crack opening displacement and the stresses in the vicinity of crack decreases.

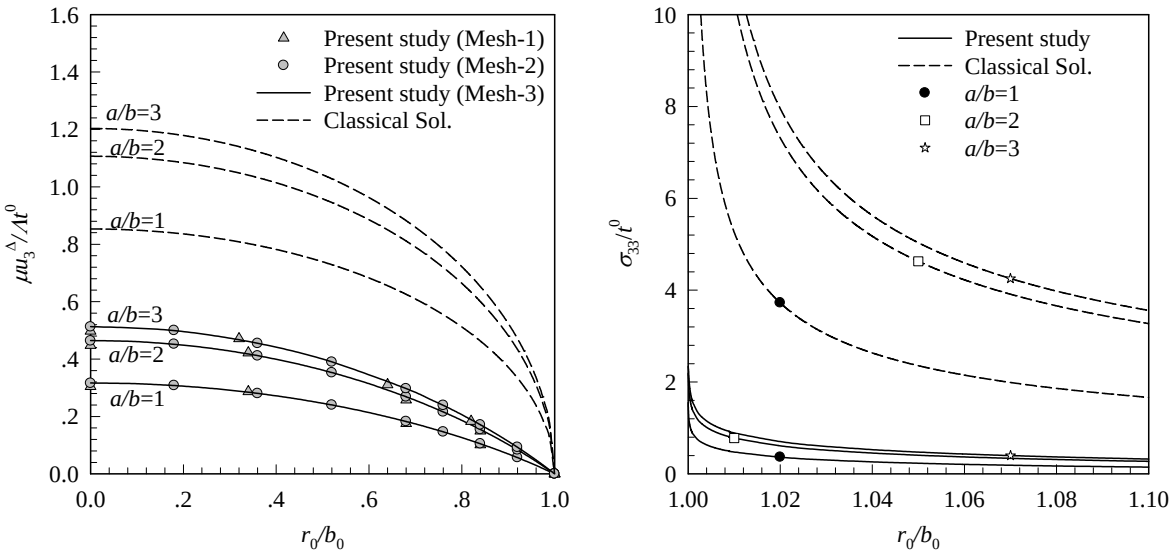

(a) (b)

Figure 4.3.6 Elliptical crack under uniformly distributed normal traction, for different aspect ratios $a/b = 1,2,3$ for $E = 107\ GPa, \nu = 0.33$, $\tau^s = 0.6056\ N/m$: (a) Normalized crack opening displacement along minor axis and (b) Normalized stress σ_{33}/t^0 in the vicinity of crack-front along minor axis.

In order to investigate the influence of residual surface tension, the normalized crack opening displacement and the normalized vertical stress σ_{33} in the vicinity of crack-front with different values residual surface tension τ^s ranging from 0 to 1.0 *N/m* are shown in Figure 4.3.7. Aspect ratios $a/b=2,3$ are considered in this case. As shown in Figure 4.3.7, the influence of residual surface tension is also significant and the medium is stiffer when the residual surface tension increases. To examine the size-dependent behavior of results due to the influence of residual surface tension, the crack opening displacement and the vertical stress in the vicinity of crack-front for $a_0=0.5, 1.0, 5.0$ and two aspect ratios $a/b=2,3$ are shown in Figure 4.3.8. As can be seen in Figure 4.3.8, the normalized crack opening displacement and normalized stresses in the vicinity of crack-front are size-dependent. It is contrary to the classical case (i.e., without residual surface tension effects), the solutions are size-independent. When the crack-size or the aspect ratio decreases, the influence of residual surface tension becomes significant in the sense that the medium is stiffer.

4.3.3 Two interacting penny-shaped cracks in an unbounded domain

As a final example, we demonstrate another feature of the current technique, viz. modeling multiple cracks, by considering a pair of identical penny-shaped cracks of radius *a* embedded in an isotropic, linear elastic unbounded domain as shown in Figure 4.3.9(a). The distance between the centers of the two cracks is denoted by *h*. Both cracks are subjected to a self-equilibrated, uniformly distributed normal traction $t_3^+ = -t_3^- = t^0$.

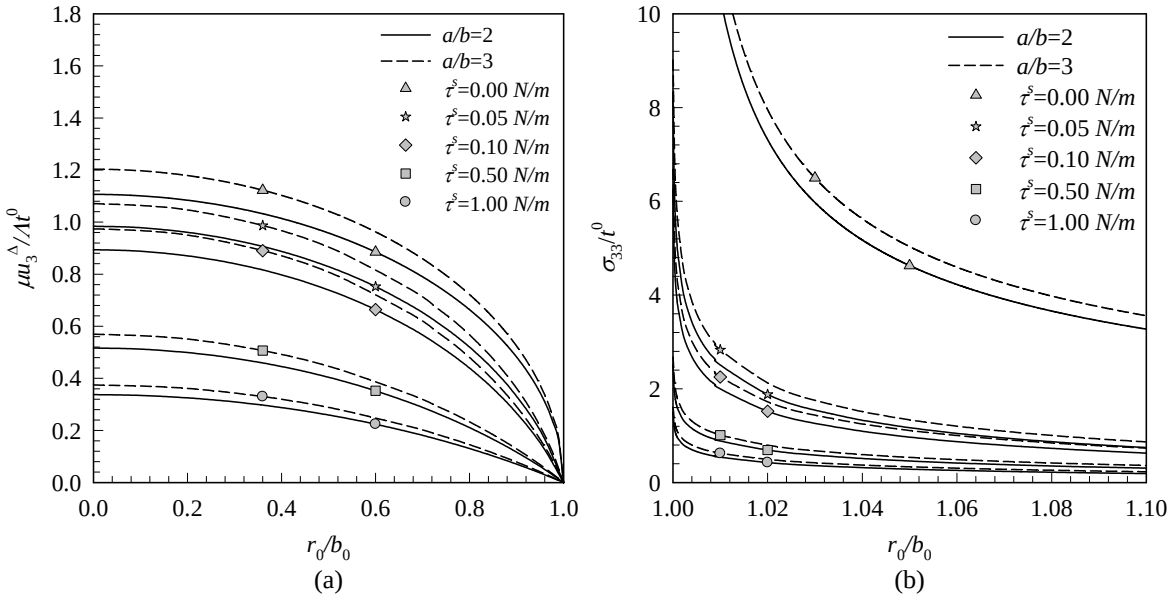

Figure 4.3.7 Elliptical crack under uniformly distributed normal traction for different residual surface tension τ^s , for $E=107\,GPa, \nu=0.33$, for different aspect ratios $a/b=2,3$: (a) Normalized crack opening displacement along minor axis and (b) Normalized stress σ_{33}/t^0 in the vicinity of crack-front along minor axis.

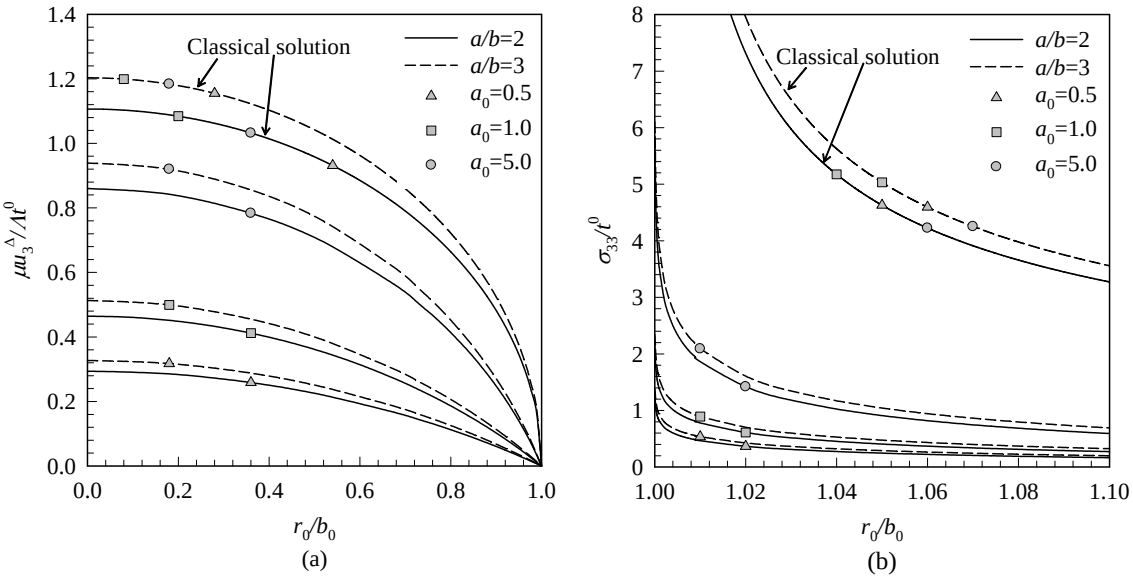

Figure 4.3.8 Elliptical crack under uniformly distributed normal traction for different crack radii $a_0 = a/\Lambda = 0.5, 1.0, 5.0$ for $E = 107\,GPa$, $\nu = 0.33$, $\tau^s = 0.6056\ N/m$, for different aspect ratios $a/b = 2, 3$: (a) Normalized crack opening displacement along minor axis and (b) Normalized stress σ_{33}/t^0 in the vicinity of crack-front along minor axis.

Here, the influence of the interaction between the two cracks on the maximum crack opening displacement is considered. To investigate size-dependent behavior, two cases are considered where the normalized radii of the identical penny-shaped cracks are taken as $a_0 = 1$ and 10. The three meshes showing in Figure 4.3.9(b) are used to test the convergence of numerical solution.

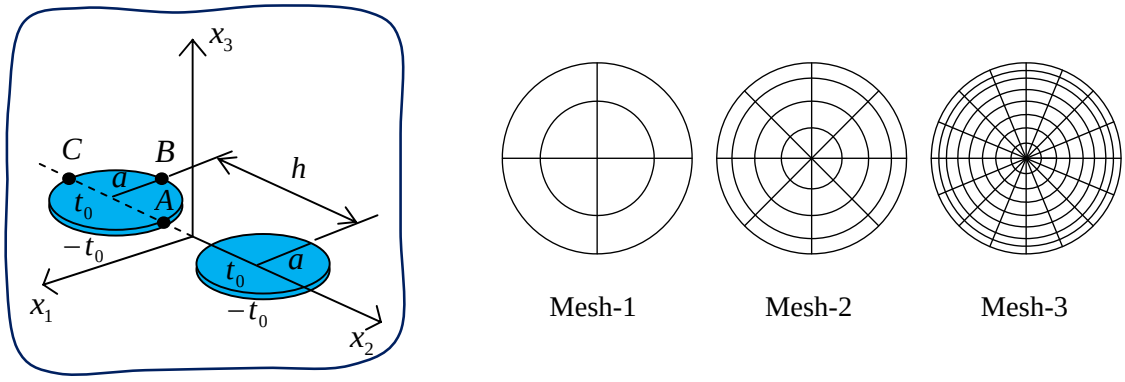

(a) (b)

Figure 4.3.9 (a) Schematic of a pair of penny-shaped cracks of radius *a* embedded in an isotropic, linear elastic infinite medium subjected to uniformly distributed normal traction $t_3^+ = -t_3^- = t^0$ and (b) Meshes adopted for each crack. Mesh-1: 8 elements and 29 nodes. Mesh-2: 32 elements and 105 nodes. Mesh-3: 128 elements and 401 nodes.

The normalized crack opening displacement of one of the penny-shaped cracks with radius $a_0 = 10$ is shown in Figure 4.3.10 for $h/a = 2.4$. It is seen that convergent results of the normalized crack opening displacement are obtained and the residual surface tension has a significant influence on the crack opening displacement. To study the interaction between two cracks, the normalized maximum crack opening displacement is plotted for different values of h/a in Figure 4.3.10. It can be seen in Figure 4.3.10 that, in agreement with previous examples of a penny-shaped crack and an elliptical crack, the maximum crack opening displacement decreases when the residual surface tension increases. The medium becomes much stiffer with the presence of the residual surface tension.

It can also be observed from Figure 4.3.11(a), (b) and (c) that results for the case of two interacting cracks converge very fast to those of a single crack when the residual surface tension increases. In particular, as the value of h/a is greater than 8, 5 and 3.5 for the classical case, $\tau^s = 0.6056\,N/m$, and $\tau^s = 1N/m$, respectively, the normalized maximum crack opening displacement of the two interacting crack and that of the single crack are nearly identical. This not only implies the significant reduction of the interaction between the two cracks due to the presence of the residual surface tension but also provides the applicable range of the aspect ratio h/a to allow the replacement of the two-crack model by a single crack model. In addition, as clearly indicated in Figure 4.3.11(a) and (d), the interaction between the two interacting cracks for the classical case is size-independent (i.e., solutions of the two cracks converge asymptotically to that of the single crack in the identical manner). In the contrary, when the residual surface tension is incorporated in the mathematical model, the size-dependent behavior can be clearly observed by comparing results in Figure 4.3.11(b), (e) and results in Figure 4.3.11(c), (f), respectively. The decrease in the crack size also lowers the interaction between the two cracks.

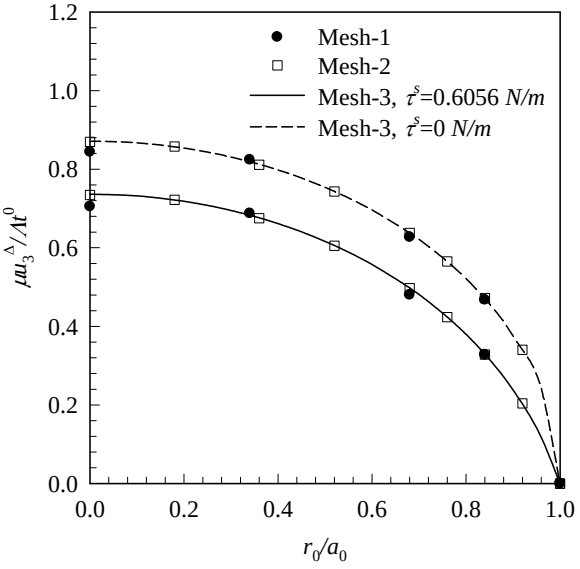

Figure 4.3.10 Normalized crack opening displacement for a pair of penny-shaped cracks with radius $a_0 = 10$ and $h/a = 2.4$ under uniformly distributed normal traction, for $E = 107\,GPa$, $\nu = 0.33$ and $\tau^s = 0.6056\,N/m$.

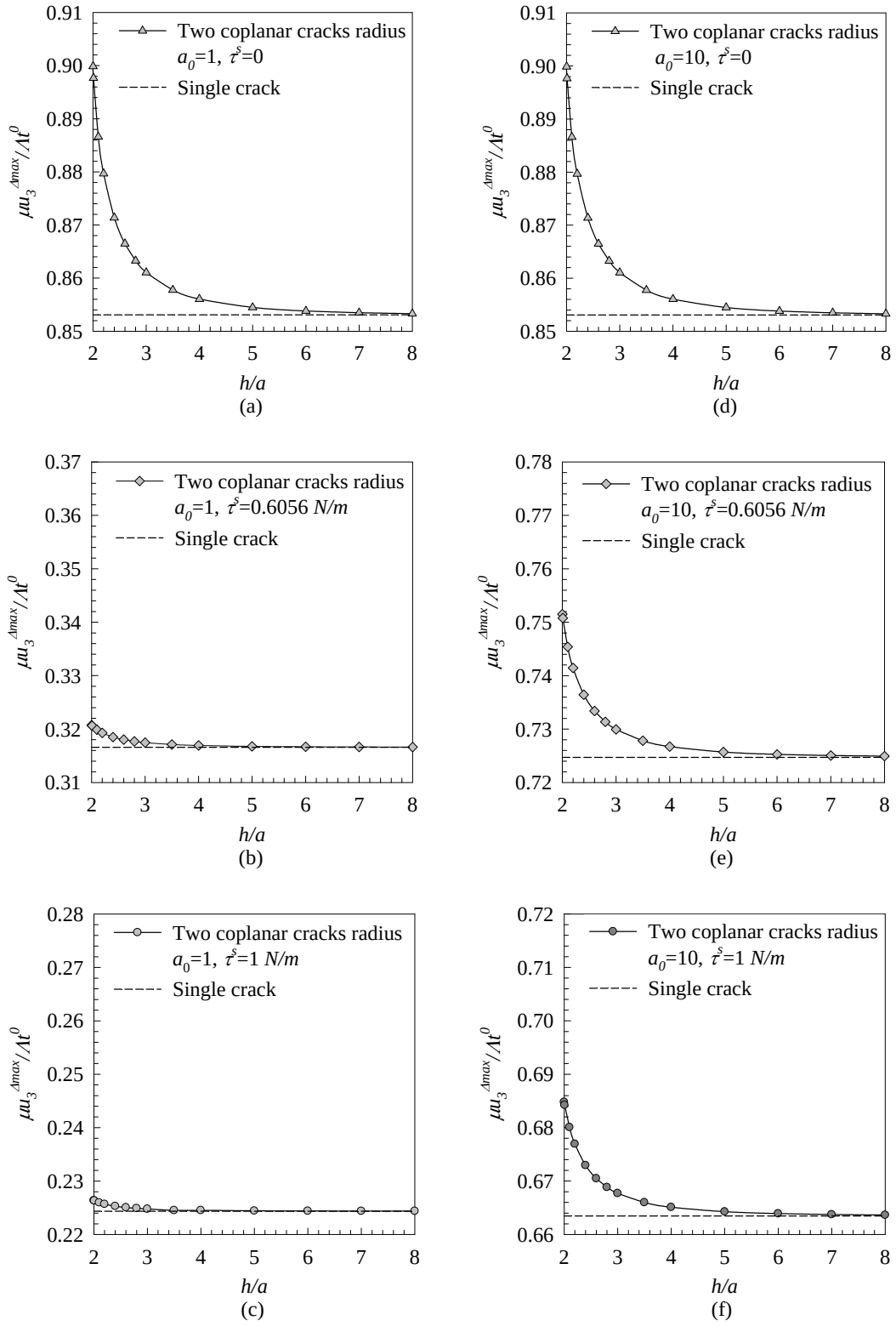

Figure 4.3.11 Normalized maximum crack opening displacement for a pair of identical penny-shaped cracks under uniform normal traction, for E = 107 *GPa*, ν = 0.33: (a)-(c) $a_0 = 1$ and (d)-(f) $a_0 = 10$.

CHAPTER V

CONCLUSION

An efficient and accurate numerical technique based on the weakly singular symmetric Galerkin boundary element method (SGBEM) and the coupling of SGBEM and the standard finite element method (FEM) have been successfully developed, in the present study, for analysis of three-dimensional linear elasticity and fracture problems. The technique has been established in a general context allowing various boundary value problems including problems associated with determination of the stress intensity factors and T-stresses of cracks in isotropic and generally anisotropic elastic infinite and finite media, problems concerning an infinite medium containing localized complex zone and cracks, and problems related to nano-cracks, to be treated.

In the formulation, a pair of weakly singular, weak-form boundary integral equations for the displacement and the traction has been established capable for treating both infinite and finite media made of isotropic and generally anisotropic media. Such boundary integral equations are completely regularized using a systematic technique based on the special decompositions of strongly singular and hyper singular kernels and the integration by parts via Stokes' theorem. All involved kernels are only weakly singular of order $1/r$ and this renders all involved integrals exist in an ordinary sense and their validity only requires the continuity of the boundary data. The pair of displacement and traction boundary integral equations has been used in the formulation of governing equations for cracks in isotropic and anisotropic elastic media and the resulting symmetric formulation constitutes a basis for the development of the weakly singular SGBEM. In addition, such pair of boundary integral equations has also been used along with the domain decomposition and principle of virtual work to establish the SGBEM-FEM coupling formulation for modeling a three-dimensional infinite medium containing localized complex zone and isolated cracks. Finally, the formulation for modeling cracks of nano-size (with proper treatment of nano-scale influence via the surface elasticity theory) in an infinite elastic media has been established in a coupling form between the boundary integral equations and weak-form equations.

Standard numerical procedure based on the SGBEM and FEM has been adopted to construct numerical solutions of involved systems of governing equations. Galerkin approximation strategy with standard continuous interpolation functions has been used to discretize both the boundary integral equations and weak-form finite element equations. Except for a local region along the crack front, special continuous interpolation functions have been utilized to approximate the relative crack-face displacement in the vicinity of the crack front. Use of such special interpolation functions allows the near tip field to be captured accurately by relatively coarse meshes. To further enhance the computational accuracy and efficiency, all involved kernels for generally anisotropic materials have been computed using the interpolation technique in order to avoid the massive calculations associated with the direct evaluation of line integrals for all pairs of source and field points resulting from the numerical quadrature. In addition, the weakly singular and nearly singular double surface integrals resulting from the discretization of the governing boundary integral equations have been evaluated numerically using a special quadrature scheme. A family of variable

transformations has been introduced to eliminate the weak singularity and regularize the rapid variation of all integrands to ensure that the final integrals can be efficiently integrated by standard Gaussian quadrature. Once all primary unknowns have been solved, various quantities such as stress intensity factors, T-stresses, displacements and stresses within the body have been post-processed. In the present study, the stress intensity factors and the T-stresses have been computed accurately via two explicit, interpolation-free formula related to the jump and sum of the displacement across the crack surface in the vicinity of the crack front, respectively. Finally, the coupling procedure between the in-house SGBEM code and the reliable commercial finite element packages has been established to employ their advanced computational features.

To verify both the formulation of governing equations and numerical implementation of SGBEM and SGBEM-FEM coupling, numerical results have been extensively compared with available benchmark solutions for various boundary value problems. It can be concluded from such numerical study that the proposed technique yield highly accurate results, especially the crack opening displacement, stress intensity factors, and T-stresses, and obtained results also exhibit good convergence behavior. Due to the use of special crack-tip elements along the crack front, relatively coarse meshes can yield results of reasonably high accuracy. From extensive numerical experiments on complex and relatively large-scale problem, the proposed technique has been found promising and robust and, as a result, constituted an attractive computational tool for analysis of three-dimensional elasticity and fracture problems.

While the formulation and the proposed technique have been restricted mainly to three-dimensional elastic media, they can possibly be extended to treat multi-field media such as those made from piezoelectric materials, piezo-magnetic materials, and piezo-electro-magnetic materials. In addition, the current technique can be generalized to treat other body models such as half-space domain and bi-material domain.

REFERENCES

[1] Ananthasayanam B, Capitaneanu M, Joseph PF. Determination of higher order coefficients and zones of dominance using a singular integral equation approach. *Engineering Fracture Mechanics*, **74**, 2007, pp. 2009-2131.

[2] Anderson TL. Fracture Mechanics: Fundamentals and Applications, third edition. Taylor & Francis, New York, 2005.

[3] Ariza MP, Dominguez J. Boundary element formulation for 3D transversely isotropic cracked bodies. *International Journal for Numerical Methods in Engineering*, **60**, 2004, pp. 719-753.

[4] Bathe KJ. Finite Element Procedures, Prentice-Hall, New Jersey, 1990.

[5] Belytschko T, Liu WK, Moran B. Nonlinear finite elements for continua and structures, John Wiley & Sons, New York, 2000.

[6] Blandford GE, Ingraffea AR, Ligget JA. Two-dimensional stress intensity factor computation using boundary element method. *International Journal for Numerical Methods in Engineering*, **17**, 1981, pp. 387-440.

[7] Bonnet M. Regularized direct and indirect symmetric variational BIE formulations for three-dimensional elasticity. *Engineering Analysis with Boundary Elements*, **15**, 1995, pp. 93-102.

[8] Bonnet M, Maier G, Polizzotto C. Symmetric Galerkin boundary element methods. *Applied Mechanics Review*, 51, 1998, pp. 669-703.

[9] Broek D. Elementary Engineering Fracture Mechanics, third edition. Martinus Nijhoff Publishers, Boston, 1982.

[10] Bui HD. An integral equations method for solving the problem of a plane crack of arbitrary shape. Journal of Mechanics and Physics of Solids, **25**, 1977, pp. 29-39.

[11] Chen YZ. Closes form solutions of T-stress in plane elasticity crack problems. *International Journal of Solids and Structures*, **37**, 2000, pp. 1629-1637.

[12] Chen YZ, Wang ZX, Lin XY. Crack front position and crack back position techniques for evaluating the T-stress at crack tip using functions of a complex variable. *Journal of Mechanics of Materials and Structures*, **3**, 2008, pp. 1659-1673.

[13] Chen YZ, Wang ZX, Lin XY. Evaluation of the T-stress for interacting cracks. *Computational Materials Science*, **45**, 2009, pp. 349-357.

[14] Cotterell B, Rice JR. Slightly curved or kinked cracks. *International Journal of Fracture*, **16**, 1980, pp. 155-169.

[15] Cruse TA, Dominguez J. Boundary Element Analysis in Computational Fracture Mechanics. Kluwer Academic Publishers, Dordrecht, 1988.

[16] Du ZZ, Hancock JW. The effect of non-singular stresses on crack tip constraint. *Journal of the Mechanics and Physics of Solids*, **39**, 1991, pp. 555–567.

[17] Fabrikant VI. Applications of Potential Theory in Mechanics: A Selection of New Results. Kluwer Academic Publishers, Dordrecht, 1989.

[18] Fett T. A Green's function for T-stresses in an edge-cracked rectangular plate. *Engineering Fracture Mechanics*, **54**, 1997, PP. 365-373.

[19] Fett T. T-stresses in rectangular plates and circular disks. *Engineering Fracture Mechanics*, **60**, 1998, pp. 631-652.

[20] Fett T, Rizzi G. T-stress of cracks loaded by near-tip tractions. *Engineering Fracture Mechanics*, **73**, 2006, pp. 1940–1946.

[21] Fett T, Rizzi G, Bahr H-A. Green's functions for the T-stress of small kink and fork cracks. *Engineering Fracture Mechanics*, **73**, 2006, pp. 1426–1435.
[22] Frangi A, Novati G, Springhetti R, Rovizzi M. 3D fracture analysis by the symmetric Galerkin BEM. *Computational Mechanics*, **28**, 2002, pp. 220-232.
[23] Gu H, Yew CH. Finite element solution of a boundary integral equation for mode I embedded three-dimensional fractures. *International Journal for Numerical Methods in Engineering*, **26**, 1988, pp. 1525-1540.
[24] Gurtin ME, Murdoch AI. A continuum theory of elastic material surfaces. *Archive for Rational Mechanics and Analysis*, **57**, 1975, pp. 291-323.
[25] Gurtin ME, Murdoch AI. Surface stress in solids. *International Journal of Solids and Structures*, **14**, 1978, pp. 431-440.
[26] Hayami K, Brebbia CA. Quadrature methods for singular and nearly singular integrals in 3-D boundary element method, Boundary Element X, pp. 237-264, Springer-Verlag, Berlin, 1988.
[27] Hayami K. A projection transformation method for nearly singular surface boundary element integrals. In: Brebbia, c.a., Orszag, S.A. (eds) Lecture notes in Engineering, 1992, **73**, pp. 1-2. Springer-Verlag, Berlin.
[28] Hayami K, Matsumoto H. A numerical quadrature for nearly singular boundary element integrals. *Engineering Analysis with Boundary Elements*, **13**, 1994, pp. 143-154.
[29] Intarit P, Senjuntichai T, Rungamornrat J, Rajapakse RKND. Stress analysis of penny-shaped crack considering the effects of surface elasticity. Proceedings of 20th Annual International Conference on Composites or Nano Engineering (ICCE-20), Ramada Beijing North Hotel, Beijing, P.R. China 2012.
[30] Intarit P. Solutions of elastic medium with surface stress effects, Ph.D. Dissertation, Chulalongkorn University, Thailand, 2013.
[31] Kassir MK, Sih GC. Mechanics of fracture, Three-dimensional crack problems, volume 2. Noordhoff International Publishing, Leyden, 1975.
[32] Kirilyuk VS, Levchuk OI. Elastic T-stress solutions for flat elliptical cracks under tension and bending. *Engineering Fracture Mechanics*, **74**, 2007, pp. 2881-2891.
[33] Leblond JB. Crack paths in plane situations – I: General form of the expansion of the stress intensity factors. *International Journal of Solids and Structures*, **25**, 1989, pp. 1311-1325.
[34] Leblond JB and Torlai O. The stress field near the front of an arbitrarily shaped crack in a three-dimensional elastic body. *Journal of Elasticity*, **29**, 1992, pp. 97-131.
[35] Lewis T, Wang X. The T-stress solutions for through-wall circumferential cracks in cylinders subjected to general loading conditions. *Engineering Fracture Mechanics*, **75**, 2008, pp. 3206-3225.
[36] Li S, Mear ME, Xiao L. Symmetric weak-form integral equation method for three-dimensional fracture analysis. *Computer Methods in Applied Mechanics and Engineering*, **151**, 1998, pp. 435-459.
[37] Li HB, Han GM. A new method for evaluating singular integral in stress analysis of solids by the direct boundary element method. *International Journal for Numerical Methods in Engineering*, **21**, 1985, pp. 2071-2098.
[38] Lubiliner J. Plasticity theory, Macmillan Publishing Company, New York, 1990.

[39] Martha LF, Gray LJ, Ingraffea AR. Three-dimensional fracture simulation with a single-domain, direct boundary element formulation. *International Journal for Numerical Methods in Engineering*, **35**, 1992, pp. 1907-1921.
[40] Meshii T, Tanaka T, Lu K. T-Stress solutions for a semi-elliptical axial surface crack in a cylinder subjected to mode-I non-uniform stress distributions. *Engineering Fracture Mechanics*, **77**, 2010, pp. 2467–2478.
[41] Miller RE, Shenoy VB. Size-dependent elastic properties of nanosized structural elements. *Nanotechnology*, 11, 2000, pp.139-147
[42] Molla-Abbasi K, Schutte H. On the full set of elastic T-stress terms of internal elliptical cracks under mixed-mode loading condition. *Engineering Fracture Mechanics*, **75**, 2008, pp. 1545-1568.
[43] Nan H, Wang B. Effect of residual surface stress on the fracture of nanoscale materials. Mechanics Research Communications, **44**, 2012, pp. 30-34.
[44] Oden JT, Carey GF. Finite elements: Special problems in solid mechanics, volume 5, Prentice-Hall, New Jersey, 1984.
[45] Pan E, Yuan FG. Boundary element analysis of three-dimensional cracks in anisotropic solids. *International Journal for Numerical Methods in Engineering*, **48**, 2000, pp. 211-237.
[46] Pinyochotiwong Y, Rungamornrat J, Senjuntichai T. Rigid frictionless indentation on elastic half space with influence of surface stresses. *International Journal of Engineering Science*, **71**, pp. 15-35.
[47] Profant T, Sevecek O, Kotoul M. Calculation of K-factors and T-stress for cracks in anisotropic bimaterials. *Engineering Fracture Mechanics*, **75**, 2008, pp. 3707-3727.
[48] Qu J, Wang X. Solutions of T-stresses for quarter-elliptical corner cracks in finite thickness plates subject to tension and bending. *International Journal of Pressure Vessels and Piping*, **83**, 2006, pp. 593–606.
[49] Rice JR. Limitations to the small scale yielding approximation for crack tip plasticity. *Journal of the Mechanics and Physics of Solids*, **22**, 1974, pp. 17–26.
[50] Rungamornrat J, Mear ME. Weakly-singular, weak-form integral equations for cracks in three-dimensional anisotropic media. *International Journal of Solids and Structures*, **45**, 2008a, pp. 1283-1301.
[51] Rungamornrat J, Mear ME. A weakly-singular SGBEM for analysis of cracks in 3D anisotropic media. *Computer Methods in Applied Mechanics and Engineering*, **197**, 2008b, pp. 4319-4332.
[52] Rungamornrat J. Determination of strength of singularity induced by discontinuity in a three-dimensional, linear, finite domain. *Proceedings of the 12th International Conference on Fracture*, Ottawa, Canada, July 12-17, 2009.
[53] Rungamornrat J, Senjuntichai T. Regularized boundary integral representations for dislocation for dislocations and cracks in smart media. *Smart Materials and Structures*, **18**, 2009, 074010(14pp).
[54] Rungamornrat J, Mear ME. SGBEM-FEM coupling for analysis of cracks in 3D anisotropic media. *International Journal for numerical methods in Engineering*, **86**, 2011, pp.224-248.
[55] Saez A, Ariza MP, Dominguez J. Three-dimensional fracture analysis in transversely isotropic solids. *Engineering Analysis with Boundary Elements*, **20**, 1997, pp. 287-298.
[56] Sanford RJ. Principles of Fracture Mechanics. Prentice Hall, New Jersey, 2003.

[57] Schutte H, Molla-Abbasi K. On the full set of elastic T-stress terms of internal circular cracks under mixed-mode loading conditions. *Engineering Fracture Mechanics*, 74, 2007, pp. 2770-2787.
[58] Shah PD, Tan CL, Wang X. T-stress solutions for two-dimensional crack problems in anisotropic elasticity using the boundary element method. *Fatigue & Fracture of Engineering Materials & Structures*, **29**, 2006, pp. 343-356.
[59] Sokolnikoff IS. Mathematical Theory of Elasticity, McGraw-Hill, New York, 1956.
[60] Ting TCT. Asymptotic solution near the apex of an elastic wedge with curved boundaries. *Quarterly of Applied Mathematics*, **42**, 1985, pp. 467-476.
[61] Wang X. Elastic T-stress for cracks in test specimens subjected to non-uniform stress distribution. *Engineering Fracture Mechanics*, **69**, 2002, pp. 1339–1352.
[62] Wang X. Elastic T-stress solutions for semi-elliptical surface cracks in finite thickness plates. *Engineering Fracture Mechanics*, **70**, 2003, pp. 731–756.
[63] Wang X. Elastic T-stress solutions for penny-shaped cracks under tension and bending. *Engineering Fracture Mechanics*, **71**, 2004, pp. 2283-2298.
[64] Wang X, Bell R. Elastic T -stress solutions for semi-elliptical surface cracks in finite thickness plates subject to non-uniform stress distributions. Engineering *Fracture Mechanics*, **71**, 2004, pp. 1477–1496.
[65] Weaver J. Three-dimensional crack analysis. *International Journal of Solids and Structures*, **13**, 1977, pp. 321-330.
[66] Westergaard HM. Bearing pressures and cracks. *Journal of Applied Mechanics*, **6**, 1939, pp. A49-A53.
[67] William ML. On the stress distribution at the base of a stationary crack. *Journal of Applied Mechanics*, **24**, 1957, pp. 109-114.
[68] Xiao L, Symmetric weak-form integral equation method for three dimensional fracture analysis, Ph.D. Dissertation, The University of Texas at Austin, Texas, 1998.
[69] Xu G, Ortiz M. A variational boundary integral method for the analysis of 3-D cracks of arbitrary geometry modeled as continuous distributions of dislocation loops. *International Journal for Numerical Methods in Engineering*, **36**, 1993, pp. 3675-3701.
[70] Xu G. A variational boundary integral method for the analysis of three-dimensional cracks of arbitrary geometry in anisotropic elastic solids. *Journal of Applied Mechanics*, **67**, 2000, pp. 403-408.
[71] Yu J, Tan CL, Wang X. T-stress solutions for crack emanating from a circular hole in a finite plate. *International Journal of Fracture*, **140**, 2006, pp. 293-298.
[72] Zhou Z, Xu X, Leung YTA, Huang Y. Stress intensity factors and T-stress for an edge interface crack by symplectic expansion. *Engineering Fracture Mechanics*, **102**, 2013, pp. 334–347.

Appendix A Publications

International paper 1 (published):

Rungamornrat J, Sripirom S. “Stress Analysis of Three-dimensional Media Containing Localized Zone by FEM-SGBEM Coupling”. *Mathematical Problems in Engineering*, 2011, Article Number 702082, 27 pages, doi:10.1155/2011/702082. Impact Factor (2012): 1.383

International paper 2 (under review):

Nguyen TB, Rungamornrat J, Senjuntichai T, Wijeyewickrema AC. “FEM-SGBEM coupling for modeling of mode-I planar cracks in three-dimensional elastic media with residual surface tension effects”. *Engineering Analysis with Boundary Elements*, Under review. Impact Factor (2012): 1.596

Appendix B Reprints

Hindawi Publishing Corporation
Mathematical Problems in Engineering
Volume 2011, Article ID 702082, 27 pages
doi:10.1155/2011/702082

Research Article

Stress Analysis of Three-Dimensional Media Containing Localized Zone by FEM-SGBEM Coupling

Jaroon Rungamornrat and Sakravee Sripirom

Department of Civil Engineering, Faculty of Engineering, Chulalongkorn University, Bangkok 10330, Thailand

Correspondence should be addressed to Jaroon Rungamornrat, jaroon.r@chula.ac.th

Received 24 May 2011; Accepted 5 August 2011

Academic Editor: Delfim Soares Jr.

This paper presents an efficient numerical technique for stress analysis of three-dimensional infinite media containing cracks and localized complex regions. To enhance the computational efficiency of the boundary element methods generally found inefficient to treat nonlinearities and non-homogeneous data present within a domain and the finite element method (FEM) potentially demanding substantial computational cost in the modeling of an unbounded medium containing cracks, a coupling procedure exploiting positive features of both the FEM and a symmetric Galerkin boundary element method (SGBEM) is proposed. The former is utilized to model a finite, small part of the domain containing a complex region whereas the latter is employed to treat the remaining unbounded part possibly containing cracks. Use of boundary integral equations to form the key governing equation for the unbounded region offers essential benefits including the reduction of the spatial dimension and the corresponding discretization effort without the domain truncation. In addition, all involved boundary integral equations contain only weakly singular kernels thus allowing continuous interpolation functions to be utilized in the approximation and also easing the numerical integration. Nonlinearities and other complex behaviors within the localized regions are efficiently modeled by utilizing vast features of the FEM. A selected set of results is then reported to demonstrate the accuracy and capability of the technique.

1. Introduction

A physical modeling of three-dimensional solid media by an idealized mathematical domain that occupies the full space is standard and widely used when inputs and responses of interest are only localized in a zone with its length scale much smaller than that of the body. Influence of the remote boundary of a domain on such responses is generally insignificant for this particular case and can, therefore, be discarded in the modeling without loss of accuracy of the predicted solutions. Such situations arise in various engineering applications

such as the simulation of crack growth in hydraulic fracturing process in which the fracture is generally treated as an isolated crack in an infinite medium, the evaluation and assessment of service life of large-scale structures in which the influence of embedded initial defects can be characterized by small pre-existing flaws, and the determination of effective properties of materials possessing a microstructure such as cracks, voids, inclusions, and localized inelastic zones. Unlike the stress analysis of linear elasticity problems, complexity of a mathematical model can substantially increase when an infinite body contains additionally a line of singularity and/or a localized nonlinear region. The former situation arises naturally when a surface of displacement discontinuities (e.g., cracks and dislocations) is present whereas the latter may result from applications of high-intensity loads, complex constitutive laws, containment of small defects and inhomogeneities, and localized non-mechanical effects (such as temperature change). Besides various practical applications, such present complexity renders the modeling itself theoretically and computationally challenging.

Various analytical techniques (e.g., integral transform methods, methods based on stress and displacement representations, techniques related to potential theories, etc.) have been proposed and used extensively in the stress analysis of solid media (e.g., [1–5]). However, their applications are very limited to either two-dimensional boundary value problems involving simple data or three-dimensional problems with extremely idealized settings. Such limitation becomes more apparent when complexity of involved physical phenomena increases (e.g., complexity introduced by the presence of material nonlinearities, inhomogeneities, and embedded singularities). For those particular situations, a more sophisticated mathematical model is generally required in order to accurately predict responses of interest, and, as a major consequence, an analytical or closed-form solution of the corresponding boundary value problem cannot readily be obtained and numerical techniques offer better alternatives in the solution procedure.

The finite element method (FEM) and the boundary element method (BEM) are two robust numerical techniques extensively used in the modeling of various field problems. Both techniques possess a wide range of applications, and there are various situations that favor the FEM over the BEM and vice versa. The FEM has proven to be an efficient and powerful method for modeling a broad class of problems in structural and solid mechanics (e.g., [6–8]). In principle, the basis of the FEM is sufficiently general allowing both nonlinearities and inhomogeneities present within the domain to be treated. In addition, a final system of discrete algebraic equations resulting from this method possesses, in general, desirable properties (e.g., symmetry, sparseness, positive definiteness of the coefficient matrix, etc.). Nevertheless, the conventional FEM still exhibits some major shortcomings and requires nontrivial treatments when applied to certain classes of problems. For instance, a standard discretization procedure cannot directly be applied to boundary value problems involving an infinite domain. A domain truncation supplied by a set of remote boundary conditions is commonly employed to establish an approximate domain of finite dimensions prior to the discretization. It should be noted that defining such suitable truncated surface and corresponding boundary conditions remains the key issue and it can significantly influence the quality of approximate solutions. Another limited capability of the method to attain adequately accurate results with reasonably cheap computational cost is apparent when it is applied to solve fracture problems. In the analysis, it generally requires substantially fine meshes in a region surrounding the crack front in order to accurately capture the complex (singular) field and extract essential local fracture information such as the stress intensity factors (e.g., [9–11]).

The boundary element method (BEM) has been found computationally efficient and attractive for modeling certain classes of linear boundary value problems since, for

a homogeneous domain that is free of distributed sources, the key governing equation involves only integrals on the boundary of the domain (e.g., [12–23]). As a direct consequence, the discretization effort and cost are significantly reduced, when compared to the FEM, due to the reduction of spatial dimensions of the governing equation by one. Another apparent advantage of the method is associated with its simplicity in the modeling of an infinite media. In such particular situation, the remote boundary of the domain can basically be discarded without loss via an appropriate treatment of remote conditions (e.g., [14, 17, 19, 23]). Among various strategies utilized to form the BEM, the weakly singular symmetric Galerkin boundary element method (SGBEM) has become a well-established and well-known technique and, during the past two decades, has proven robust for three-dimensional analysis of linear elasticity problems (e.g., [15, 16]), linearly elastic infinite media containing isolated cracks (e.g., [14, 19, 23]), and cracks in finite bodies (e.g., [16, 18, 20, 21, 23]). Superior features of this particular technique over other types of the BEM are due mainly to that all kernels appearing in the governing integral equations are only weakly singular of $\mathcal{O}(1/r)$ and that a final system of linear algebraic equations resulting from the discretization possesses a symmetric coefficient matrix. The weakly singular nature not only renders all involved integrals to be interpreted in an ordinary sense and evaluated numerically using standard quadrature but also allows standard C^0 interpolation functions to be employed in the approximation procedure. It has been also demonstrated that the weakly singular SGBEM along with the proper enrichment of an approximate field near the crack front yields highly accurate fracture data (e.g., mixed-mode stress intensity factors) even that relatively coarse meshes are employed in the discretization (e.g., [18, 21, 23]). While the weakly singular SGBEM has gained significant success in the analysis of linear elasticity and fracture problems, the method still contains certain unfavorable features leading to its limited capability to solve various important classes of boundary value problems. For instance, the method either becomes computationally inefficient or experiences mathematical difficulty when applied to solve problems involving nonlinearity and nonhomogeneous media. As the geometry of the domain becomes increasingly complex and its size and surface to volume ratio are relatively large (requiring a large number of elements to reasonably represent the entire boundary of the domain), the method tends to consume considerable computational resources in comparison with the standard FEM. Although the SGBEM yields a symmetric system of linear equations, the coefficient matrix is fully dense and each of its entries must be computed by means of a double surface integration.

In the past two decades, various investigators have seriously attempted to develop efficient and accurate numerical procedures for analysis of elasticity and fracture problems by exploiting positive features of both the BEM and the FEM. The fundamental idea is to decompose the entire domain into two regions and then apply the BEM to model a linearly elastic region with small surface-to-volume ratio and possibly containing the displacement discontinuities (e.g., cracks and dislocations) and the FEM to model the remaining majority of the domain possibly exhibiting complex behavior (e.g., material nonlinearity and nonhomogeneous data). The primary objective is to compromise between the requirement of computational resources and accuracy of predicted results. Within the context of linear elasticity, there have been several investigations directed towards the coupling of the conventional BEM and the standard FEM (e.g., [24–26]) and the coupling of the strongly singular SGBEM and the standard FEM (e.g., [27–30]). It should be emphasized that the former type of coupling procedure generally destroys the desirable symmetric feature of the entire system of linear algebraic equations whereas the latter type requires special numerical treatment of strongly and hyper singular integrals (e.g., [31, 32]). Extensive review

of various types of coupling between boundary integral equation methods and finite element techniques can be found in [33]. Among those existing techniques, a particular symmetric coupling strategy between the weakly singular SGBEM and the standard FEM has been found computationally efficient and has recently become an attractive alternative for performing comprehensive stress and fracture analysis. This is due primarily to (i) the symmetry feature of the SGBEM that leads to the symmetric coupling formulation and (ii) the weakly singular nature of all involved boundary integrals requiring simpler theoretical and numerical treatment in comparison with strongly singular and hypersingular integrals. Xiao [16] first presented such coupling formulation for cracks in isotropic, linearly elastic finite bodies; more precisely, a pair of weakly singular, weak-form displacement and traction integral equations was utilized along with the principle of virtual work and the proper enforcement of continuity conditions on the interface to establish the symmetric coupling formulation. Later, Frangi and Novati [34] successfully implemented Xiao's formulation to analyze cracked bodies subjected to pure traction boundary conditions. Besides its accuracy and robustness, the technique was still restricted to the conforming discretization of the interface between the two regions. Springhetti et al. [35] relaxed such limitation by allowing the weak enforcement of continuity across the interface and also generalized the technique to treat both potential and elastostatic problems. Nevertheless, their main focus is on uncracked bodies made of linearly isotropic materials. Recently, Rungamornrat and Mear [36] extended the work of Xiao [16] to enable the treatment of both material anisotropy and nonmatching interface. While this particular coupling scheme has been well-established for decades, on the basis of an extensive literature survey, applications of this technique to model a problem of an infinite space containing isolated cracks and localized complex zones have not been recognized.

In this paper, a numerical procedure based on the symmetric coupling between the weakly singular SGBEM and the standard FEM is implemented to perform three-dimensional stress analysis of an infinite medium containing displacement discontinuities and localized complex zones. Vast features of the FEM are exploited to allow the treatment of very general localized zones, for instance, those exhibiting material nonlinearity, material nonuniformity, and other types of complexity. The weakly singular SGBEM is utilized to readily and efficiently model the remaining unbounded region. A pair of weakly singular boundary integral equations proposed by Rungamornrat and Mear [22] is employed as a basis for the development of SGBEM, and this, therefore, allows the treatment of the unbounded region that is made of an anisotropic linearly elastic material and contains cracks. It is worth emphasizing that while the present study is closely related to the work of Frangi and Novati [34], Springhetti et al. [35], and Rungamornrat and Mear [36], the proposed technique offers additional crucial capabilities to treat an infinite domain, material nonlinearity in localized zones, and general material anisotropy. Following sections of this paper present basic equations and the coupling formulation, essential components for numerical implementations, numerical results and discussions, and conclusions and useful remarks.

2. Formulation

Consider a three-dimensional infinite medium, denoted by Ω, containing a crack and a localized complex zone as shown schematically in Figure 1(a). The crack is represented by two geometrical coincident surfaces S_C^+ and S_C^- with their unit outward normal being denoted by $\mathbf{n}^+$ and $\mathbf{n}^-$, respectively, and the localized complex zone is denoted by Ω^L. In the present study, the medium is assumed to be free of a body force and loading on its remote boundary, and both surfaces of the crack are subjected to prescribed self-equilibrated traction defined by

$\mathbf{t}_C = \mathbf{t}_C^+ = -\mathbf{t}_C^-$. Now, let us introduce an imaginary surface S_I to decompose the body Ω into two subdomains, an unbounded "BEM-region" denoted by Ω^B and a finite "FEM-region" denoted by Ω^F, as indicated in Figure 1(b). The surface S_I is selected such that the localized complex zone and the crack are embedded entirely in the FEM-region and in the BEM-region, respectively (i.e., $S_C^+ \cup S_C^- \subset \Omega^B$ and $\Omega^L \subset \Omega^F$), and, in addition, the BEM-region must be linearly elastic. To clearly demonstrate the role of the interface between the two subregions in the formulation presented below, we define $\{S_{BI}, \mathbf{t}_{BI}, \mathbf{u}_{BI}\}$ and $\{S_{FI}, \mathbf{t}_{FI}, \mathbf{u}_{FI}\}$ as the interface, the unknown traction, and the unknown displacement on the interface of the BEM-region Ω^B and the FEM-region Ω^F, respectively. It is important to emphasize that the interfaces S_{BI} and S_{FI} are in fact identical to the imaginary surface S_I. While the formulation is presented, for brevity, only for a domain containing a single crack and a single localized complex zone, it can readily be extended to treat multiple cracks and multiple complex zones; in such particular case, multiple FEM-regions are admissible.

2.1. Governing Equations for Ω^B

The total boundary of the BEM-region Ω^B, denoted by S_B, consists of the reduced crack surface $S_{BC} \equiv S_C^+$ on which the traction is fully prescribed and the interface S_{BI} where neither the traction nor the displacement is known a priori. Note again that the subscript "B" is added only to emphasize that those surfaces are associated with the BEM-region. To form a set of governing integral equations for this region, a pair of weakly singular, weak-form displacement and traction boundary integral equations developed by Rungamornrat and Mear [22] is employed. These two integral equations were derived from standard boundary integral relations for the displacement and stress along with a systematic regularization technique. The final form of completely regularized integral equations is well suited for establishing the symmetric formulation for the weakly singular SGBEM. Such pair of integral equations is given here, for convenience in further reference, by

$$\begin{aligned}
\frac{1}{2}\int_{S_{BI}} \widetilde{t}_k(\mathbf{y}) u_k(\mathbf{y}) dS(\mathbf{y}) = {} & \int_{S_{BI}} \widetilde{t}_k(\mathbf{y}) \int_{S_{BI}} U_i^k(\boldsymbol{\xi}-\mathbf{y}) t_i(\boldsymbol{\xi}) dS(\boldsymbol{\xi}) dS(\mathbf{y}) \\
& + \int_{S_{BI}} \widetilde{t}_k(\mathbf{y}) \int_{S_B} G_{mj}^k(\boldsymbol{\xi}-\mathbf{y}) D_m v_j(\boldsymbol{\xi}) dS(\boldsymbol{\xi}) dS(\mathbf{y}) \\
& - \int_{S_{BI}} \widetilde{t}_k(\mathbf{y}) \int_{S_B} n_i(\boldsymbol{\xi}) H_{ij}^k(\boldsymbol{\xi}-\mathbf{y}) v_j(\boldsymbol{\xi}) dS(\boldsymbol{\xi}) dS(\mathbf{y}),
\end{aligned} \tag{2.1}$$

$$\begin{aligned}
-\int_{S_B} c(\mathbf{y}) \widetilde{v}_k(\mathbf{y}) t_k(\mathbf{y}) dS(\mathbf{y}) = {} & \int_{S_B} D_t \widetilde{v}_k(\mathbf{y}) \int_{S_{BI}} G_{tk}^j(\boldsymbol{\xi}-\mathbf{y}) t_j(\boldsymbol{\xi}) dS(\boldsymbol{\xi}) dS(\mathbf{y}) \\
& + \int_{S_B} D_t \widetilde{v}_k(\mathbf{y}) \int_{S_B} C_{mj}^{tk}(\boldsymbol{\xi}-\mathbf{y}) D_m v_j(\boldsymbol{\xi}) dS(\boldsymbol{\xi}) dS(\mathbf{y}) \\
& + \int_{S_B} \widetilde{v}_k(\mathbf{y}) \int_{S_{BI}} n_l(\mathbf{y}) H_{lk}^j(\boldsymbol{\xi}-\mathbf{y}) t_j(\boldsymbol{\xi}) dS(\boldsymbol{\xi}) dS(\mathbf{y}),
\end{aligned} \tag{2.2}$$

where $\widetilde{t}_k$ and $\widetilde{v}_k$ are sufficiently smooth test functions; $D_m(\cdot) = n_i \varepsilon_{ism} \partial(\cdot)/\partial \xi_s$ is a surface differential operator with ε_{ism} denoting a standard alternating symbol; $v_j(\boldsymbol{\xi}) = u_j(\boldsymbol{\xi})$ for $\boldsymbol{\xi} \in S_{BI}$ and $\Delta u_j(\boldsymbol{\xi})$ for $\boldsymbol{\xi} \in S_{BC}$ with $\Delta u_j(\boldsymbol{\xi}) = u_j^+(\boldsymbol{\xi}) - u_j^-(\boldsymbol{\xi})$ denoting the jump in

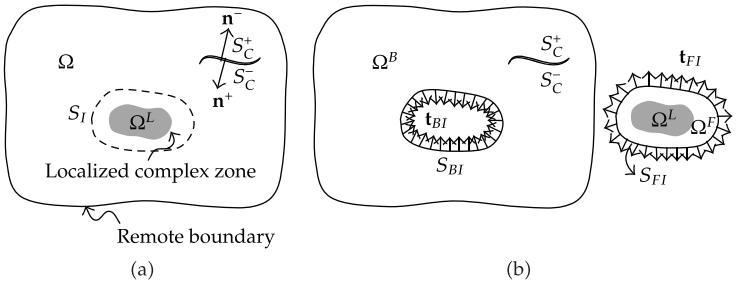

Figure 1: (a) Schematic of three-dimensional infinite medium containing crack and localized complex zone and (b) schematic of BEM-region Ω^B and FEM-region Ω^F.

the displacement across the crack surface; the geometry-dependent constant $c(\mathbf{y})$ is defined by $c(\mathbf{y}) = 1/2$ for $\boldsymbol{\xi} \in S_{BI}$ and 1 for $\boldsymbol{\xi} \in S_{BC}$. All involved kernels, that is, $H_{ij}^p(\boldsymbol{\xi}-\mathbf{y})$, $U_i^p(\boldsymbol{\xi}-\mathbf{y})$, $G_{mj}^p(\boldsymbol{\xi}-\mathbf{y})$, $C_{mj}^{tk}(\boldsymbol{\xi}-\mathbf{y})$, are given, for generally anisotropic materials, by

$$H_{ij}^p(\boldsymbol{\xi}-\mathbf{y}) = -\frac{(\xi_i - y_i)\delta_{pj}}{4\pi r^3}, \tag{2.3}$$

$$U_i^p(\boldsymbol{\xi}-\mathbf{y}) = K_{mp}^{mi}(\boldsymbol{\xi}-\mathbf{y}), \tag{2.4}$$

$$G_{mj}^p(\boldsymbol{\xi}-\mathbf{y}) = \varepsilon_{abm}E_{ajdc}K_{cp}^{bd}(\boldsymbol{\xi}-\mathbf{y}), \tag{2.5}$$

$$C_{mj}^{tk}(\boldsymbol{\xi}-\mathbf{y}) = A_{mjdn}^{tkoe}K_{dn}^{oe}(\boldsymbol{\xi}-\mathbf{y}), \tag{2.6}$$

where δ_{pj} is a standard Kronecker-delta symbol; E_{ijkl} are elastic moduli; A_{mjdn}^{tkoe} and $K_{jl}^{ik}(\boldsymbol{\xi}-\mathbf{y})$ are defined by

$$A_{mjdn}^{tkoe} = \varepsilon_{pam}\varepsilon_{pbt}\left(E_{bknd}E_{ajeo} - \frac{1}{3}E_{ajkb}E_{dneo}\right), \tag{2.7}$$

$$K_{jl}^{ik}(\boldsymbol{\xi}-\mathbf{y}) = \frac{1}{8\pi^2 r}\oint_{\mathbf{z}\cdot\mathbf{r}=0}(\mathbf{z},\mathbf{z})_{kl}^{-1}z_i z_j ds(\mathbf{z}), \tag{2.8}$$

in which $\mathbf{r} = \boldsymbol{\xi}-\mathbf{y}$, $r = \|\mathbf{r}\|$, $(\mathbf{z},\mathbf{z})_{jk} = z_i E_{ijkl} z_l$ and the closed contour integral is to be evaluated over a unit circle $\|\mathbf{z}\| = 1$ on a plane defined by $\mathbf{z}\cdot\mathbf{r} = 0$. It is evident that the kernel $H_{ij}^p(\boldsymbol{\xi}-\mathbf{y})$ is given in an explicit form independent of material properties and the kernels $n_i(\boldsymbol{\xi})H_{ij}^p(\boldsymbol{\xi}-\mathbf{y})$, $n_i(\mathbf{y})H_{ij}^p(\boldsymbol{\xi}-\mathbf{y})$, $U_i^p(\boldsymbol{\xi}-\mathbf{y})$, $G_{mj}^p(\boldsymbol{\xi}-\mathbf{y})$, $C_{mj}^{tk}(\boldsymbol{\xi}-\mathbf{y})$ are singular only at $\boldsymbol{\xi} = \mathbf{y}$ of $\mathcal{O}(1/r)$ (see details in Xiao [16] for discussion of the singularity behavior of the kernel $H_{ij}^p(\boldsymbol{\xi}-\mathbf{y})$). It should be remarked that for isotropic materials, the kernels $U_i^p(\boldsymbol{\xi}-\mathbf{y})$, $G_{mj}^p(\boldsymbol{\xi}-\mathbf{y})$, $C_{mj}^{tk}(\boldsymbol{\xi}-\mathbf{y})$ possess an explicit form in terms of elementary functions (see [18, 22]).

Towards obtaining a system of governing integral equations for the BEM-region Ω^B, the weak-form boundary integral equation for the traction (2.2) is applied directly to the crack surface S_{BC} (with the test function being chosen such that $\tilde{\mathbf{v}} = 0$ on S_{BI}) and to

the interface S_{BI} (with the test function being chosen such that $\tilde{\mathbf{v}} = 0$ on S_{BC}), and the weak-form boundary integral equation for the displacement (2.1) is applied only to the interface S_{BI}. A final set of three integral equations is given concisely by

$$\begin{aligned}
\mathcal{A}_{CC}(\tilde{\mathbf{v}}, \Delta\mathbf{u}) + \mathcal{B}_{IC}(\mathbf{t}_{BI}, \tilde{\mathbf{v}}) + \mathcal{A}_{CI}(\tilde{\mathbf{v}}, \mathbf{u}_{BI}) &= -2\mathcal{F}_{BC}(\tilde{\mathbf{v}}, \mathbf{t}_C), \\
\mathcal{B}_{IC}\left(\tilde{\mathbf{t}}_{BI}, \Delta\mathbf{u}\right) + \mathcal{C}_{II}\left(\tilde{\mathbf{t}}_{BI}, \mathbf{t}_{BI}\right) + \mathfrak{D}_{II}\left(\tilde{\mathbf{t}}_{BI}, \mathbf{u}_{BI}\right) &= 0, \\
\mathcal{A}_{IC}(\tilde{\mathbf{u}}_{BI}, \Delta\mathbf{u}) + \mathfrak{D}_{II}(\mathbf{t}_{BI}, \tilde{\mathbf{u}}_{BI}) + \mathcal{A}_{II}(\tilde{\mathbf{u}}_{BI}, \mathbf{u}_{BI}) &= -2\mathcal{F}_{BI}(\tilde{\mathbf{u}}_{BI}, \mathbf{t}_{BI}),
\end{aligned} \tag{2.9}$$

where $\{\tilde{\mathbf{u}}_{BI}, \tilde{\mathbf{t}}_{BI}\}$ are test functions defined on the interface S_{BI} and all involved bilinear integral operators are defined, with subscripts $P, Q \in \{I, C\}$ being introduced to clearly indicate the surface of integration, by

$$\mathcal{A}_{PQ}(\mathbf{X}, \mathbf{Y}) = \int_{S_{BP}} D_t X_k(\mathbf{y}) \int_{S_{BQ}} C_{mj}^{tk}(\boldsymbol{\xi} - \mathbf{y}) D_m Y_j(\boldsymbol{\xi}) dS(\boldsymbol{\xi}) dS(\mathbf{y}), \tag{2.10}$$

$$\begin{aligned}
\mathcal{B}_{IP}(\mathbf{X}, \mathbf{Y}) = &\int_{S_{BI}} X_k(\mathbf{y}) \int_{S_{BP}} G_{mj}^{k}(\boldsymbol{\xi} - \mathbf{y}) D_m Y_j(\boldsymbol{\xi}) dS(\boldsymbol{\xi}) dS(\mathbf{y}) \\
&- \int_{S_{BI}} X_k(\mathbf{y}) \int_{S_{BP}} n_m(\boldsymbol{\xi}) H_{mj}^{k}(\boldsymbol{\xi} - \mathbf{y}) Y_j(\boldsymbol{\xi}) dS(\boldsymbol{\xi}) dS(\mathbf{y}),
\end{aligned} \tag{2.11}$$

$$\mathcal{C}_{II}(\mathbf{X}, \mathbf{Y}) = \int_{S_{BI}} X_k(\mathbf{y}) \int_{S_{BI}} U_i^k(\boldsymbol{\xi} - \mathbf{y}) Y_i(\boldsymbol{\xi}) dS(\boldsymbol{\xi}) dS(\mathbf{y}), \tag{2.12}$$

$$\mathcal{F}_{BP}(\mathbf{X}, \mathbf{Y}) = \frac{1}{2} \int_{S_{BP}} X_i(\mathbf{y}) Y_i(\mathbf{y}) dS(\mathbf{y}), \tag{2.13}$$

$$\mathfrak{D}_{II}(\mathbf{X}, \mathbf{Y}) = \mathcal{B}_{II}(\mathbf{X}, \mathbf{Y}) - \mathcal{F}_{BI}(\mathbf{X}, \mathbf{Y}). \tag{2.14}$$

It should be noted that the linear operator $\mathcal{A}_{PQ}(\mathbf{X}, \mathbf{Y})$ is in a symmetric form satisfying the condition $\mathcal{A}_{PQ}(\mathbf{X}, \mathbf{Y}) = \mathcal{A}_{QP}(\mathbf{Y}, \mathbf{X})$, and, as a consequence, it renders the left hand side of the system (2.9) being in a symmetric form. Although such symmetric formulation can readily be obtained, the right-hand side of (2.9) still contains the unknown traction on the interface $\mathbf{t}_{BI}$. The treatment of a term $\mathcal{F}_{BI}(\tilde{\mathbf{u}}_{BI}, \mathbf{t}_{BI})$ will be addressed once the formulation for the FEM-region Ω^F is established.

2.2. Governing Equations for Ω^F

Let us consider, next, the FEM-region Ω^F. For generality, the entire boundary of this particular region can be decomposed into two surfaces: the interface S_{FI} on which both the traction $\mathbf{t}_{FI}$ and the displacement $\mathbf{u}_{FI}$ are unknown a priori and the surface S_{FT} on which the traction $\mathbf{t}_{FT}$ is fully prescribed. The existence of the surface S_{FT} is apparent for the case that the FEM-region contains embedded holes or voids. It is also important to emphasize that, in the development of a key governing equation for Ω^F, the traction $\mathbf{t}_{FI}$ is treated, in a fashion different from that for the BEM-region, as unknown data instead of the primary unknown variable. In addition, to be capable of modeling a complex localized

zone embedded within the FEM-region, a constitutive model governing the material behavior utilized in the present study is assumed to be sufficiently general allowing the treatment of material nonlinearity, anisotropy, and inhomogeneity. The treatment of such complex material models has been extensively investigated and well established within the context of nonlinear finite element methods (e.g., [6, 37, 38]), and those standard procedures also apply to the current implementation and will not be presented for brevity. Here, we only outline the key governing equation for the FEM-region and certain unknowns and necessary data connected to those for the BEM-region.

Following standard formulation of the finite element technique, the weak-form equation governing the FEM-region can readily be obtained via the principle of virtual work [6–8] and the final equation can be expressed in a concise form by

$$\mathcal{K}_{FF}(\tilde{\mathbf{u}}, \boldsymbol{\sigma}) = 2\mathcal{F}_{FI}(\tilde{\mathbf{u}}_{FI}, \mathbf{t}_{FI}) + 2\mathcal{F}_{FT}(\tilde{\mathbf{u}}_{FT}, \mathbf{t}_{FT}), \tag{2.15}$$

where $\boldsymbol{\sigma}$ is a stress tensor; $\tilde{\mathbf{u}}$ is a suitably well-behaved test function defined over the domain Ω^F; $\tilde{\mathbf{u}}_{FI}$ and $\tilde{\mathbf{u}}_{FT}$ are the restriction of $\tilde{\mathbf{u}}$ on the interface S_{FI} and boundary S_{FT}, respectively; the integral operators are defined, with subscripts $P \in \{I, T\}$, by

$$\mathcal{K}_{FF}(\tilde{\mathbf{u}}, \boldsymbol{\sigma}) = \int_{\Omega^F} \tilde{\varepsilon}_{ij}(\mathbf{y})\sigma_{ij}(\mathbf{y})dV(\mathbf{y}), \tag{2.16}$$

$$\mathcal{F}_{FP}(\mathbf{X}, \mathbf{Y}) = \frac{1}{2}\int_{S_{FP}} X_i(\mathbf{y})Y_i(\mathbf{y})dS(\mathbf{y}), \tag{2.17}$$

in which $\tilde{\varepsilon}_{ij}(\mathbf{y})$ denotes the virtual strain tensor defined by $\tilde{\varepsilon}_{ij}(\mathbf{y}) = (\partial\tilde{u}_i/\partial y_j + \partial\tilde{u}_j/\partial y_i)/2$. Note again that a function form of the stress tensor in terms of the primary unknown depends primarily on a constitutive model employed. For a special case of the FEM-region being made of a homogeneous, linearly elastic material, the stress tensor can be expressed directly and explicitly in terms of elastic constants E_{ijkl} and the strain tensor $\boldsymbol{\varepsilon}$ (i.e., $\sigma_{ij} = E_{ijkl}\varepsilon_{kl}$), and, within the context of an infinitesimal deformation theory (i.e., $\varepsilon_{ij}(\mathbf{y}) = (\partial u_i/\partial y_j + \partial u_j/\partial y_i)/2$), the integral operator $\mathcal{K}_{FF}$ can be expressed directly in terms of the displacement $\mathbf{u}$ as

$$\mathcal{K}_{FF}(\tilde{\mathbf{u}}, \mathbf{u}) = \int_{\Omega^F} \tilde{u}_{i,j}(\mathbf{y})E_{ijkl}u_{k,l}(\mathbf{y})dV(\mathbf{y}). \tag{2.18}$$

It should be remarked that the factor of one half in the definition (2.17) has been introduced for convenience to cast this term in a form analogous to that for $\mathcal{F}_{BP}$ given by (2.13), and this, as a result, leads to the factor of two appearing on the right-hand side of (2.15). It is also worth noting that the first term on the right-hand side of (2.15) still contains the unknown traction on the interface $\mathbf{t}_{FI}$.

2.3. Governing Equations for Ω

A set of governing equations of the entire domain Ω can directly be obtained by combining a set of weakly singular, weak-form boundary integral equations (2.9) and the virtual work

equation (2.15). In particular, the last equations of (2.9) and (2.15) are properly combined, and this finally leads to

$$\begin{aligned}
\mathcal{A}_{CC}(\tilde{\mathbf{v}}, \Delta\mathbf{u}) + \mathcal{B}_{IC}(\mathbf{t}_{BI}, \tilde{\mathbf{v}}) + \mathcal{A}_{CI}(\tilde{\mathbf{v}}, \mathbf{u}_{BI}) &= -2\mathcal{F}_{BC}(\tilde{\mathbf{v}}, \mathbf{t}_C), \\
\mathcal{B}_{IC}\left(\tilde{\mathbf{t}}_{BI}, \Delta\mathbf{u}\right) + \mathcal{C}_{II}\left(\tilde{\mathbf{t}}_{BI}, \mathbf{t}_{BI}\right) + \mathcal{D}_{II}\left(\tilde{\mathbf{t}}_{BI}, \mathbf{u}_{BI}\right) &= 0, \\
\mathcal{A}_{IC}(\tilde{\mathbf{u}}_{BI}, \Delta\mathbf{u}) + \mathcal{D}_{II}(\mathbf{t}_{BI}, \tilde{\mathbf{u}}_{BI}) + \mathcal{A}_{II}(\tilde{\mathbf{u}}_{BI}, \mathbf{u}_{BI}) - \mathcal{K}_{FF}(\tilde{\mathbf{u}}, \sigma) &= \mathcal{E} - 2\mathcal{F}_{FT}(\tilde{\mathbf{u}}_{FT}, \mathbf{t}_{FT}),
\end{aligned} \tag{2.19}$$

where $\mathcal{E}$ is given by

$$\mathcal{E} = -2[\mathcal{F}_{BI}(\tilde{\mathbf{u}}_{BI}, \mathbf{t}_{BI}) + \mathcal{F}_{FI}(\tilde{\mathbf{u}}_{FI}, \mathbf{t}_{FI})]. \tag{2.20}$$

From the continuity of the traction and displacement across the interface of the BEM-region and FEM-region (i.e., $\mathbf{t}_{BI}(\mathbf{y}) + \mathbf{t}_{FI}(\mathbf{y}) = \mathbf{0}$ and $\mathbf{u}_{BI}(\mathbf{y}) = \mathbf{u}_{FI}(\mathbf{y})$ for all $\mathbf{y} \in S_I = S_{BI} = S_{FI}$), the test functions $\tilde{\mathbf{u}}_{BI}$ and $\tilde{\mathbf{u}}$ are chosen such that $\tilde{\mathbf{u}}_{BI}(\mathbf{y}) = \tilde{\mathbf{u}}_{FI}(\mathbf{y})$ for all $\mathbf{y} \in S_I = S_{BI} = S_{FI}$ and, as a direct consequence, $\mathcal{E}$ identically vanishes. It is therefore evident that the right-hand side of (2.19) involves only prescribed boundary data, and, in addition, if the integral operator $\mathcal{K}_{FF}$ possesses a symmetric form, (2.19) constitutes a symmetric formulation for the boundary value problem currently treated.

3. Numerical Implementation

This section briefly summarizes numerical procedures adopted to construct approximate solutions of a set of governing equations (2.19) and to postprocess certain quantities of interest. The discretization of the BEM-region and the FEM-region is first discussed. Then, components essential for numerical evaluation of weakly singular and nearly singular double-surface integrals, evaluations of kernels, and determination of general mixed-mode stress intensity factors are addressed. Finally, the key strategy for establishing the coupling between the in-house weakly singular SGBEM code and the reliable commercial finite element package is discussed.

3.1. Discretization

Standard Galerkin strategy is adopted to construct an approximate solution of the governing equation (2.19). For the BEM-region Ω^B, only the crack surface S_{BC} and the interface S_{BI} need to be discretized. In such discretization, standard isoparametric C^0 elements (e.g., 8-node quadrilateral and 6-node triangular elements) are employed throughout except along the crack front where special 9-node crack-tip elements are employed to accurately capture the asymptotic field near the singularity zone. Shape functions of these special elements are properly enriched by square root functions, and, in addition, extra degrees of freedom are introduced along the element boundary adjacent to the crack front to directly represent the gradient of the relative crack-face displacement [18, 21, 23]. These positive features also enable the calculation of the mixed-mode stress intensity factors (i.e., mode-I, mode-II, and mode-III stress intensity factors) in an accurate and efficient manner with

use of reasonably coarse meshes. For the FEM-region Ω^F, standard three-dimensional, isoparametric C^0 elements (e.g., ten-node tetrahedral elements, fifteen-node prism elements, and twenty-node brick elements) are utilized throughout in the domain discretization.

It is important to note that the BEM-region and the FEM-region are discretized such that meshes on the interface of the two regions conform (i.e., the two discretized interfaces are geometrically identical). A simple means to generate those conforming interfaces is to mesh the FEM-region first and then use its surface mesh as the interface mesh of the BEM-region. With this strategy, all nodal points on both discretized interfaces are essentially coincident. The key advantage of using conforming meshes is that the strong continuity of the displacement, the traction, and the test functions across the interface can be enforced exactly, and, as a result, the condition $\mathcal{E} = 0$ is also satisfied in the discretization level. It should be emphasized also that nodes on the interface of the BEM-region contain six degrees of freedom (i.e., three displacement degrees of freedom and three traction degrees of freedom) while nodes on the FEM-region contain only three displacement degrees of freedom.

3.2. Numerical Integration

For the FEM-region, all integrals arising from the discretization of the weak-form equation contain only regular integrands, and, as a result, they can be efficiently and accurately integrated by standard Gaussian quadrature. On the contrary, numerical evaluation of integrals arising from the discretization of the BEM-region is nontrivial since it involves the treatment of three types of double surface integrals (i.e., regular integrals, weakly singular integrals, and nearly singular integrals). The regular double surface integral arises when it involves a pair of remote outer and inner elements (i.e., the distance between any source and field points is relatively large when compared to the size of the two elements). This renders its integrand nonsingular and well-behaved and, as a result, allows the integral to be accurately and efficiently integrated by standard Gaussian quadrature.

The weakly singular double surface integral arises when the outer surface of integration is the same as the inner surface. For this particular case, the source and field points can be identical and this renders the integrand singular of order $1/r$. While the integral of this type exists in an ordinary sense, it was pointed out by Xiao [16] that the numerical integration by Gaussian quadrature becomes computationally inefficient and such inaccurate evaluation can significantly pollute the quality of approximate solutions. To circumvent this situation, a series of transformations such as a well-known triangular polar transformation and a logarithmic transformation is applied first both to remove the singularity and to regularize the rapid variation of the integrand. The final integral contains a nonsingular integrand well suited to be integrated by Gaussian quadrature. Details of this numerical quadrature can be found in [16, 39, 40].

The most challenging task is to compute nearly singular integrals involving relatively close or adjacent inner and outer elements. Although the integrand is not singular, it exhibits rapid variation in the zone where both source and field points are nearly identical. Such complex behavior of the integrand was found very difficult and inefficient to be treated by standard Gaussian quadrature [16]. To improve the accuracy of such quadrature, the triangular polar transformation is applied first and then a series of logarithmic transformations is adopted for both radial and angular directions to further regularize the rapid variation integrand. The resulting integral was found well-suited for being integrated by standard Gaussian quadrature [16, 40–42].

3.3. Evaluation of Kernels

To further reduce the computational cost required to form the coefficient matrix contributed from the BEM-region, all involved kernels $n_i(\boldsymbol{\xi})H^p_{ij}(\boldsymbol{\xi}-\mathbf{y})$, $n_i(\mathbf{y})H^p_{ij}(\boldsymbol{\xi}-\mathbf{y})$, $U^p_i(\boldsymbol{\xi}-\mathbf{y})$, $G^p_{mj}(\boldsymbol{\xi}-\mathbf{y})$, $C^{tk}_{mj}(\boldsymbol{\xi}-\mathbf{y})$ must be evaluated in an efficient manner for any pair of source and field points $\{\boldsymbol{\xi},\mathbf{y}\}$. For the first two kernels $n_i(\boldsymbol{\xi})H^p_{ij}(\boldsymbol{\xi}-\mathbf{y})$ and $n_i(\mathbf{y})H^p_{ij}(\boldsymbol{\xi}-\mathbf{y})$, they only involve the calculation of a unit normal vector $\mathbf{n}$ and the elementary function H^p_{ij}. As a result, this task can readily be achieved via a standard procedure. For the last three kernels, the computational cost is significantly different for isotropic and anisotropic materials. For isotropic materials, such kernels only involve elementary functions and can therefore be evaluated in a straightforward fashion. On the contrary, the kernels $U^p_i(\boldsymbol{\xi}-\mathbf{y})$, $G^p_{mj}(\boldsymbol{\xi}-\mathbf{y})$, and $C^{tk}_{mj}(\boldsymbol{\xi}-\mathbf{y})$ for general anisotropy are expressed in terms of a line integral over a unit circle (see (2.4)–(2.6), and (2.8)). Direct evaluation of such line integral for every pair of points $(\boldsymbol{\xi},\mathbf{y})$ arising from the numerical integration is obviously computationally expensive. To avoid this massive computation, a well-known interpolation technique (e.g., [21, 23, 36]) is adopted to approximate values of those kernels. Specifically, the interpolant of each kernel is formed based on a two-dimensional grid using standard quadratic shape functions. Values of kernels at all grid points are obtained by performing direct numerical integration of the line integral (2.8) via Gaussian quadrature and then using the relations (2.4)–(2.6). The accuracy of such approximation can readily be controlled by refining the interpolation grid.

3.4. Determination of Stress Intensity Factors

Stress intensity factors play an important role in linear elastic fracture mechanics in the prediction of crack growth initiation and propagation direction and also in the fatigue-life assessment. This fracture data provides a complete measure of the dominant behavior of the stress field in a local region surrounding the crack front. To obtain highly accurate stress intensity factors, we supply the developed coupling technique with two crucial components, one associated with the use of special crack-tip elements to accurately capture the near-tip field and the other corresponding to the use of an explicit formula to extract such fracture data. The latter feature is a direct consequence of the extra degrees of freedom being introduced along the crack front to represent the gradient of relative crack-face displacement. Once a discretized system of algebraic equations is solved, nodal quantities along the crack front are extracted and then postprocessed to obtain the stress intensity factors.

An explicit expression for the mixed-mode stress intensity factors in terms of nodal data along the crack front, local geometry of the crack front, and material properties can be found in the work of Li et al. [18] for cracks in isotropic media and Rungamornrat and Mear [23, 36] for cracks in general anisotropic media. In the current investigation, both formulae are implemented.

3.5. Coupling of SGBEM and Commercial FE Package

To further enhance the modeling capability, the weakly singular SGBEM can be coupled with a reliable commercial finite element code that supports user-defined subroutines. The key objective is to exploit available vast features of such FE package (e.g., mesh generation, user-defined elements, powerful linear and nonlinear solvers, and various material models, etc.) to treat a complex, localized FEM-region and utilize the SGBEM in-house code to supply

information associated with the majority of the domain that is unbounded and possibly contains isolated discontinuities.

In the coupling procedure, the governing equation for the BEM-region is first discretized into a system of linear algebraic equations. The corresponding coefficient matrix and the vector involving the prescribed data are constructed using the in-house code, and they can be viewed as a stiffness matrix and a load vector of a "super element" containing all degrees of freedom of the BEM-region. This piece of information is then imported into the commercial FE package via a user-defined subroutine channel and then assembled with element stiffness matrices contributed from the discretized FEM-region. Since meshes of both interfaces (one associated with the BEM-region and the other corresponding to the FEM-region) are conforming, the assembly procedure can readily be achieved by using a proper numbering strategy. Specifically, nodes on the interface of the BEM-region are named identical to nodes on the interface of the FEM-region (associated with the same displacement degrees of freedom). It is important to emphasize that all interface nodes of the BEM-region possess six degrees of freedom (i.e., three displacement degrees of freedom and three traction degrees of freedom) but there are only three (displacement) degrees of freedom per interface node of the FEM-region. To overcome such situation, each interface node of the BEM-region is fictitiously treated as double nodes where the first node is chosen to represent the displacement degrees of freedom and is numbered in the same way as its coincident interface node of the FEM-region whereas the second node is chosen with different name to represent the traction degrees of freedom. With this particular scheme, the assembling procedure follows naturally that for a standard finite element technique.

Once the coupling analysis is complete, nodal quantities associated with the BEM-region are extracted from the output file generated by the FE package and then postprocessed for quantities of interest. For instance, the displacement and stress within the BEM-region can readily be computed from the standard displacement and stress boundary integral relations [17, 22], and the stress intensity factors can be calculated using an explicit expression proposed in [18, 23].

4. Numerical Results and Discussion

As a means to verify both the formulation and the numerical implementations, we first carry out numerical experiments on boundary value problems in which the analytical solution exists. In the analysis, a series of meshes is adopted in order to investigate both the convergence and accuracy of the numerical solutions. Once the method is tested, it is then applied to solve more complex boundary value problems in order to demonstrate its capability and robustness. For brevity of the presentation, a selected set of results are reported and discussed as follows.

4.1. Isolated Spherical Void under Uniform Pressure

Consider an isolated spherical void of radius a embedded in a three-dimensional infinite medium as shown schematically in Figure 2(a). The void is subjected to uniform pressure σ_0. In the analysis, two constitutive models are investigated: one associated with an isotropic, linearly elastic material with Young's modulus E and Poisson ratio $\nu = 0.3$ and the other chosen to represent an isotropic hardening material obeying J_2-flow theory of plasticity [43].

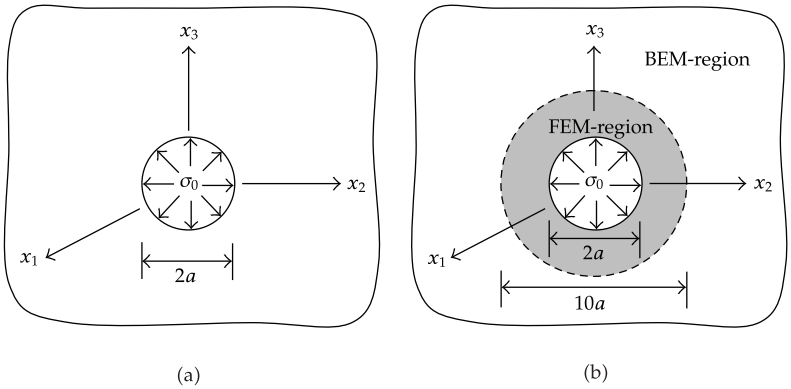

Figure 2: (a) Schematic of three-dimensional infinite medium containing spherical void and (b) schematic of BEM-region and FEM-region.

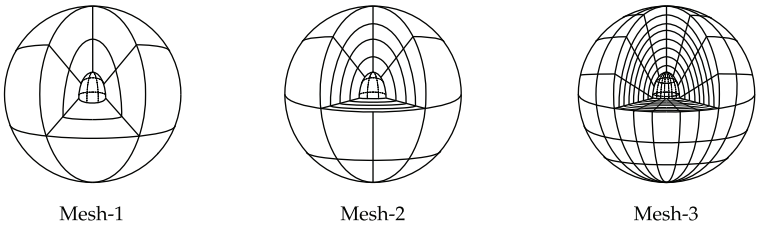

Figure 3: Three meshes adopted in the analysis for FEM-region; meshes for BEM-region are identical to the interface mesh of FEM-region.

For the latter material, the uniaxial stress-strain relation is assumed in a bilinear form with E_1 and E_2 denoting the modulus in the elastic regime and the modulus of the hardening zone, respectively, and σ_y and ε_y denoting the initial yielding stress and its corresponding strain, respectively.

To test the coupling technique, we first decompose the body into two regions by a fictitious spherical surface of radius $5a$ and centered at the origin as shown by a dashed line in Figure 2(b). It is important to remark that such a surface must be chosen relatively large compared to the void to ensure that the inelastic zone that may exist (for the second constitutive model) is fully contained in the FEM-region. In the experiments, three different meshes are adopted as shown in Figure 3. Although meshes for the BEM-region are not shown, they can simply obtain from the interface meshes of the FEM-region. As clearly illustrated in the figure, mesh-1, mesh-2, and mesh-3 consist of 12, 32, 144 boundary elements and 24, 128, 1152 finite elements, respectively.

4.1.1. Results for Isotropic Linearly Elastic Material

For linear elasticity, this particular boundary value problem admits the closed form solution (e.g., [44]). Since the problem is spherically symmetric, only the radial displacement u_r and the normal stress components $\{\sigma_{rr}, \sigma_{\theta\theta}, \sigma_{\phi\phi}\}$ are nonzero and they are given explicitly by

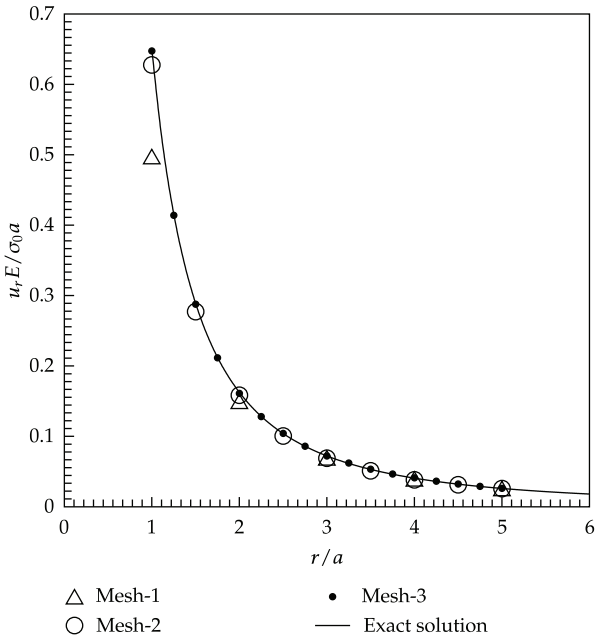

Figure 4: Normalized radial displacement versus normalized radial coordinate for isotropic, linearly elastic material with $\nu = 0.3$.

(note that these quantities are referred to a standard spherical coordinate system $\{r, \theta, \phi\}$ with its origin located at the center of the void)

$$u_r(r) = \frac{1+\nu}{2E}\sigma_0 \frac{a^3}{r^2}, \tag{4.1}$$

$$\sigma_{rr}(r) = -2\sigma_{\theta\theta}(r) = -2\sigma_{\phi\phi}(r) = -\sigma_0 \left(\frac{a}{r}\right)^3. \tag{4.2}$$

This analytical solution is employed as a means to validate the proposed formulation and the numerical implementation. Numerical solutions for the radial displacement obtained from the three meshes are reported and compared with the exact solution in Figure 4. As evident from this set of results, the radial displacements obtained from the mesh-2 and the mesh-3 are highly accurate with only slight difference from the exact solution while that obtained from the mesh-1 is reasonably accurate except in the region very near the surface of the void. The discrepancy of solutions observed in the mesh-1 is due to that the level of refinement is too coarse to accurately capture the geometry and responses in the local region near the surface of the void.

We further investigate the quality of numerical solutions for stresses. Since all nonzero stress components are related by (4.2), only results for the radial stress component are reported. Figure 5 shows the normalized radial stress obtained from the three meshes and the exact solution versus the normalized radial coordinate. It is observed that the mesh-3 yields results that are almost indistinguishable from the exact solution, whereas the mesh-1 and mesh-2 give accurate results for relatively large r, and the level of accuracy

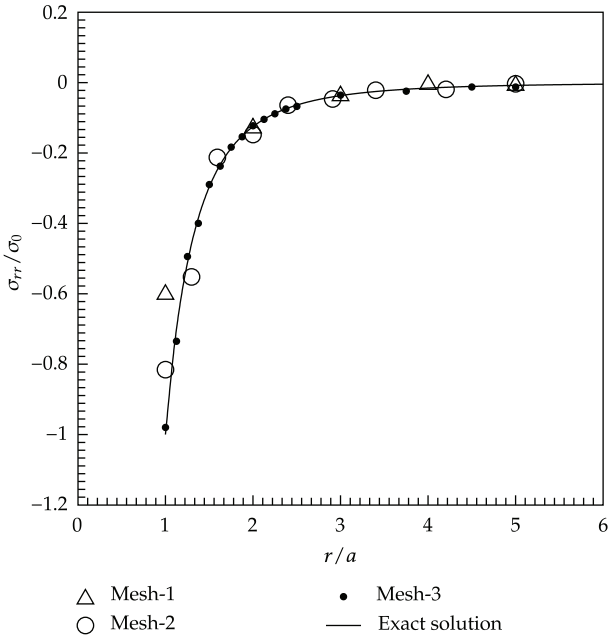

Figure 5: Normalized radial stress versus normalized radial coordinate for isotropic, linearly elastic material with $\nu = 0.3$.

decreases as the distance r approaches a. It is noted by passing that the degeneracy of the accuracy in computing stress is common in a standard, displacement-based, finite element technique.

To demonstrate the important role of the SGBEM in the treatment of an unbounded part of the domain instead of truncating the body as practically employed in the finite element modeling, we perform another FE analysis of the FEM-region alone without coupling with the BEM-region but imposing zero displacement condition at its interface. The radial displacement and the radial stress obtained for this particular case using the mesh-3 are reported along with the exact solution and those obtained from the coupling technique in Figures 6 and 7, respectively. As evident from these results, numerical solutions obtained from the FEM with a domain truncation strategy deviate from the exact solution as approaching the truncation surface while the proposed technique yields almost identical results to the exact solution. The concept of domain truncation to obtain a finite body is simple, but it still remains to choose a proper truncation surface and boundary conditions to be imposed on that surface to mimic the original boundary value problem. This coupling technique provides an alternative to treat the whole domain without any truncation and difficulty to treat the remote boundary.

4.1.2. Isotropic Hardening Material

For this particular case, we focus attention to the material with no hardening modulus (i.e., $E_2 = 0$) since the corresponding boundary value problem admits the closed form solution. For a sufficiently high applied pressure σ_0, a layer close to the boundary of the void becomes inelastic and the size of such inelastic zone (measured by the radius r_0) becomes larger as

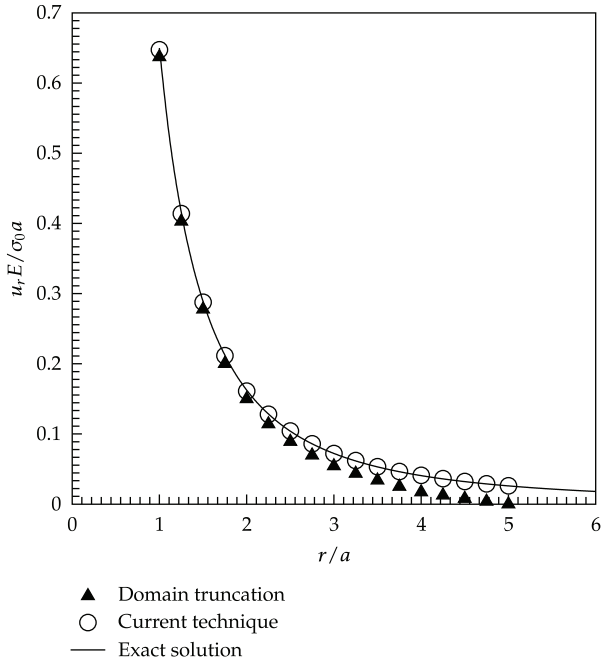

Figure 6: Normalized radial displacement versus normalized radial coordinate for isotropic, linearly elastic material with $\nu = 0.3$. Results are obtained from mesh-3 for both the coupling technique and the FEM with domain truncation.

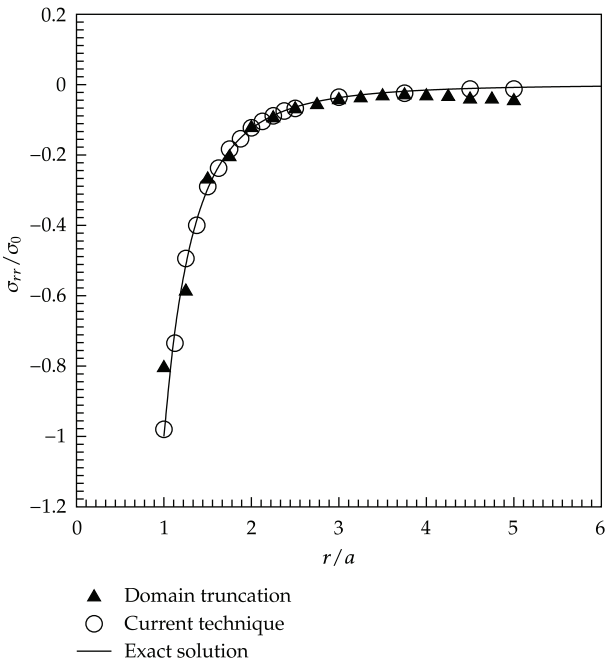

Figure 7: Normalized radial stress versus normalized radial coordinate for isotropic, linearly elastic material with $\nu = 0.3$. Results are obtained from mesh-3 for both the coupling technique and the FEM with domain truncation.

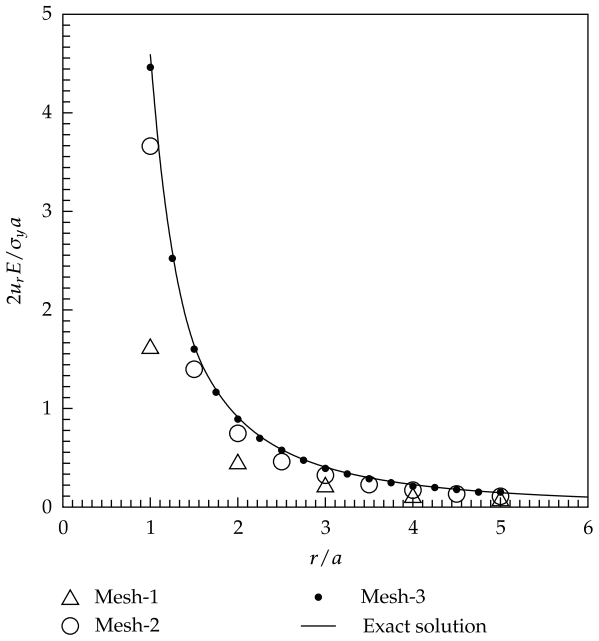

Figure 8: Normalized radial displacement versus normalized radial coordinate for isotropic hardening material with $E_2 = 0$.

σ_0 increases. By incorporating J_2-flow theory of plasticity and spherical symmetry, the radial displacement and the radial stress can be obtained exactly as given below:

$$u_r(r) = \begin{cases} \dfrac{1-2\nu}{E}\left\{2\sigma_y \ln\left(\dfrac{r}{a}\right) - \sigma_0\right\} r + \dfrac{1-\nu}{E}\sigma_y \left(\dfrac{r_0^3}{r^2}\right), & r < r_0, \\ \dfrac{\sigma_y(1+\nu)}{3E}\left(\dfrac{r_0^3}{r^2}\right), & r \geq r_0, \end{cases}$$

$$\sigma_{rr}(r) = \begin{cases} 2\sigma_y \ln\left(\dfrac{r}{a}\right) - \sigma_0, & r < r_0, \\ -\dfrac{2\sigma_y}{3}\left(\dfrac{r_0}{r}\right)^3, & r \geq r_0, \end{cases} \tag{4.3}$$

where the Poisson ratio ν is taken to be 0.3 and $r_0 = ae^{((\sigma_0/2\sigma_y)-(1/3))}$ is the radius of an inelastic zone.

In the analysis, the pressure $\sigma_0 = 1.625\sigma_y$ is chosen to ensure that the medium contains an inelastic zone; in fact, this selected applied pressure corresponds to $r_0 = 1.615a$. Numerical results obtained from the current technique are reported along with the exact solution in Figure 8 for the normalized radial displacement and in Figure 9 for the normalized radial stress. It can be concluded from computed solutions that they finally converge to the exact solution as the mesh is refined. In particular, results obtained from the mesh-3 are nearly indistinguishable from the benchmark solution. It should be pointed out that results obtained from the same level of mesh refinement for this particular case are less accurate than those

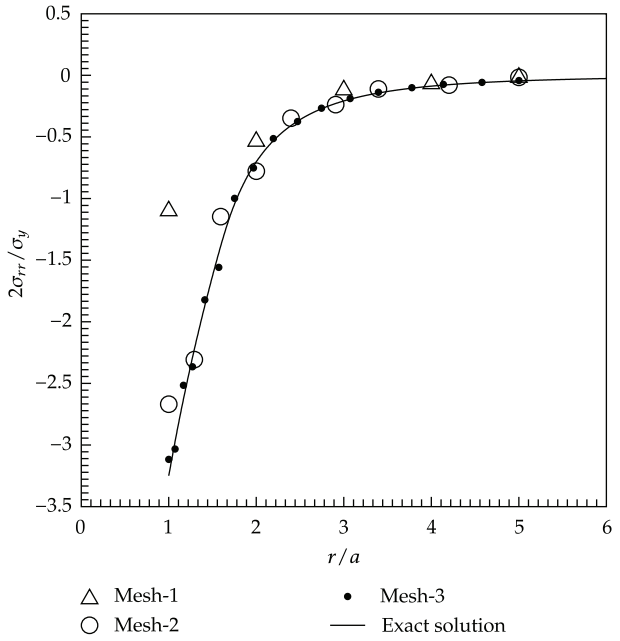

Figure 9: Normalized radial stress versus normalized radial coordinate for isotropic hardening material with $E_2 = 0$.

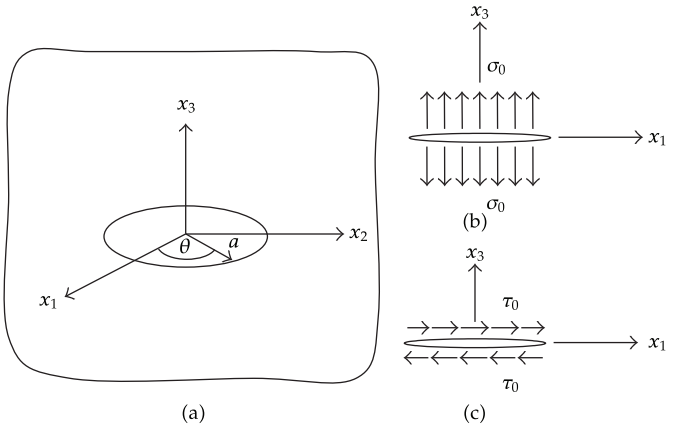

Figure 10: (a) Schematic of infinite medium containing penny-shaped crack, (b) crack under uniform normal traction σ_0, and (c) crack under uniform shear traction τ_0.

obtained for the linear elastic case. This is due to the complexity posed by the presence of an inelastic zone near the surface of the void, and, in order to capture this behavior accurately, it requires sufficiently fine meshes.

4.2. Isolated Penny-Shaped Crack in Infinite Medium

Consider, next, a penny-shaped crack of radius a which is embedded in a linearly elastic, infinite medium as shown schematically in Figure 10(a). The body is made of either an

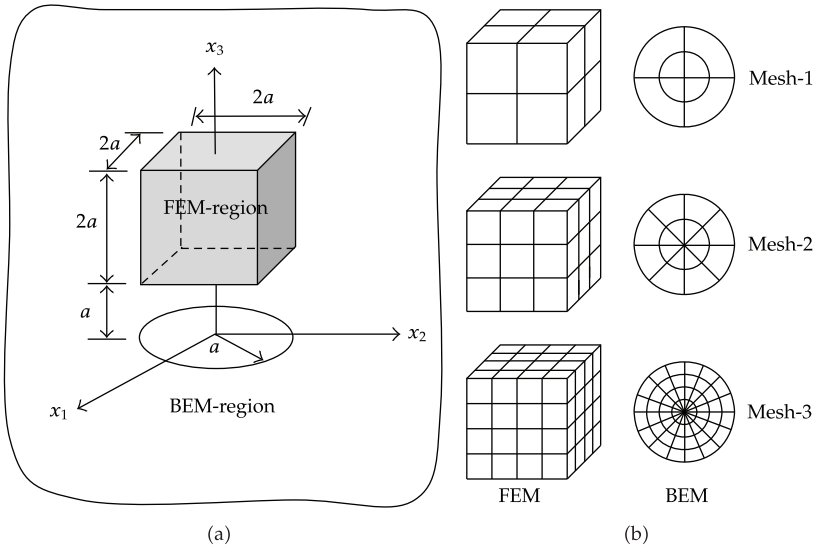

Figure 11: (a) Schematic of selected FEM-region and the remaining BEM-region and (b) three meshes adopted in the analysis.

Table 1: Nonzero elastic constants for zinc and graphite-reinforced composite (where axis of material symmetry is taken to direct along the x_3-coordinate direction).

Nonzero elastic constants	($\times 10^6$) psi	
	Zinc	Graphite-reinforced composite
E_{1111}	16.09	14.683
E_{1122}	3.35	6.986
E_{1133}	5.01	5.689
E_{3333}	6.10	144.762
E_{1313}	3.83	4.050

isotropic material with Poisson's ratio $\nu = 0.3$ or zinc and graphite-reinforced composite. The last two materials are transversely isotropic with the axis of material symmetry directing along the x_3-axis, and their elastic constants are given in Table 1. The crack is subjected to two types of traction boundary conditions: the uniform normal traction σ_0 (i.e., $t_1 = t_2 = 0,\ t_3 = \sigma_0$) as shown in Figure 10(b) and the uniform shear traction τ_0 along the x_1-axis (i.e., $t_1 = \tau_0,\ t_2 = t_3 = 0$) as shown in Figure 10(c).

The first loading condition gives rise to a pure opening-mode problem with the mode-I stress intensity factor along the crack front being constant and independent of material properties, while the second loading condition yields nonzero mode-II and mode-III stress intensity factors that vary along the crack front. The analytical solutions for both cases can be found in the work of Fabrikant [4]. As a means to verify the coupling formulation and implementation, we choose the FEM-region to be a cube of dimensions $2a \times 2a \times 2a$ centered at $(0,\ 0,\ 2a)$ as illustrated in Figure 11(a). In the analysis, we generate three meshes for both the crack surface and the FEM-region as shown in Figure 11(b).

For the first loading condition, numerical solutions for the mode-I stress intensity factor normalized by the exact solution are reported in Table 2 for all three materials. Clearly

Table 2: Normalized mode-I stress intensity factor for isolated penny-shaped crack subjected to uniform normal traction.

Mesh	Isotropic material, $K_1/K_{1,\text{ exact}}$		Transversely isotropic material, $K_1/K_{1,\text{exact}}$			
			Zinc		Graphite-reinforced composite	
	$\theta^\circ = 0$	$\theta^\circ = 90$	$\theta^\circ = 0$	$\theta^\circ = 90$	$\theta^\circ = 0$	$\theta^\circ = 90$
1	0.9919	0.9920	0.9890	0.9890	0.9841	0.9841
2	1.0008	1.0008	1.0001	1.0001	1.0053	1.0053
3	1.0002	1.0002	1.0004	1.0004	1.0006	1.0001

from these results, the current technique yields highly accurate stress intensity factors with error less than 1.6%, 0.6%, and 0.1% for mesh-1, mesh-2, and mesh-3, respectively. The weak dependence of numerical solutions on the level of mesh refinement is due mainly to the use of special crack-tip elements to model the near-tip field and directly capture the gradient of relative crack-face displacement along the crack front. Relatively coarse meshes can therefore be employed in the analysis to obtain sufficiently accurate stress intensity factors.

For the second loading condition, the normalized mode-II and mode-III stress intensity factors (K_2 and K_3) are shown in Figure 12 for isotropic material, zinc and graphite-reinforced composite. Based on this set of results, it can be concluded again that numerical solutions obtained from the three meshes are in excellent agreement with the exact solution; in particular, a coarse mesh also yields results of high accuracy. It should also be remarked that for this particular loading condition, the material anisotropy plays a significant role on values of the mixed-mode stress intensity factors.

4.3. *Infinite Medium Containing Both Penny-Shaped Crack and Spherical Void*

As a final example, we choose to test the proposed technique by solving a more complex boundary value problem in order to demonstrate its capability. Let us consider an infinite medium containing a spherical void of radius a and a penny-shaped crack of the same radius as shown schematically in Figure 13. The medium is subjected to uniform pressure σ_0 on the surface of the void, whereas the entire surface of the crack is traction-free. In the analysis, two constitutive models are investigated: one associated with an isotropic, linearly elastic material with Young's modulus E and Poisson ratio $\nu = 0.3$ and the other corresponding to an isotropic hardening material with the bilinear uniaxial stress-strain relation similar to that employed in Section 4.1. The primary quantity to be sought is the mode-I stress intensity factor along the crack front induced by the application of the pressure to the void. In addition, influence of an inelastic zone induced in the high-load-intensity region on such fracture data is also of interest.

In the modeling, we first decompose the medium into the FEM-region and the BEM-region using a fictitious spherical surface of radius $4a$ centered at the same location as that of the void as shown in Figure 14(a). Three meshes are adopted in numerical experiments as shown in Figure 14(b). In particular, the FEM-region, the interface, and the crack surface consist of {24, 12, 8}, {128, 32, 16}, and {1024, 128, 64} elements for mesh-1, mesh-2, and mesh-3, respectively. It should be noted also that the mesh-1 is obviously very coarse; in particular, only eight elements are utilized to discretize the entire crack surface and only four relatively large crack-tip elements are used along the crack front.

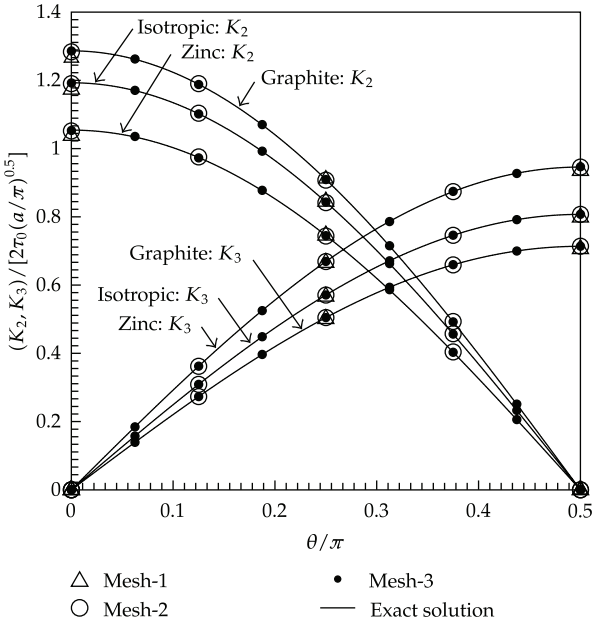

Figure 12: Normalized mode-II and mode-III stress intensity factors for isolated penny-shaped crack subjected to shear traction. Results are reported for isotropic material with $\nu = 0.3$, zinc and graphite-reinforced composite.

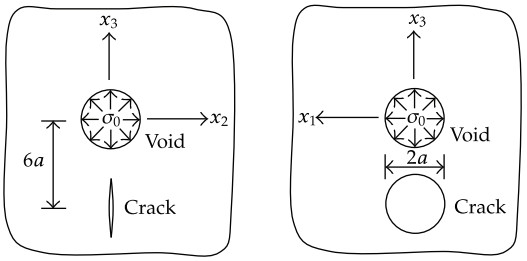

Figure 13: Schematic of infinite medium containing spherical void of radius a and penny-shaped crack of radius a and subjected to uniform pressure at surface of void.

First, the analysis is carried out for the elastic material with Poisson ratio $\nu = 0.3$, and the computed mode-I stress intensity factors are normalized and then reported as a function of angular position along the crack front for all three meshes in Figure 15. This set of results implies that the obtained numerical solutions exhibit good convergence; in particular, results obtained from the mesh-2 and mesh-3 are of comparable quality while results obtained from the mesh-1 still deviate from the converged solution. As confirmed by this convergence study, only the mesh-3 is used to generate other sets of useful results.

Next, we consider a medium made of an isotropic hardening material. In the analysis, we choose the modulus $E_1 = E$ and Poisson ratio $\nu = 0.3$ for the linear regime and choose either $E_2 = E/3$ or $E_2 = 0$ for the hardening regime. With this set of material parameters, the behavior in the linear regime (for a small level of applied pressure) is identical to that obtained in the previous case. To investigate the influence of the inelastic zone induced near

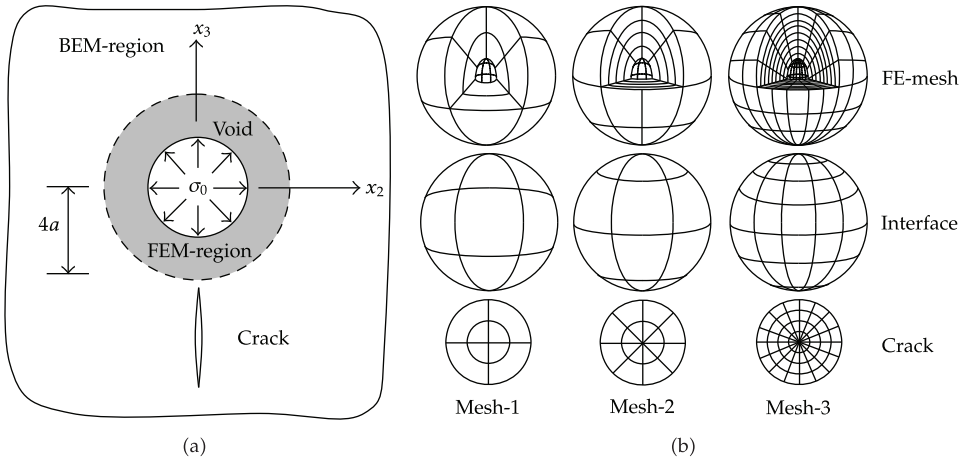

Figure 14: (a) Decomposition of domain into BEM-region and FEM-region by a fictitious spherical surface of radius $4a$ and (b) three meshes adopted in analysis.

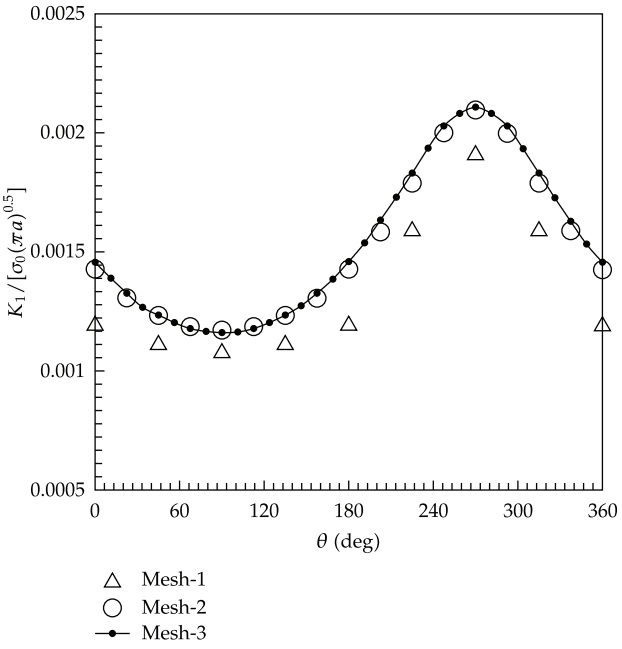

Figure 15: Normalized mode-I stress intensity factors of penny-shaped crack embedded within infinite medium containing spherical void under uniform pressure. Results are reported for isotropic linearly elastic material with $\nu = 0.3$.

the surface of the void on the stress intensity factor along the crack front, we carry out various experiments by varying the applied pressure σ_0. The distribution of the stress intensity factor along the crack front is reported in Figure 16 for a hardening material with $E_1 = E$ and $E_2 = E/3$ under five levels of the applied pressure $\sigma_0 \in \{0.25\sigma_y, 1.00\sigma_y, 1.25\sigma_y, 1.50\sigma_y, 1.75\sigma_y\}$. The body is entirely elastic at $\sigma_0 = 0.25\sigma_y$, slightly passes the initial yielding at $\sigma_0 = 1.00\sigma_y$, and possesses a larger inelastic zone as the pressure increases further. It is obvious from Figure 16

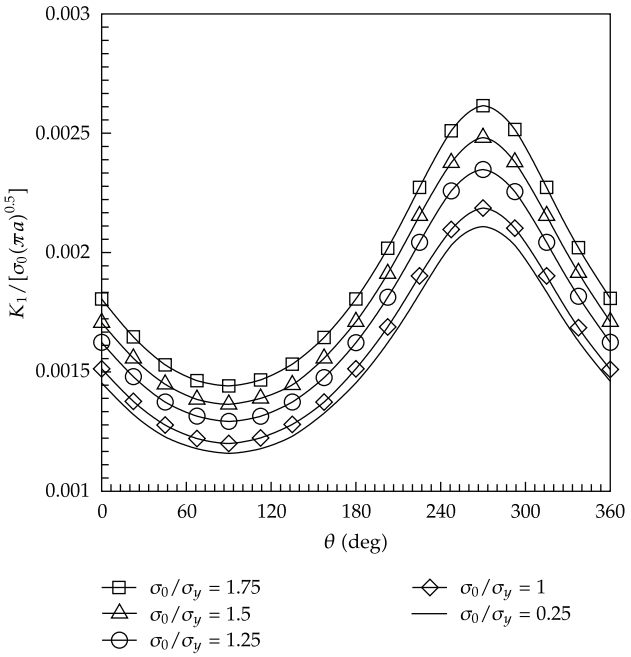

Figure 16: Normalized mode-I stress intensity factor of penny-shaped crack embedded within infinite medium containing spherical void under uniform pressure. Results are reported for isotropic hardening material with $E_1 = E$ and $E_2 = E/3$.

that the presence of an elastic zone significantly alters the normalized values of the stress intensity factor from the linear elastic solution and such discrepancy becomes more apparent as the level of applied pressure increases. The localized inelastic zone acts as a stress riser, that is, it produces the stress field of higher intensity around the crack, and this therefore yields the higher normalized stress intensity factor when compared with the linear elastic case. Figure 17 shows an additional plot between the maximum normalized stress intensity factors versus the normalized applied pressure for both an isotropic linearly elastic material and two isotropic hardening materials (associated with $E_2 = 0$ and $E_2 = E/3$). Results for both materials are identical for a low level of the applied pressure (since the entire body is still elastic), and, for a higher level of the applied pressure, the maximum stress intensity factor for the case of the hardening material is significantly larger than that for the linear elastic material. In addition, such discrepancy tends to increase as the hardening modulus decreases.

5. Conclusions and Remarks

The coupling procedure between a standard finite element method (FEM) and a weakly singular, symmetric Galerkin boundary element method (SGBEM) has been successfully established for stress analysis of a three-dimensional infinite medium. The proposed technique has exploited the positive features of both the FEM and the SGBEM to enhance the modeling capability. The vast and very general features of the FEM have been employed as a basis to treat a localized region that may embed a zone exhibiting complex behavior, whereas the SGBEM has been used specifically to model the majority of the medium that is unbounded and possibly contains the surface of displacement discontinuities such as cracks

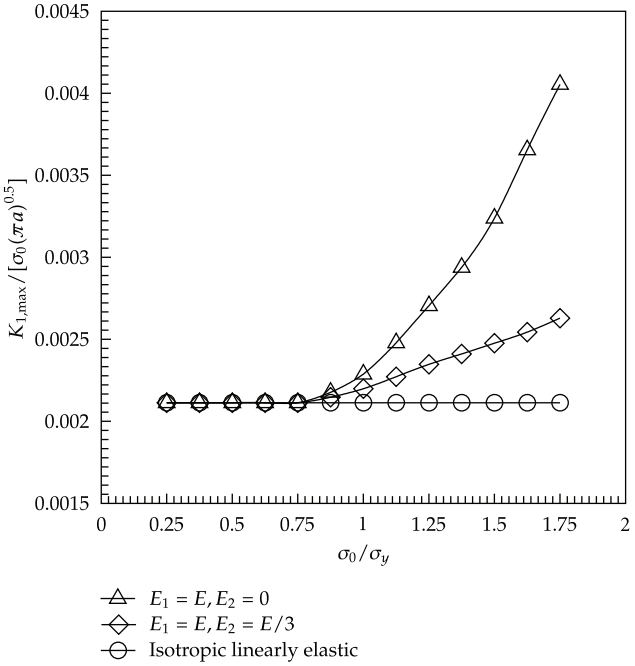

Figure 17: Maximum normalized mode-I stress intensity factor versus applied pressure at surface of void. Results are reported for isotropic linearly elastic material with $\nu = 0.3$ and two isotropic hardening materials.

and dislocations. The coupling formulation has been based primarily on the domain decomposition technique along with the proper enforcement of continuity of the displacement and traction on the interface of the two regions (one modeled by the SGBEM and the other by the FEM) to form the coupling equations. For the FEM subdomain, the key formulation follows directly the well-known principle of virtual work, whereas, for the SGBEM subdomain, the governing equation is formulated based on a pair of weakly singular, weak-form boundary integral equations for the displacement and traction. The advantage of using the weakly singular integral equations is associated with the permission to apply a space of continuous interpolation functions in the discretization of primary unknowns on the SGBEM subdomain.

In the numerical implementation, various aspects have been considered in order to enhance the accuracy and computational efficiency of the coupling technique. For instance, special crack-tip elements have been employed to better approximate the near-tip field. Shape functions of these special elements have properly been enriched by a square root function such that the resulting interpolation functions can capture the relative crack-face displacement with sufficiently high level of accuracy. As a direct consequence, it allows relatively large crack-tip elements to be employed along the crack front while still yielding very accurate stress intensity factors. Another important consideration is the use of an interpolation strategy to approximate values of kernels for generally anisotropic materials; this substantially reduces the computational cost associated with the direct evaluation of the line integral. Finally, special numerical quadratures have been adopted to efficiently evaluate both the weakly singular and nearly singular double surface integrals. To demonstrate and gain an insight into the coupling strategy, the formulation has been implemented first in terms of an in-house computer code for linear elasticity boundary value problems. Subsequently,

the weakly singular SGBEM has successfully been coupled with a reliable commercial finite element package in order to exploit its rich features to model more complex localized region such as inelastic zones and inhomogeneities. As indicated by results from extensive numerical experiments, the current technique has been found promising and, in particular, numerical solutions exhibit good convergence and weak dependence on the level of mesh refinement.

As a final remark, while the developed technique is still restricted to an infinite domain and to conforming interfaces, it offers insight into the SGBEM-FEM coupling strategy in terms of the formulation, the implementation procedure, and its performance. This coupling strategy can directly be generalized to solve more practical boundary value problems involving a half space, for example, cracks and localized complex zone near the free surface. Another crucial extension is to enhance the feature of the current technique by using the weak enforcement of continuity across the interface. This will supply the flexibility of mesh generation.

Acknowledgments

The first author gratefully acknowledges financial supports provided by "Chulalongkorn University for development of new faculty staff" and "Stimulus Package 2 (SP2) of Ministry of Education under the theme of Green Engineering for Green Society."

References

[1] S. Timoshenko and N. Goodier, *The Theory of Elasticity*, McGraw-Hill, New York, NY, USA, 2nd edition, 1951.

[2] I. N. Sneddon, *Fourier Transform*, McGraw-Hill, New York, NY, USA, 1951.

[3] I. N. Sneddon, *Mixed Boundary Value Problems in Potential Theory*, John Wiley & Sons, New York, NY, USA, 1965.

[4] V. I. Fabrikant, *Applications of Potential Theory in Mechanics: A Selection of New Results*, vol. 51 of *Mathematics and Its Applications*, Kluwer Academic Publishers, Dordrecht, The Netherlands, 1989.

[5] V. I. Fabrikant, *Mixed Boundary Value Problems of Potential Theory and Their Applications in Engineering*, vol. 68 of *Mathematics and Its Applications*, Kluwer Academic Publishers, Dordrecht, The Netherlands, 1991.

[6] J. T. Oden and G. F. Carey, *Finite Elements: Special Problems in Solid Mechanics*, vol. 5, Prentice-Hall, Englewood Cliffs, NJ, USA, 1984.

[7] T. J. R. Hughes, *The Finite Element Method: Linear Static and Dynamic Finite Element Analysis*, Dover Publications, Mineola, NY, USA, 2000.

[8] O. C. Zienkiewicz and R. L. Taylor, *The Finite Element Method: Solid Mechanics*, vol. 2, Butterworth-Heinemann, Oxford, UK, 5th edition, 2000.

[9] D. V. Swenson and A. R. Ingraffea, "Modeling mixed-mode dynamic crack propagation nsing finite elements: theory and applications," *Computational Mechanics*, vol. 3, no. 6, pp. 381–397, 1988.

[10] L. F. Martha, P. A. Wawrzynek, and A. R. Ingraffea, "Arbitrary crack representation using solid modeling," *Engineering with Computers*, vol. 9, no. 2, pp. 63–82, 1993.

[11] A. O. Ayhan, A. C. Kaya, J. Laflen, R. D. McClain, and D. Slavik, "Fracture analysis of cracks in orthotropic materials using ANSYS," Tech. Rep. GRC370, GEGlobal Research, General Electric Company, 2003.

[12] T. A. Cruse, *Boundary Element Analysis in Computational Fracture Mechanics*, vol. 1 of *Mechanics: Computational Mechanics*, Kluwer Academic Publishers, Dordrecht, The Netherlands, 1988.

[13] C. A. Brebbia and J. Dominguez, *Boundary Elements: An Introductory Course*, McGraw-Hill, New York, NY, USA, 1989.

[14] G. Xu and M. Ortiz, "A variational boundary integral method for the analysis of 3-D cracks of arbitrary geometry modelled as continuous distributions of dislocation loops," *International Journal for Numerical Methods in Engineering*, vol. 36, no. 21, pp. 3675–3701, 1993.

[15] M. Bonnet, "Regularized direct and indirect symmetric variational BIE formulations for three-dimensional elasticity," *Engineering Analysis with Boundary Elements*, vol. 15, no. 1, pp. 93–102, 1995.
[16] L. Xiao, *Symmetric weak-form integral equation method for three-dimensional fracture analysis*, Ph.D. Dissertation, University of Texas at Austin, Austin, Tex, USA, 1998.
[17] S. Li and M. E. Mear, "Singularity-reduced integral equations for displacement discontinuities in three-dimensional linear elastic media," *International Journal of Fracture*, vol. 93, no. 1–4, pp. 87–114, 1998.
[18] S. Li, M. E. Mear, and L. Xiao, "Symmetric weak-form integral equation method for three-dimensional fracture analysis," *Computer Methods in Applied Mechanics and Engineering*, vol. 151, no. 3-4, pp. 435–459, 1998.
[19] G. Xu, "A variational boundary integral method for the analysis of three-dimensional cracks of arbitrary geometry in anisotropic elastic solids," *Journal of Applied Mechanics*, vol. 67, no. 2, pp. 403–408, 2000.
[20] A. Frangi, G. Novati, R. Springhetti, and M. Rovizzi, "3D fracture analysis by the symmetric Galerkin BEM," *Computational Mechanics*, vol. 28, no. 3-4, pp. 220–232, 2002.
[21] J. Rungamornrat, "Analysis of 3D cracks in anisotropic multi-material domain with weakly singular SGBEM," *Engineering Analysis with Boundary Elements*, vol. 30, no. 10, pp. 834–846, 2006.
[22] J. Rungamornrat and M. E. Mear, "Weakly-singular, weak-form integral equations for cracks in three-dimensional anisotropic media," *International Journal of Solids and Structures*, vol. 45, no. 5, pp. 1283–1301, 2008.
[23] J. Rungamornrat and M. E. Mear, "A weakly-singular SGBEM for analysis of cracks in 3D anisotropic media," *Computer Methods in Applied Mechanics and Engineering*, vol. 197, no. 49-50, pp. 4319–4332, 2008.
[24] E. Schnack and K. Türke, "Domain decomposition with BEM and FEM," *International Journal for Numerical Methods in Engineering*, vol. 40, no. 14, pp. 2593–2610, 1997.
[25] W. M. Elleithy, H. J. Al-Gahtani, and M. El-Gebeily, "Iterative coupling of BE and FE methods in elastostatics," *Engineering Analysis with Boundary Elements*, vol. 25, no. 8, pp. 685–695, 2001.
[26] W. M. Elleithy and M. Tanaka, "Interface relaxation algorithms for BEM-BEM coupling and FEM-BEM coupling," *Computer Methods in Applied Mechanics and Engineering*, vol. 192, no. 26-27, pp. 2977–2992, 2003.
[27] S. Ganguly, J. B. Layton, and C. Balakrishna, "Symmetric coupling of multi-zone curved Galerkin boundary elements with finite elements in elasticity," *International Journal for Numerical Methods in Engineering*, vol. 48, no. 5, pp. 633–654, 2000.
[28] M. Haas and G. Kuhn, "Mixed-dimensional, symmetric coupling of FEM and BEM," *Engineering Analysis with Boundary Elements*, vol. 27, no. 6, pp. 575–582, 2003.
[29] M. Haas, B. Helldörfer, and G. Kuhn, "Improved coupling of finite shell elements and 3D boundary elements," *Archive of Applied Mechanics*, vol. 75, no. 10–12, pp. 649–663, 2006.
[30] B. Helldörfer, M. Haas, and G. Kuhn, "Automatic coupling of a boundary element code with a commercial finite element system," *Advances in Engineering Software*, vol. 39, no. 8, pp. 699–709, 2008.
[31] L. J. Gray, L. F. Martha, and A. R. Ingraffea, "Hypersingular integrals in boundary element fracture analysis," *International Journal for Numerical Methods in Engineering*, vol. 29, no. 6, pp. 1135–1158, 1990.
[32] P. A. Martin and F. I. Rizzo, "Hypersingular integrals: how smooth must the density be?" *International Journal for Numerical Methods in Engineering*, vol. 39, no. 4, pp. 687–704, 1996.
[33] M. Bonnet, G. Maier, and C. Polizzotto, "Symmetric Galerkin boundary element methods," *Applied Mechanics Reviews*, vol. 51, no. 11, pp. 669–703, 1998.
[34] A. Frangi and G. Novati, "BEM-FEM coupling for 3D fracture mechanics applications," *Computational Mechanics*, vol. 32, no. 4–6, pp. 415–422, 2003.
[35] R. Springhetti, G. Novati, and M. Margonari, "Weak coupling of the symmetric galerkin BEM with FEM for potential and elastostatic problems," *Computer Modeling in Engineering and Sciences*, vol. 13, no. 1, pp. 67–80, 2006.
[36] J. Rungamornrat and M. E. Mear, "SGBEM-FEM coupling for analysis of cracks in 3D anisotropic media," *International Journal for Numerical Methods in Engineering*, vol. 86, no. 2, pp. 224–248, 2011.
[37] K. J. Bathe, *Finite Element Procedures*, Prentice-Hall, Upper Saddle River, NJ, USA, 1990.
[38] T. Belytschko, W. K. Liu, and B. Moran, *Nonlinear Finite Elements for Continua and Structures*, John Wiley & Sons, New York, NY, USA, 2000.
[39] H. B. Li, G. M. Han, and H. A. Mang, "A new method for evaluating singular integrals in stress analysis of solids by the direct boundary element method," *International Journal for Numerical Methods in Engineering*, vol. 21, no. 11, pp. 2071–2098, 1985.

[40] K. Hayami and C. A. Brebbia, "Quadrature methods for singular and nearly singular integrals in 3-D boundary element method," in *Boundary Elements X*, pp. 237–264, Springer, Berlin, Germany, 1988.
[41] K. Hayami, "A projection transformation method for nearly singular surface boundary element integrals," in *Lecture Notes in Engineering*, C. A. Brebbia and S. A. Orszag, Eds., vol. 73, pp. 1–2, Springer, Berlin, Germany, 1992.
[42] K. Hayami and H. Matsumoto, "A numerical quadrature for nearly singular boundary element integrals," *Engineering Analysis with Boundary Elements*, vol. 13, no. 2, pp. 143–154, 1994.
[43] J. Lubiliner, *Plasticity Theory*, Macmillan, New York, NY, USA, 1990.
[44] I. S. Sokolnikoff, *Mathematical Theory of Elasticity*, McGraw-Hill, New York, NY, USA, 1956.

FEM-SGBEM coupling for modeling of mode-I planar cracks in three-dimensional elastic media with residual surface tension effects

T. B. Nguyen[1], J. Rungamornrat[1,*], T. Senjuntichai[1] and A. C. Wijeyewickrema[2]

[1]Department of Civil Engineering, Faculty of Engineering, Chulalongkorn University, Bangkok 10330, Thailand

[2]Department of Civil and Environmental Engineering, Tokyo Institute of Technology, Tokyo 152-8552, Japan

Abstract

A computationally efficient numerical technique capable of modeling mode-I planar cracks in three-dimensional linear elastic media by taking the influence of residual surface tension into account, is presented in this paper. The elastic medium (i.e., the bulk material) is modeled by the classical theory of linear elasticity, whereas the crack surface is treated as a zero-thickness layer perfectly bonded to the bulk material with its behavior governed by the special case of Gurtin-Murdoch surface elasticity model. Governing equations of the bulk material are formulated in terms of weakly singular, weak-form boundary integral equations, whereas those of the surface are cast in a weak form using a weighted residual technique. The solution of the final system of governing equations is subsequently accomplished by using a numerical procedure based primarily on a standard finite element technique and a weakly singular, symmetric Galerkin boundary element method. Extensive numerical simulations are conducted and the results are compared with available benchmark solutions to verify the formulation and numerical implementation. Applications of the technique to the analysis of nano-crack problems are presented for some selected cases, to study nano-scale influence and size-dependency behavior.

Keywords: Crack opening displacement, Gurtin-Murdoch model, Nano-cracks, Residual surface tension, SGBEM, Surface elasticity

1. Introduction

Due to the rapid growth of the application of nano-sized devices and nano-structured materials in various fields, the physical modeling and corresponding comprehensive analysis to gain an insight into their complex behavior become important aspects in the optimal design of nano-scale products. Failure/damage analysis and assessment is one of the essential steps that must be properly considered to ensure their safety and integrity in the design procedure. To aid such crucial tasks, a classical approach based on the stress analysis of a body containing assumed pre-existing defects or cracks is usually considered. While conventional linear elastic fracture mechanics has been well

* Corresponding author. Tel.: +66-2-218-6460-2

E-mail address: Jaroon.r@chula.ac.th (J. Rungamornrat)

established and employed in the modeling of cracks in linear elastic media, an enhancement of the classical model to incorporate the nano-scale influence is required. Atomistic calculation studies have pointed out that atoms near the free surface of solids behave differently from their bulk. In this sense, the whole body is not completely homogeneous, but when its size is in the range of micrometers or larger, the surface free energy effect can be neglected due to its insignificant influence on overall material properties. Unlike macro-structures, in the case of nano-sized objects (e.g., thin films, quantum dots, nano-wires, nano-tubes and nano-composites), the surface to volume ratio is much higher and, as a direct consequence, the surface free energy effect often plays a crucial role in the mechanical behavior [1]. Therefore, the classical theory of continuum-based mechanics commonly used in the modeling of macroscopic bodies cannot be directly applied to treat the problem of nano-sized cracks.

To be capable of capturing the surface free energy effect, a model that properly takes into account the surface free energy must be utilized. The most widely used continuum-based models which incorporate surface free energy effects are those using Gurtin-Murdoch surface elasticity theory. Gurtin and Murdoch [2, 3] proposed a mathematical framework to study the mechanical behavior of material surfaces through a continuum-based model which includes surface stress. The elastic surface is assumed to be very thin and modeled as a mathematical layer of zero thickness. This layer is perfectly bonded to the bulk material. In addition, such an idealized surface has different elastic moduli from those of the bulk material.

The Gurtin-Murdoch model has been widely used to study various size-dependent, nano-scale problems. For instance, He et al. [4], Dingreville et al. [5] and Huang [6] employed the Gurtin-Murdoch surface elasticity model to clearly elucidate the size-dependent elastic properties of nano-structured elements such as wires and films, while Tian and Rajapakse [7, 8, 9] applied such model to demonstrate influence of surface stress effects on stress and displacement fields of nano-inhomogeneity problems. More recently, Pinyochotiwong et al. [10] investigated the effects of surface energy in the analysis of an axisymmetric rigid frictionless indentor acting on an isotropic, linearly elastic half-space by using the complete version of the Gurtin-Murdoch continuum model for surface elasticity.

The continuum-based surface/interface model of Gurtin and Murdoch has also been employed in the modeling of nano-sized cracks. Based upon an investigation of an elliptic void, Wu [11] argued that the presence of the surface stress has the capability of containing the severity of deformations of a blunt crack. Wang et al. [12] studied the surface stress effect on near-tip stresses for both mode-I and mode-III blunt cracks and found that when the curvature radius of the crack-front decreases to

nanometers, surface energy significantly affects the stress intensities near the crack tip. Fu et al. [13, 14] incorporated the surface elasticity model into the finite element method (via ANSYS® and ABAQUS®) to study the influence of surface stresses on the mode-I and mode-II crack-tip fields and concluded that when the curvature radius of the blunt crack root decreases to micro-/nano-meters, surface elasticity exhibits significant influence on the stresses near the crack tip. Fang et al. [15] analyzed the influence of surface effects on dislocation emission from an elliptically blunt crack under mode-I and mode-II loading conditions and showed that the impact of surface stresses on the critical stress intensity factors for dislocation emission becomes remarkable when the size of the blunted crack is very small, typically of a nanometer scale. Kim et al. [16, 17, 18] examined mode-I, mode-II and mode-III crack problems including surface stress effects which assumed that the stresses at the sharp crack-tip are finite. Recently, Nan and Wang [19] considered the effect of the residual surface tension on the crack surface, to investigate the mode-I crack problem and demonstrated that the surface effect on the crack deformation and crack-tip field are prominent at nanoscale. Moreover, the results are influenced by the residual surface tension not only on the surface near the crack-tip region but also on the entire crack-face. Intarit et al. [20, 21] analytically investigated a nano-sized, penny-shaped crack in three-dimensional, linear elastic media under mode-I loading conditions.

On the basis of an extensive literature survey, it can be said that work related to the modeling of defects/cracks at nano-scale level has been very limited. Most of the studies are restricted to situations where cracks can be treated either within the context of two-dimensional boundary value problems [11-19] or within the context of relatively simple three-dimensional problems [20, 21]. However, bodies or components containing existing defects/flaws involved in practical applications are, in general, relatively complex in terms of geometries, loading conditions, and influences to be treated (e.g., surface free energy). The existing mathematical models are therefore of limited scope and insufficient for the prediction of response in practical cases. This, as a result, necessitates the development of fully three-dimensional models, supplemented by efficient and powerful numerical procedures.

Numerical techniques based on boundary integral equations have been well-established and proven powerful for both two-dimensional and three-dimensional fracture analysis (e.g., [22-27]). The techniques possess attractive characteristics, such as governing equations with spatially reduced dimensions and simplicity of treating remote boundaries and infinite bodies, rendering them computationally efficient and convenient for modeling crack problems. The weakly singular, symmetric Galerkin boundary element method (SGBEM), which is a principal numerical technique

proposed to model the cracks in the present study, is a particular boundary integral equation method that has been continuously developed and widely adopted by various investigators in the past four decades. This special numerical technique has been widely and successfully employed to solve both linear elasticity and linear elastic fracture problems [28-38], since it has several important features. For instance, the governing integral equations contain only weakly singular kernels (of $\mathcal{O}(1/r)$); the technique is applicable for modeling cracks with arbitrary configurations and under general loading conditions and for treating an infinite body efficiently; and the formulation is established in a symmetric weak-form such that it gives rise to a system of linear equations with a symmetric coefficient matrix. The first feature renders that all involved integrals exist in an ordinary sense and their validity requires only the continuity of the boundary data; i.e., in the numerical implementation, it is possible to employ standard C^0 elements in the approximation of the primary unknowns and to apply existing quadrature schemes to numerically evaluate all involved integrals (e.g. [31, 32, 37, 38]). In addition, the last feature also allows the SGBEM to be conveniently coupled with the standard finite element procedure to enhance its computational efficiency and capability (e.g. [39, 40]). Extensive review of the weakly singular SGBEM can be found in Bonnet et al. [41], in Rungamornrat and Mear [37] and Rungamornrat and Senjuntichai [38] for its application to three-dimensional fracture analysis, in Rungamornrat and Mear [40] for its coupling with the standard FEM.

In this paper, a computationally efficient numerical technique capable of modeling planar cracks in three-dimensional isotropic, linear elastic media including the influence of residual surface tension is presented. The residual surface tension effects are modeled using the well-known Gurtin-Murdoch theory of surface elasticity. A numerical procedure based primarily on the coupling of a standard finite element method (FEM) and a weakly singular, symmetric Galerkin boundary element method is employed. The former technique is utilized to efficiently handle the governing equation of the surface. Extensive numerical simulations are conducted and the results are compared with available benchmark solutions to verify the formulation and numerical implementation. Application of the technique to the analysis of mode-I, nano-sized, crack problems are presented for some selected cases, to study nano-scale influence and size-dependency behavior.

2. Formulation

This section begins with the clear description and essential assumptions of the boundary value problem that is the focus of the present study. All basic field equations and the development of governing equations for both the bulk material and the crack surface are then briefly presented. Finally, the system of weak-form equations governing the primary unknowns on the crack surface is derived.

2.1. Problem description

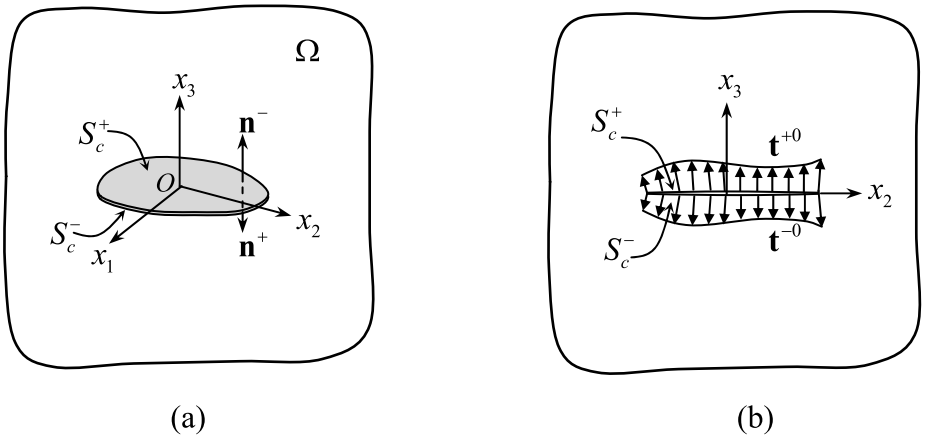

(a) (b)

Fig. 1. (a) Schematic of three-dimensional infinite elastic medium containing an isolated crack; (b) prescribed traction on crack surfaces.

Consider a three-dimensional, infinite, elastic medium Ω containing an isolated, planar crack as shown schematically in Fig. 1(a). The reference Cartesian coordinate system $\{O; x_1, x_2, x_3\}$ is also shown. The bulk material is made of a homogeneous, isotropic, linearly elastic material with shear modulus μ and Poisson's ratio ν. The crack surfaces which are geometrically identical are represented by S_c^+ and S_c^- and with corresponding outward unit normal $\mathbf{n}^+$ and $\mathbf{n}^-$, respectively. The medium is assumed to be free of body forces and remote loading but subjected to prescribed tractions $\mathbf{t}^{+0}$ and $\mathbf{t}^{-0}$ on S_c^+ and S_c^-, respectively (Fig. 1(b)). In addition, infinitesimally thin layers on the crack surfaces (mathematically modeled by zero thickness layers perfectly bonded to the crack surfaces) possess constant residual surface tension under unstrained conditions which is denoted by τ^s.

In the formulation of the boundary value problem, the medium is decomposed into three parts: the bulk material, the zero-thickness layer S_c^+ and the zero-thickness layer S_c^- as shown in Fig. 2. The bulk material is simply the whole medium without the two infinitesimally thin layers on the crack surfaces. Since both layers have zero thickness, the geometry of the bulk material is therefore identical to that of the whole medium (i.e., it can also be completely described by the region Ω and the two crack surfaces S_c^+ and S_c^-).

The key difference between the bulk material and the original medium is that the bulk material is homogeneous and the crack surfaces S_c^+ and S_c^- in the bulk material part are subjected to unknown

tractions (exerted directly by the two layers) $\mathbf{t}^{+b}$ and $\mathbf{t}^{-b}$, respectively. The layer S_c^+ is treated as a two-sided surface with one side subjected to the prescribed traction $\mathbf{t}^{+0}$ and the other side subjected to the traction $\mathbf{t}^{+s}$ exerted by the bulk material (Fig. 2(b)). Similarly, the layer S_c^- is treated as a two-sided surface with one side subjected to the prescribed traction $\mathbf{t}^{-0}$ and the other side subjected to the traction $\mathbf{t}^{-s}$ exerted by the bulk material (Fig. 2(c)). In what follows, Greek subscripts denote field quantities associated with the surface and take the values 1, 2 while the Latin subscripts take the values 1, 2, 3. We remark that, in the development to follow, it will suffice to make reference to the single crack surface $S_c \equiv S_c^+$.

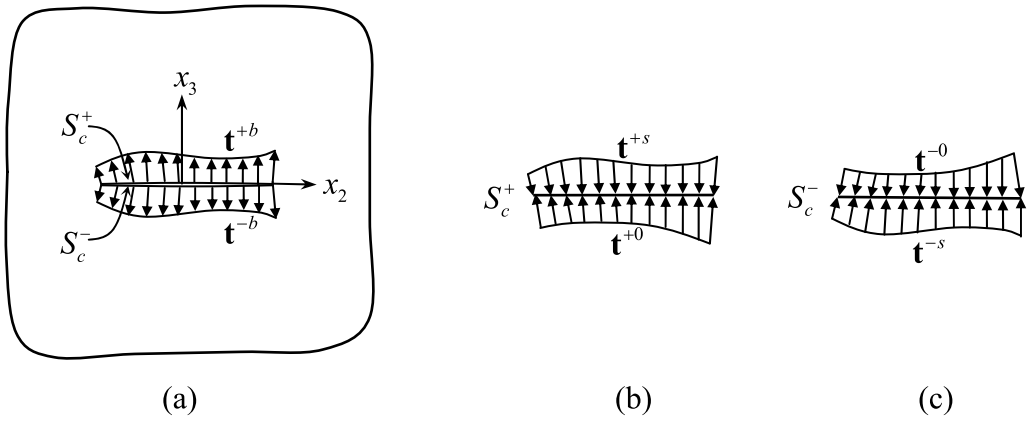

(a) (b) (c)

Fig. 2. Schematics of (a) the bulk material, (b) the zero-thickness layer S_c^+ and (c) the zero-thickness layer S_c^-.

2.2. Governing equations for bulk material

Since the bulk material is made of homogeneous, isotropic, linear elastic material, its behavior is governed by the classical theory of linear elasticity. From results developed in the work of Rungamornrat and Mear [36] and Rungamornrat and Senjuntichai [38], the displacement and stress components at any interior point $\mathbf{x}$, denoted respectively by $u_p(\mathbf{x})$ and $\sigma_{ij}(\mathbf{x})$, can be expressed in terms of the traction data $\mathbf{t}^{+b}$ and and the displacement data $\mathbf{u}^{+b}$ and $\mathbf{u}^{-b}$ on the crack surfaces S_c^+ and S_c^- as

$$\begin{aligned} u_p(\mathbf{x}) = & \int_{S_c} U_j^p(\boldsymbol{\xi}-\mathbf{x}) t_j^{b\Sigma}(\boldsymbol{\xi}) dS(\boldsymbol{\xi}) \\ & + \int_{S_c} G_{mj}^p(\boldsymbol{\xi}-\mathbf{x}) D_m u_j^{b\Delta}(\boldsymbol{\xi}) dS(\boldsymbol{\xi}) - \int_{S_c} H_{ij}^p(\boldsymbol{\xi}-\mathbf{x}) n_i(\boldsymbol{\xi}) u_j^{b\Delta}(\boldsymbol{\xi}) dS(\boldsymbol{\xi}) \end{aligned} \tag{1}$$

$$\sigma_{ij}(\mathbf{x}) = \int_{S_c} \varepsilon_{irt} C^{tj}_{lk,r}(\boldsymbol{\xi}-\mathbf{x}) D_l u_k^{b\Delta}(\boldsymbol{\xi}) dS(\boldsymbol{\xi}) + \int_{S_c} \varepsilon_{irt} G^{p}_{tj,r}(\boldsymbol{\xi}-\mathbf{x}) t_p^{b\Sigma}(\boldsymbol{\xi}) dS(\boldsymbol{\xi}) - \int_{S_c} H^{p}_{ij}(\boldsymbol{\xi}-\mathbf{x}) t_p^{b\Sigma}(\boldsymbol{\xi}) dS(\boldsymbol{\xi}) \tag{2}$$

where $D_t(\cdot) = \varepsilon_{tmj} n_m \partial(\cdot)/\partial \xi_j$ is a surface differential operator, $t_j^{b\Sigma} = t_j^{+b} + t_j^{-b}$, $u_j^{b\Delta} = u_j^{+b} - u_j^{-b}$, ε_{irt} is the standard alternating symbol, the kernels $\{U_j^p, G_{mj}^p, C_{mj}^{tk}, H_{ij}^p\}$ for isotropic elastic materials are given by

$$U_j^p(\boldsymbol{\xi}-\mathbf{x}) = \frac{1}{16\pi(1-\nu)\mu r}\left[(3-4\nu)\delta_{pj} + \frac{(\xi_p - x_p)(\xi_j - x_j)}{r^2}\right] \tag{3}$$

$$G_{mj}^p(\boldsymbol{\xi}-\mathbf{x}) = \frac{1}{8\pi(1-\nu) r}\left[(1-2\nu)\varepsilon_{mpj} + \frac{(\xi_p - x_p)(\xi_a - x_a)}{r^2}\varepsilon_{ajm}\right] \tag{4}$$

$$C_{mj}^{tk}(\boldsymbol{\xi}-\mathbf{x}) = \frac{\mu}{4\pi(1-\nu) r}\left[(1-\nu)\delta_{tk}\delta_{mj} + 2\nu\delta_{km}\delta_{tj} - \delta_{kj}\delta_{tm} - \frac{(\xi_k - x_k)(\xi_j - x_j)}{r^2}\delta_{tm}\right] \tag{5}$$

$$H_{ij}^p(\boldsymbol{\xi}-\mathbf{x}) = -\frac{(\xi_i - x_i)\delta_{jp}}{4\pi r^3} \tag{6}$$

with $r = \| \boldsymbol{\xi} - \mathbf{x} \|$ and ν, μ are Poisson's ratio and the shear modulus, respectively. The boundary integral relations (1) and (2) allow the displacement and stress at any interior point to be determined once the data $\mathbf{t}^{+b}$, $\mathbf{t}^{-b}$, $\mathbf{u}^{+b}$ and $\mathbf{u}^{-b}$ are known. To establish the integral equations governing the unknown data $\mathbf{t}^{+b}$, $\mathbf{t}^{-b}$, $\mathbf{u}^{+b}$ and $\mathbf{u}^{-b}$, the integral relations (1) and (2) are utilized along with the limiting process to any point on the crack surface and the standard procedure using Stokes' theorem to obtain the weak-form equations. The final weak-form, boundary integral equations are given by (see details of the development in Rungamornrat and Mear [36] and Rungamornrat and Senjuntichai [38])

$$\begin{aligned}\frac{1}{2}\int_{S_c} \tilde{t}_p^{\Sigma}(\mathbf{y}) u_p^{b\Sigma}(\mathbf{y}) dS(\mathbf{y}) = &\int_{S_c} \tilde{t}_p^{\Sigma}(\mathbf{y}) \int_{S_c} U_j^p(\boldsymbol{\xi}-\mathbf{y}) t_j^{b\Sigma}(\boldsymbol{\xi}) dS(\boldsymbol{\xi}) dS(\mathbf{y}) \\ &+ \int_{S_c} \tilde{t}_p^{\Sigma}(\mathbf{y}) \int_{S_c} G_{mj}^p(\boldsymbol{\xi}-\mathbf{y}) D_m u_j^{b\Delta}(\boldsymbol{\xi}) dS(\boldsymbol{\xi}) dS(\mathbf{y}) \\ &- \int_{S_c} \tilde{t}_p^{\Sigma}(\mathbf{y}) \int_{S_c} H_{ij}^p(\boldsymbol{\xi}-\mathbf{y}) n_i(\boldsymbol{\xi}) u_j^{b\Delta}(\boldsymbol{\xi}) dS(\boldsymbol{\xi}) dS(\mathbf{y})\end{aligned} \tag{7}$$

$$\begin{aligned}-\frac{1}{2}\int_{S_c} \tilde{u}_k^{\Delta}(\mathbf{y}) t_k^{b\Delta}(\mathbf{y}) dS(\mathbf{y}) = &\int_{S_c} D_t \tilde{u}_k^{\Delta}(\mathbf{y}) \int_{S_c} C_{mj}^{tk}(\boldsymbol{\xi}-\mathbf{y}) D_m u_j^{b\Delta}(\boldsymbol{\xi}) dS(\boldsymbol{\xi}) dS(\mathbf{y}) \\ &+ \int_{S_c} D_t \tilde{u}_k^{\Delta}(\mathbf{y}) \int_{S_c} G_{tk}^j(\boldsymbol{\xi}-\mathbf{y}) t_j^{b\Sigma}(\boldsymbol{\xi}) dS(\boldsymbol{\xi}) dS(\mathbf{y}) \\ &+ \int_{S_c} \tilde{u}_k^{\Delta}(\mathbf{y}) \int_{S_c} H_{lk}^j(\boldsymbol{\xi}-\mathbf{y}) n_l(\mathbf{y}) t_j^{b\Sigma}(\boldsymbol{\xi}) dS(\boldsymbol{\xi}) dS(\mathbf{y})\end{aligned} \tag{8}$$

where $u_j^{b\Sigma} = u_j^{+b} + u_j^{-b}$, $t_j^{b\Delta} = t_j^{+b} - t_j^{-b}$, and $\{\tilde{t}_p^{\Sigma}, \tilde{u}_k^{\Delta}\}$ are sufficiently smooth test functions. The pair of equations (7) and (8) has been well recognized as the weak-form boundary integral equations for the sum of the displacement $u_j^{b\Sigma}$ and the jump of the traction $t_j^{b\Delta}$ across the crack surface, respectively. It is worth noting that both integral equations contain only weakly singular kernels $\{U_j^p, G_{mj}^p, C_{mj}^{tk}, H_{ij}^p n_j\}$ of $\mathcal{O}(1/r)$. This positive feature renders all involved double surface integrals to exist in an ordinary sense and their validity requires only C^0- boundary data.

2.3. Governing equations for two layers

The two layers S_c^+ and S_c^- shown in Figs. 2(b) and 2(c) are considered as infinitesimally thin membranes adhered perfectly to the bulk material. The behavior of these two layers is modeled by Gurtin-Murdoch surface elasticity theory by ignoring terms associated with the surface elastic constants. It has been pointed out by various investigations that the influence of the surface Lamé constants on the out-of-plane responses in the region very near the surface is negligibly weak [10, 19-21]. The simplified version of the Gurtin-Murdoch model is therefore considered suitable for modeling planar crack problems when mode-I behavior is of primary interest.

The equilibrium equations, the surface constitutive relations and the strain-displacement relationship of the layers S_c^+ and S_c^- are therefore given by [2, 3]

$$\sigma_{i\beta,\beta}^s + t_i^s + t_i^o = 0 \tag{9}$$

$$\sigma_{\alpha\beta}^s = \tau^s \delta_{\alpha\beta} + \tau^s \varepsilon_{\gamma\gamma}^s \delta_{\alpha\beta} - 2\tau^s \varepsilon_{\alpha\beta}^s + \tau^s u_{\alpha,\beta}^s \quad , \quad \sigma_{3\beta}^s = \tau^s u_{3,\beta}^s \tag{10}$$

$$\varepsilon_{\alpha\beta}^s = \tfrac{1}{2}\left(u_{\alpha,\beta}^s + u_{\beta,\alpha}^s\right) \tag{11}$$

where $\sigma_{i\beta}^s, \varepsilon_{\alpha\beta}^s, u_i^s$ represent stress, strain and displacement components within the layer.

To construct the weak-form equation, we multiply the equilibrium equation (9) with a sufficiently smooth test function $\tilde{u}_i^s$ and then integrate the result over the entire crack surface to obtain

$$\int_{S_c} \tilde{u}_i^s \sigma_{i\beta,\beta}^s dS + \int_{S_c} \tilde{u}_i^s t_i^s dS + \int_{S_c} \tilde{u}_i^s t_i^0 dS = 0 \tag{12}$$

By using the fact that τ^s is spatially independent, it can be readily verified that $\sigma_{\alpha\beta,\beta}^s = 0$. With such condition along with carrying out the integration by parts of the first term using the Gauss-divergence theorem, it leads to

$$\int_{S_c} \tilde{u}^s_{3,\beta}\sigma^s_{3\beta}dS - \int_{S_c} \tilde{u}^s_i t^s_i dS = \int_{\partial S_c} \tilde{u}^s_3\sigma^s_{3\beta}n_\beta dS + \int_{S_c} \tilde{u}^s_i t^0_i dS \tag{13}$$

Substituting (10) into (13) finally yields

$$\tau^s \int_{S_c} \tilde{u}^s_{3,\beta}u^s_{3,\beta}dS - \int_{S_c} \tilde{u}^s_i t^s_i dS = \int_{\partial S_c} \tilde{u}^s_3\sigma^s_{3\beta}n_\beta dS + \int_{S_c} \tilde{u}^s_i t^0_i dS \tag{14}$$

Note that the weak-form equation (14) applies to both crack surfaces. For instance, the weak-form equations for the surface S_c^+ and surface S_c^- can be obtained explicitly by

$$\tau^s \int_{S_c} \tilde{u}^{+s}_{3,\beta}u^{+s}_{3,\beta}dS - \int_{S_c} \tilde{u}^{+s}_i t^{+s}_i dS = \int_{\partial S_c} \tilde{u}^{+s}_3\sigma^{+s}_{3\beta}n_\beta dS + \int_{S_c} \tilde{u}^{+s}_i t^{+0}_i dS \tag{15}$$

$$\tau^s \int_{S_c} \tilde{u}^{-s}_{3,\beta}u^{-s}_{3,\beta}dS - \int_{S_c} \tilde{u}^{-s}_i t^{-s}_i dS = \int_{\partial S_c} \tilde{u}^{-s}_3\sigma^{-s}_{3\beta}n_\beta dS + \int_{S_c} \tilde{u}^{-s}_i t^{-0}_i dS \tag{16}$$

where superscripts "+" and "–" are added to differentiate quantities defined on each crack surface. Since the integral equations governing the bulk are derived in terms of the unknown sum and jump of quantities across the crack surface, it is natural to establish the weak-form equations governing the surface in terms of the same type of unknowns. This can be readily accomplished by forming two linear combinations of (15) and (16) as follows: (i) choosing $\tilde{u}^{+s}_i = \tilde{u}^{-s}_i = \tilde{u}^{s\Sigma}_i$ and then adding (15) to (16) and (ii) choosing $\tilde{u}^{+s}_i = \tilde{u}^{-s}_i = \tilde{u}^{s\Delta}_i$ and then subtracting (15) from (16). Such pair of equivalent weak-form equations is given by

$$\tau^s \int_{S_c} \tilde{u}^{s\Sigma}_{3,\beta}u^{s\Sigma}_{3,\beta}dS - \int_{S_c} \tilde{u}^{s\Sigma}_i t^{s\Sigma}_i dS = \int_{\partial S_c} \tilde{u}^{s\Sigma}_3\sigma^{s\Sigma}_{3\beta}n_\beta dS + \int_{S_c} \tilde{u}^{s\Sigma}_i t^{0\Sigma}_i dS \tag{17}$$

$$\tau^s \int_{S_c} \tilde{u}^{s\Delta}_{3,\beta}u^{s\Delta}_{3,\beta}dS - \int_{S_c} \tilde{u}^{s\Delta}_i t^{s\Delta}_i dS = \int_{\partial S_c} \tilde{u}^{s\Delta}_3\sigma^{s\Delta}_{3\beta}n_\beta dS + \int_{S_c} \tilde{u}^{s\Delta}_i t^{0\Delta}_i dS \tag{18}$$

where superscripts "Σ" and "Δ" indicate the sum and jump of quantities across the crack surface. It should be remarked further that since the jump of the displacement along the crack-front vanishes identically, the test function $\tilde{u}^{s\Delta}_i$ is chosen to satisfy the homogeneous condition $\tilde{u}^{s\Delta}_i = 0$ on ∂S_c. The weak-form equations (17) and (18) now take the form

$$\tau^s \int_{S_c} \tilde{u}^{s\Sigma}_{3,\beta}u^{s\Sigma}_{3,\beta}dS - \int_{S_c} \tilde{u}^{s\Sigma}_i t^{s\Sigma}_i dS = \int_{S_c} \tilde{u}^{s\Sigma}_i t^{0\Sigma}_i dS \tag{19}$$

$$\tau^s \int_{S_c} \tilde{u}_{3,\beta}^{s\Delta} u_{3,\beta}^{s\Delta} dS - \int_{S_c} \tilde{u}_i^{s\Delta} t_i^{s\Delta} dS = \int_{S_c} \tilde{u}_i^{s\Delta} t_i^{0\Delta} dS \tag{20}$$

Equations (19) and (20) constitute a set of weak-form equations governing the unknown quantities $\{u_i^{s\Delta}, t_i^{s\Delta}, u_i^{s\Sigma}, t_i^{s\Sigma}\}$. It is worth noting that the formulation presented above is not restricted only to applied normal traction to the crack surface, although the mathematical model of the surface is suitable for pure mode-I loading. Due to the vanishing $\sigma_{\alpha\beta,\beta}^s$, the equilibrium equation (9) indicates that the applied shear traction is transmitted directly to the crack surface of the bulk material.

2.4. Governing equations for whole medium

Since the two layers S_c^+ and S_c^- are adhered perfectly to the bulk material, the displacements and tractions along the interface of the two layers and the bulk material must be continuous. This yields the following continuity conditions:

$$u_i^{s\Delta} = u_i^{b\Delta} \equiv u_i^{\Delta} \tag{21}$$

$$u_i^{s\Sigma} = u_i^{b\Sigma} \equiv u_i^{\Sigma} \tag{22}$$

$$t_i^{s\Delta} = -t_i^{b\Delta} \equiv -t_i^{\Delta} \tag{23}$$

$$t_i^{s\Sigma} = -t_i^{b\Sigma} \equiv -t_i^{\Sigma} \tag{24}$$

Substituting (21)-(24) into (7), (8), (19) and (20), leads to a system of four equations involving four unknown functions $\{u_i^{\Delta}, t_i^{\Delta}, u_i^{\Sigma}, t_i^{\Sigma}\}$. By choosing appropriate test functions, (8) and (20) can be combined and the unknown t_i^{Δ} can be eliminated. The final system of three equations involving three unknown functions $\{u_i^{\Delta}, u_i^{\Sigma}, t_i^{\Sigma}\}$ is given by

$$\begin{aligned}
&\mathcal{A}(\tilde{\mathbf{u}}^{s\Sigma}, \mathbf{u}^{\Sigma}) + \mathcal{B}(\tilde{\mathbf{u}}^{s\Sigma}, \mathbf{t}^{\Sigma}) && = \mathcal{R}_1(\tilde{\mathbf{u}}^{s\Sigma}) \\
&\mathcal{B}(\tilde{\mathbf{t}}^{\Sigma}, \mathbf{u}^{\Sigma}) + \mathcal{C}(\tilde{\mathbf{t}}^{\Sigma}, \mathbf{t}^{\Sigma}) + \mathcal{D}(\tilde{\mathbf{t}}^{\Sigma}, \mathbf{u}^{\Delta}) && = 0 \\
&\qquad\quad \mathcal{D}(\mathbf{t}^{\Sigma}, \tilde{\mathbf{u}}^{\Delta}) + \mathcal{E}(\tilde{\mathbf{u}}^{\Delta}, \mathbf{u}^{\Delta}) && = \mathcal{R}_2(\tilde{\mathbf{u}}^{\Delta})
\end{aligned} \tag{25}$$

where the bilinear integral operators $\mathcal{A}, \mathcal{B}, \mathcal{C}, \mathcal{D}, \mathcal{E}$ are defined by

$$\mathcal{A}(\mathbf{X}, \mathbf{Y}) = \frac{\tau^s}{2} \int_{S_c} X_{3,\alpha}(\mathbf{y}) Y_{3,\alpha}(\mathbf{y}) dS(\mathbf{y}) \tag{26}$$

$$\mathscr{B}(\mathbf{X},\mathbf{Y}) = \frac{1}{2}\int_{S_c} X_p(\mathbf{y}) Y_p(\mathbf{y}) dS(\mathbf{y}) \tag{27}$$

$$\mathscr{C}(\mathbf{X},\mathbf{Y}) = -\int_{S_c} X_p(\mathbf{y}) \int_{S_c} U_j^p(\boldsymbol{\xi}-\mathbf{y}) Y_j(\boldsymbol{\xi}) dS(\boldsymbol{\xi}) dS(\mathbf{y}) \tag{28}$$

$$\begin{aligned}\mathscr{D}(\mathbf{X},\mathbf{Y}) = &-\int_{S_c} X_p(\mathbf{y}) \int_{S_c} G_{mj}^p(\boldsymbol{\xi}-\mathbf{y}) D_m Y_j(\boldsymbol{\xi}) dS(\boldsymbol{\xi}) dS(\mathbf{y}) \\ &+\int_{S_c} X_p(\mathbf{y}) \int_{S_c} H_{ij}^p(\boldsymbol{\xi}-\mathbf{y}) n_i(\boldsymbol{\xi}) Y_j(\boldsymbol{\xi}) dS(\boldsymbol{\xi}) dS(\mathbf{y})\end{aligned} \tag{29}$$

$$\mathscr{E}(\mathbf{X},\mathbf{Y}) = -\int_{S_c} D_t X_k(\mathbf{y}) \int_{S_c} C_{mj}^{tk}(\boldsymbol{\xi}-\mathbf{y}) D_m Y_j(\boldsymbol{\xi}) dS(\boldsymbol{\xi}) dS(\mathbf{y}) + \mathscr{A}(\mathbf{X},\mathbf{Y}) \tag{30}$$

where the linear integral operators $\{\mathscr{R}_1, \mathscr{R}_2\}$ are defined, in terms of prescribed data $\mathbf{t}^{0\Sigma}$ and $\mathbf{t}^{0\Delta}$, by

$$\mathscr{R}_1(\mathbf{X}) = \frac{1}{2}\int_{S_c} X_l(\mathbf{y}) t_l^{0\Sigma}(\mathbf{y}) dS(\mathbf{y}) \tag{31}$$

$$\mathscr{R}_2(\mathbf{X}) = \frac{1}{2}\int_{S_c} X_l(\mathbf{y}) t_l^{0\Delta}(\mathbf{y}) dS(\mathbf{y}) \tag{32}$$

3. Numerical implementation

In this section, all numerical treatments including the discretization and numerical integration are briefly discussed. In general, standard procedures for the weakly singular SGBEM (e.g., [31, 32, 35, 37]) and those for the standard finite element method (e.g., [42-44]) are utilized to form the discretized system of linear algebraic equations.

3.1. Discretization

Standard Galerkin approximation is employed in the discretization of the system of governing equations (25). Since all involved boundary integrals contain only weakly singular kernels of $\mathscr{O}(1/r)$, standard C^0 interpolation functions are utilized in the approximation of both trial and test functions. In particular, the following approximation for the test functions and the trial functions is introduced:

$$\tilde{u}_i^{s\Sigma} = \sum_{p=1}^{N} \tilde{U}_{3(p-1)+i}^{s\Sigma} \Phi_p \;;\;\; u_i^{\Sigma} = \sum_{q=1}^{N} U_{3(q-1)+i}^{\Sigma} \Phi_q \tag{33}$$

$$\tilde{u}_i^{\Delta} = \sum_{p=1}^{N} \tilde{U}_{3(p-1)+i} \Phi_p \;;\;\; u_i^{\Delta} = \sum_{q=1}^{N} U_{3(q-1)+i}^{\Delta} \Phi_q \tag{34}$$

$$\tilde{t}_i^{\Sigma}=\sum_{p=1}^{N}\tilde{T}_{3(p-1)+i}\Phi_p\;;\quad t_i^{\Sigma}=\sum_{q=1}^{N}T_{3(q-1)+i}^{\Sigma}\Phi_q \tag{35}$$

where N is the number of nodal points; Φ_q is nodal basis functions at node q; $U_{3(q-1)+i}^{\Sigma}$, $U_{3(q-1)+i}^{\Delta}$, and $T_{3(q-1)+i}^{\Sigma}$ are nodal degrees of freedom associated with the sum of the displacement, the jump of the displacement and the sum of the traction across the crack surfaces, respectively; and $\tilde{U}_{3(p-1)+i}^{s\Sigma}$, $\tilde{U}_{3(p-1)+i}$, and $\tilde{T}_{3(p-1)+i}$ are arbitrary nodal quantities. Substituting (33)-(35) into (25) along with using the arbitrariness of $\tilde{U}_{3(p-1)+i}^{s\Sigma}$, $\tilde{U}_{3(p-1)+i}$, and $\tilde{T}_{3(p-1)+i}$, leads to a system of linear algebraic equations

$$\begin{bmatrix}\mathbf{A} & \mathbf{B} & \mathbf{0}\\ \mathbf{B}^T & \mathbf{C} & \mathbf{D}\\ \mathbf{0} & \mathbf{D}^T & \mathbf{E}\end{bmatrix}\begin{Bmatrix}\mathbf{U}^{\Sigma}\\ \mathbf{T}^{\Sigma}\\ \mathbf{U}^{\Delta}\end{Bmatrix}=\begin{Bmatrix}\mathbf{R}_1\\ \mathbf{0}\\ \mathbf{R}_2\end{Bmatrix} \tag{36}$$

where the sub-matrices $\mathbf{A},\mathbf{B},\mathbf{C},\mathbf{D},\mathbf{E}$ are associated with the bilinear operators $\mathscr{A},\mathscr{B},\mathscr{C},\mathscr{D},\mathscr{E}$; sub-vector $\mathbf{R}_1,\mathbf{R}_2$ correspond to the linear operators $\mathscr{R}_1,\mathscr{R}_2$; $\mathbf{U}^{\Sigma}$ is vector of nodal quantities of the sum of the displacement; $\mathbf{U}^{\Delta}$ is vector of nodal quantities of the jump of the displacement and $\mathbf{T}^{\Sigma}$ is vector of nodal quantities of the sum of the traction. The sub-matrices **A**, **B**, **C**, **D**, **E** and sub-vectors $\mathbf{R}_1,\mathbf{R}_2$ are given explicitly by

$$[\mathbf{A}]_{3(p-1)+3,3(q-1)+3}=\frac{\tau^s}{2}\int_{S_c}\Phi_{p,\gamma}(\boldsymbol{y})\Phi_{q,\gamma}(\boldsymbol{y})dS(\boldsymbol{y}) \tag{37}$$

$$[\mathbf{B}]_{3(p-1)+i,3(q-1)+j}=\frac{1}{2}\int_{S_c}\delta_{ij}\Phi_p(\boldsymbol{y})\Phi_q(\boldsymbol{y})dS(\boldsymbol{y}) \tag{38}$$

$$[\mathbf{C}]_{3(p-1)+i,3(q-1)+j}=-\int_{S_c}\Phi_p(\boldsymbol{y})\int_{S_c}U_j^i(\xi-\boldsymbol{y})\Phi_q(\xi)dS(\xi)dS(\boldsymbol{y}) \tag{39}$$

$$\begin{aligned}[\mathbf{D}]_{3(p-1)+i,3(q-1)+j}=&-\int_{S_c}\Phi_p(\boldsymbol{y})\int_{S_c}G_{mj}^i(\boldsymbol{\xi}-\boldsymbol{y})D_m\Phi_q(\boldsymbol{\xi})dS(\boldsymbol{\xi})dS(\boldsymbol{y})\\&+\int_{S_c}\Phi_p(\boldsymbol{y})\int_{S_c}H_{mj}^i(\boldsymbol{\xi}-\boldsymbol{y})n_m(\boldsymbol{\xi})\Phi_q(\boldsymbol{\xi})dS(\boldsymbol{\xi})dS(\boldsymbol{y})\end{aligned} \tag{40}$$

$$[\mathbf{E}]_{3(p-1)+i,3(q-1)+j}=-\int_{S_c}D_t\Phi_p(\boldsymbol{y})\int_{S_c}C_{mj}^{ti}(\boldsymbol{\xi}-\boldsymbol{y})D_m\Phi_q(\boldsymbol{\xi})dS(\boldsymbol{\xi})dS(\boldsymbol{y})+[\mathbf{A}]_{3(p-1)+i,3(q-1)+j} \tag{41}$$

$$[\mathbf{R}_1]_{3(p-1)+i}=\frac{1}{2}\int_{S_c}\Phi_p(\mathbf{y})t_i^{0\Sigma}(\mathbf{y})dS(\mathbf{y})\;;\quad[\mathbf{R}_2]_{3(p-1)+i}=\frac{1}{2}\int_{S_c}\Phi_p(\mathbf{y})t_i^{0\Delta}(\mathbf{y})dS(\mathbf{y}) \tag{42}$$

$$[\mathbf{U}^{\Sigma}]_{3(q-1)+i}=U_{3(q-1)+i}^{\Sigma}\;;\quad[\mathbf{U}^{\Delta}]_{3(q-1)+i}=U_{3(q-1)+i}^{\Delta}\;;\quad[\mathbf{T}^{\Sigma}]_{3(q-1)+i}=T_{3(q-1)+i}^{\Sigma} \tag{43}$$

3.2. Numerical integration

To evaluate the sub-matrices **A**, **B**, **C**, **D**, **E** and sub-vectors $\mathbf{R}_1$, $\mathbf{R}_2$ numerically, the single and double surface integrals must be properly treated. All single surface integrals contain regular integrands and can be efficiently and accurately integrated using standard Gaussian quadrature. Unlike single surface integrals, double surface integrals can be categorized into three types depending on a pair of elements resulting from the discretization of the surface S_c. The first type is termed a regular double surface integral since its integrand is not singular with only mild variation. This type of integral arises when both elements in a pair are relatively remote in comparison with their characteristic size. Similar to the single surface integral, all regular double surface integrals can be accurately integrated by Gaussian quadrature. The second type, termed weakly singular double surface integrals, arises when both elements in a pair are identical and, therefore, the integrand is weakly singular due to the involved kernels. Although these integrals exist in an ordinary sense, it was pointed out by Xiao [45] that they cannot be accurately integrated by standard Gaussian quadrature. To circumvent such difficulty, similar techniques based on integrand regularization via a series of transformations proposed by Li and Han [46], Hayami and Brebbia [47] and Xiao [45] are employed. The last type of double surface integrals, which are considered most challenging, is a nearly singular integral. The integrand of these integrals is nearly singular since both elements in a pair are relatively close in comparison with their characteristic size and this renders the kernels appearing in those integrals nearly singular and exhibiting rapid variation. Similar to the weakly singular integrals, Gaussian quadrature cannot be used to integrate nearly singular integrals efficiently. Special techniques proposed by Hayami [48], Hayami and Matsumoto [49], and Xiao [45] are adopted to perform the numerical integration.

4. Numerical results

First, to verify the formulation and numerical implementation, the penny-shaped crack in an unbounded domain is considered, to compare results with existing benchmark solutions. Next the elliptical crack and two interacting penny-shaped cracks in an unbounded domain are considered.

In the analysis, three meshes with different levels of refinement are utilized to investigate the convergence of solutions. Nine-node isoparametric elements are used to discretize the entire crack-front while the other parts of the crack surfaces are discretized by eight-node and six-node isoparametric elements. The material Si [100] is used for all of numerical examples, where properties of the bulk material and residual surface tension $E = 107\,GPa$, $\nu = 0.33$ and $\tau^s = 0.6056\,N/m$ are obtained from Miller and Shenoy [50]. For convenience in the handling of

numerical analysis, presentation of results and demonstration of the influence of residual surface tension, all involved quantities are normalized in a proper fashion. For instance, the unknown sum of the traction is normalized by the shear modulus μ (i.e., $t_0^{\Sigma} = t^{\Sigma}/\mu$); the unknown sum and jump of the crack-face displacement are normalized by a special length scale $\Lambda = \tau^s/\mu = 0.01506\ nm$ (i.e., $u_0^{\Delta} = u^{\Delta}/\Lambda$ and $u_0^{\Sigma} = u^{\Sigma}/\Lambda$); all characteristic lengths representing the geometry of the crack such as the crack radius *a*, semi-major axis *a* and semi-minor axis *b* are normalized by the length scale Λ (e.g., $a_0 = a/\Lambda$ and $b_0 = b/\Lambda$); and the prescribed traction on the crack surface is normalized by the shear modulus μ (i.e., $t_{i0} = t_i^0/\mu$) .

4.1. Penny-shaped crack in an unbounded domain

As a means for verifying the current technique, the problem of a penny-shaped crack of radius *a* embedded in an isotropic, linear elastic infinite medium is considered (Fig. 3(a)). The crack is subjected to self-equilibrated, uniformly distributed normal traction $t_3^+ = -t_3^- = t^0$. This problem has been previously solved by [20, 21] using Hankel integral transforms with a solution technique for dual integral equations and will be the benchmark solution to validate the proposed FEM-SGBEM technique. The three meshes of the crack surface are shown in Fig. 3(b).

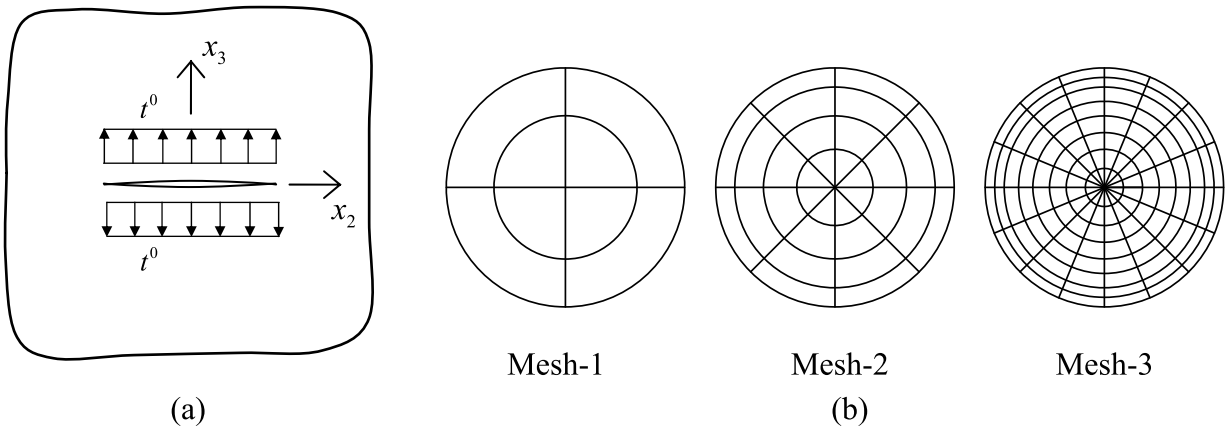

Fig. 3. (a) Schematic of a penny-shaped crack of radius *a* embedded in an isotropic, linear elastic infinite medium subjected to uniformly distributed normal traction $t_3^+ = -t_3^- = t^0$; (b) Meshes adopted in the analysis. Mesh-1: 8 elements and 29 nodes. Mesh-2: 32 elements and 105 nodes. Mesh-3: 128 elements and 401 nodes.

The normalized crack opening displacement and normalized stresses in the vicinity of crack-front, when the influence of the residual surface tension is taken into account, are shown in Fig. 4. Results are compared with those obtained by an analytical technique [20, 21]. It is seen that

the current technique yields solutions that agree very well with the benchmark solutions for both crack opening displacement and stresses σ_{11}, σ_{22}, σ_{33} in the vicinity of crack-front.

To further examine the influence of residual surface tension, the normalized crack opening displacement and the normalized vertical stress σ_{33} in the vicinity of crack-front with different values of residual surface tension τ^s ranging from 0 to 1.0 *N/m* are shown in Fig. 5. It can be concluded that the residual surface tension exhibits significant influence on the crack opening displacement and the vertical stress. In particular, as τ^s becomes larger, the deviation of results from the classical case (i.e., without residual surface tension) significantly increases and, clearly, it makes the elastic medium much stiffer.

To demonstrate the size-dependent behavior of results due to the presence of residual surface tension, the crack opening displacement and the vertical stress in the vicinity of the crack-front are shown in Fig. 6 for both the classical case and the present study. It is evident that, by including the residual surface tension effects in the mathematical model, the solutions exhibit size-dependent behavior. In particular, the normalized crack opening displacement and vertical stress in the vicinity of crack-front depend significantly on the crack size and this is in contrast with the classical case where the normalized crack opening displacement and normalized vertical stress are independent of crack radius.

4.2. Elliptical crack in infinite domain

To demonstrate the capability of the proposed technique for treating mode-I cracks of arbitrary shape, an elliptical crack embedded in an isotropic, linear elastic infinite domain is considered (see Fig. 7(a)). The crack-front is parameterized in terms the parameter t by

$$x_1 = a\cos t, \quad x_2 = b\sin t, \quad x_3 = 0; \quad t \in [0, 2\pi] \tag{44}$$

where a and b are the major and minor semi-axes of the crack, respectively. The crack is subjected to a self-equilibrated, uniformly distributed normal traction $t_3^+ = -t_3^- = t^0$. Numerical results are presented for the aspect ratio $a/b = 1, 2, 3$ with the three meshes shown in Fig. 7(b) used to model the elliptic crack.

The normalized crack opening displacement and the normalized stress σ_{33}/t^0 along the minor axis, when the influence of the residual surface tension is included, are presented in Fig. 8 for aspect ratio $a/b = 1, 2, 3$. Clearly, convergent results of crack opening displacement are obtained with Mesh-2 and Mesh-3 for all three aspect ratios (see Fig. 8(a)). As be seen in Fig. 8, when the aspect

ratio a/b increases, the influence of residual surface tension on the crack opening displacement and the stresses in the vicinity of crack decreases.

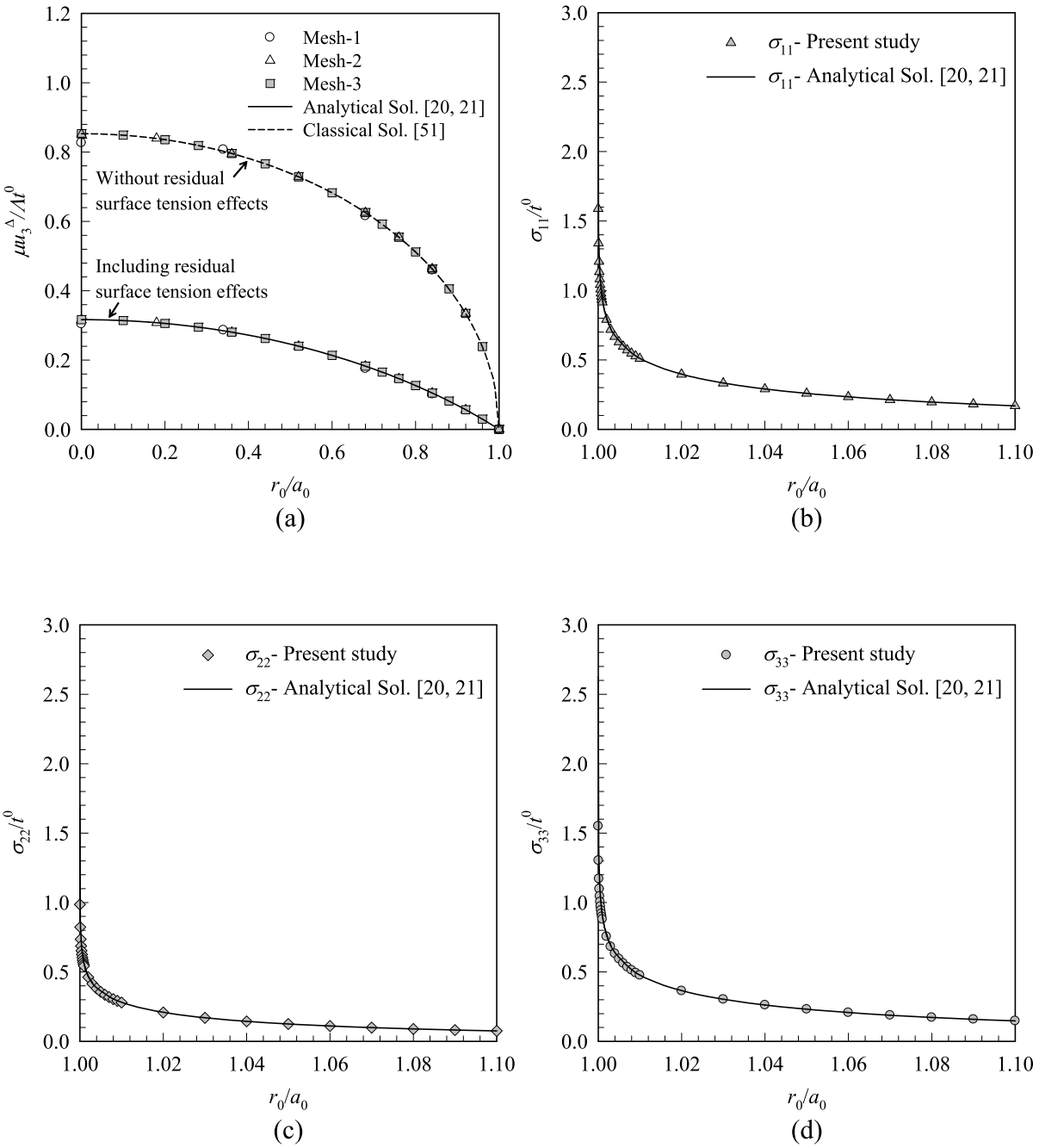

Fig. 4. Penny-shaped crack under uniformly distributed normal traction, for $E = 107\ GPa$, $\nu = 0.33$ and residual surface tension $\tau^s = 0.6056\ N/m$: (a) Normalized crack opening displacement, (b) Normalized stress σ_{11}/t^0 in the vicinity of crack-front, (c) Normalized stress σ_{22}/t^0 in the vicinity of crack-front, and (d) Normalized stress σ_{33}/t^0 in the vicinity of crack-front.

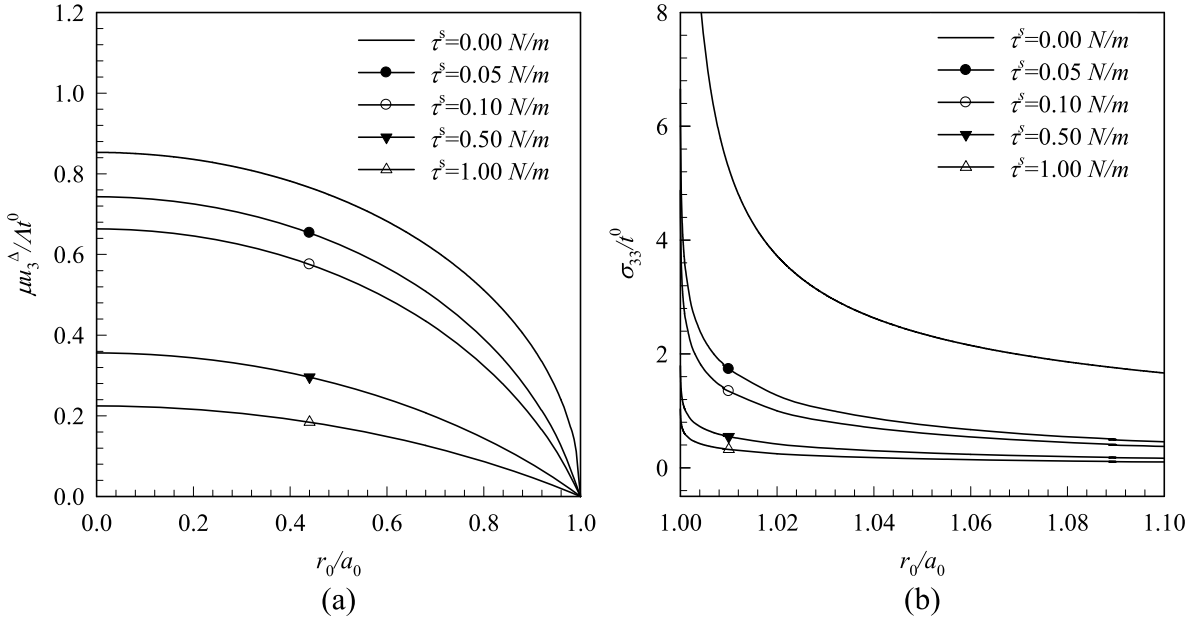

Fig. 5. Penny-shaped crack under uniformly distributed normal traction, for $E = 107\ GPa$, $\nu = 0.33$ for different residual surface tension τ^s : (a) Normalized crack opening displacement and (b) Normalized stress σ_{33}/t^0 in the vicinity of crack-front.

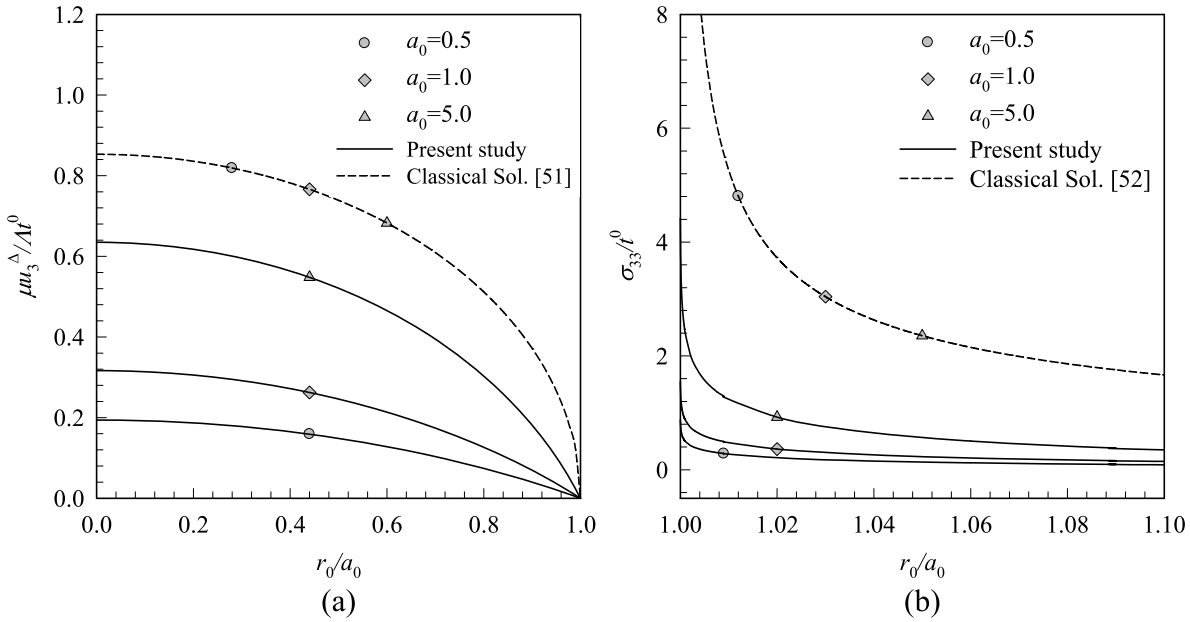

Fig. 6. Penny-shaped crack under uniformly distributed normal traction, for different crack radii $a_0 = a/\Lambda = 0.5, 1.0, 5.0$ for $E = 107\ GPa$, $\nu = 0.33$, $\tau^s = 0.6056\ N/m$: (a) Normalized crack opening displacement and (b) Normalized stress σ_{33}/t^0 in the vicinity of crack-front.

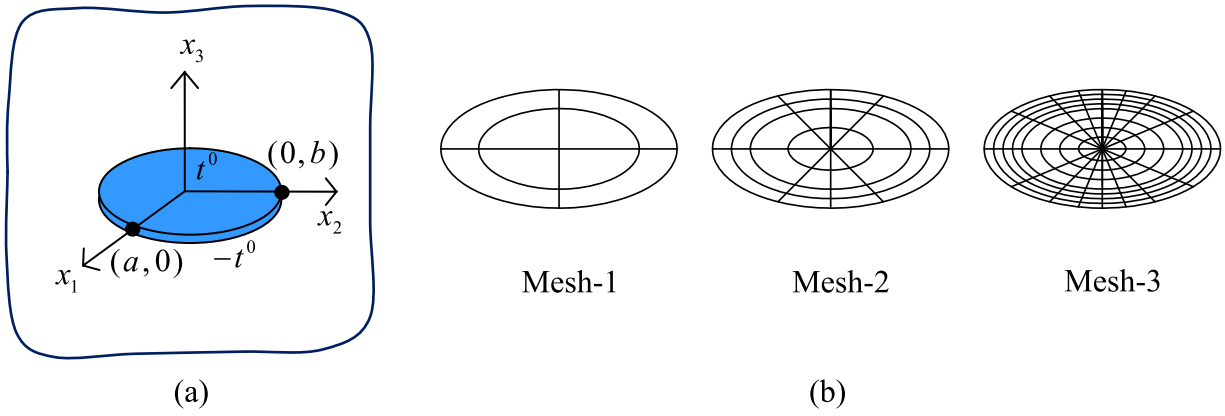

Fig. 7. (a) Schematics of an elliptical crack embedded in an isotropic, linear elastic infinite medium subjected to uniformly distributed normal traction $t_3^+ = -t_3^- = t^0$ and (b) Meshes adopted in the analysis. Mesh-1: 8 elements and 29 nodes. Mesh-2: 32 elements and 105 nodes. Mesh-3: 128 elements and 401 nodes.

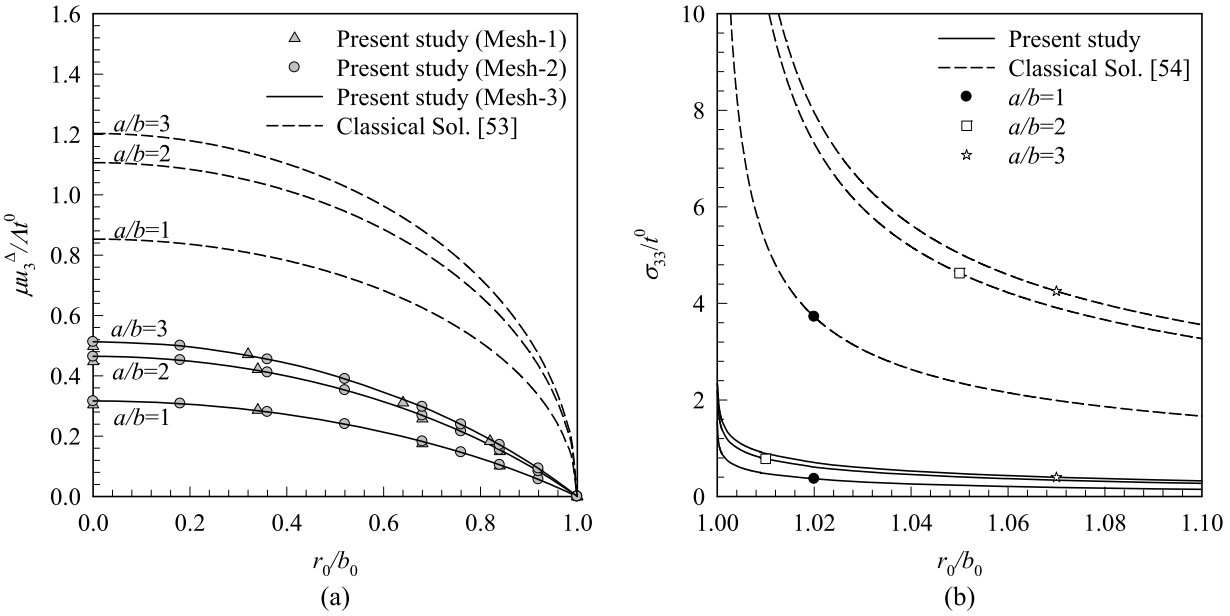

Fig. 8. Elliptical crack under uniformly distributed normal traction, for different aspect ratios $a/b = 1,2,3$ for $E = 107\ GPa, \nu = 0.33$, $\tau^s = 0.6056\ N/m$: (a) Normalized crack opening displacement along minor axis and (b) Normalized stress σ_{33}/t^0 in the vicinity of crack-front along minor axis.

In order to investigate the influence of residual surface tension, the normalized crack opening displacement and the normalized vertical stress σ_{33} in the vicinity of crack-front with different values residual surface tension τ^s ranging from 0 to 1.0 *N/m* are shown in Fig. 9. Aspect ratio $a/b = 2,3$ are considered in this case. As shown in Fig. 9, the influence of residual surface tension is also significant and the medium is stiffer when the residual surface tension increases.

To examine the size-dependent behavior of results due to the influence of residual surface tension, the crack opening displacement and the vertical stress in the vicinity of crack-front for $a_0 = 0.5, 1.0, 5.0$ and two aspect ratios $a/b = 2,3$ are shown in Fig. 10. As can be seen in Fig. 10, the normalized crack opening displacement and normalized stresses in the vicinity of crack-front are size-dependent. It is contrary to the classical case (i.e., without residual surface tension effects), the solutions are size-independent. When the crack-size or the aspect ratio decreases, the influence of residual surface tension becomes significant in the sense that the medium is stiffer.

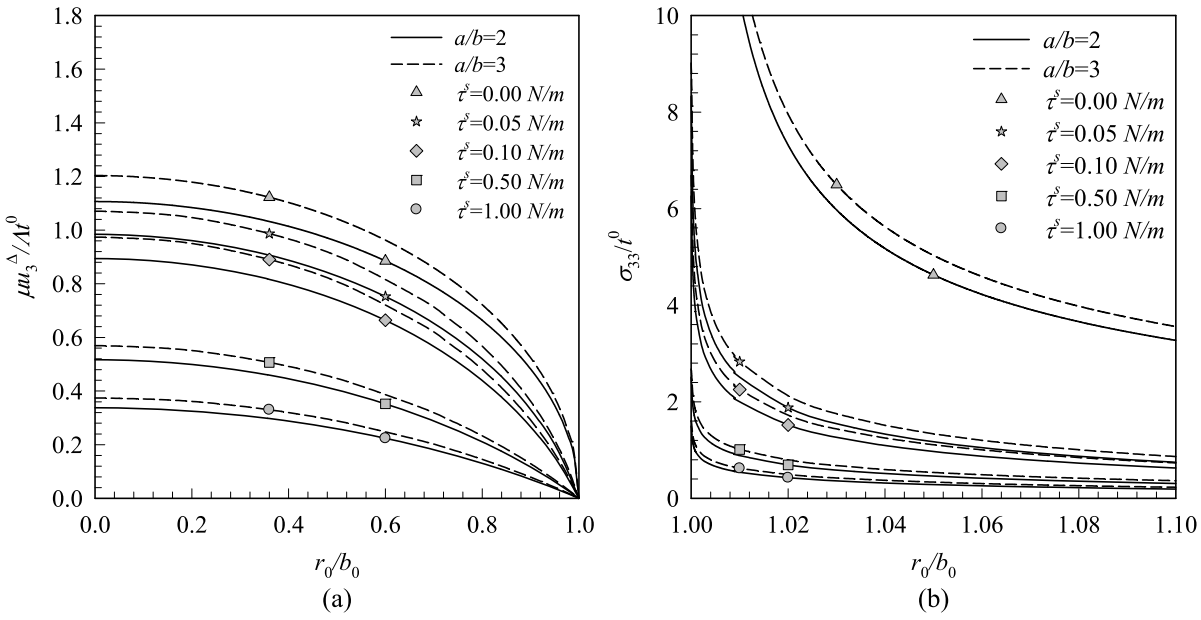

Fig. 9. Elliptical crack under uniformly distributed normal traction for different residual surface tension τ^s , for $E = 107\ GPa, \nu = 0.33$, for different aspect ratios $a/b = 2,3$: (a) Normalized crack opening displacement along minor axis and (b) Normalized stress σ_{33}/t^0 in the vicinity of crack-front along minor axis.

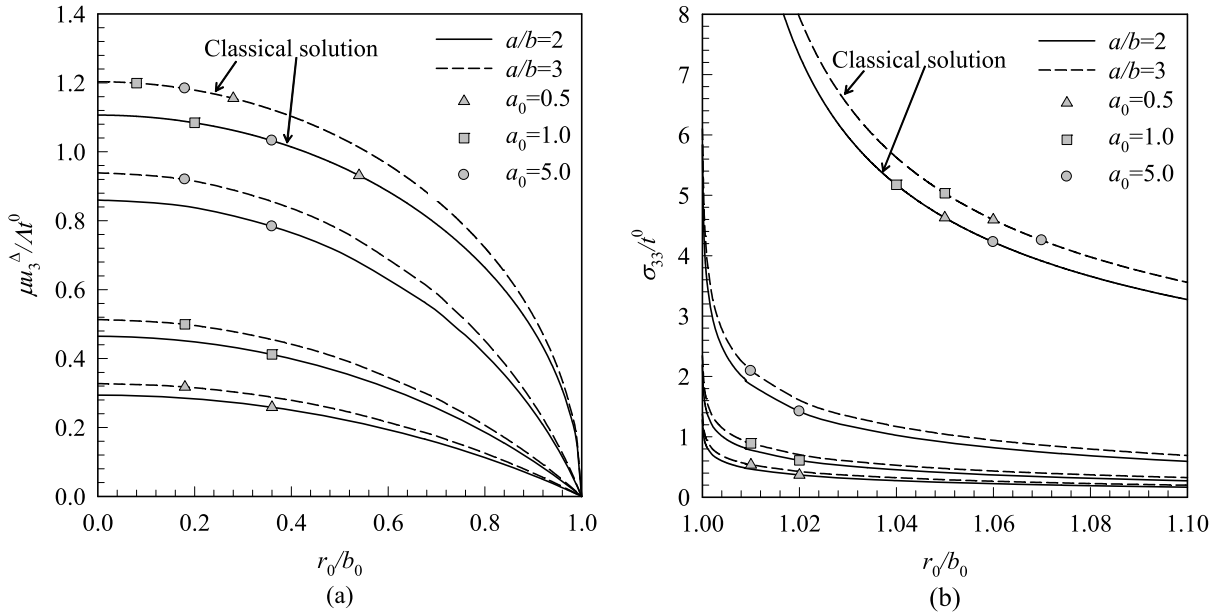

Fig. 10. Elliptical crack under uniformly distributed normal traction for different crack radii $a_0 = a/\Lambda = 0.5, 1.0, 5.0$ for $E = 107\ GPa$, $\nu = 0.33$, $\tau^s = 0.6056\ N/m$, for different aspect ratios $a/b = 2, 3$: (a) Normalized crack opening displacement along minor axis and (b) Normalized stress σ_{33}/t^0 in the vicinity of crack-front along minor axis.

4.3. Two interacting penny-shaped cracks in an unbounded domain

As a final example, we demonstrate another feature of the current technique, viz. modeling multiple cracks, by considering a pair of identical penny-shaped cracks of radius *a* embedded in an isotropic, linear elastic unbounded domain as shown in Fig. 11(a). The distance between the centers of the two cracks is denoted by *h*. Both cracks are subjected to a self-equilibrated, uniformly distributed normal traction $t_3^+ = -t_3^- = t^0$. Here, the influence of the interaction between the two cracks on the maximum crack opening displacement is considered. To investigate size-dependent behavior, two cases are considered where the normalized radii of the identical penny-shaped cracks are taken as $a_0 = 1$ and 10. The three meshes showing in Fig. 11(b) are used to test the convergence of numerical solution.

The normalized crack opening displacement of one of the penny-shaped cracks with radius $a_0 = 10$ is shown in Fig. 12 for $h/a = 2.4$. It is seen that convergent results of the normalized crack opening displacement are obtained and the residual surface tension has a significant influence on the crack opening displacement.

To study the interaction between two cracks, the normalized maximum crack opening displacement is plotted for different values of h/a in Fig. 13. It can be seen in Fig. 13 that, in agreement with previous examples of a penny-shaped crack and an elliptical crack, the maximum crack opening displacement decreases when the residual surface tension increases. The medium becomes much stiffer with the presence of the residual surface tension.

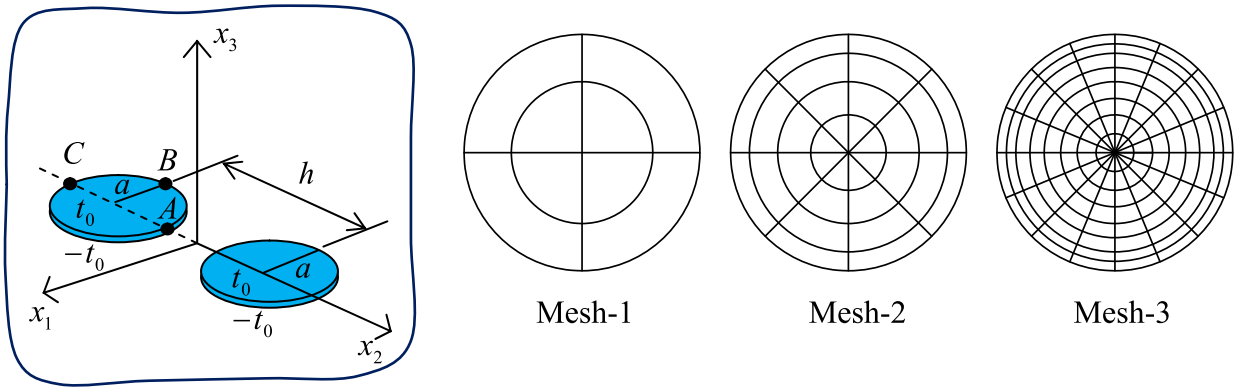

(a) (b)

Fig. 11. (a) Schematic of a pair of penny-shaped cracks of radius a embedded in an isotropic, linear elastic infinite medium subjected to uniformly distributed normal traction $t_3^+ = -t_3^- = t^0$ and (b) Meshes adopted for each crack. Mesh-1: 8 elements and 29 nodes. Mesh-2: 32 elements and 105 nodes. Mesh-3: 128 elements and 401 nodes.

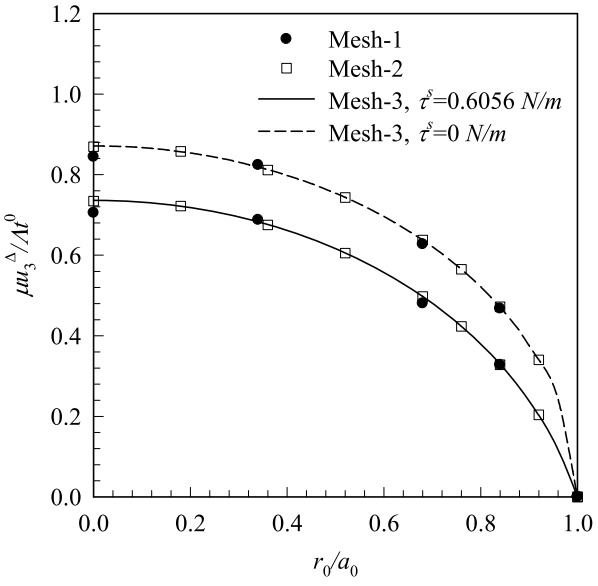

Fig. 12. Normalized crack opening displacement for a pair of penny-shaped cracks with radius $a_0 = 10$ and $h/a = 2.4$ under uniformly distributed normal traction, for $E = 107\,GPa$, $\nu = 0.33$ and $\tau^s = 0.6056\,N/m$.

It can also be observed from Figs. 13(a), 13(b) and 13(c) that results for the case of two interacting cracks converge very fast to those of a single crack when the residual surface tension increases. In particular, as the value of h/a is greater than 8, 5 and 3.5 for the classical case, $\tau^s = 0.6056\,N/m$, and $\tau^s = 1\,N/m$, respectively, the normalized maximum crack opening displacement of the two interacting crack and that of the single crack are nearly identical. This not only implies the significant reduction of the interaction between the two cracks due to the presence of the residual surface tension but also provides the applicable range of the aspect ratio h/a to allow the replacement of the two-crack model by a single crack model. In addition, as clearly indicated in Figs. 13(a) and 13(d), the interaction between the two interacting cracks for the classical case is size-independent (i.e., solutions of the two cracks converge asymptotically to that of the single crack in the identical manner). In the contrary, when the residual surface tension is incorporated in the mathematical model, the size-dependent behavior can be clearly observed by comparing results in Figs. 13(b), 13(e) and results in Figs. 13(c), 13(f), respectively. The decrease in the crack size also lowers the interaction between the two cracks.

5. Conclusions

A computationally efficient numerical technique capable of modeling mode-I planar cracks in three-dimensional, linearly elastic media incorporating the influence of residual surface tension has been established. The governing equations have been formulated based on the classical theory of linear elasticity for the bulk medium and the Gurtin-Murdoch surface elasticity model for the infinitesimally thin layers on the crack surfaces. The system of governing equations has been solved numerically by using the FEM-SGBEM coupling procedure. Numerical results for the penny-shaped crack problem have been compared with the analytical solution to validate the proposed FEM-SGBEM method. By solving both the elliptical crack and two interacting cracks problems, the current technique has been found computationally promising to treat mode-I planar cracks including residual surface tension effects, for arbitrary shaped cracks and multiple cracks in three-dimensional isotropic linear elastic media. It has also been shown that the residual surface tension has a significant influence on the crack opening displacement and stresses in the vicinity of crack-front. Consideration of the surface stresses in the mathematical model not only renders the material stiffer but also introduces the size-dependency behavior of the solution. The presence of residual surface tension also tends to weaken the interaction between multiple cracks.

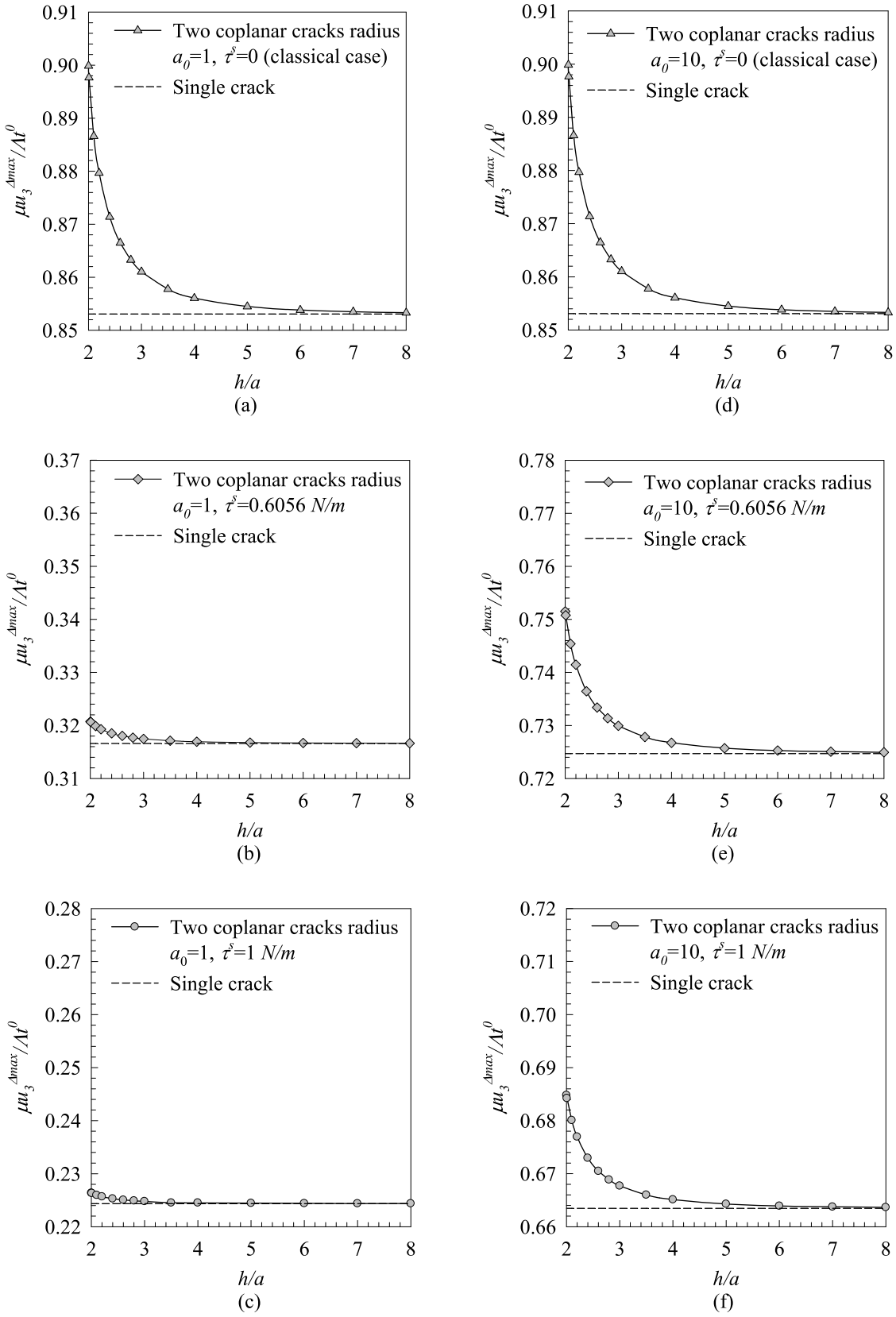

Fig. 13. Normalized maximum crack opening displacement for a pair of identical penny-shaped cracks under uniformly distributed normal traction, for $E = 107\ GPa$, $\nu = 0.33$: (a)-(c) $a_0 = 1$ and (d)-(f) $a_0 = 10$.

Acknowledgements

The first author is very grateful for a JICA AUN/SEED-Net scholarship. Financial support from JICA AUN/SEED-Net and Thailand Research Fund through Grant No. MRG5380159 and Grant No. BRG5480006 are gratefully acknowledged. Some parts of the work presented in this paper were completed while the first author was visiting Tokyo Institute of Technology.

References

[1] Yakobson, B. I., Nanomechanics. In: Goddard, W. A., Brenner, D. W., Lyshevski, S. E. and Iafrate G. J. editors, Handbook of nanoscience, engineering and technology. CRC Press, Boca Raton, 2003, pp. 17-1–17-18.

[2] Gurtin, M. E. and Murdoch, A. I., A continuum theory of elastic material surfaces, Archive for Rational Mechanics and Analysis 1975; 57(4):291-323.

[3] Gurtin, M. E. and Murdoch, A. I., Surface stress in solids, International Journal of Solids and Structures 1978; 14(6):431-440.

[4] He, L. H., Lim, C. W. and Wu, B. S., A continuum model for size-dependent deformation of elastic films of nano-scale thickness, International Journal of Solids and Structures 2004; 41(3-4): 847-857.

[5] Dingreville, R., Qu, J. and Cherkaoui, M., Surface free energy and its effect on the elastic behavior of nano-sized particles, wires and films, Journal of the Mechanics and Physics of Solids 2005; 53(8):1827-1854.

[6] Huang, D. W., Size-dependent response of ultra-thin films with surface effects, International Journal of Solids and Structures 2008; 45(2):568-579.

[7] Tian, L. and Rajapakse, R. K. N. D., Finite element modeling of nanoscale inhomogeneities in an elastic matrix, Computational Materials Science 2007; 41(1):44-53.

[8] Tian, L. and Rajapakse, R. K. N. D., Analytical Solution for Size-Dependent Elastic Field of a Nanoscale Circular Inhomogeneity, ASME Journal of Applied Mechanics 2007; 74(3):568-574.

[9] Tian, L. and Rajapakse, R. K. N. D., Elastic field of an isotropic matrix with a nanoscale elliptical inhomogeneity, International Journal of Solids and Structures 2007; 44(24):7988-8005.

[10] Pinyochotiwong, Y., Rungamornrat, J., Senjuntichai, T., Rigid frictionless indentation on

elastic half space with influence of surface stresses, International Journal of Engineering Science 2013; 71(0): 15-35.

[11] Wu, C. H., The effect of surface stress on the configurational equilibrium of voids and cracks, Journal of the Mechanics and Physics of Solids 1999; 47(12):2469-2492.

[12] Wang, G. F., Feng, X. Q., Wang, T. J. and Gao, W., Surface Effects on the Near-Tip Stresses for Mode-I and Mode-III Cracks, ASME Journal of Applied Mechanics 2008; 75(1):011001-011005.

[13] Fu, X. L., Wang, G. F. and Feng, X. Q., Surface effects on the near-tip stress fields of a mode-II crack, International Journal of Fracture 2008; 151(2):95-106.

[14] Fu, X. L., Wang, G. F. and Feng, X. Q., Surface effects on mode-I crack tip fields: A numerical study, Engineering Fracture Mechanics 2010; 77(7):1048-1057.

[15] Fang, Q. H., Liu, Y., Liu, Y. W. and Huang, B. Y., Dislocation emission from an elliptically blunted crack tip with surface effects, Physica B: Condensed Matter 2009; 404(20):3421-3424.

[16] Kim, C. I., Schiavone, P. and Ru, C. Q., Analysis of a mode-III crack in the presence of surface elasticity and a prescribed non-uniform surface traction, Zeitschrift für angewandte Mathematik und Physik 2010; 61(3):555-564.

[17] Kim, C. I., Schiavone, P. and Ru, C. Q., The effect of surface elasticity on a Mode-III interface crack, Archives of Mechanics 2011; 63(3):267-286.

[18] Kim, C. I., Schiavone, P. and Ru, C. Q., Analysis of Plane-Strain Crack Problems (Mode-I & Mode-II) in the Presence of Surface Elasticity, Journal of Elasticity 2011; 104(1):397-420.

[19] Nan, H. and Wang, B., Effect of residual surface stress on the fracture of nanoscale materials, Mechanics Research Communications 2012; 44(0):30-34.

[20] Intarit, P., Senjuntichai, T., Rungamornrat, J. and Rajapakse, R. K. N. D., Stress analysis of penny-shaped crack considering the effects of surface elasticity, Proceedings of 20th Annual International Conference on Composites or Nano Engineering (ICCE-20), Ramada Beijing North Hotel, Beijing, P.R. China 2012.

[21] Intarit, P., Solutions of elastic medium with surface stress effects, Ph.D. Dissertation 2013, Chulalongkorn University, Thailand.

[22] Blandford, G. E., Ingraffea, A. R. and Liggett, J. A., Two-diemnsional stress intensity factor computation using boundary element method, International Journal for Numerical Methods in

Engineering 1981; 17: 387-440

[23] Cruse, T. A., Boundary element analysis in computational fracture mechanics, Kluwer Academic Publishers, Dordrecht, 1988.

[24] Gray, L. J., Martha, L. F. and Ingraffea, A. R., Hypersingular integrals in boundary element fracture analysis, International Journal for Numerical Methods in Engineering 1990; 29: 1135-1158.

[25] Sutradhar, A. and Paulino, G. H., Symmetric Galerkin boundary element computation of T-stress and stress intensity factors for mixed-mode cracks by the interaction integral method, Engineering Analysis with Boundary Elements 2004; 28(11): 1335-1350

[26] Pan, E. and Yuan, F. G., Boundary element analysis of three-dimensional cracks in anisotropic solids, International Journal for Numerical Methods in Engineering 2000; 48: 211-237

[27] Saez, A., Ariza, M. P. and Dominguez, J., Three-dimensional fracture analysis in transversely isotropic solids, Engineering Analysis with Boundary Elements 1997; 20: 287-298.

[28] Gu, H. and Yew, C. H., Finite element solution of a boundary integral equation for mode I embedded three-dimensional fractures, International Journal for Numerical Methods in Engineering 1988; 26:1525-1540.

[29] Xu, G., Ortiz, M., A variational boundary integral method for the analysis of 3-D cracks of arbitrary geometry modeled as continuous distributions of dislocation loops, International Journal for Numerical Methods in Engineering 1993; 36: 3675-3701.

[30] Bonnet, M., Regularized direct and indirect symmetric variational BIE formulations for three-dimensional elasticity, Engineering Analysis with Boundary Elements 1995; 15: 93-102.

[31] Li, S., Mear, M. E., Singularity-reduced integral equations for displacement discontinuities in three-dimensional linear elastic media, International Journal of Fracture 1998; 93: 87-114.

[32] Li, S., Mear, M. E. and Xiao, L., Symmetric weak-form integral equation method for three-dimensional fracture analysis, Computer Methods in Applied Mechanics and Engineering 1998; 151: 435-459.

[33] Xu, G., A variational boundary integral method for the analysis of three-dimensional cracks of arbitrary geometry in anisotropic elastic solids, Journal of Applied Mechanics 2000; 67: 403-408.

[34] Frangi, A., Novati, G., Springhetti, R. and Rovizzi, M., 3D fracture analysis by the symmetric

Galerkin BEM, Computational Mechanics 2002; 28: 220-232.

[35] Rungamornrat, J., Analysis of 3D cracks in anisotropic multi-material domain with weakly singular SGBEM, Engineering Analysis with Boundary Elements 2006; 30 (10): 834-846.

[36] Rungamornrat, J. and Mear, M. E., Weakly-singular, weak-form integral equations for cracks in three-dimensional anisotropic media, International Journal of Solids and Structures 2008; 45(5):1283-1301.

[37] Rungamornrat, J. and Mear, M. E., A weakly-singular SGBEM for analysis of cracks in 3D anisotropic media, Computer Methods in Applied Mechanics and Engineering 2008; 197:4319-4332.

[38] Rungamornrat, J. and Senjuntichai, T., Regularized boundary integral representations for dislocations and cracks in smart media, Smart materials and structures 2009; 18:074010 (14pp).

[39] Frangi, A. and Novati, G., BEM-FEM coupling for 3D fracture mechanics applications, Computational Mechanics 2003; 32: 415-422

[40] Rungamornrat, J. and Mear, M. E., SGBEM-FEM coupling for analysis of cracks in 3D anisotropic media, International Journal for numerical methods in Engineering 2011; 86: 224-248.

[41] Bonnet, M., Maier, G. and Polizzotto, C., Symmetric Galerkin boundary element methods, Applied Mechanics Reveiws 1998; 51: 669-703.

[42] Bathe, K.J., Finite Element Procedures, Prentice-Hall, New Jersey, 1990.

[43] Hughes, T.J.R., The finite element method: linear static and dynamic finite element analysis, Dover Publications, New Jersey, 2000.

[44] Zienkiewicz, O.C., Taylor, R.L., The finite element method: Solid mechanics, volume 2, Butterworth-Heinemann, Oxford, 2000.

[45] Xiao, L., Symmetric weak-form integral equation method for three-dimensional fracture analysis, Ph.D. Dissertation 1998, The University of Texas at Austin, Texas.

[46] Li, H.B. and Han, G.M., A new method for evaluating singular integral in stress analysis of solids by the direct boundary element method, International Journal for Numerical Methods in Engineering 1985; 21: 2071-2098.

[47] Hayami, K. and Brebbia, C.A., Quadrature methods for singular and nearly singular integrals

in 3-D boundary element method, Boundary Element X, 1988, 237-264, Springer-Verlag, Berlin.

[48] Hayami, K., A projection transformation method for nearly singular surface boundary element integrals. In: Brebbia, c.a., Orszag, S.A. (eds) Lecture notes in Engineering 1992; 73; 1-2. Springer-Verlag, Berlin.

[49] Hayami, K. and Matsumoto, H., A numerical quadrature for nearly singular boundary element integrals, Engineering Analysis with Boundary Elements 1994; 13: 143-154.

[50] Miller, R. E. and Shenoy, V. B., Size-dependent elastic properties of nanosized structural elements, Nanotechnology 2000; 11(3):139-147.

[51] Tada, H., Paris, P. C., and Irwin, G. R., The Stress Analysis of Cracks Handbook, American Society of Mechanical Engineers, 2000.

[52] Kassir, M.K., Sih, G.C., Three-dimensional Crack Problems: A New Selection of Crack Solutions in Three-dimensional Elasticity, vol. 2, Noordhoff International Publishing, Leyden, 1975.

[53] Zeng-shen, C., Discussion on the SIF for points on border of elliptical flat crack inside infinite solid under uniform tension, Applied Mathematics and Mechanics 1982; 3(4): 521-526.

[54] Green, A. E., Sneddon, I. N., The distribution of stress in the neighborhood of a flat elliptical crack in an elastic solid, Mathematical Proceedings of the Cambridge Philosophical Society 1950; 46(1):159–163.